This is to certify that the
dissertation entitled

ELECTROCHEMICAL OXIDATION AND DETECTION OF ALIPHATIC POLYAMINES AT BORON-DOPED DIAMOND THIN-FILM ELECTRODES

presented by

Małgorzata A. Witek

has been accepted towards fulfillment
of the requirements for the

Ph.D. degree in Chemistry

Greg M. Swain
Major Professor's Signature

12-3-2002
Date

MSU is an Affirmative Action/Equal Opportunity Institution

ELECTROCHEMICAL OXIDATION AND DETECTION OF ALIPHATIC POLYAMINES AT BORON-DOPED DIAMOND THIN-FILM ELECTRODES

By

Małgorzata A. Witek

A DISSERTATION

Submitted to
Michigan State University
in partial fulfillment of the requirements
for the degree of

DOCTOR OF PHILOSOPHY

DEPARTMENT of CHEMISTRY

2002

ABSTRACT

ELECTROCHEMICAL OXIDATION AND DETECTION OF ALIPHATIC POLYAMINES AT BORON-DOPED DIAMOND THIN-FILM ELECTRODES

By

Małgorzata A. Witek

The electrochemical responsiveness of boron-doped microcrystalline and nanocrystalline diamond thin films was investigated by cyclic voltammetry. The morphology and microstructure of both types of diamond was studied with atomic force microscopy (AFM), scanning electron microscopy (SEM), transmission electron microscopy (TEM), x-ray diffraction (XRD), visible Raman spectroscopy, and secondary ion mass spectrometry (SIMS).

Highly boron-doped microcrystalline and nanocrystalline diamond thin-film electrodes exhibited a wide working potential window in aqueous electrolytes (3-3.5 V), a low voltammetric background current, and an excellent responsiveness toward a number of redox systems (i.e., $Fe(CN)_6^{-3/-4}$, $Ru(NH_3)_6^{+2/+3}$, $IrCl_6^{-2/-3}$, and methyl viologen) without pretreatment. The relatively large heterogeneous electron transfer rate constants (10^{-2}-10^{-1} cm/s) for all the couples indicated that diamond has a sufficient charge carrier density over the wide potential range to support a rapid electron transfer.

The electrochemical response of both types of films for the oxidation of aliphatic polyamines was also studied. Boron-doped diamond is unique in the carbon electrode family in that it provides an active and stable response for this class of analytes. The electrode's ability to support the amine oxidation, a reaction that involves anodic oxygen

transfer, strongly depends on the chemical composition at film surface (i.e., presence of surface boron sites and sp^2-bonded non-diamond carbon impurities). A model for amine oxidation was proposed in which the non-diamond carbon impurity sites, located primarly in the grain boundaries, generate hydroxyl radical (OH•) at lower overpotential than surrounding diamond matrix. The radical attacks the polyamine molecule coordinated at a surface boron site nearby. The fastest reaction rates for amine oxidation were observed for diamond electrodes at which the formation of OH• had appreciable rate, and that were heavily doped with boron. It was shown that aliphatic polyamines can be quantitatively electrooxidized at both boron-doped microcrystalline and nanocrystalline diamond thin-film electrodes.

Flow injection analysis investigations of cadaverine, putrescine, spermine and spermidine indicated that these analytes can be detected stably and reproducibly in alkaline media at constant applied potential. A linear dynamic range from 0.1 to 1000 μM and a limit of detection near 0.1 μM, 20 μL inj., (S/N=3) were commonly observed for these analytes. Response variability as low as 2-4 % was achieved. The long-term response stability was excellent with no evidence of permanent electrode fouling by the reaction products. Liquid chromatographic results demonstrated the possibility of separating the amines isocratically in a revered-phase mode, and detecting the polyamines at constant applied potential.

Polycrystalline boron-doped diamond thin film electrodes possessed the requisite surface structure and chemical composition to support and sustain the oxidation of aliphatic polyamines via an oxygen transfer reaction. The major advantages of using diamond are that no pre- or post-column derivatization, no mobile phase pH adjustment and no pulsed amperometric waveform are necessary for detection.

ACKNOWLEDGMENTS

It's time to say goodbye...

My sincere thanks go to my advisor, Dr. Swain who provided academic directions, support, and who was reminding me of keeping the "good attitude"! I thank you for your patience and a good word you always had. I would also like to thank the members of my committee: Dr. Blanchard, Dr. Posey, and Dr. Baker. Thank you for all the comments concerning my research, but also for your kindness. When I was accepted to graduate school at USU, Dr. B. Brown, Dr. S. Bialkowski, Dr. B. Davidson, Dr. M. Koppang, and Prof. Strojek were always very supportive and helpful. I will always be grateful for the encouragement and help they were willing to offer.

There is the "significant other" in my life, without whom all of this would have never happen. Thank you Mateusz for your courage in life and love throughout.

I would like to thank "The Great People of The Swain Group": Mike, Chen, Jishou, Jian, Show, Grace, Gloria, Prerna, J.B., Jason S., Jin Woo, Zuzanka, Josef, John, Amy, and Doug. It was a pleasure knowing you all and be a part of the team!

Without friends the life would be dreary! Thank you Shannon, Michelle, Sandra, Cindy, Wiesia, and Bogdan! I will always cherish your friendship!

Finally and most importantly, I would like to thank my wonderful family: Mom, Dad, and Sebastian. You have been with me every step of the way! Thank you for your love and support! To my Mother and Father in Law, Kasia, Marek and Martyna - Thank you for your constant encouragement!

I dedicate this dissertation to my wonderful Grandma, who was supportive throughout my life, and taught me to have dreams. What is the most important she taught me to believe, that they can come true...

Małgorzata

Table of Contents

List of Tables ix

List of Figures xii

List of Symbols and Notations xxv

Chapter 1 1

BACKGROUND AND MOTIVATIONS 1

1.1. Aliphatic Polyamines 1

1.1.1. Biological and Enviromental Importance 1

1.1.2. Aliphatic Amine Detection 3

1.2. Properties and Applications of Conductive Diamond Films 8

1.3. Diamond Film Deposition and Doping 13

1.4. Outline of the Dissertation 19

Chapter 2 21

EXPERIMENTAL SECTION 21

2.1. Boron-Doped Diamond Thin Film Growth 21

2.1.1. Microcrystalline Diamond Electrodes Doped Using a Solid State Source. ... 22

2.1.2. Diamond Electrodes Doped with B_2H_6 24

2.1.3. Diamond Acid Washing and Hydrogenation Procedure 26

2.2. Diamond Thin Film Characterization 27

2.2.1. Scanning Electron Microscopy (SEM) 28

2.2.2. Transmission Electron Microscopy (TEM) 28

2.2.3. Atomic Force Microscopy (AFM) 29

2.2.4. Raman Spectroscopy 29

2.2.5. X-Ray Diffraction (XRD) 29
2.2.6. Boron Nuclear Reaction (BNR) 30
2.2.7. Secondary Ion Mass Spectrometry (SIMS) 30
2.2.8. Resistivity 30
2.3. Electrochemical Measurements 31
2.3.1. Cyclic Voltammetry Experiments 31
2.3.2. Rotating Disc Electrode (RDE) Experiments 32
2.3.3. Double-Layer Capacitance 33
2.4. Flow Injection Analysis (FIA) 33
2.5. HPLC System 35
2.6. Chemicals and Reagents 35
Chapter 3 38
THE CHARACTERIZATION AND ELECTROCHEMICAL RESPONSIVENES OF BORON-DOPED MICROCRYSTALLINE DIAMOND THIN-FILM ELECTRODES . 38
3.1. Introduction 38
3.2. Results and Discussion 40
3.2.1. Electrochemical Characteristics 40
3.2.2. Material Characterization 54
3.3. Conclusions 63
Chapter 4 65
THE CHARACTERIZATION AND ELECTROCHEMICAL RESPONSIVENESS OF BORON-DOPED NANOCRYSTALLINE DIAMOND THIN-FILM ELECTRODES... 65
4.1. Introduction 65
4.2. Results and Discussion 68
4.2.1. Electrochemical Responsiveness 68
4.2.2. Material Characterization 78

4.3. Conclusions 86

Chapter 5 ..... **87**

CYCLIC VOLTAMMETRIC STUDIES OF THE ELECTROOXIDATION OF ALIPHATIC POLYAMINE AT BORON-DOPED DIAMOND THIN FILMS **87**

5.1. Introduction 87

5.1.1. Model for Polyamine Oxidation at Polycrystalline Diamond 91

5.2. Results and Discussion 92

5.2.1. Cyclic Voltammetry of Polyamines 92

5.2.2. Effect of the Electrolyte on the Voltammetric Response 97

5.2.3. Effect of pH on the Voltammetric Response 97

5.2.4. Effect of Scan Rate on the Voltammetric Response 101

5.2.5 Effect of Amine Concentration on the Voltammetric Response 103

5.2.6. Importance of Non-Diamond Carbon Impurities 104

5.2.7. Effect of CH_4/H_2 Ratio on the Voltammetric Response 106

5.2.8. Effect of Boron on the Voltammetric Response 112

5.3. Conclusions 130

Chapter 6 ..... **134**

INVESTIGATIONS OF ALIPHATIC POLYAMINE OXIDATION REACTION MECHANISM AT BORON-DOPED DIAMOND THIN-FILM ELECTRODES **134**

6.1. Introduction 134

6.1.1. Non-Active Electrodes 137

6.1.2. Active Electrodes 139

6.2. Results and Discussion 143

6.2.1. Irreversibility of the Process 143

6.2.2. Reaction of the Primary and Secondary Amine Groups 144

6.2.3. Determination of the Ratio Between Number of Protons and Number of Electrons 148
6.2.4. Quantification of Adsorption 149
6.2.5. Rotating Disk Voltammetric Studies 151
6.3. Conclusions 161
Chapter 7 ..... **166**
FLOW INJECTION ANALYSIS INVESTIGATIONS OF ALIPHATIC POLYAMINE OXIDATION AT BORON-DOPED DIAMOND THIN-FILM ELECTRODES **166**
7.1. Introduction 166
7.2. Results and Discussion 168
7.2.1. Hydrodynamic Voltammetric i-E Curves 168
7.2.2. Calibration Curves 181
7.2.3. Response Variability and Stability 188
7.3. Conclusions 196
Chapter 8 ..... **200**
REVERSED-PHASE HPLC SEPARATION AND AMPEROMETRIC DETECTION OF ALIPHATIC POLYAMINES AT BORON-DOPED DIAMOND THIN-FILM ELECTRODES **200**
8.1. Introduction 200
8.2. Results and Discussion 201
8.2.1. Cyclic Voltammetry and Flow Injection Analysis 201
8.2.2. Liquid Chromatography 210
8.3. Conclusion 217
Chapter 9 ..... **218**
SUMMARY **218**
REFERENCES **218**

List of Tables

Table1.1 Analytical Methods Used for Polyamine Separation and Detection 4

Table 2.1 Microcrystalline Diamond Thin Film Deposition Parameters..... 24

Table 2.2 Nanocrystalline Diamond Thin Film Deposition Parameters..... 25

Table 2.3 Boron Concentration and Resistivity for a Nanocrystalline Diamond 26

Table 2.4 Microcrystalline Diamond Thin Film Deposition Parameters..... 27

Table 2.5 Analytical Techniques Used for Film Characterization..... 28

Table 2.6 Molecular Formula and Properties of the Aliphatic Amines 37

Table 3.1 Summary of Cyclic Voltammetric Data and Apparent Heterogeneous Electron Transfer Rate Constants for Boron-Doped Microcrystalline Diamond Films 54

Table 4.1 Cyclic Voltammetric Data for a Boron-Doped Nanocrystalline Diamond Film 71

Table 4.2 Lattice Spacings and Relative Peak Intensities Obtained from XRD Patterns of a Nanocrystalline Diamond Film and a Cubic Diamond Standard 83

Table 5.1 Cyclic Voltammetric Data for 0.1 mM Aliphatic Amine Oxidation 94

Table 5.2 Cyclic Voltammetric Charge Data for 1 mM Amines in 0.01 M Borax Buffer/0.1 M $NaClO_4$..... 99

Table 5.3 Cyclic Voltammetric Background Current Data for Boron-Doped Microcrystalline Diamond Films..... 109

Table 5.4 Cyclic Voltammetric Peak Current and Potential Data for Amines Oxidation at Microcrystalline Diamond Films Deposited with Different CH_4/H_2 Ratios. 112

Table 5.5 Cyclic Voltammetric Data for $Fe(CN)_6^{-3/-4}$, $Ru(NH_3)_6^{+3/+2}$, $IrCl_6^{-2/-3}$ at Boron-Doped Nanocrystalline Diamond Films 118

Table 5.6 Cyclic Voltammetric Data for $Fe^{+2/+3}$ and t-Butyl Catechol at Boron-Doped Nanocrystalline Diamond Films 119

Table 5.7 Summary of Cyclic Voltammetric Peak Current Data for Boron-Doped Nanocrystalline Diamond Electrodes 123

Table 5.8 Summary of Cyclic Voltammetric Peak Potential Data for Boron-Doped Nanocrystalline Diamond Electrode 124

Table 5.9 Summary of Cyclic Voltammetric Data for Boron-Doped Microcrystalline Diamond Electrode 127

Table 5.10 Summary of Cyclic Voltammetric Data for Aliphatic Amines at Boron-Doped Microcrystalline Diamond Electrode 129

Table 6.1 Aliphatic $E_{p/2}$ values as a Function of Solution pH 149

Table6.2 Kinetic Parameters for Amines Oxidation (pH11) at 20 ppm Microcrystalline Boron-Doped Diamond 159

Table 6.3 Kinetic Parameters for Anodic Oxidation of Amines 160

Table 7.1 FIA-EC Background and Noise Signal for Microcrystalline Diamond Film in Carbonate Buffer pH10 169

Table 7.2 FIA-EC Background and Noise Signal for Nanocrystalline Diamond Film in Borax Buffer pH 11. 170

Table 7.3 Amperometric Data Obtained During FIA of Aliphatic Amines at pH 11..... 178

Table 7.4 FIA-EC Data for Aliphatic Polyamines Detection at Microcrystalline Diamond Thin-Film Electrode in Borax Buffer, pH 11.2 183

Table 7.5 FIA-EC Data for Aliphatic Polyamines at a Nanocrystalline Diamond Thin Film Deposited from a 1/94/5 $CH_4/Ar/H_2$ source gas ratio with 20 ppm B_2H_6. 185

Table 7.6 FIA-EC Response Variability Data for Aliphatic Polyamines at a Microcrystalline Diamond Thin Film..... 190

Table 7.7 FIA-EC Data for Aliphatic Mono- and Diamine 198

Table 8.1 Amperometric Detection Figures of Merit for the HPLC Separation of the Aliphatic Polyamines 214

Table 8.2 Amperometric Detection Reproducibility and Stability for the HPLC Separation of the Aliphatic Polyamines 216

List of Figures

Figure 1.1 Structural models of (A) HOPG, (B) GC, and (C) fcc diamond lattice. 9

Figure 1.2 Plot of boron-doped diamond related papers over the last four decades. Results based on SciFinder® search engine..... 10

Figure 1.3 Schematic representation of the physical and chemical processes occurring during CVD diamond growth. 14

Figure 1.4 A diagram for the band structure of boron-doped diamond. 18

Figure 2.1 A photo of the microwave-assisted CVD reactor: (a) diborane and Ar cylinder cabinet, (b) hydrogen cylinder cabinet, (c) methane cylinder cabinet, (d) microwave generator, (e) reactor, (f) mass flow controller and stop valve, (g) power supply for microwave generator, (h) pressure gauge, (i) water chiller, and (j) rotary pump.... 22

Figure 2.2 Design of the electrochemical, three-electrode glass cell. 31

Figure 2.3 Design of the rotating disk electrode. 32

Figure 2.4 Design of the thin-layer electrochemical flow cell. 34

Figure 3.1 Capacitance-potential profiles in 1.0 M KCl for uncoated tungsten and molybdenum, and diamond thin films deposited on W, Mo, and Si substrates. Capacitance values are normalized to the geometric area (0.2 cm^2) of the electrodes. Frequency = 40 Hz. AC amplitude = 10 mV. 41

Figure 3.2 Background cyclic voltammetric i-E curves in 1.0 M KCl for boron-doped microcrystalline diamond thin films deposited on (A) Si, (B) Mo, and (C) W. Scan rate = 0.1 V/s. Electrode geometric = 0.2 cm^2. 43

Figure 3.3 Background cyclic voltammetric i-E curves in 1.0 M KCl for boron-doped, microcrystalline diamond films deposited on (A) Si, (B) Mo, and (C) W. Scan rate = 0.1 V/s. Electrode geometric area = 0.2 cm^2. 44

Figure 3.4 Background cyclic voltammetric i-E curves in 1.0 M HNO_3 for boron-doped, microcrystalline diamond thin films deposited on (A) W and (B) Mo. Scan rate = 0.1 V/s. Electrode geometric area = 0.2 cm^2. 46

Figure 3.5 A Cyclic votammetric i-E curves for 1.0 mM $Fe(CN)_6^{-3/-4}$ in 1 M KCl at diamond films deposited on different substrates. Scan rate = 0.1 V/s. Working electrode area = 0.2 cm^2. 49

Figure 3.5 B Cyclic votammetric i-E curves for 1.0 mM $Ru(NH_3)_6^{+2/+3}$ in 1 M KCl at a diamond films deposited on different substrates. Scan rate = 0.1 V/s. Working electrode area = 0.2 cm^2. 50

Figure 3.5 Cyclic votammetric i-E curves for (C) 0.5 mM $IrCl_6^{-2/-3}$ and (D) 0.1 mM methyl viologen in 1 M KCl, at diamond films deposited on different substrates. Scan rate = 0.1 V/s. Working electrode area = 0.2 cm^2. 51

Figure 3.6 Plots of i_p^{ox} vs scan $rate^{1/2}$ for (A) $Fe(CN)_6^{-3/-4}$, (B) $Ru(NH_3)_6^{+2/+3}$,(C) $IrCl_6^{-2/-3}$, and (D) methyl viologen at diamond films deposited on Si, Mo, and W substrates.53

Figure 3.7 Atomic force microscope images (6 x 6 μm) of boron-doped, micro-crystalline diamond films deposited on (A)silicon, (B)molybdenum, and (C) tungsten. 55

Figure 3.8 SEM image of a boron-doped microcrystalline diamond film deposited on Si. 56

Figure 3.9 Grazing incidence XRD measurement of a boron-doped microcrystalline diamond film deposited on Si at a 0.5 degrees incidence angle. 57

Figure 3.10 Macro-Raman spectra for boron-doped microcrystalline diamond films deposited on W, Mo, and Si. Enlargement of the spectra reveals the weak scattering intensity by non-diamond sp^2-bonded carbon impurity centered at ~1500 cm^{-1}. 59

Figure 3.11 SIMS data for boron-doped microcrystalline diamond films deposited on (A) Si, (B) Mo, and (C) W. 62

Figure 4.1 Background cyclic voltammetric i-E curve in 1.0 M KCl for a boron-doped nanocrystalline diamond film deposited on Si. Scan rate = 0.1 V/s. Electrode geometric area = 0.2 cm^2. Deposition time = 2h. Source gas mixture = $CH_4/H_2/Ar$ (1%/5%/94%) (v/v) with 10 ppm B_2H_6 added. Power = 800 W. Pressure = 140 torr. Substrate temperature = ~800 °C 69

Figure 4.2 Background cyclic voltammetric i-E curve in 1.0 M KCl for a boron-doped nanocrystalline diamond film. Scan rate = 0.1 V/s. Electrode geometric area = 0.2 cm^2. The deposition conditions are the same as stated in Figure 4.1 71

Figure 4.3 Cyclic voltammetric i-E curves for (A) $Fe(CN)_6^{-3/-4}$, (B) $Ru(NH_3)_6^{+3/+2}$, (C) $IrCl_6^{-2/-3}$, (D) methyl viologen ($MV^{+2/+1/0}$) in 1 M KCl, and (E) 4-*tert*-butylcatechol, and (F) $Fe^{+2/+3}$ in 0.1 M $HClO_4$ at a boron-doped nanocrystalline diamond thin film. Scan rate = 0.1 V/s. Electrode geometric area = 0.2 cm^2. The diamond deposition conditions are the same as stated in Figure 4.1 72

Figure 4.4 Plot of i_p^{ox} vs scan $rate^{1/2}$ for $Fe(CN)_6^{-3/-4}$, $Ru(NH_3)_6^{+3/+2}$, $IrCl_6^{-2/-3}$, methyl viologen ($MV^{+2/+}$), 4-*tert*-butylcatechol, and $Fe^{+2/+3}$ at a boron-doped nanocrystalline diamond film. The scan rate was varied from 100 to 500 mV/s. The diamond deposition conditions are the same as stated in Figure 4.1. 75

Figure 4.6 SEM images of a boron-doped nanocrystalline diamond film deposited on Si in (A) cross-section and (B) top-view image modes. The deposition conditions are the same as stated in Figure 4.1. 79

Figure 4.7 Atomic force microscope images (10x10μm) of a boron-doped, nanocrystalline diamond film deposited Si in the (A) deflection and (B) height image modes. The deposition conditions are the same as stated in Figure 4.1. 80

Figure 4.8 Transmission electron micrograph of a nanocrystalline boron-doped diamond film. The deposition conditions are the same as stated in Figure 4.1 81

Figure 4.9 Transmission electron diffraction pattern for a grain in the boron-doped nanocrystalline diamond thin film. The deposition conditions are the same as stated in Figure 4.1 82

Figure 4.10 XRD pattern for a boron-doped nanocrystalline diamond film deposited on Si. The deposition conditions are the same as stated in Figure 4.1 83

Figure 4.11 Visible Raman spectrum for a boron-doped nanocrystalline diamond film deposited on Si. The deposition conditions are the same as stated in Figure 4.1.. 84

Figure 5.1 Cyclic voltammetric i-E curves, background (dashed line) and total current (solid line), for 1.0 mM (A) CAD (B) PUT, (C) SPMD, and (D) SPM in 0.01 M borax buffer/0.1 M NaCl, pH 11. The working electrode was a microcrystalline diamond film deposited from a 0.5% CH_4/H_2 ratio and 10 ppm B_2H_6. Scan rate = 0.1 V/s. Electrode geometric area = 0.2 cm^2. 93

Figure 5.2 Cyclic voltammetric i-E curves for 1.0 mM CAD in 0.01M borax buffer/0.1 M NaCl, pH 11.2, at a nanocrystalline boron-doped diamond thin film. The nanocrystalline diamond electrode was deposited from a 0.5% CH_4/H_2/Ar ratio and 1 ppm B_2H_6. Scan rate = 0.1 V/s. Electrode geometric area = 0.2 cm^2. 96

Figure 5.3 Cyclic voltammetric i-E curves for 1 mM cadaverine in (a) 0.01 M phosphate buffer, pH 7.2; (b) 0.01 M carbonate buffer/0.1 M $NaClO_4$, pH 9,; (c) 0.01 M carbonate buffer/0.1 M $NaClO_4$, pH 10, and (d) 0.01 M carbonate buffer/0.1 M $NaClO_4$, pH 11 at microcrystalline diamond film deposited from a 0.5% CH_4/H_2 ratio and 1 ppm B_2H_6. Scan rate = 0.1 V/s. Electrode area = 0.2 cm^2 98

Figure 5.4 The fractional composition of protonate/unprotonated forms of (A) CAD and (B) SPM as a function of pH. 100

Figure 5.5 Plots of the cyclic voltammetric oxidation peak current, i_p^{ox} versus scan $rate^{1/2}$ for (A) 0.1 mM amines at moderately doped microcrystalline film, (B) 1 mM amines at highly doped microcrystalline film in CBpH10.6. (C) Plots of the oxidation peak

potential, E_p^{ox}, versus scan rate for 0.1 mM amines in 0.01 M carbonate buffer, pH10.6. 102

Figure 5.6 Linear sweep voltammetric i-E curves for ethylenediamine at concentrations of (a) 0.1, (b) 0.5, (c) 1, (d) 2, (e) 3, (f) 4, and (g) 5 mM at microcrystalline diamond film deposited from a 0.5% CH_4/H_2 ratio. Scan rate = 0.1 V/s. Electrode geometric area = 0.2 cm^2. 103

Figure 5.7 Cyclic voltammetric i-E curves for 1 mM cadaverine in 0.01 M carbonate buffer/0.1 M $NaClO_4$, pH10.6, at a microcrystalline diamond film deposited from a 0.67% CH_4/H_2 ratio. (A) "as deposited", and (B) acid washed and rehydrogenated diamond film. Scan rate = 10 mV/s. 105

Figure 5.8 Contact-mode atomic force microscopy images of a microcrystalline diamond films deposited from a (A) 0.33%, (B) 0.67%, and (C) 1% CH_4/H_2 ratio. All images have the same x, y, z scales. 106

Figure 5.9 Visible Raman spectra for diamond films deposited using a (a) 0.33%, (b) 0.67%, and (c) 1% CH_4/H_2 ratio. 514.4 nm laser source and 10 s integration time. 108

Figure 5.10 Background cyclic voltammetric i-E curves for a microcrystalline diamond films deposited using a (A) 0.33%, (B) 0.50%, and (C) 1% CH_4/H_2 ratio. The solution pH was (a) 8.4, (b) 9, (c) 10, (d) 10.6, (e) 11, and (f) 12. Scan rate = 0.1 V/s. Electrode geometric area = 0.2 cm^2. 110

Figure 5.11 Cyclic voltammetric i-E curves for 1 mM cadaverine in 0.01 M carbonate buffer/0.1 M $NaClO_4$, pH10.6, at diamond films deposited using CH_4/H_2 source gas ratios of (a) 0.33%, (b) 0.5%, and (c) 1%. Scan rate = 0.1 V/s. Electrode geometric area = 0.2 cm^2. 111

Figure 5.12 Cyclic voltammetric i-E curves for 1 mM CAD, along with the corresponding background current (dashed line), in a 0.01 M borax buffer, pH 11.2, at (A) a boron-

doped nanocrystalline diamond thin-film electrode and at (B) a nanocrystalline diamond thin-film electrode deposited without intentionally added boron. Scan rate = 0.1V/s. Electrode geometric area = 0.2 cm^2 113

Figure 5.13 A-E Visible Raman spectra for boron-doped nanocrystalline diamond films deposited from a 1/94/5 $CH_4/Ar/H_2$ (v/v) source gas ratio with (A) 0, (B) 1, (C) 10, (D) 20, and (E) 30 ppm of added B_2H_6. 532 nm laser source and 10 s integration time..... 115

Figure 5.14 (A) Cyclic voltammetric i-*E* curves for boron-doped nanocrystalline diamond films in 1 M KCl over (A) wide potential range showing the working potential window and (B) a narrow potential range. Films deposited using a 1/94/5 $CH_4/Ar/H_2$ (v/v) source gas ratio and (a) 1, (b) 10, (c) 20, (d) 30 ppm of added B_2H_6. Scan rate = 0.1 V/s. Electrode geometric area = 0.2 cm^2 117

Figure 5.15 Cyclic voltammetric i-E curves for boron-doped nanocrystalline diamond films in borax buffer pH 10.6. The films were deposited with (a) 1, (b) 20, (c) 30 ppm B_2H_6. Scan rate = 0.1 V/s. Electrode geometric area = 0.2 cm^2..... 121

Figure 5.16 Cyclic voltammetric i-E curves for 1.0 mM cadaverine, putrescine, spermidine, and 0.8 mM spermine in BBpH10.6 at boron-doped nanocrystalline diamond films deposited with (A) 1 ppm (B) 10 ppm , (C) 20 ppm, and (D) 30 ppm of added B_2H_6. 122

Figure 5.17 A-C Raman spectra for three microcrystalline films, deposited from a 0.5 % CH_4/H_2 volumetric ratio with (A) 1, (B) 10, and (C) 20 ppm B_2H_6 added. The doping level was in the range of 10^{19} to 10^{20} B/cm^3 126

Figure 5.18 Cyclic voltammetric i-E curves for (A) 1.0 mM PUT, (B) 1.0 mM SPMD, and (C) 0.8 mM SPM, in the BBpH10.6 at three microcrystalline diamond films deposited from a 0.5 % CH_4/H_2 volumetric ratio with (A) 1, (B) 10, and (C) 20 ppm B_2H_6 added..... 128

Figure 5.19 Model of the competition between the O_2 evolution (OER) and O-transfer reaction (OTR). 132

Figure 6.1 (A) Cyclic voltammetric i-E curves for 1.0 mM PUT (dashed line) and 0.8 mM SPM (solid line) in borax buffer pH 11 at a boron-doped nanocrystalline film. Scan rate=0.1 V/s. Electrode area = 0.2 cm^2. (B) Subtracted SPM-PUT voltammogram. 145

Figure 6.2 Cyclic voltammetric i-E curves, background (dashed line) and total current (solid line) for (A) 1.0 mM PUT, (B) 1.0 mM EDA, and (C) 1 mM SPM in phosphate buffer, pH 7.2 at a boron-doped nanocrystalline film. Scan rate = 0.1 V/s. Electrode area = 0.2 cm^2. 146

Figure 6.3 (A) Peak current vs concentration profiles for 1 mM cadaverine at boron-doped microcrystalline diamond electrodes deposited in a 0.5 % CH_4/H_2 ratio with (a) 1 ppm B_2H_6, and (b) 10 ppm B_2H_6. (B) Reciprocal plots of peak current versus cadaverine concentration at (a) 1 ppm B_2H_6, (b) 10 ppm B_2H_6 diamond electrode. 151

Figure 6.4 Voltammetric response for 1 mM $Fe(CN)_6^{-3/-4}$ in 1 M KCl at a rotating microcrystalline diamond disk electrode as a function of rotation speed. The electrode was deposited with a 0.5 % CH_4/H_2 ratio and 10 ppm B_2H_6. Scan rate = 0.1 V/s. Rotational velocites (rad/s) = (a) 52.2, (b) 104.7, (c) 157.1, (d) 209.4, (e) 261.8, and (f) 314.2..... 153

Figure 6.5 Voltammetric response for 1 mM $Ru(NH_3)_6^{+3/+2}$ in 1 M KCl at rotating microcrystalline diamond disk electrode as a function of rotation speed. The electrode was deposited with 0.5 % CH_4/H_2 ratio and 10 ppm B_2H_6.Scan rate = 0.1 V/s. Rotational velocites (rad/s): (a) 52.2, (b) 104.7, (c) 157.1, (d) 209.4, (e) 261.8, and (f) 314.2. 154

Figure 6.6 Voltammetric response for 0.2 mM CAD (forward scan) in borax buffer pH 11 at a boron-doped microcrystalline diamond disk electrode as a function of rotational speed. The electrode was deposited with 0.5 % CH_4/H_2 and 1 ppm B_2H_6. Scan rate = 0.1 V/s. Rotational velocities (rad/s) = (a) 52.2, (b) 104.7, (c) 157.1, (d) 209.4, (e) 261.8, and (f) 314.2 155

Figure 6.7 Voltammetric response for borax buffer, pH 11, at a boron-doped microcrystalline diamond disk electrode as a function of rotational speed. The electrode was deposited with 0.5% CH_4/H_2 and 20 ppm B_2H_6. Scan rate = 0.05 V/s. Rotational velocities (rad/s) = (a) 52.2, (b) 104.7, (c) 157.1, (d) 209.4, (e) 261.8, and (f) 314.2. 156

Figure 6.8 Voltammetric response for 0.2 mM SPM (forward scan) in borax buffer, pH 11, at a boron-doped microcrystalline diamond disk electrode as a function of rotational speed. The electrode was deposited with 0.5% CH_4/H_2 and 20 ppm B_2H_6. Scan rate = 0.05 V/s. Rotational velocities (rad/s) = (a) 52.2, (b) 104.7, (c) 157.1, (d) 209.4, (e) 261.8, and (f) 314.2. 157

Figure 6.9 Koutecký-Levich plots for the oxidation of 0.2 mM amines at a boron-doped microcrystalline diamond disc electrode deposited with 0.5% CH_4/H_2 and 20 ppm B_2H_6. Scan rate = 0.05 V/s. Potential: 0.7 V vs Ag/AgCl 158

Figure 6.10 Proposed surface SN2-type mechanism of aliphatic amine oxidation at boron-doped diamond electrode 163

Figure 7.1 FIA-EC hydrodynamic voltammetric background i-E curves for a microcrystalline diamond film deposited using 0.33%, 0.50% and 0.67% CH_4/H_2 ratio in carbonate buffer, pH 10. Flow rate = 1.0 mL/min. 168

Figure 7.2 FIA-EC hydrodynamic voltammetric background i-E curves for boron-doped nanocrystalline diamond films deposited with 1 ppm, 10 ppm, and 20 ppm of added B_2H_6 in borax buffer, pH 11. Flow rate = 1.0 mL/min. 171

Figure 7.3 Background current-time profile in FIA after detector turn-on in borax buffer, pH 11, for a nanocrystalline diamond film deposited from 1/94/5 $CH_4/Ar/H_2$ (v/v) ratio and 1 ppm B_2H_6. Detection potential = +695 mV vs Ag/AgCl. Electrode area = 0.08 cm^2. Flow rate =1 mL/min..... 172

Figure 7.4 Hydrodynamic voltammetric i-E curves for 20 µL injections of (A) 1.0 mM SPMD and (B) 1.0 mM CAD. The carrier solution was 0.1M $NaClO_4$ + 0.01 carbonate buffer, pH 10. Plots of the S/B ratio versus the applied potential are shown for (C) SPMD and (D) CAD. Flow rate =1.0 mL/min. 174

Figure 7.5 Hydrodynamic voltammetric i-E curves for 20 µL injections of 0.1 mM amines. The carrier solution was 0.1M NaCl + 0.01 borax buffer, pH 11. Nanocrystalline diamond films were deposited from a 1/94/5 $CH_4/Ar/H_2$ (v/v) ratio with (A) 1 ppm, (B) 10 ppm, and (C) 20 ppm of added B_2H_6. Flow rate=1.0 mL/min. 176

Figure 7.5 Plots of the S/B ratio versus the applied potential for 0.1 mM amines. The carrier solution was 0.1M NaCl + 0.01 borax buffer, pH 11. Nanocrystalline diamond film were deposited from a 1/94/5 $CH_4/Ar/H_2$ (v/v) ratio with (D) 1 ppm, (E) 10 ppm, and (F) 20 ppm of added B_2H_6. Flow rate = 1.0 mL/min. 177

Figure 7.6 Variation of the SPMD/CAD current ratio, as a function of pH of the mobile phase. The carrier solution was 0.01 borax buffer/0.1M NaCl. Microcrystalline diamond films deposited with 0.5% CH_4/H_2 source gas mixture. Flow rate = 1.0 mL/min..... 180

Figure 7.7 Calibration curves obtained for (A) SPMD and (B) CAD at boron-doped microcrystalline diamond films deposited withdifferent CH_4/H_2 source gas ratios. The carrier solution was 0.01M carbonate buffer/0.1M $NaClO_4$, pH 10. Injected volume = 20 µL. Flow rate =1.0 mL/min. Applied potential = +700 mV..... 182

Figure 7.8 Calibration curves for aliphatic amines at a boron-doped nanocrystalline diamond electrode deposited from a 1/94/5 $CH_4/Ar/H_2$ (v/v) source gas ratio with 20 ppm B_2H_6. Injected volume = 20µL. Flow rate = 1.0 mL/min..... 184

Figure 7.9 FIA-EC responses for a series of 10 µL injections of 0.1µM amine: (a) CAD, (b) EDA, (c) DAP, (d) DA, (e) DEP, (f) SPM, (g) PUT, and (h) SPMD. The carrier solution was 0.01 borax buffer/0.1 M NaCl, pH 11.2. Detection potential=+ 660 mV. 186

Figure 7.10 Relationship between the FIA peak current and first pK_a for (a) MA, (b) EA, (c) PA, (d) CAD, (e) PUT, (f) SPMD, (g) SPM, (h) EDA, (i) HA, (j) DAP, (k) SPMD (2,2), (l) SPMD (3,3). Data collected at two microcrystalline films for 0.1 mM amines (Fig.A and C), and a nanocrystalline film for 0.5 mM amines (Fig. B)..... 187

Figure 7.11 FIA-EC responses for a multiple injections of 1.0 mM CAD at as "deposited" 0.33% CH_4/H_2 diamond film. The carrier solution was carbonate buffer pH10. Detection potential=+ 810 mV. Injection volume=20 µL. Flow rate=1.0 mL/min... 189

Figure 7.12 FIA-EC responses for a multiple injections of **(A)** 1.0 mM CAD and **(B)** 1.0 mM SPMD at a well "conditioned" 0.50% C/H film. The carrier solution was CBpH10. A detection potential=855 mV and 3-minute delay between injections was used for CAD. A detection potential=780 mV and a 6-minute delay between injections was used for SPMD. Injection volume = 20 µL. Flow rate = 1.0 mL/min. 191

Figure 7.13 FIA-EC responses for a multiple injections of CAD and SPMD at a HOPG, GC and a nanocrystalline boron-doped diamond thin-film electrode. Applied potential=655 mV vs Ag/AgCl. Flow rate = 1.0 mL/min..... 193

Figure 7.14 FIA-EC responses for a multiple injections of 0.1 mM CAD, PUT, SPMD and SPM at a boron-doped nanocrystalline film deposited from 1/94/5 $CH_4/Ar/H_2$ (v/v)

ratio with 1 ppm of added B_2H_6. The carrier solution was borax buffer pH 11. Applied potential=+665 mV. Injection volume of CAD and PUT = 30μL, and SPMD and SPM = 10μL. Flow rate = 1.0 mL/min. 195

Figure 7.15 FIA-EC series of responses for 0.05 mM DAP at a boron-doped nanocrystalline thin film deposited from a 1/94/5 $CH_4/Ar/H_2$ (v/v) ratio and 10 ppm B_2H_6. The carrier solution was borax buffer, pH 11. Applied potential=+665 mV. Injection volume = 10 μL. 196

Figure 8.1 Background cyclic voltammetric i-E curves in 0.01 M borax buffer, pH 10.6, for a boron-doped microcrystalline diamond film deposited from a 0.4% CH_4/H_2 ratio. Presented are the 1st, 2nd, 25th, 45th, 60th scans. Scan rate = 0.1V/s. Electrode area = 0.2 cm^2. 202

Figure 8.2 Background current-time profile in FIA after detector turn-on for (A) a microcrystalline diamond and (B) glassy carbon.[30] The carrier solution for diamond was 7/93 (v/v) acetonitrile/borax buffer, pH 11.2. The carrier solution for GC was borax buffer, pH 11.2. Detection potential = 665 mV vs Ag/AgCl. Electrode area = 0.08 cm^2. Flow rate = 1 mL/min. 203

Figure 8.3 Cyclic voltammetric i-E curves for 1 mM CAD and 1 mM SPMD in 0.01 M borax buffer, pH 11.2, along with the corresponding background current, for a boron-doped microcrystalline diamond film deposited from a 0.4% CH_4/H_2 ratio. Scan rate = 0.1 V/s. 204

Figure 8.4 Cyclic voltammetric i-E curves in 0.1 mM CAD plus (A) 0.01 M borax buffer, pH 10.6, and (B) 93/7 (v/v) 0.01 M borax buffer, pH 10.6 / CH_3CN, for a boron-doped microcrystalline diamond film deposited from a 0.4% CH_4/H_2 ratio. Scan rate =0.1 V/s. 206

Figure 8.5 A Hydrodynamic voltammetric i-E curves for a boron-doped microcrystalline diamond film (0.4% CH_4/H_2 ratio), in 100 μM (a) SPM, (b) SPMD, (c) PUT, and (d) CAD. The carrier solution was 7/93 (v/v) acetonitrile/borax buffer, pH 11.2 (e). Injection volume = 20μL. 207

Figure 8.5 B Plots of the S/B ratio versus the applied potential for a boron-doped microcrystalline diamond film (0.4% CH_4/H_2 ratio), in 100 μM (a) SPM, (b) SPMD, (c) PUT, and (d) CAD. The S/B ratio was calculated as $I_{total} - I_{background} / I_{background}$.. 208

Figure 8.6 FIA-EC responses for a boron-doped microcrystalline diamond film (0.4% CH_4/H_2) during a multiple injections of **(A)** 5 μM PUT and **(B)** 2 μM SPMD. The carrier solution was a 7/93 (v/v) acetonitrile/borax buffer, pH 11.2. Detection potential = 665 mV vs. Ag/AgCl. Injection volume = 20 μL. Flow rate = 1.0 mL/min. 209

Figure 8.7 FIA-EC calibration responses for a boron-doped microcrystalline diamond film (0.4% CH_4/H_2) during multiple injections of 5 μM SPM. Injected volumes were (a-h) 2 to 20 μL. The carrier solution was a 7/93 (v/v) acetonitrile/borax buffer, pH 11.2. Applied potential = 665 mV vs Ag/AgCl. Flow rate = 1.0 mL/min. 210

Figure 8.8 Reversed-phase liquid chromatographic separation of (A) 47 μM PUT, CAD, SPMD, and SPM, and (B) 0.5 μM PUT, CAD, and SPM on a C_{18} column (X-Terra, 5 μm particle size, 4.6 x 150 mm). The mobile phase was a 7/93 (v/v) acetonitrile/borax buffer, pH 11.2. Detection potential = 665 mV vs. Ag/AgCl. Injection volume = 20 μL. Flow rate = 1.0 mL/min. The boron-doped microcrystalline diamond film was deposited from a 0.4% CH_4/H_2 ratio. 212

Figure 8.9 Reversed-phase liquid chromatographic separation of PUT, SPMD, and SPM on a C_{18} column. The solution mixture contained 20 μM of each amine. The mobile phase was a 16/84 (v/v) acetonitrile/borax buffer, pH 11.2. Detection potential = 665

mV vs. Ag/AgCl. Injection volume = 20 μL. Flow rate = 1.0 mL/min. The boron-doped microcrystalline diamond film was deposited from a 0.4% CH_4/H_2 ratio.... 213

List of Symbols and Notations

A.....geometric electrode area [cm^2]

v.....scan rate

ΔE_p.....peak potential separation

AFM.....atomic force microscopy

BB.....borax buffer

BNR.....boron nuclear reaction

CAD.....cadaverine

C_{dl}.....double-layer capacitance

CV.....cyclic voltammetry

CVD.....chemical vapor deposition

DA.....Dytek® A

DAP.....diaminopropane

DEP.....Dytek® EP

E.....potential

EA.....ethylamine

EDA.....ethylenediamine

E_p.....peak potential

$E_{p/2}$.....half-peak potential

F.....Faraday constant (96486 C/eq)

FIA.....flow injection analysis

FIA-EC.....flow injection analysis with electrochemical detection

FWHM.....full width at half-maximum

GC.....glassy carbon

HA.....hexanediamine

HOPG.....highly ordered pyrolytic graphite

HPLC.....high performance liquid chromatography

i.....current

i_p.....peak current

k^o_{app}.....heterogeneous electron transfer rate constants [cm/s]

LC.....liquid chromatography

LOD.....limits of detection

LOQ.....limits of quantitation

MA.....methylamine

MV.....methyl viologen

n.....number of electrons

NHE.....normal hydrogen electrode

OER.....oxygen evolution reaction

OTR.....oxygen transfer reaction

ox.....oxidation

PA.....propylamine

PAD.....pulsed amperometric detection

PUT.....putrescine

Q.....charge

R.....molar gas constant (8.314 J/molK)

RDE.....rotating disc electrode

red.....reduction

RSD.....relative standard deviation

S/B.....signal-to-background ratio

S/N.....signal-to-noise ratio

SEM.....scanning electron microscopy

SIMS.....secondary ion mass spectrometry

SPMD 2,2..... spermidine 2,2

SPM.....spermine

SPMD 3,3.....spermidine 3,3

SPMD.....spermidine

T.....temperature [K]

TEM.....transmission electron microscopy

XPS.....x-ray photoelectron spectroscopy

XRD.....x-ray diffraction spectroscopy

ρ.....resistivity

Chapter 1

BACKGROUND AND MOTIVATIONS

1.1. Aliphatic Polyamines

1.1.1. Biological and Enviromental Importance

The diamine, putrescine, and the polyamines, spermidine and spermine, are ubiquitous substances found in virtually all cells from higher prokaryotes to eukaryotes.[1-3] As polycations, polyamines are known to interact directly with nucleic acids, proteins, and phospholipids, playing critical roles in the proliferation and differentiation of normal and neoplastic cells.[2-9] The general function of the polyamines as growth factors, antioxidants, and metabolic regulators, and as nutrients and second messengers has been proposed.[8-11] Cadaverine is a diamine, which is normally produced from lysine by the action of lysine decarboxylase, and under normal conditions, mammalian cells do not produce this diamine.[12,13] Thus, the presence of cadaverine in physiological fluids may indicate the presence of infection in the host. [12,13 and references therein]

Elevated levels of intracellular polyamines are a common finding in rapidly proliferating tumors cells, in contrast with lower levels measured in their non-malignant

counterparts.[1,2,4,14,15] A number of studies have indicated higher concentrations of putrescine, spermidine, and spermine, or total polyamine contents, in cancer patients, compared to healthy patients.[1,2,4] For example, in the biological samples of healthy patients polyamines were present in concentrations ranging from 0.5-6.0 nmole/mg of creatinine for spermine, cadaverine, and spermidine, and to 12-14 nmole/mg creatinine for putrescine. In the same study, the concentration of amines was shown to be three times higher in the urine of colon cancer patients. Chowdhury et al.[4] explored the relationship of polyamine presence and concentration to the degree of malignancy in breast cancer patients. The results showed that polyamine levels increased with clinical staging of the disease and showed a direct relationship with the advancement of the disease.[4]

Aliphatic amines are of concern, since they occur in various environmental matrices. Aliphatic amines are produced in vast quantities and are, thus, likely to be encountered in the environmenta.[16] Amines are of industrial interest as important precursors in the synthesis of dyes, pharmaceuticals, stabilizers, and corrosion inhibitors.[16,17] Amines can be formed as secondary pollutants from the biodegradation of nitrogen-containing compounds. They can be a source of formation of carcenogenic N-nitrosoamines.[18] Aliphatic polyamines may be present at high concentrations in foods and beverages produced using fermentation processes or exposed to microbial contamination during processing.[19-22] They are synthesized by microbial decarboxylation of amino acids. In healthy individuals, dietary polyamines, such as histamine, putrescine, cadaverine, tyramine, tryptamine, phenylethylamine, spermine, and spermidine can be rapidly detoxified by the action of amine oxidases. However, humans with low-amine oxidase activity are at risk of amine toxicity. Aliphatic polyamines have been proposed as potential indicators of the extent of food spoilage.[23]

The Food and Drug Administration (FDA) presented a report on the relationship between the post-mortem formation of biogenic amines in fish tissue and consumer illness.[18] The conclusion was that histamine is most closely linked to the development of illness, however, other biogenic aliphatic polyamines, (i.e., putrescine, cadaverine, spermine, and spermidine) could induce a toxic effect, by inhibiting histamine-metabolizing enzymes, such as diamine oxidase.[18,24]

1.1.2. Aliphatic Amine Detection

There is a significant interest in the development of sensitive, reproducible, and stable detection schemes for aliphatic polyamines due to their biological and toxicological importance. These analytes are not detected directly using optical methods (i.e., UV-Vis, fluorescence) because they are not natively chromophoric or fluorophoric. As a consequence, separation and detection requires pre- or post-column derivatization. The most commonly used derivatization agents for primary and secondary amines are o-phthaldehyde (OPA), fluorescamine, dansyl chloride, benzoyl chloride and 1-naphtyl isocyanate.[25 and references therein] Such derivatization procedures increase the complexity of the assay, the analysis time, and the risk for possible indeterminate error.

Several separation and detection schemes for aliphatic polyamines have been reported.[16,25,26 and references therein] The most often employed detection methods are reversed-phase liquid chromatography (10-100 pmol detection limits) and ion-exchange chromatography (1-200 pmol detection limits), both coupled with absorbance or fluorescence detection.[26] Capillary zone electrophoresis, with spectrophotometric detection (1-3 nmol/L sensitivity), has also been reported and shown to be superior to HPLC in terms of sensitivity and sample volume required, but the reproducibility was less than adequate.[27] Gas chromatography (1-600 pmol) with electron-capture detector

(ECD), nitrogen-phosphorus detection (NPD) or mass spectrometry has been also used for the analysis of polyamines in biological samples.[28] A review of the analytical methods used to assay biogenic aliphatic polyamines was published recently.[25] The review examines the prospects and the limitations of polyamines as cancer markers. Table 1.1 gives summary of the separation and detection methods for aliphatic polyamines.

Table1.1 Analytical Methods Used for Polyamine Separation and Detection

Method	Derivatization	Sensitivity
Paper Chromatography	Ninhydrin	0.1-0.5 µmol
TLC	Ninhydrin dansyl derivatives	5-100 nmol 10-100 pmol
Overpressure TLC	Ninhydrin + Cd^{+2}	2-60 nmol
HPLC	Fluorescamine derivatives Enzymatic+chemiluminescent Dansyl derivatives	50-200 pmol 5-500 pmol 10-100 pmol
Ion-exchange chromatography	Ninhydrin Fluorescamine O-Phthaldehyde	1-50 pmol 5-200 pmol 5-200 pmol
GC	N-Trifluoroacetyl (N-TFA)	100-600 pmol
Electrophoresis	Ninhydrin	5-200 pmol
MS	N-Trifluoroacetyl (N-TFA) Dansyl derivatives	10-100 pmol 10-100 pmol
GC-MS	N-Trifluoroacetyl (N-TFA) + deuterated internal standards	1-10 pmol
Enzymatic Assay	----------	5-10 nmol

Data adapted from J. Chromatogr. B 764 (2001) 385-407

Electrochemistry is an analytical technique characterized by instrumental simplicity, moderate cost, and portability. Electrochemical detectors can be readily combined with separation techniques (e.g., IC, CE, HPLC).

Several electrochemical detection schemes for aliphatic polyamines have been reported, involving the use of noble metal electrodes, transition metal electrodes and chemically modified electrodes (CME).[29-34] The amperometric detection of aliphatic polyamines at a nickel-modified glassy carbon electrode in flow injection analysis (FIA) produces limits of detection of 4-10 pmol.[33,34] Amperometric detection at a cobalt wire electrode was reported, however, the electrode response was unstable and poorly reproducible.[35] The potentiometric detection of amines, coupled with ion-chromatography, at a copper electrode was reported with limits of detection near 1μM (50 pmol).[36]

One of the most successful electrochemical detection schemes for aliphatic amines was developed using a gold electrode. Johnson and coworkers demonstrated the effective separation and detection of several polyamines using ion exchange liquid chromatography coupled with pulsed amperometric detection (PAD). [29,30] PAD was developed to circumvent the problem of electrode fouling during the oxidation of carbohydrates, alcohols, and polyamines.[29,37-40] In this method, the electrode activity is maintained by a series of positive and negative potential pulses (E_1, E_2, and E_3). The pulsed waveform involves a three step procedure: (E_1) amperometric detection, (E_2) oxidative surface cleaning, and (E_3) reductive surface reactivation. This procedure accomplishes (i) oxidation of the amine, (ii) desorption of adsorbed carbonaceous species, and (iii) regeneration of a clean and oxide-free surface. [32-34] The group demonstrated the effective separation and detection of several polyamines with detection limits of 200 pmole for putrescine.[33]

Pulsed amperometric detection is successful but somewhat complicated to implement and, even though the detector is commercially available, detection at constant applied potential is the method of choice for most routine analysis. Several years ago, the Johnson group began designing and testing metal alloy composite electrodes (e.g., Ag-PbO_2, Fe-PbO_2, Bi-PbO_2, Cu-Mn)[41-49], which can be used to stably detect/oxidize various analytes (i.e., carbohydrates, amino acids, phenol, and benzene) at constant applied potential.[50-55] The group demonstrated that Ag-doped PbO_2 electrodes were useful for the amperometric detection of aliphatic polyamines.[54,55] For example, these electrodes provided a linear dynamic range of three orders of magnitude and limit of detection of 0.3 μM (6 pmol) for diaminopropane. The amine oxidation reaction at these and all electrodes involves anodic oxygen transfer with the oxidant being OH•, produced during the discharge of H_2O.[31,32,56] It was a premise of Johnson and coworkers that OH• is adsorbed at specific surface sites on the electrode surface, and transferred to the reactants via an electrocatalytic oxygen transfer reaction (OTR) mechanism.

The authors proposed several properties necessary for an electrode to stably support anodic oxygen transfer reactions: (i) the use of metal oxides with minimal solubility at the pH conditions of the application, (ii) the existence of a low density of surface sites at which the anodic discharge of H_2O (evolution of O_2) occurs with lower potential than the surrounding matrix, and (iii) the existence of surface sites that are effective for coordinating the analytes. The authors indicated that silver, as a doping agent in the composite electrodes, serves several functions: (i) a low H_2O discharge overpotential compared to PbO_2, (ii) capability of adsorbing the OH• generated during H_2O discharge, and (iii) capability of adsorbing the reactant species (i.e., amines).[55,57,58] The group has discussed the specific properties of these composite

electrodes in several seminal publications that render them useful for anodic oxygen transfer reactions.[46,54] *It was the reports from their group and the identified composite electrode properties that were the impetus for our efforts to fabricate and test boron-doped diamond electrodes, designed with the appropriate properties, for anodic oxygen transfer reactions.*

Boron-doped diamond thin films can be considered a "composite materials" that possess the necessary properties to support anodic oxygen transfer reaction. First, high-quality diamond films are stable and resistant to corrosion in strongly acidic and alkaline media.[59-61 and references therein] Therefore, at the anodic potentials used to detect the polyamines, the electrode structure is stable. Second, the films may contain sp^2-bonded non-diamond carbon impurities, distributed very locally over the surface. These impurities can exist at the grain boundaries or as extended defects within the diamond film. Most importantly, they have a lower overpotential for oxygen evolution than does the surrounding diamond, and they can also be controllably introduced into the films through adjustment in the diamond deposition conditions.[62,63] This means that reactive OH• will be generated locally at these sites at low overpotential, and not to any appreciable extent on the diamond lattice. Third, boron dopant atoms located at the surface can serve as adsorption/coordination sites for the analyte (e.g., polyamine). Boron atoms can insert directly into the growing diamond lattice, but they can also cluster and accumulate in the grain boundaries. The polyamine adsorption/coordination at the boron sites near the grain boundaries is supposed to be important mechanistically, as these sites are very near where OH• is being generated at low overpotential.

The goal of the research described herein was to experimentally verify that properly designed boron-doped diamond films possess the required properties to support oxidation of aliphatic polyamines via oxygen transfer reaction. A model for amine

oxidation at diamond, similar to one recognized by Johnson and coworkers for Ag-PbO_2, was proposed and evaluated. The mechanistic and kinetic aspects of the polyamine oxidation reaction were also investigated. The research, as well, aimed to development of a sensitive, reproducible and stable electrochemical detection scheme for these biologically- and environmentally- important molecules. The amperometric detection was performed using both flow injection analysis and reversed-phase liquid chromatography.

1.2. Properties and Applications of Conductive Diamond Films

Until the mid 1980s, the only allotropic form of carbon used as an electrode material was in an sp^2 configuration. Carbon materials, in the forms of highly ordered pyrolytic graphite (HOPG), glassy carbon (GC), carbon fibers, and carbon paste, have found a niche in the electrochemical community for several reasons. [64-69 and references therein] First, the surface chemistry of graphitic materials can be modified and manipulated to control electron transfer kinetics and molecular adsorption. Second, graphitic electrodes exhibit a fairly wide working potential window and generally stable electroanalytical responses, and third, these materials are commercially available and inexpensive.

Single crystal graphite and HOPG are benchmark carbon materials that embody the perfect anisotropic characteristics. These well ordered materials have dimensions on the order of a few μm compared to tens of angstroms for more disordered materials like GC and carbon black. Highly ordered pyrolytic graphite (HOPG) consists of parallel planes of condensed six membered rings (graphite sheets), with an interplane distance of 3.354 Å. The structure of hexagonal graphite is shown in Figure 1.1 A. The structure of glassy carbon (GC) is shown in Figure 1.1 B. GC resembles a twisted, bent, and

interlocked mass of graphite ribbons. The interplanar spacing is 3.48 Å, slightly larger than that of HOPG. The graphitic ribbons are composed of so-called basic structural units made up of 10-20 rings stacked up more or less in parallel by two to four layers. GC contains graphite-like domains ranging from 25 Å to 100 Å. GC is one of the most widely used sp^2 carbon electrode materials, in particular for electroanalytical applications.[69]

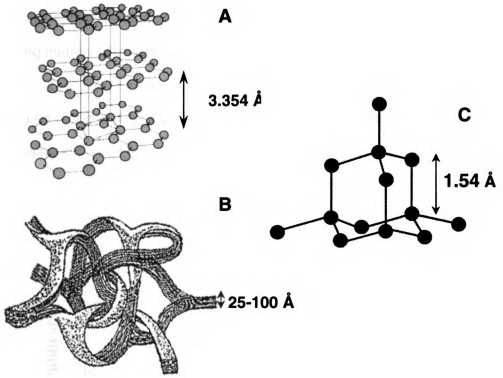

Figure 1.1 Structural models of (A) HOPG, (B) GC, and (C) fcc diamond lattice.

Diamond with a tetrahedral, face-centered cubic (fcc) crystal structure, is shown in Figure1.1C. Diamond consists of sp^3-bonded carbon and in contrast to the conventional carbon electrodes is isotropic and thus does not exhibit severe differences in surface microstructure. Diamond offers some of the most extreme

physical properties of any material. It is the hardest known material. It has the highest thermal conductivity at room temperature (e.g., about 5 times larger than the value for copper). It is the stiffest material, and is inert to most chemical reagents. These attributes of diamond are a consequence of the small interatomic distance of the carbon atoms in the diamond lattice, and the hydrogen termination of the surface. [70-73] With such a wide range of exceptional properties, it is not surprising that diamond has been referred to as 'the ultimate engineering material'. [74] The advent of low pressure diamond synthesis along with the facility of dopant incorporation, has prompted a growing number of investigations into its use as an electrode material.

The first reports of electrochemical investigations of diamond thin films appeared in the mid 1980s, and since that time, the application of diamond is showing increasing interest. Figure 1.2 presents the plot of the number of published papers on diamond, over the last four decades.

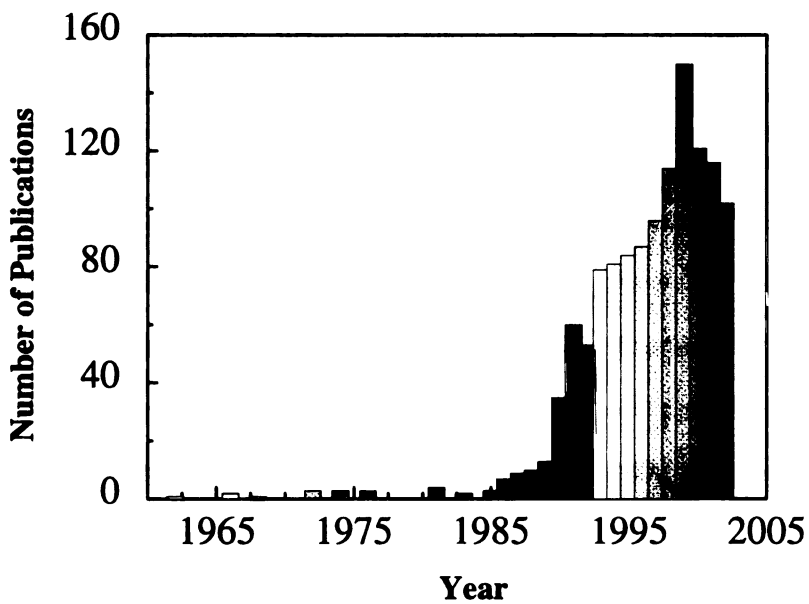

Figure 1.2 Plot of boron-doped diamond related papers over the last four decades. Results based on SciFinder® search engine.

Several interesting and electroanalytically-important electrochemical properties distinguish boron-doped diamond thin films from conventional carbon electrodes. Boron-doped diamond thin-film electrodes possess some strong attributes that are very important for electroanalysis. They include (i) a large working potential window (3 to 3.5 V) in aqueous media, (ii) a low background current, (iii) morphological and microstructural stability, (iv) good responsiveness for analytes without pretreatment, and (v) good long-term stability.[63] and references therein.

The wide working potential (± 100 μA) of diamond in aqueous media stems from the observed large overpotentials for the hydrogen (HER) and oxygen evolution reactions (OER).[75,76-81] The wide potential window and response stability of diamond electrodes permit electrochemical reactions at potentials that otherwise would be difficult or impossible to accomplish. The low background current and noise magnitude on diamond gives improved signal-to-background (S/B) and signal-to-noise (S/N) ratios.[82] The double layer capacitance of diamond electrodes is low and is attributed to a couple of factors. First, the relative absence of electroactive carbon-oxygen functionalifies on the hydrogen-terminated diamond surface results in a lower current. The absence of these functionalities can explain some, but not all of the small non-faradaic current and capacitance for diamond.[63] The second and most important contributing factor may be a slightly lower density of surface electronic states near the Fermi level, caused by the semiconductor nature of boron doped diamond.[63] A lower surface charge carrier density at a given potential would lead to a reduced accumulation of counter-balancing ions and water dipoles on the solution side of the interface, thereby lowering the background current and capacitance.

A striking characteristic of diamond electrodes is their stability compared to conventional carbon electrodes. The inertness of diamond electrodes arises from its

atomic density and its sp^3 bonding, the most stable among all carbon-carbon bonds. Diamond films are stable during anodic polarization in harsh acidic and alkaline media. Only after polarization at high current densities does the O/C ratio increase, suggesting the formation of carbon-oxygen functionalities on the surface. Diamond is very stable in reducing environments. The "as deposited" boron-doped diamond electrode surface is hydrogen-terminated, but over time with use, surface oxygen is incorporated.[59,61]

As mentioned earlier, the hydrogen, oxygen, and chlorine evolution reactions are kinetically sluggish on diamond, (i.e., require large overpotentials above the equilibrium potential to proceed at appreciable rates). However, simple, one-electron transfer reactions that do not involve a specific surface sites, e.g., $Ru(NH_3)_6^{+2/+3}$, $Fe(CN)_6^{-3/-4}$, $IrCl_6^{-2/-3}$, and $MV^{+2/+1/0}$ proceed reversibly to quasi-reversibly on diamond.[77,78,82,83]

There are a number of factors that can influence the electrochemical responsiveness of polycrystalline diamond films: (i) non-diamond carbon impurity phases, (ii) the surface termination (H vs. 0), (iii) the dopant type, level, and distribution, (iv) the grain boundaries and other morphological defects, and (v) the primary crystallographic orientation. The complexity of the diamond electrode nature resulting from these factors is well known, but is still not completely understood. While interesting and, in some cases, unique behavior of diamond electrodes has been demonstrated, there are sometimes significant variabilities in the reported response. Several groups have contributed to the development and applications of diamond electrodes (i.e., aspects of growth and nucleation mechanisms of diamond, the factors influencing the electrochemical response, application in electroanalysis and electrocatalysis). Among those are groups, Fujishima et al. (Japan),[84-94] Pleskov et al. (Russia),[95-106 107-110], Angus et al.,[72,73,111-123] Miller et al. (U.S.A.)[124-131] and Compton et al. (England).[132-143], Gruen et. al.[144-155]

No other material shows as much versatility as an electrode as does electrically conducting diamond. The material can be used in electroanalysis to provide sensitive detection of analytes with superb precision and stability; for high current density electrolysis (1-10 A/cm^2) in aggressive solution environments without any microstructural or morphological degradation; and as an optically transparent electrodes for spectroelectrochemical measurements in the UV/Vis and IR regions of the electromagnetic spectrum.[156-160]

Electrically conductive diamond thin films have been successfully used in amperometric detection schemes for several analytes (e.g. azides,[161] nitrite, hydrazine,[162,163] phenols, chlorophenols,[164-167] chlorpromazine[63], carbamate pesticides,[85] histamine and serotonine,[91 29,30,168], cysteine, [92] Diamond has been used also for detection of trace metal ions using anodic stripping voltammetry.[169] In general, hydrogen-terminated diamond provides superior detection figures of merit as compared to all other sp^2 carbon electrodes, specifically linear dynamic range, limit of detection, response variability and response stability.[141,170-176]

1.3. Diamond Film Deposition and Doping

Synthetic diamond can be produced by high-pressure high-temperature (HPHT) techniques or by low-pressure chemical vapor deposition (CVD).[74] During the HPHT process, solid carbon is heated (2000 K) under extreme pressure (tens of thousands of atmospheres) in the presence of a molten salt catalyst. The diamond crystals produced are used for a wide range of industrial applications, which require thermal conductivity, hardness and wear resistance. A drawback, however, is the cost, and the fact that the method produces diamond only in the form of single crystals.[70,72,177,178]

All CVD techniques for producing diamond require activation of gas phase precursor molecules. This activation can be accomplished thermally (e.g., a hot filament), by electric discharge (e.g., DC, RF or microwave), or by a combustion flame (e.g., an oxyacetylene torch).[70,72,74,177] Microwave plasma CVD (MWCVD) is the most widely used method for diamond growth. In this method, microwave power is coupled into the chamber via a dielectric window to create a discharge. The microwaves transfer energy into electrons in the gas phase, which in turn transfer their energy to the gas molecules through collisions. This leads to heating and dissociation of the gas molecules, and the formation of active species, which react on the substrate surface to form diamond.[70,72,74,177] The complex chemical and physical processes which occur during diamond CVD comprise several different features and are illustrated in Figure 1.3.[74]

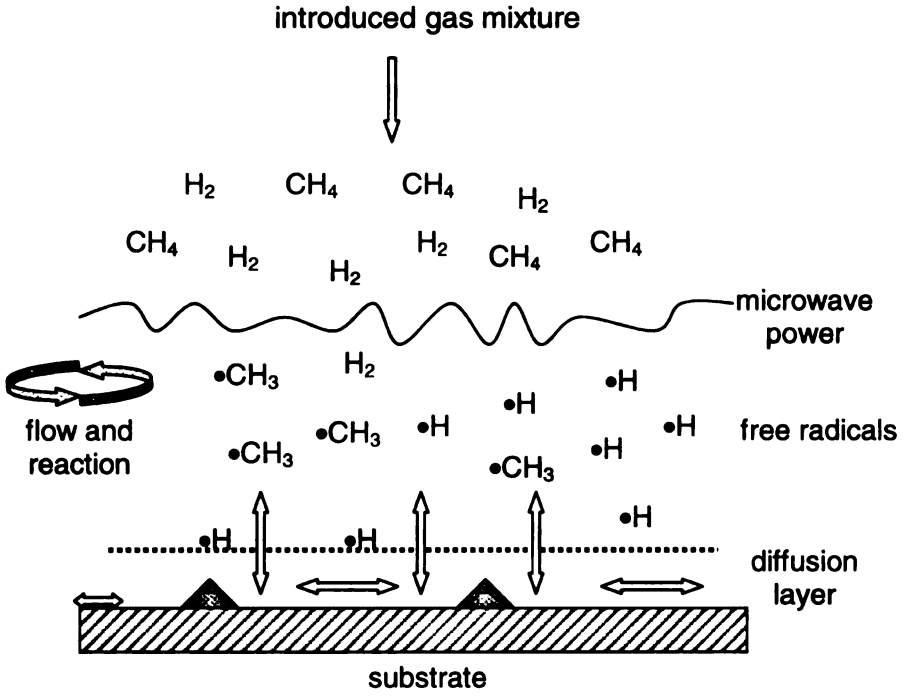

Figure 1.3 Schematic representation of the physical and chemical processes occurring during CVD diamond growth.

Diamond is deposited from a hydrogen-rich hydrocarbon gas mixture (CH_4/H_2).[179-181] It is recognized that hydrogen, specifically atomic hydrogen found in the plasma, plays a critical role in diamond growth. Hydrogen atoms react with neutral species such as CH_4 to create $CH_3\bullet$ reactive radicals, which can attach to surface sites. Atomic H is known to etch graphitic sp^2, the H atoms serve to remove back to the gas phase any graphitic clusters that may form on the surface, while leaving the diamond clusters behind. H atoms are also scavengers of long-chained hydrocarbons. This prevents the build-up of polymers or large ring structures in the gas phase, which might ultimately deposit onto the growing surface and inhibit diamond growth. The bulk of diamond is fully sp^3 bonded, but at the surface during the growth a dangling bonds are present, which need to be terminated in order to prevent reconstruction of the surface to graphite. This surface termination is performed by hydrogen, which keeps the sp^3 diamond lattice stable.

CVD diamond film can be found with two different morphologies: microcrystalline and nanocrystalline.[74] The microcrystalline diamond CVD growth uses hydrocarbon-hydrogen (e.g., 1% CH_4/99% H_2) gas mixtures, while nanocrystalline films are deposited from $CH_4/Ar/H_2$ (0.5-1 %) gas mixtures. Work on the $CH_4/H_2/Ar$ system has made it clear that growth species change as a function of gas phase composition and chemistry. The nanocrystallinity is a result of a new growth and nucleation mechanism, which involves the insertion of C_2, carbon dimer, into surface carbon-carbon and carbon-hydrogen bonds. Very high rates of heterogeneous nucleation are observed, and the resulting films consist of randomly oriented phase pure diamond grains with well-defined grain boundaries.[148,182] The difference in the films grown from CH_4/Ar plasmas compared with films from CH_4/H_2 plasmas is the microstructure. The nanocrystalline diamond consists of randomly oriented 3-10 nm crystallites, compared with the columnar

microstructure of the microcrystalline film, which is composed of crystallites several microns in size. The difference in individual crystallite size means that secondary nucleation rates associated with growth from hydrogen-poor plasmas are much higher than from CH_4/H_2 plasmas. [148,182] The fraction of atoms in the grain boundaries of microcrystalline films relative to the bulk is extremely small. Most of the defects conserve the tetrahedral bonding within the interface layer. Grain boundaries of a nanocrystalline diamond are different from those of microcrystalline. It was found that they are mainly threefold-coordinated and form π bonds. The electronic band structure of grains was characterized by a smaller band gap than the bulk diamond and it was shown that these states can participate in hopping conduction.[148,182] The special nature of π-bonded grain boundaries imparts unique electrical properties on nanocrystalline diamond films and the conducting grain boundaries will rule the electronic properties of undoped film. With decreasing crystallite size their number vastly increases, and the entire film becomes electrically conducting. Changes in the size of the nanocrystallites, therefore, can dramatically alter film properties. [148,182]

More detailed discussion of the film morphology and microstructure, along with evaluation of the electrochemical properties of boron-doped microcrystalline and nanocrystalline diamond is presented further in the research chapters.

The band gap of diamond is 5.5 eV rendering the material a very good insulator, however, impurity incorporation results in extrinsic semiconducting properties.[183] Naturally occurring impurities that have implications for the host diamond consist of N, H, and B. [148,182] The nitrogen incorporation gives diamond *n*-type electronic character. Substitutional nitrogen is a deep donor with ionization energy of about 1.7 eV. The

donors are typically too deep to provide any useful semiconducting properties to the material at room temperature.

It is known that the electrical properties of diamond are strongly influenced by the presence of hydrogen. Hydrogenation leads to a decrease in resistivity through increased hole conduction leading to p-type character of diamond surface region. The study by Jackman et al.,[184] suggest that hydrogen within diamond give rise to shallow acceptor states or deeper gap states, causing band bending and accumulation of holes. The origin of this effect remains still controversial.

Boron is the most often used dopant and this element can be introduced into diamond without significant distortion of the lattice. Boron may be introduced into CVD diamond film from: (i) a gaseous source, such as B_2H_6, (ii) a solid state dopant, such as B_2O_3 and h-BN, and (iii) a boron containing solution, such as boron powder dissolved in organic solvents from which vapors are carried into the reaction chamber by the growth gases.[184] Boron is an electron acceptor and provides a *p*-type electronic character to the material.[183] Doping levels ranging from 10^{16} to 10^{21} B/cm^3 can be achieved. As boron is introduced into the lattice, the activation energy of boron acceptor is near 0.37 eV above the top of the valence band. Activation energy of acceptors is observed to decrease with increasing boron concentration. This decrease of the energy can be explained by acceptor band width increase, impurity band formation and conduction as result of it. For highly doped films, activation energies as low as 2 meV have been reported.[185] For these highly doped films the impurity band conduction merges with the valence band, and metallic conduction is observed. High abundance of boron during diamond deposition can degrade the quality of the diamond,[186] which is manifested by increased point defect densities and in extreme instances by graphitization of the

diamond film.[186,183] Figure 1.4 shows the bandgap diagram for boron-doped diamond electrode.

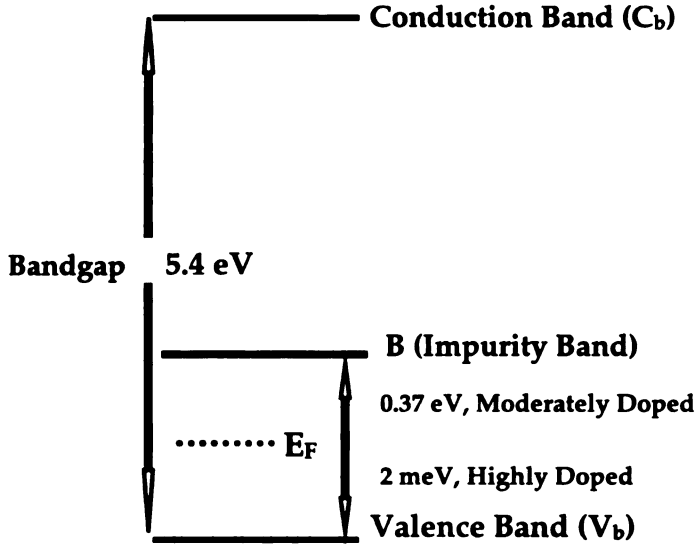

Figure 1.4 A diagram for the band structure of boron-doped diamond.

Boron-doped, polycrystalline diamond electrodes deviate from ideal p-type semiconductor behavior because of a high density of mid-gap electronic states. The mid-gap density of states results from at least four factors: (i) boron-doping level, (ii) lattice hydrogen content, (iii) inherent grain boundaries and other defects in the polycrystalline films, and (iv) non-diamond carbon impurity at the surface.[63,163]

Of the four factors presented that can influence the diamond conductivity, the surface non-diamond carbon phases exert little influence on the response of doped diamond films. It has been shown by Granger at al.;[187] that the removal of non-diamond carbon by acid washing and hydrogen plasma treatment does not inhibit the electrode electronic properties. The role of morphological defects and grain boundaries on the electrode kinetics, specifically the electrical conduction, at polycrystalline films is still not clearly understood. Diamond is host for a variety of extended defects such as stacking

faults, microtwins, dislocations, grain boundaries, and mixed habit growth features.[63 and references therein] These defects could serve as discrete sites for electron transfer or could simply affect the electronic properties of the material by increasing the density of states. The mid-gap density of states arising from grain boundaries and defects, though, is relatively low compared to the number of states arising from the boron doping and lattice hydrogen. The electrical conduction could be also inhibited by grain boundaries and defects because of a reduction in the electron and hole mobilities.

1.4. Outline of the Dissertation

All the experimental protocols are presented in Chapter 2. In Chapter 3, the electrochemical and physical properties of microcrystalline boron-doped diamond thin-film electrodes are described. The films were deposited on three different substrates (W, Mo, and Si). The purpose for this work was to learn how the substrate material directly or indirectly influences the physicochemical properties and the electrochemical response. In Chapter 4, the electrochemical and physical properties of boron-doped nanocrystalline diamond thin-film electrodes are presented. Chapter 5 contains results of voltammetric studies on electrooxidation of aliphatic polyamines: cadaverine (CAD), putrescine (PUT), spermine (SPM) and spermidine (SPMD) at microcrystalline and nanocrystalline diamond are presented. In this chapter the amine oxidation model is proposed and tested. An evidence for importance of non-diamond carbon impurities and boron surface sites in the reaction model is presented. The mechanistic and kinetic aspects of the amine oxidation reaction have been studied by voltammetric methods on stationary and rotated disc diamond electrodes and are presented in Chapter 6. Amperometric detection of aliphatic amine, using diamond has been coupled with flow injection

analysis. Results from these studies are presented in Chapter 7. Finally, in Chapter 8 the results from the reversed-phase liquid chromatography with amperometric detection, using boron-doped diamond thin-film electrodes for the determination of aliphatic polyamines are presented.

Chapter 2

EXPERIMENTAL SECTION

2.1. Boron-Doped Diamond Thin Film Growth

Boron-doped diamond thin films were deposited using a commercial chemical vapor deposition (CVD) system (1.5 kW ASTeX Corp., Lowell, MA). Microwave energy (2.45 GHz), originating from a magnetron, was directed into a quartz reaction chamber, from above, to generate a plasma. Deposition occurred on the surface of the substrate placed on the stainless steel stage positioned in the middle of the reaction chamber. Boron doping was accomplished using two methods: a solid source of boron (B_2O_3 + h-BN) placed inside reaction chamber and gaseous B_2H_6 was mixed, in a controlled way, with a source gas mixture. Figure 2.1 shows the microwave-assisted CVD reactor. Details of the deposition conditions and substrate preparation procedures are presented in the following paragraphs.

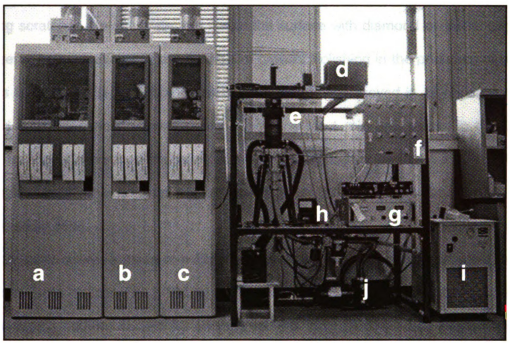

Figure 2.1 A photo of the microwave-assisted CVD reactor: (a) diborane and Ar cylinder cabinet, (b) hydrogen cylinder cabinet, (c) methane cylinder cabinet, (d) microwave generator, (e) reactor, (f) mass flow controller and stop valve, (g) power supply for microwave generator, (h) pressure gauge, (i) water chiller, and (j) rotary pump.

2.1.1. Microcrystalline Diamond Electrodes Doped Using a Solid State Source.

The films were deposited on boron-doped p-Si (100) (Virginia Semiconductor, Inc., Fredricksburg, VA), tungsten (Goodfellow Metals, Cambridge, England), and molybdenum (Goodfellow Metals). The substrates, ca. 1 cm^2, were first rinsed with ultrapure water, toluene, methylene chloride, acetone, propanol, methanol, and ultrapure water. The silicon substrates were subsequently etched in concentrated hydrofluoric acid (HF) for 60 s. After rinsing with ultrapure water and drying, the substrates were mechanically polished by hand for 5 min with a mixture of 2 parts B_2O_3 powder (Aldrich) and 1 part diamond powder (0.1 μm, GE Superabrasives, Worthington, OH). The

polishing scratches the substrate and seeds the surface with diamond particles, both of which serve as nucleation centers during film growth. Polishing in the presence of B_2O_3 appears to lead to a higher doping level than is normally achieved in its absence. The polished substrates were ultrasonicated in acetone for 1 min and placed in the CVD reactor on top of a boron diffusion source (GS 126, B_2O_3-containing disk, BoronPlus, Technoglas, Inc.). The nominal particle coverage of 10^8 cm^{-2}, after sonication, was determined by AFM.

In some cases, a piece of h-BN (Goodfellow Metals) was placed adjacent to the substrates in the reactor. The h-BN, in addition to the embedded B_2O_3 particles, and the boron diffusion source, served as sources for the incorporated boron dopant atoms during deposition.

Ultrahigh purity (99.999%) methane and hydrogen were used. The films were deposited from either a 0.33, 0.40, 0.50, 0.67, or 1.0% methane/hydrogen (CH_4/H_2) source gas mixture, a total gas flow of 200 sccm, a forward power of 1 kW, a deposition pressure of 35 torr, an estimated substrate temperature of 800-850 ^{o}C, and a growth time of ca. 15-20 h. The plasma was ignited with all gases flowing into the reactor. After deposition, the CH_4 flow was stopped and the films remained exposed to the H_2 plasma for an additional 15 min at the growth conditions. After this annealing period, the plasma power and system pressure were gradually reduced, over a 30 min period, to 400 W and 20 torr, in order to cool the samples (<400 ^{o}C) in the presence of atomic hydrogen. Post-growth annealing in atomic hydrogen is critical for etching adventitious non-diamond phases, minimizing dangling bonds, and ensuring full hydrogen termination. The plasma was then extinguished and the films further cooled to room temperature under a flow of hydrogen. Table 2.1 lists the typical deposition conditions for microcrystalline diamond thin film growth.

Table 2.1 Microcrystalline Diamond Thin Film Deposition Parameters

Deposition Parameters	
Substrate	Si, Mo, W,
CH_4/H_2 (v/v) ratio	0.3 - 1 %
Plasma forward power	1 kW
Deposition pressure	30 - 40 torr
Deposition time	15-20 h
Substrate temperature	800-850 °C
Boron dopant source	B_2O_3, h-BN
Doping level	~$1x10^{19}$-$1x10^{20}$ B/cm^3
Resistivity	0.1-0.01 Ω-cm

A doping level of approximately ~$1x10^{19}$-$1x10^{20}$ B/cm^3 was typical for the films, as determined by boron nuclear reaction analysis (BNR) measurements. The film thickness was nominally 4 to 6 μm and the apparent in-plane resistivity was 0.01 Ω-cm or less.

2.1.2. Diamond Electrodes Doped with B_2H_6

2.1.2.1. Nanocrystalline Boron-Doped Diamond Thin Films

The boron-doped nanocrystalline diamond thin films were deposited on p-type Si(100) substrates (~10^{-3} Ω-cm, Virginia Semiconductor Inc., Fredricksburg, VA). The surface of the Si substrate was mechanically scratched on a felt polishing pad with 0.1 μm diameter diamond powder (GE Superabrasives, Worthington, OH). The scratched substrate was then sequentially washed with ultrapure water, isopropyl alcohol (IPA),

acetone, IPA, and ultrapure water to remove polishing debris. The scratching treatment enhances the rates of nucleation during the initial growth.

The films were deposited from CH_4/ Ar / H_2 Typical flow rates were 1, 94 and 5 sccm, respectively, for CH_4, Ar, and H_2 gas mixtures. The microwave power and deposition pressure were maintained at 800 W and 140 torr, respectively. Table 2.2 lists the typical deposition conditions. The substrate temperature was estimated by an optical pyrometer to be about 800 ^{o}C. The deposition time was 2 h, and the resulting films were approximately 4 μm thick, as estimated from the substrate weight change. The plasma was ignited with all gases flowing into the reactor. At the end of the deposition period, the CH_4 flow was stopped and the Ar and H_2 flows continued. The films remained exposed an H_2/Ar plasma for approximately 10 min. The substrate was then cooled in the presence of atomic hydrogen to an estimated temperature of less than 300 ^{o}C by slowly reducing the power and pressure over a 4 min period. This leads to the formation of a thin and continuous nanocrystalline diamond film in a relatively short period of time.

Table 2.2 Nanocrystalline Diamond Thin Film Deposition Parameters

Deposition Parameters	
Substrate	p-Si (100) or (111)
CH_4/Ar/H_2 (v/v) ratio	1/94/5
Plasma forward power	0.8 kW
System pressure	140 torr
Substrate temperature	~800 ^{o}C
Deposition time	2 h
Boron dopant source	B_2H_6
Doping level (B/C in gas phase)	200-10,000 ppm

The doping level was determined from boron nuclear reaction analysis measurements. Table 2.3 presents a summary of the doping level, apparent resistivity as a function of the B2H6 concentration in the source gas mixture.

Table 2.3 Boron Concentration and Resistivity for a Nanocrystalline Diamond

B_2H_6 concentration introduced (ppm)	B/C ratio (ppm)	Boron concentration (ppm)	Resistivity (Ω-cm)
0 ppm	0*	50	0.3-0.5
1 ppm	200	500	0.3
10 ppm	2,000	810	0.1
20 ppm	4,000	-----	0.05
30 ppm	6,000	-----	0.03
50 ppm	10,000	3300	0.02

Note: *- no intentionally added B_2H_6

2.1.2.2. Microcrystalline Boron-Doped Diamond Thin Films

The substrate preparation protocol for the boron-doped microcrystalline diamond films was the same as that for nanocrystalline films. The growth parameters, however, were different and are presented in Table 2.4.

2.1.3. Diamond Acid Washing and Hydrogenation Procedure

Prior to electrochemical testing, the diamond films were often cleaned by a 2-step Chemical treatment. The first step involved immersing the films in warm aqua regia for 30 min, followed by rinsing with ultrapure water. The second step involved exposing the samples to a warm solution of H_2O_2 (30%) for 30 min, followed by rinsing with ultrapure water, and drying. The films were then hydrogen plasma treated (microwave-assisted CVD) for 1h to remove the surface oxides formed during the acid washing and

to terminate the surface with hydrogen. The hydrogen was introduced into the reactor at a flow rate of 200 sccm. The plasma power, system pressure, and temperature were 1 kW, 35 torr, and 800 ^{o}C, respectively.

Table 2.4 Microcrystalline Diamond Thin Film Deposition Parameters

Deposition Parameters	
Substrate	p-Si (100) or (111)
CH_4/H_2 (v/v) ratio	0.5 %
Microwave power	1 kW
Deposition pressure	45 torr
Substrate temperature	800 ^{o}C
Deposition time	10 h
Boron dopant source	B_2H_6
Doping level	~$1x10^{19}$-$1x10^{20}$ B/cm^3
Resistivity	0.1- 0.01 Ω-cm

2.2. Diamond Thin Film Characterization

The films were comprehensively characterized by scanning electron microscopy (SEM), atomic force and scanning tunneling microscopy (AFM/STM), Raman spectroscopy, powder x-ray diffraction (XRD), boron nuclear reaction analysis, and static secondary ion mass spectrometry (SIMS). At a minimum, every film was examined by AFM and Raman spectroscopy. Table 2.5 presents a summary of the techniques used, along with information each technique provides.

Table 2.5 Analytical Techniques Used for Film Characterization

Technique	Information
Scanning Electron Microscopy	Morphology
Transmission Electron Microscopy	Morphology
Atomic Force Microscopy	Morphology
Raman Spectroscopy	Microstructure
X-Ray Diffraction	Crystallinity
Boron Nuclear Reaction	Boron dopant concentration
X-Ray Photoelectron Spectroscopy	Surface chemical composition
Secondary Ion Mass Spectrometry	Boron dopant concentration

2.2.1. Scanning Electron Microscopy (SEM)

SEM was performed with a JEOL-6400V electron microscope. Images were collected at a 2048x1536 pixel resolution with an ADDA II digital image acquisition system and AnalySIS Pro 3.2 image acquisition software (both Soft Imaging System GmbH, Munster, Germany). Typically, an accelerating voltage of 15 kV was employed. The samples were mounted on aluminum stubs with conductive carbon tape.

2.2.2. Transmission Electron Microscopy (TEM)

TEM was performed with a JEM-4000EX electron microscope. The samples were prepared by growing a nanocrystalline diamond thin film for 10 min on a Si substrate and then dissolving the substrate using an HF/HNO_3 solution. The free-standing pieces of diamond were collected from solution and washed on a gold TEM grid.

2.2.3. Atomic Force Microscopy (AFM)

AFM was performed with a NanoScope III instrument (Digital Instruments, Santa Barbara, CA) in the contact mode. Si_3N_4 probe tips, mounted on Au cantilevers (100 μm) with spring constants ranging from 0.54 to 0.06 N/m, were used to acquire topographical images of the films, in air.

2.2.4. Raman Spectroscopy

Raman spectra were obtained in a back-scattered collection mode with a Raman 2000 spectrometer equipped with a microprobe attachment (2080) and a direct video module (2090) (Chromex, Inc., Albuquerque, NM). The spectra were obtained using a 1200 grove/mm holographic grating. Excitation was from a frequency-doubled Nd-YAG (532 nm, 30 mW) laser. The laser beam was focused to a spot size of approximately ~5 μm yielding an estimated power density of 150 kW/cm^2. Spectra were collected with a 10 s acquisition time. The spectrometer, prior to use, was calibrated with a single crystal (Type IIa) diamond standard (100 orientation, Harris Diamond).

2.2.5. X-Ray Diffraction (XRD)

2θ x-ray diffraction analysis was performed using a Philips X-Pert MPD diffractometer in the continuous scan mode. X-rays of 1.540 Å were generated from a Cu anode. The scan range was from 20 to 125 degrees, using a step size of 0.05 degrees. A count time of 1 s/step and a generator power of 45 kV at 40 mA were used. The diffractometer was equipped with a parallel plate collimator, a flat graphite monochromator, and a Xe proportional counter detector. Diffraction profiles were collected, using incident angles of 0.5, 2.0, and 5.0 degrees with respect to the sample surface. The samples were mounted onto a top referencing, zero background sample

holder, and supported from the backside with wax. The XRD was performed as a courtesy by Dr. Jennifer Spear at Philips.

2.2.6. Boron Nuclear Reaction (BNR)

The boron dopant concentration was deterimined by boron nuclear reaction analysis (Surface Characterization Facility, Case Western Reserve University). Calibration was performed with a piece of high-quality boron nitride.

2.2.7. Secondary Ion Mass Spectrometry (SIMS)

The secondary mass ion mass spectrometry (SIMS) was performed using a Cameca/ION-TOF SIMS IV instrument (Muenster, Germany) with a time-of-flight mass analyzer. Positive-ion spectra were acquired using Ar ions at 11 keV. The data were obtained as a courtesy by Prof. Tom Beebe at the University of Utah.

2.2.8. Resistivity

Measurements of the in-plane film resistivity were made using a tungsten four point probe with a 1 mm probe spacing. Currents (μA range) were applied between the outer two probes and the resulting voltage drop between the inner probes was measured. Five measurements were taken and V/I or R values were determined by averaging the measurements. No correction factor was used for edge effects or probe placement. The resistivity was calculated using:

$$\rho = \left(\frac{\pi l}{\ln(2)}\right) \times \left(\frac{V}{I}\right)$$

where l is the film thickness (mm).

2.3. Electrochemical Measurements

2.3.1. Cyclic Voltammetry Experiments

The cyclic voltammetric measurements were made with a CYSY-2000 computerized potentiostat (Cypress System Inc., Lawrence, KS), using a single-compartment, three-electrode glass cell, presented in Figure 2.2. [63]

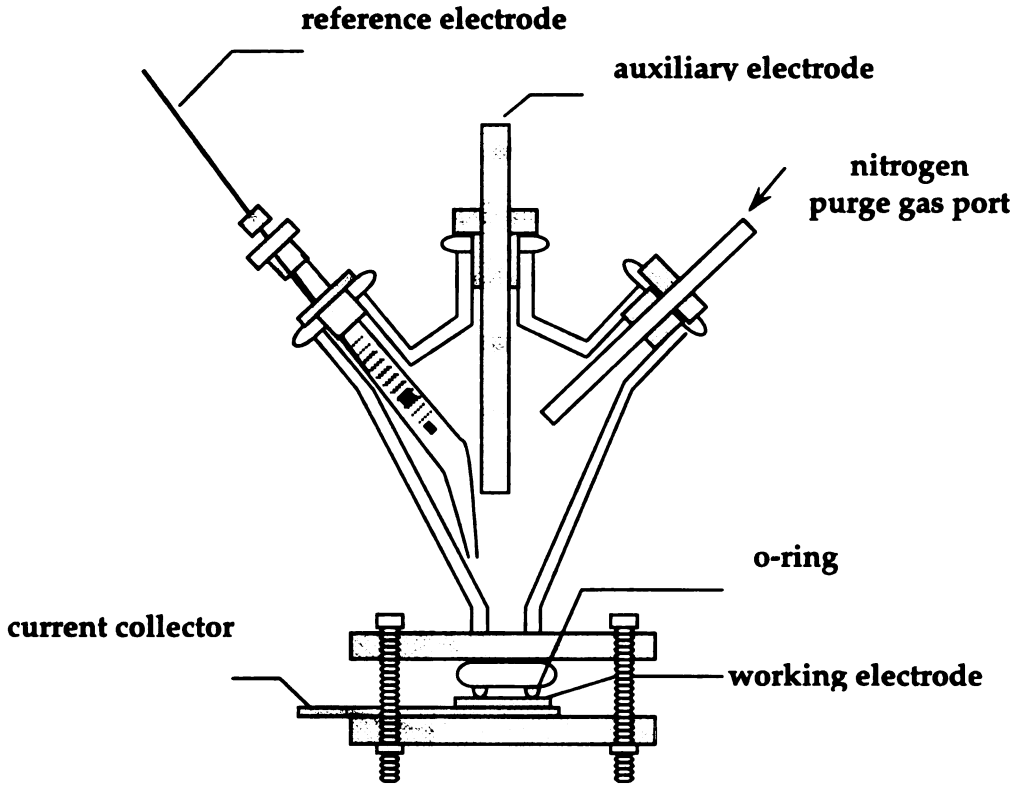

Figure 2.2 Design of the electrochemical, three-electrode glass cell.

The diamond thin-film working electrode was pressed against a Viton® o-ring and clamped to the bottom of the glass cell. Ohmic contact was made by pressing a copper plate against the backside of the scratched and cleaned Si substrate, which contained a bead of Ga/In alloy or silver paste. A graphite rod was used as the counter electrode, and a commercial Ag/AgCl electrode (3 M NaCl, Cypress Systems, Inc.) served as the

reference. The geometric area of the working electrode was ca. 0.2 cm^2. All measurements were performed at room temperature, ~25°C.

2.3.2. Rotating Disc Electrode (RDE) Experiments

For the RDE measurements, a diamond electrode disc (0.11 and 0.2 cm^2) was perpendicularly attached to the stainless steel rod, using conductive epoxy resin. The electrode was then sealed with an insulating epoxy resin. The stainless steel rod was inserted into the Teflon ™ holder and then attached to the rotor. This arrangement allowed the electrode to be rotated at angular velocities ($\omega=2\pi f$). ranging from 500 to 3000 n/min (52.2-314.2 rad/s). The RDE measurements were performed with a Metrohm Model 628-10 rotator (Metrohm, Switzerland) connected to a CYSY-2000 computerized potentiostat (Cypress System Inc., Lawrence, KS)

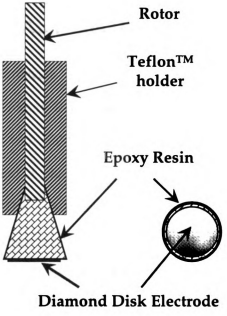

Figure 2.3 Design of the rotating disk electrode.

2.3.3. Double-Layer Capacitance

The double-layer capacitance (C_{dl}) measurements were made using a SR830 DSP lock-in-amplifier (LIA, Stanford Research Systems) connected in series with the Omni-90 analog potentiostat (Cypress System Inc., Lawrence, KS). The potentiostat had a low pass filter built into the design with a 20 μs time constant. A 10 mV r.m.s. and 40 Hz sine wave was co-added to constant dc potentials between -500 and +1000 mV (100 mV increments), and the imaginary component of the total impedance was monitored. All values reported are normalized to the electrode geometric area of 0.2 cm^2. The capacitance was calculated from the relationship:

$$C_{dl} = \frac{1}{\omega Z_{im}} = \frac{1}{2\pi f Z_{im}}$$

where C_{dl} is the double-layer capacitance [$\mu F/cm^2$], Z_{im} is the imaginary component of the total impedance [V/A], and ω is the angular frequency.

2.4. Flow Injection Analysis (FIA)

Flow injection analysis studies were performed using a thin-layer, electrochemical flow cell. Figure 2.4 shows a cell diagram. [188]The two-piece thin-layer flow cell was constructed with Kel-f™. The top piece contained the entrance and exit ports for the fluid flow and a place for the Ag/AgCl reference electrode (3 M NaCl, Cypress Systems, Inc.). The exit port was fitted with a short piece of stainless steel tubing (-6 cm In length), which served as the auxiliary electrode. The bottom piece of the cell supported the working electrode. Electrical contact was made by pressing a piece of copper foil against the backside of the conducting substrate. Sometimes the copper was mated to the substrate, using silver paste, or after scratching the backside with a graphite pencil. A 0.1 cm-thick neoprene rubber gasket separated the surface of the

working electrode (~0.11 cm^2) from the top piece of the cell. A rectangular groove (1.1 x 0.1cm^2) was manually cut into the gasket, and this defined the flow channel. Assuming a 25% compression of the gasket with the two pieces of the cell clamped together, the cell volume was estimated to be ~8 μL.

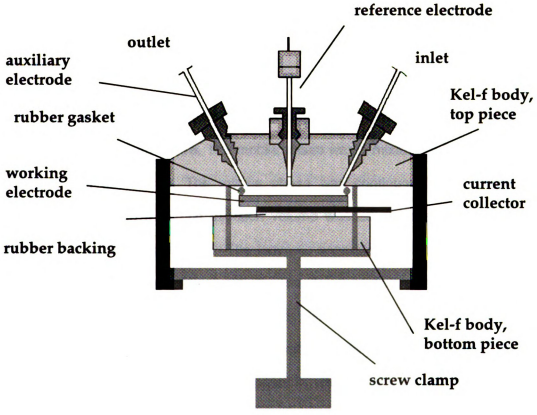

Figure 2.4 Design of the thin-layer electrochemical flow cell.

Flow injection analysis (FIA) was conducted with components of commercial HPLC system (Shimadzu Scientific Inc.): an autoinjector (SIL-10ADVP), a controller (SCL-10AVP), a gradient pump (LC-10 AD VP), and a degasser (DGU-14 A). All the components were electrically grounded to a common point, and the electrochemical flow cell was housed in Faraday cage to reduce the pick-up of spurious electrical noise. FIA

measurements were made with an Omni 90 analog potentiostat (Cypress System Inc., Lawrence, KS). Data acquisition and processing were performed with the Shimadzu Class-VP 7 chromatography software package. The carrier solution was deoxygenated on-line, using the degasser, and aspirated through a suction filter. Additionally, the carrier solution was continuously purged with nitrogen. The injection volume was 20 μL and the flow rate was 1 mL/min, unless stated otherwise.

2.5. HPLC System

The reversed-phase liquid chromatography was performed with the commercial HPLC system described above. The mobile phase was a mixture of 0.01 M borax buffer (pH 11.2) and acetonitrile. The mobile phase was continuously deoxygenated with nitrogen (99%) purge gas. The injection volume was 20 μL, and the flow rate was 1 mL/min, unless stated otherwise. The isocratic separation of the aliphatic polyamines was carried out using a guard column (X-Terra, 5 μm particle size, 3.9 x 20 mm) and a C_{18} reversed-phase column (X-Terra, 5 μm particle size, 4.6 x 150 mm) in series (Waters). The stationary phase was 3-(chlorodimethylsilyl)propyl-N-dodecyl carbamate. This column has a modified silica support in which some of the silicon atoms are replaced with carbon. This substitution reduces the solubility at high pH, yet leaves sufficient silanol activity to enable the use of traditional bonding chemistry to covalently attach the stationary phase. The polyamine solutions were passed through a PTFE syringe filter (0.2 μm) before being placed in the glass sample vials of the autoinjector.

2.6. Chemicals and Reagents

Reagent grade quality chemicals and ultrapure deionized water (18 MΩ, Barnstead E-pure) were used to prepare all solutions. Sodium perchlorate hydrate (99%,

Aldrich), sodium bicarbonate (EM Science), and sodium hydroxide (Fisher) were used to prepare the 0.01 M carbonate buffers. Sodium chloride (Aldrich), sodium borate (Fisher Scientific), and sodium hydroxide (Fisher Scientific) were used to prepare a series of borax buffers ranging in pH from 8 to 11. The borax buffer was prepared with 0.01 mol/L of $Na_2B_4O_7$ and 0.01-0.1 mol/L of NaCl, adjusted to the required pH with the addition of 6 M NaOH. The 0.1 M phosphate buffer, pH 7.2, was prepared with potassium phosphate dibasic (Mallincrodt) and potassium phosphate monobasic (Mallincrodt).

The methylamine (Aldrich), ethylamine (Aldrich), propylamine (Aldrich), ethylenediamine (Aldrich), 1,3-propyleneamine (Aldrich), putrescine (1,4-butanediamine, 99%, Sigma), cadaverine (1,5-pentanediamine, 99%, Sigma), 1,6-hexanediamine (Aldrich), spermidine (*N*-(3-Aminopropyl)-1,4-butanediamine, 99%, Sigma), spermidine (2,2) (*N*-(2-Aminoethyl)-1,2-ethylenediamine, 99%, Sigma), spermidine (3,3) (*N*-(3-Aminopropyl)-1,3-propylenediamine, 99%, Sigma), spermine (N, N'- Bis(3-aminopropyl)-1,4-butanediamine, 99%, Sigma), Dytek® A (1,5-pentanediamine, 2-methyl, DuPont Nylon), Dytek® EP (1,3-propylenediamine, 1-ethyl, DuPont Nylon), and acetonitrile (HPLC grade, Aldrich) were used without any additional purification. 1.0 mM stock solutions were prepared by dissolving the analyte in the buffer. Table 2.6 shows the molecular formula and properties of the aliphatic amines used.

The diamond film electrochemical response was characterized by cyclic voltammetry using the following inorganic and organic systems: potassium ferrocyanide ($Fe(CN)_6^{-3/-4}$, Aldrich), hexaammineruthenium (III) chloride ($Ru(NH_3)_6^{+3/+2}$, Aldrich), iridium (IV) hexachloride ($IrCl_6^{-2/-3}$, Aldrich), methyl viologen dichloride hydrate ($MV^{+2/+1/0}$, Aldrich), 4-tert-butylcatechol (4-tBC, Aldrich), and ferric sulfate hydrate ($Fe^{+2/+3}$, Aldrich). All reagents were used as received. The supporting electrolyte for $Fe(CN)_6^{-3/-4}$, $Ru(NH_3)_6^{+3/+2}$, $IrCl_6^{-2/-3}$, and methyl viologen ($MV^{+2/+1/0}$) was 1.0 M KCl.

The supporting electrolyte for 4-tert-butylcatechol, and $Fe^{+2/+3}$ was 0.1 M $HClO_4$. Potassium chloride (Fisher), nitric acid (Fisher), and perchloric acid (Aldrich) were ultrahigh purity (99.999%).

All glassware was cleaned by sequentially rinsing in a KOH/ethanol bath, an alconox solution, and ultrapure water.

Table 2.6 Molecular Formula and Properties of the Aliphatic Amines

Amine	Formula	pK_a values [5,189]	Formula Weight
methylamine (MA)	H_2NCH_3	10.62	31 g/mol
ethylamine (EA)	$H_2N(CH_2)_2$	10.70	45 g/mol
propylamine (PA)	$H_2N(CH_2)_3$	10.75	59 g/mol
ethylenediamine (EDA)	$H_2N(CH_2)_2NH_2$	6.85, 9.93	60 g/mol
diaminopropane (DAP)	$H_2N(CH_2)_3NH_2$	8.47, 10.46	74 g/mol
putrescine (PUT)	$H_2N(CH_2)_4NH_2$	9.35 , 10.6	88 g/mol
cadaverine (CAD)	$H_2N(CH_2)_5NH_2$	9.13 ,10.8	102 g/mol
hexanediamine (HA)	$H_2N(CH_2)_6NH_2$	9.8, 10.9	116 g/mol
spermidine 3,4 (SPMD)	$H_2N(CH_2)_3NH(CH_2)_4NH_2$	8.2, 9.86, 10.85	145 g/mol
spermidine 3,3 (SPMD 3,3)	$H_2N(CH_2)_3NH(CH_2)_3NH_2$	8.1, 9.70,10.70	131 g/mol
spermidine 2,2 (SPMD 2,2)	$H_2N(CH_2)_2NH(CH_2)_2NH_2$	8.0, 9.50, 10.51	103 g/mol
Dytek® A (DA)	$H_2NCH_2\ CH(CH_3\ )(CH_2)_3NH_2$	10.69	116 g/mol
Dytek® EP (DEP)	$H_2N\ CH(C_2H_5\ )(CH_2)_2NH_2$	10.69	102 g/mol
spermine (SPM)	$H_2N(CH_2)_3NH(CH_2)_4NH(CH_2)_3NH_2$	7.90 , 8.80, 10.10, 10.90	202 g/mol

Chapter 3

THE CHARACTERIZATION AND ELECTROCHEMICAL RESPONSIVENES OF BORON-DOPED MICROCRYSTALLINE DIAMOND THIN-FILM ELECTRODES

3.1. Introduction

The work reported herein was motivated by our interest in understanding the structure-function relationship of boron-doped, polycrystalline diamond thin film electrodes. An issue that has not been addressed yet is the role the substrate might have on the film's electrochemical properties. Several different substrates have been used for diamond growth, including Si,[86,190] Mo,[191,79,192] W,[75,193] Ti,[194,195] Pt,[196-198] and Ni.[196,197]

A substrate material must meet several criteria in order to serve as a substrate for diamond deposition. First, the substrate must have a melting temperature higher than the temperature required for diamond growth (700-850 ^{o}C). Second, the substrate should have a thermal expansion coefficient comparable with that of diamond. The differences in thermal expansion coefficients between the diamond and the substrate

can cause significant film stress, either compressive or tensile, depending on which has the higher expansion coefficient. This can lead to film or substrate cracking and film delamination.

Third, a useful substrate material is one capable of forming a carbide interlayer. This interfacial layer aids in the adhesion by (partial) relief of stresses at the interface caused by lattice mismatch or substrate contraction. If one considers the carbon-substrate interactions possible, then metal, alloy, and pure element substrates can be subdivided into three broad classes based upon their reactivity with carbon: (i) little or no solubility or reaction with C, (ii) solubility or reaction with C, and (iii) carbide formation.

Si is the most commonly used substrate material due to it's availability, low cost, and favorable properties. It has a sufficiently high melting point (1683 K), it forms a thin, carbide interfacial layer (a few nanometres thick), and it has a relatively low thermal expansion coefficient. Molybdenum and tungsten display similar qualities, so these are often used as well.

The chemical nature, the thermal expansion coefficient, and the lattice parameter of the substrate all influence the nucleation, growth, and adhesion of diamond films. The substrate material could impact the electrochemical response of the films in at least three ways. First, pinholes and small crevices between the grains could provide pathways for solution to permeate through the film and reach the underlying substrate. In such cases, electroactive substrates (e.g., W and Mo) will enhance the current magnitude and the potential dependent features in the background voltammetric response. Second, the plasma processing, in the case of microwave-assisted CVD, could result in the incorporation of impurities. For example, silicon impurities from the quartz reactor chamber in diamond are well known.[199] Pt nanoparticles have been detected in diamond films deposited on Pt substrates.[198] Tungsten impurities are known

to be incorporated during hot filament growth.[109] The role these metal impurities might have directly or indirectly on the film structure and electrochemical response has not yet been investigated. Metal inclusions exposed at the surface could catalyze electrochemical reactions. They could also react with the solvent/electrolyte causing an increase in the voltammetric background current. Third, deposition of diamond on non-diamond substrates could lead to internal stress.[200,201] The magnitude of the stress will depend, at least in part, on the difference in thermal expansion coefficients. The role stress plays in the electrochemical response is unknown. One possible manifestation of localized stress is less morphological and microstructural stability during exposure to harsh electrochemical conditions (e.g. electrolyte, solution pH, and current density).

The objectives of this work were: (i) to determine how different substrates affect the morphological, microstructural, chemical, and electrochemical properties of microwave-assisted CVD diamond thin-film electrodes, (ii) to determine if metal particle impurities from the substrates are incorporated during deposition, and (iii) to learn how any incorporated metal particles, if present, influence the electrochemical response.

3.2. Results and Discussion

3.2.1. Electrochemical Characteristics

Figure 3.1 shows capacitance-potential (C_{dl}-E) profiles for microcrystalline diamond films deposited on Si, W, and Mo, respectively, in 1.0 M KCl. The profiles for the uncoated metals are also shown, for comparison. There is a general trend of increasing capacitance with more positive potential for all three diamond films. The capacitance is low and ranges from 3 to 7 $\mu F/cm^2$ over this potential range, similar to previously reported results.[163]

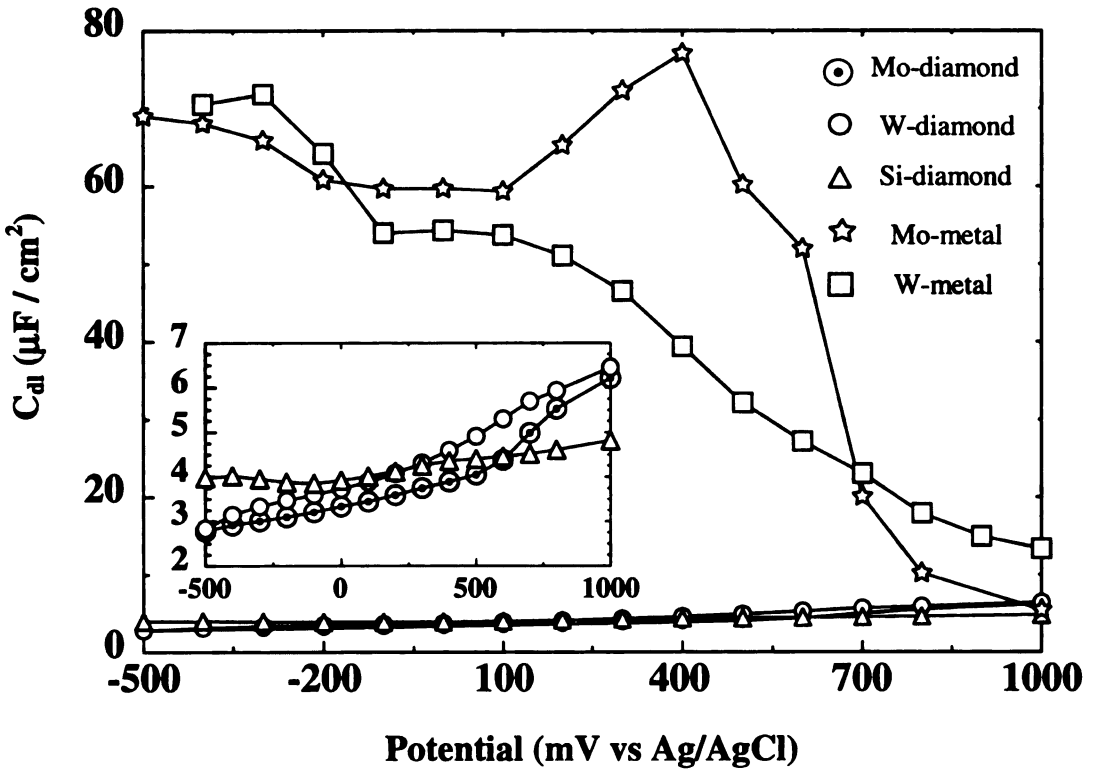

Figure 3.1 Capacitance-potential profiles in 1.0 M KCl for uncoated tungsten and molybdenum, and diamond thin films deposited on W, Mo, and Si substrates. Capacitance values are normalized to the geometric area (0.2 cm^2) of the electrodes. Frequency = 40 Hz. AC amplitude = 10 mV.

These values are over an order of magnitude lower than those for the uncoated metals, except at positive potentials where the formation of an oxide layer passivates the surface. The capacitance of the diamond films deposited on the metal substrates is a little lower at potentials from -500 to 0 mV and a little higher at potentials from 700 to 1000 mV than the capacitance of the film on Si. These data might reflect some minor differences in the electronic properties of the films grown on the metal substrates as compared with those on Si. There is, however, no evidence of any direct solution contact with the metal. The low capacitance of the diamond films, compared to glassy carbon

(25-50 μF/cm^2), for example, is attributed to (i) the absence of redox-active and ionizable surface carbon-oxygen functional groups, and (ii) differences in the electronic properties of diamond due to a lower charge carrier concentration.[63]

Figure 3.2 shows cyclic voltammetric i-E curves for microcrystalline diamond films deposited on Si (A), Mo (B), and W (C) in 1.0 M KCl. Background voltammetric i-E curves are extremely useful for evaluating the diamond film quality.[202] Both the magnitude of the background current and the working potential window are highly sensitive to the presence of electroactive metal particles and non-diamond sp^2-bonded carbon impuritiy. Both types of impurity are expected to be concentrated at grain boundaries and defect sites (i.e., dislocation). The i-E curves are all flat and featureless, with no peaks associated with redox-active surface carbon-oxygen functionalities. The scans were stable with multiple sweeps (not shown here), indicating that there is no penetration of the electrolyte solution through the grain boundaries or defects to the reactive substrate. However, the current magnitude for the film deposited on Si is a factor of 2 lower than the current for the films deposited on the metal substrates. For example, at 250 mV, the current for the film on Si is 0.6 μA, while the current for the films deposited on W and Mo is 1.2 μA and 1.1 μA, respectively. The larger background current is somewhat in contrast to the equal or lower magnitude of the double layer capacitance at this potential seen in Figure 3.1. Therefore, we assume that the slightly larger voltammetric current contains a faradaic component, possibly associated with redox processes on the surface. One possibility is surface redox processes associated with trace levels of surface non-diamond carbon impurity incompletely removed by the acid washing and rehydrogenation pretreatment.

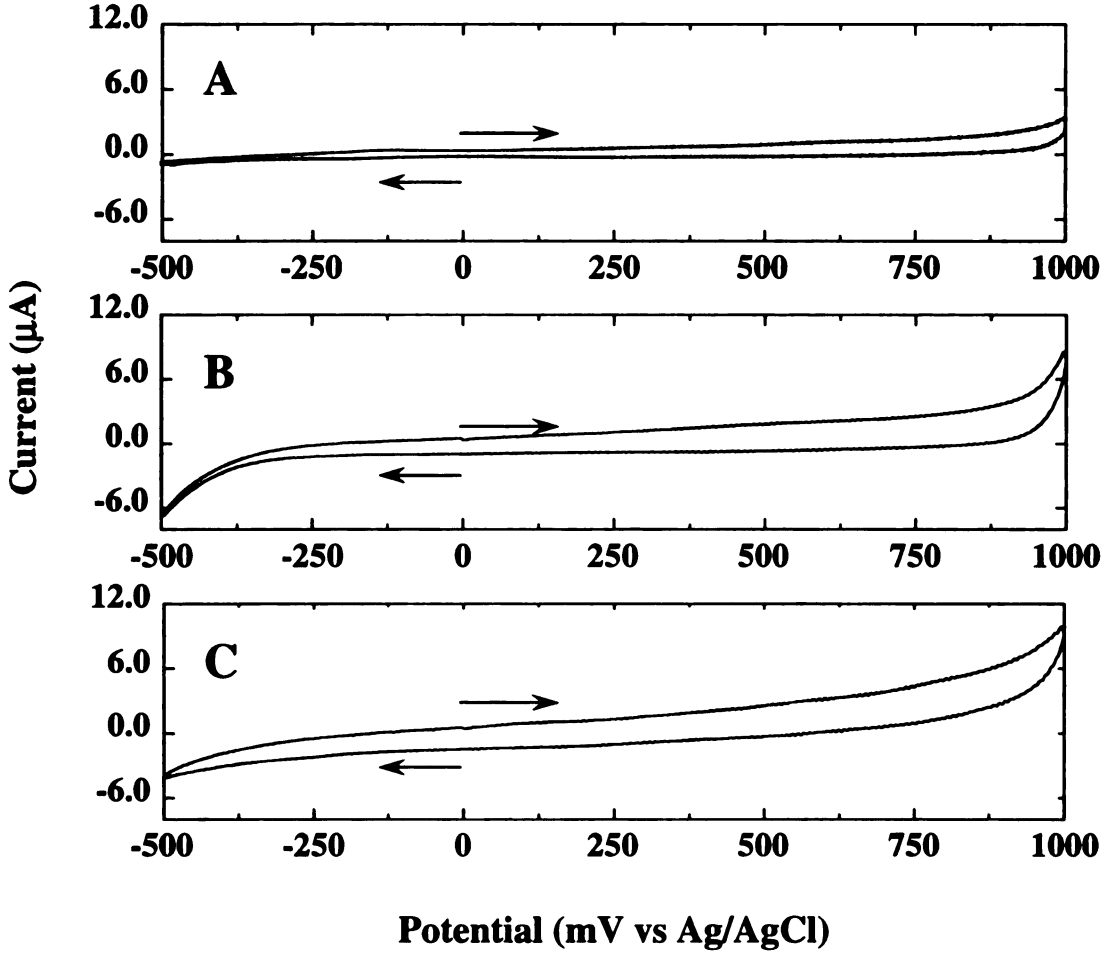

Figure 3.2 Background cyclic voltammetric i-E curves in 1.0 M KCl for boron-doped microcrystalline diamond thin films deposited on (A) Si, (B) Mo, and (C) W. Scan rate = 0.1 V/s. Electrode geometric = 0.2 cm^2.

Figure 3.3 presents background cyclic voltammetric i-E curves in 1.0 M KCl for microcrystalline diamond films deposited on Si, Mo, and W, which reveal the full working potential window. The working potential window, defined as the potential range between current limits of ± 100 μA, is 3.25 V, 3.3 V, 3.25 V for diamond deposited on Si, Mo, and W, respectively. The voltammograms all have a similar shape. The background current

is low and featureless, with approximately 1.25 V as an anodic potential limit. The current at this potential is due presumably to chlorine evolution.[124,202]

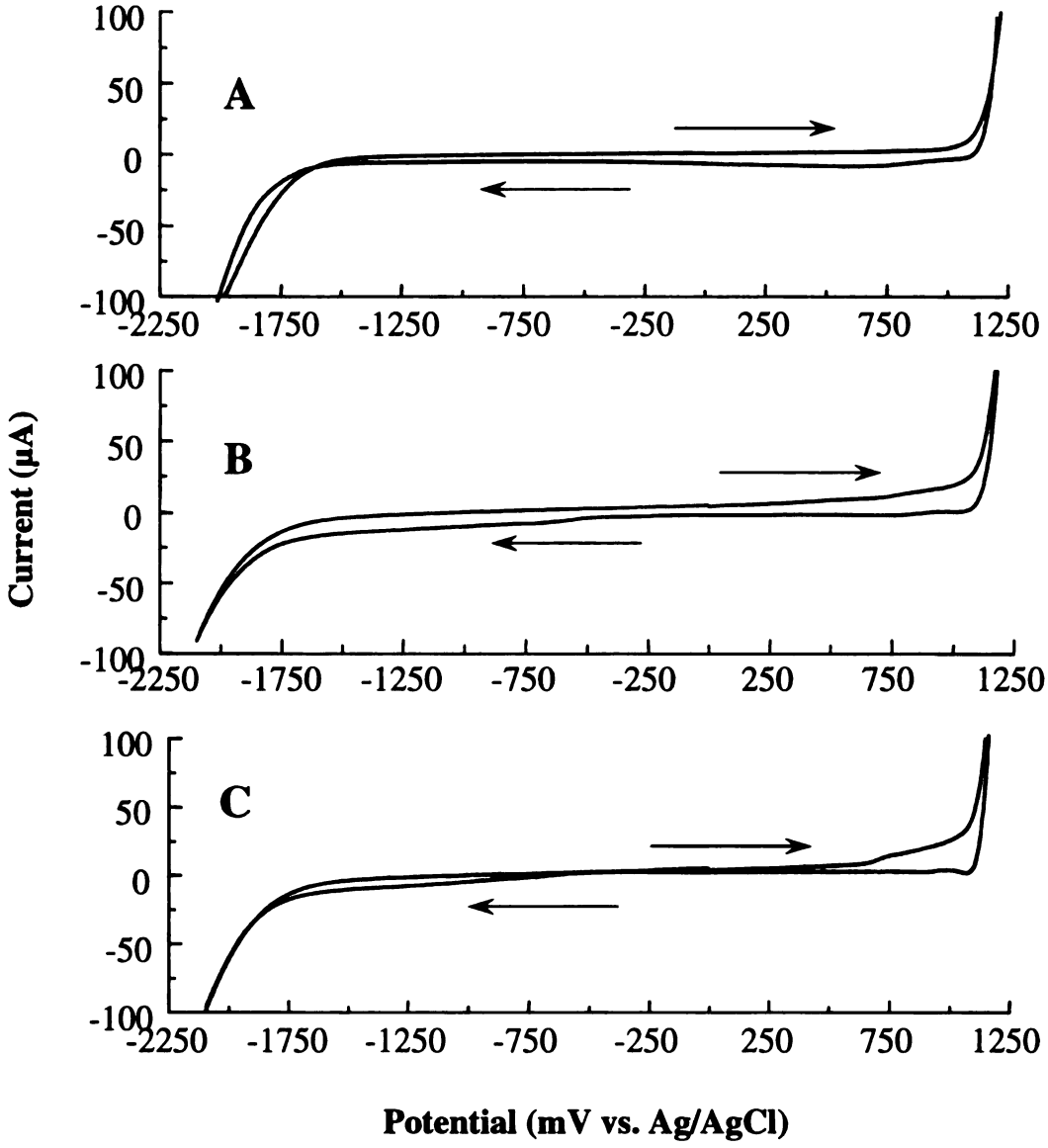

Figure 3.3 Background cyclic voltammetric i-E curves in 1.0 M KCl for boron-doped, microcrystalline diamond films deposited on (A) Si, (B) Mo, and (C) W. Scan rate = 0.1 V/s. Electrode geometric area = 0.2 cm^2.

There is some anodic current passed just prior to the onset potential for chlorine evolution for the Mo and W diamond films. This charge is likely associated with oxidation of residual non-diamond carbon impurity on the surface not removed by the acid washing and rehydrogenation treatment. This charge also may be associated with oxidation of the diamond surface involving replacement of hydrogen with different chemisorbed oxygen functionalities (e.g., OH).[73,187,203]

The reduction of chlorine back to the chloride occurs at different potentials on the three electrodes. A weak peak at ca. 550 mV is seen for this reaction at the Si film. The peak occurs at much more positive values at the Mo and W films, ca. 950 and 1000 mV, respectively. Clearly, the Mo and W films are more active for the reduction of chlorine than is the diamond film deposited on Si.[124,202]

The current at the cathodic limit (> -1700 mV) is attributed to hydrogen evolution. There is some cathodic current that flows on the negative potential sweep at the Mo and W films starting at ca. -750 mV. The current is likely associated with the reduction of trace levels of dissolved oxygen. The slope of the i-E curves in the chlorine and hydrogen evolution regions is similar for all three films. The approximate 3.3 V window for all the films indicates that the macroscopic microstructure and chemical nature of the surfaces are similar. Most importantly, these data, along with the capacitance profiles shown in Figure 3.1, suggest that influential levels of metal impurities from the substrate do not exist at the surface. This conclusion is further supported by SIMS data presented below. A low background current and wide working potential window (3 to 4 V) are characteristic features of high quality diamond. By high quality, we mean a clean, hydrogen-terminated film with negligible amounts of non-diamond carbon impurity and a low level of secondary nuclei formed on the primary diamond microcrystallites.[63,163]

Figures 3.4A and B show background cyclic voltammetric i-E curves in 1.0 M HNO_3 for microcrystalline diamond films deposited on W and Mo.

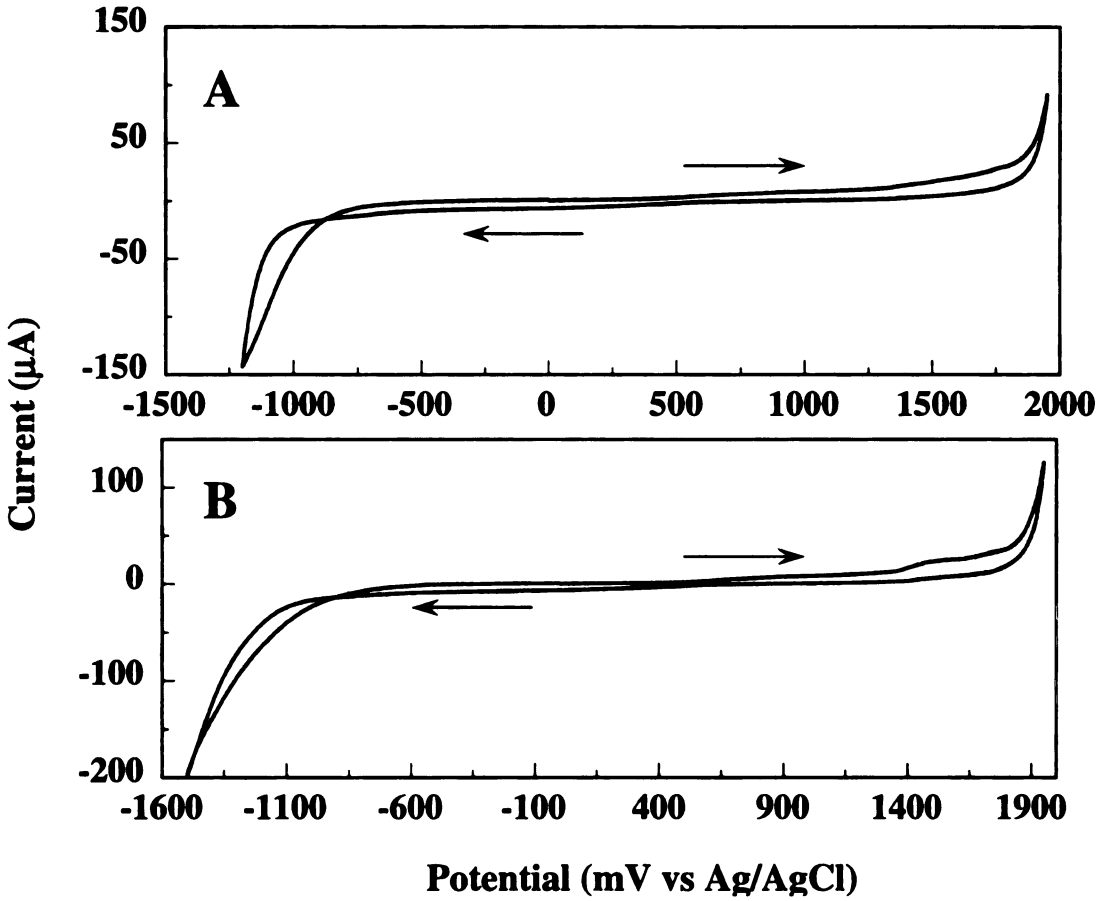

Figure 3.4 Background cyclic voltammetric i-E curves in 1.0 M HNO_3 for boron-doped, microcrystalline diamond thin films deposited on (A) W and (B) Mo. Scan rate = 0.1 V/s. Electrode geometric area = 0.2 cm^2.

The working potential windows are 3.1 and 3.3 V, respectively. A window of 3.2 V was observed for the film deposited on Si (figure not shown). The currents are low and featureless throughout most of the potential range, as was the case in KCl. The Mo film shows some excess anodic charge starting near 1500 mV just prior to the onset

potential for oxygen evolution. This is likely due to the oxidation of the reactive non-diamond carbon impurity in the grain boundaries.

The current at the anodic limit is associated primarily with oxygen evolution and the current at the cathodic limit is due to combination of nitrate reduction[163] and hydrogen evolution. There is also current cross-over during the reverse scan for the nitrate reduction/hydrogen evolution current suggesting that an activation overpotential is needed on this surface to induce the reduction reaction. It is also interesting to note that the slope of the i-E curves in this potential region is steeper for the W film than for the Mo film. The steeper slope reflects faster electrochemical reaction kinetics. No change in the shape of the traces was observed during multiple sweeps (>10) suggestive of a very stable morphology and microstructure in this corrosive medium. Importantly, long term (12h) potential cycling between these limits revealed no indication of electrolyte permeation through the film to the substrate.

Based on this observation, we can rule out the possibility of the substrate material participating directly in the electrochemical reactions. In other words, the diamond film is continuous over the surface, and the morphology and microstructure are stable such that solvent/electrolyte does not permeate the film and attack the electroactive substrate.

Four different analytes were used to probe the reactivity of the electrodes: $Ru(NH_3)_6^{+3/+2}$, methyl viologen ($MV^{+2/+1/0}$), $IrCl_6^{-2/-3}$, and $Fe(CN)_6^{-3/-4}$. The redox systems were chosen based on their E^o values, each's mechanism of electron transfer, and their sensitivity towards various surface properties, i.e., surface chemistry. The question regarding the electronic nature of the diamond electrodes was addressed with redox systems that undergo uncomplicated electron exchange. The $Ru(NH_3)_6^{+3/+2}$, and $MV^{+2/+1/0}$, and $IrCl_6^{-2/-3}$ are such redox couples. These couples undergo outer-sphere,

one-electron transfer reaction.[163] Their kinetics are rather insensitive to the presence of surface oxides or low levels of contaminants at conventional sp^2 carbon electrodes. $Ru(NH_3)_6^{+2/+3}$ and $MV^{+2/+1}$ have $E^{o'}$ values in a negative potential range from -0.17 to -0.68 V vs Ag/AgCl, respectively, and thus can be used to probe electronic properties as a function of applied potential.

$Fe(CN)_6^{-3/-4}$, on the other hand, was used to probe the surface chemistry of the electrodes.[163] This redox couple undergoes a one-electron transfer reaction with the kinetics being highly sensitive to the chemical nature of the diamond electrode surface.[163] The redox reaction proceeds via an inner-sphere route mediated by a specific surface interaction available on the hydrogen-terminated surface. Such surface interactions appear to be blocked on the oxygen-terminated surface.

Apparent heterogeneous electron transfer rate constants (k^o_{app}) were determined by employing the theory developed by Nicholson and Shain:[204]

$$\Psi = \frac{\left(\frac{D_o}{D_R}\right)^{\frac{\alpha}{2}} x\, k^o}{D_o \pi v (nF/RT)^{\frac{1}{2}}}$$

where Ψ is the kinetic parameter, D_o and D_r are the diffusion coefficients for oxidized and reduced form, respectively, α is the transfer coefficient, and v is the sweep rate [V/s]. This theory allows one to calculate k^o_{app} by determining the variation of the peak potential separation (ΔE_p), with sweep rate. No correction was made for double layer effects, therefore, the rate constants presented are referred to as apparent. Calculations of the rate constants were performed assuming a transfer coefficient, α, of 0.5 and diffusion coefficients of 6.8×10^{-6} cm^2/s for $IrCl_6^{-2/-3}$, 5.0×10^{-6} cm^2/s for methyl

viologen, 5.5 x 10^{-6} cm^2/s for $Ru(NH_3)_6^{+2/+3}$, 6.2 x 10^{-6} cm^2/s for $Fe(CN)_6^{-3}$ (ferrocyanide), and 7.6 x 10^{-6} cm^2/s for $Fe(CN)_6^{-4}$ (ferricyanide).[204]

Figure 3.5 shows cyclic voltammetric i-E curves for four redox systems: (A) $Fe(CN)_6^{-3/-4}$, (B) $Ru(NH_3)_6^{+2/+3}$, (C) $IrCl_6^{-2/-3}$, and (D) methyl viologen at diamond films deposited on the three different substrates. The voltammograms were obtained on the hydrogen-terminated surface prior to the potential cycling experiments shown in Figure 3.4.

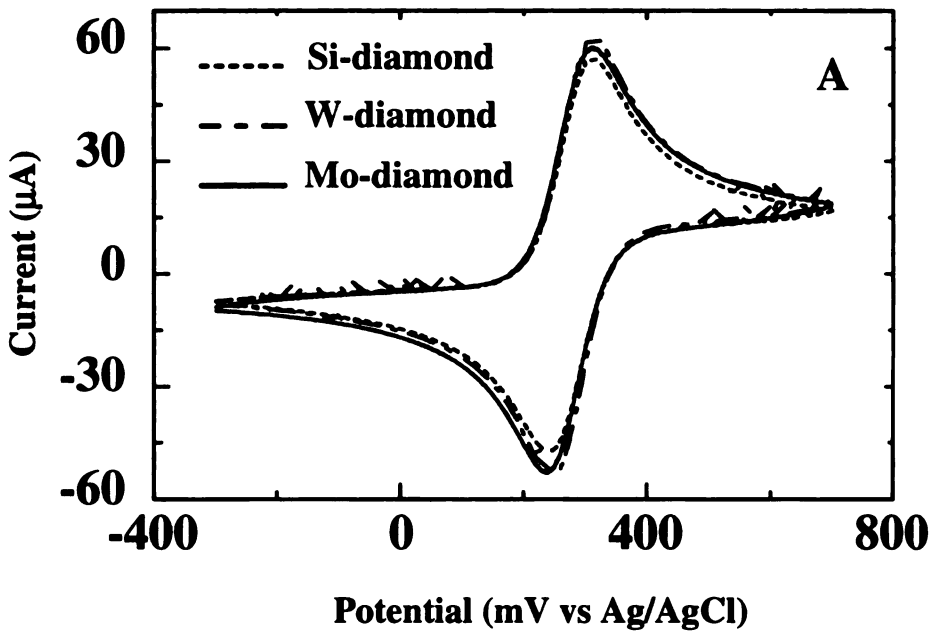

Figure 3.5 A Cyclic votammetric i-E curves for 1.0 mM $Fe(CN)_6^{-3/-4}$ in 1 M KCl at diamond films deposited on different substrates. Scan rate = 0.1 V/s. Working electrode area = 0.2 cm^2.

$Fe(CN)_6^{-3/-4}$ is a very surface sensitive redox system on diamond.[63] ΔE_p for all three films is similar (~70 mV), as are the peak currents. The low ΔE_p suggests the surface is largely oxygen free. The apparent heterogeneous electron transfer rate constant, k^o_{app} is ca. 0.02 cm/s. This value is similar to what has been recently reported

for diamond,[63] and is within an order of magnitude of the highest rate constant reported for freshly activated glassy carbon.[66]

$Ru(NH_3)_6^{+2/+3}$ is a surface insensitive redox system on diamond.[63] ΔE_p for all three films is similar (~ 77 mV), but the peak current for Si are larger than for the other two substrates. k^o_{app} is about a factor of 3 higher at the W film and a factor of 2 higher at the Si film, compared to the Mo film. The approximate value of 0.02 cm/s is similar to what has been previously reported for diamond.[63] It is supposed that differences in k^o_{app} are due to slight variations in the density of electronic states at these potentials.

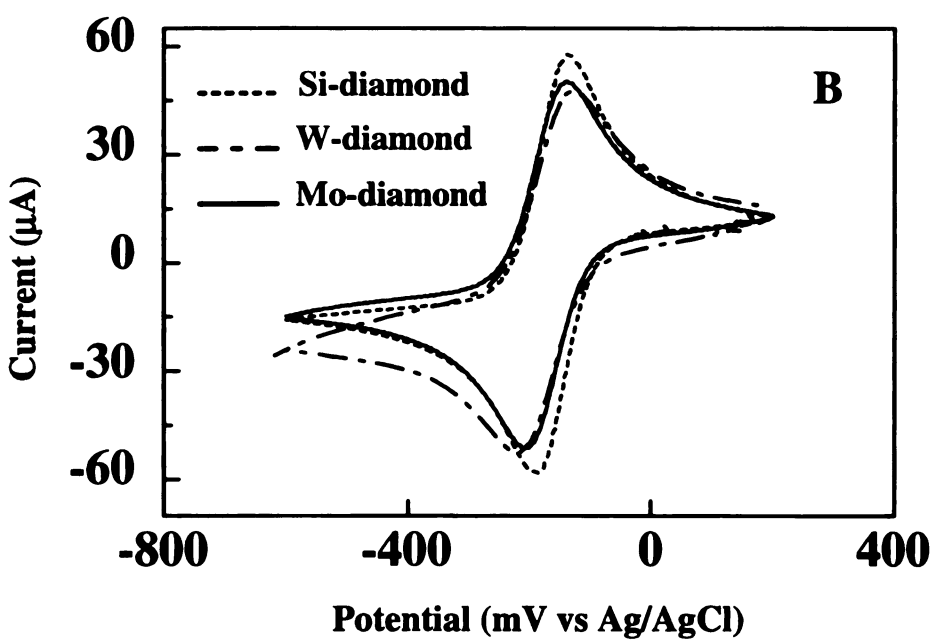

Figure 3.5 B Cyclic votammetric i-E curves for 1.0 mM $Ru(NH_3)_6^{+2/+3}$ in 1 M KCl at a diamond films deposited on different substrates. Scan rate = 0.1 V/s. Working electrode area = 0.2 cm^2.

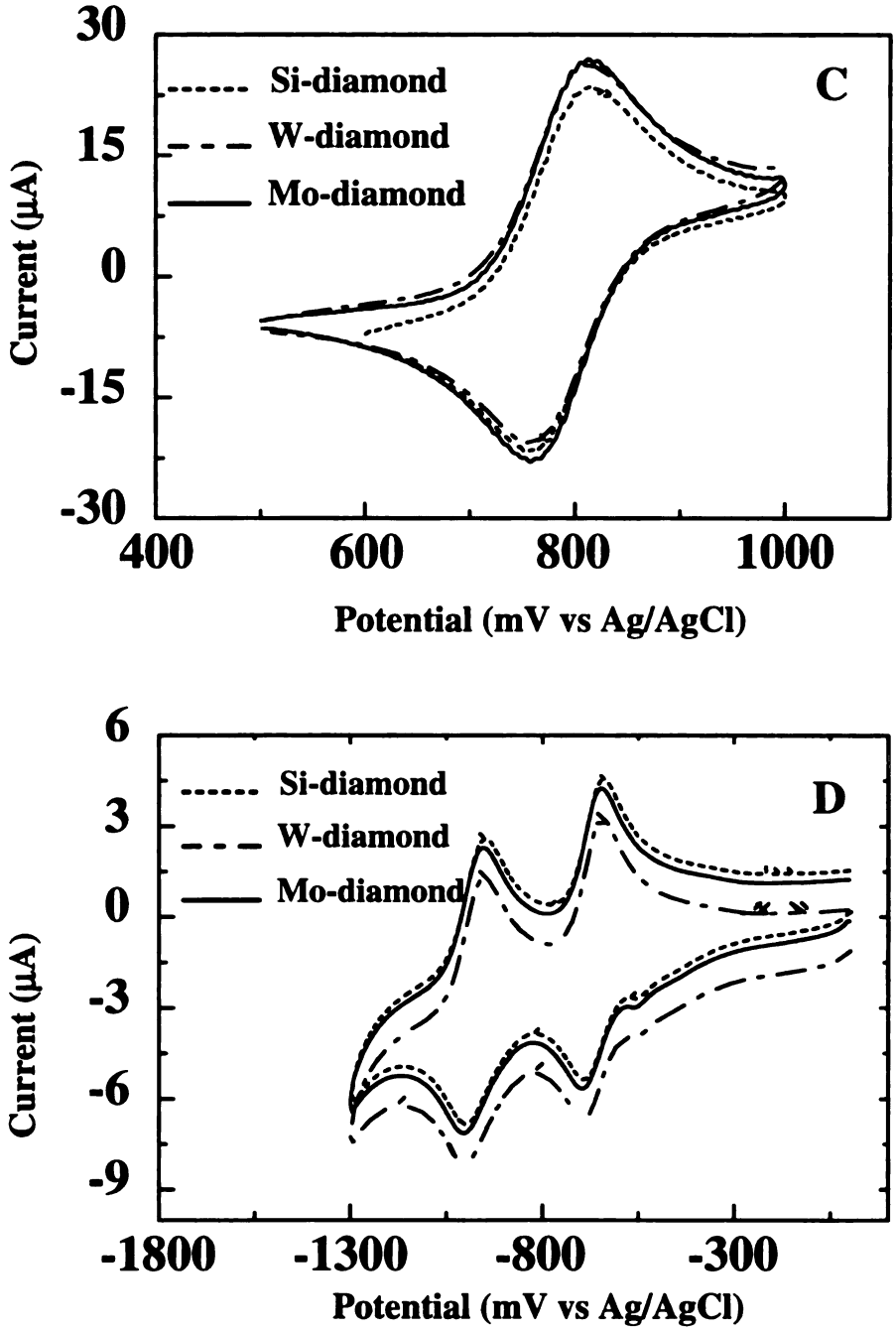

Figure 3.5 Cyclic votammetric i-E curves for (C) 0.5 mM $IrCl_6^{-2/-3}$ and (D) 0.1 mM methyl viologen in 1 M KCl, at diamond films deposited on different substrates. Scan rate = 0.1 V/s. Working electrode area = 0.2 cm^2.

$IrCl_6^{-2/-3}$ is also a surface insensitive redox system on diamond.[63] ΔE_p ranges from 59 to 67 mV and k^o_{app} is ca. 0.1 cm/s. k^o_{app} for the Si film is the largest and is about two times higher than k^o_{app} for either the Mo or W films. The k^o_{app} values reported herein for $IrCl_6^{-2/-3}$ are also the highest that have been observed for diamond.[63]

$MV^{+2/+1}$ is a surface insensitive redox system on diamond. [63] ΔE_p ranges from 59 to 66 mV and k^o_{app} is as high as 0.2 cm/s for the Si film. The k^o_{app} value is larger by about a factor of 2 for the Si film, compared to the Mo and W films. The k^o_{app} value at the Si film is the highest we have observed for diamond [63] and is very near the highest rate constant seen for freshly activated glassy carbon.[66] Typically, only the $MV^{+2/+1}$ couple is used for evaluation of the performance of the electrode, as the $MV^{+1/0}$ couple has been observed to undergo adsorption.[136] At higher concentration, the low solubility of MV^0 results in the formation of a precipitate on the electrode surface. Usually voltammetry for $MV^{+2/+1}$ shows two separate anodic stripping responses associated with an amorphous and crystalline deposit.[136] This process is dependent upon couple variables (e.g., scan rate, mass transport rate, and analyte concentration).[136] For the lower concentration of the $MV^{+2/+1}$ couple, cyclic voltammogram for all the deposited films was well resolved with diffusion limited peak current.

Figure 3.6 shows plots of i_p^{ox} vs scan rate^{½} ($\nu^{½}$). For all films and all redox systems i_p^{ox} varies linearly with $\nu^{½}$ (0.1 -0.5 V/s) (r^2=0.996 to 0.999) with a near-zero y-axis intercept. A of i_p^{ox}/i_p^{red} ratio near 1.0 was also observed. This response linearity is indicative of reaction rates (i.e., current) limited by semiinfinite linear diffusion of reactants to the interfacial reaction zone.

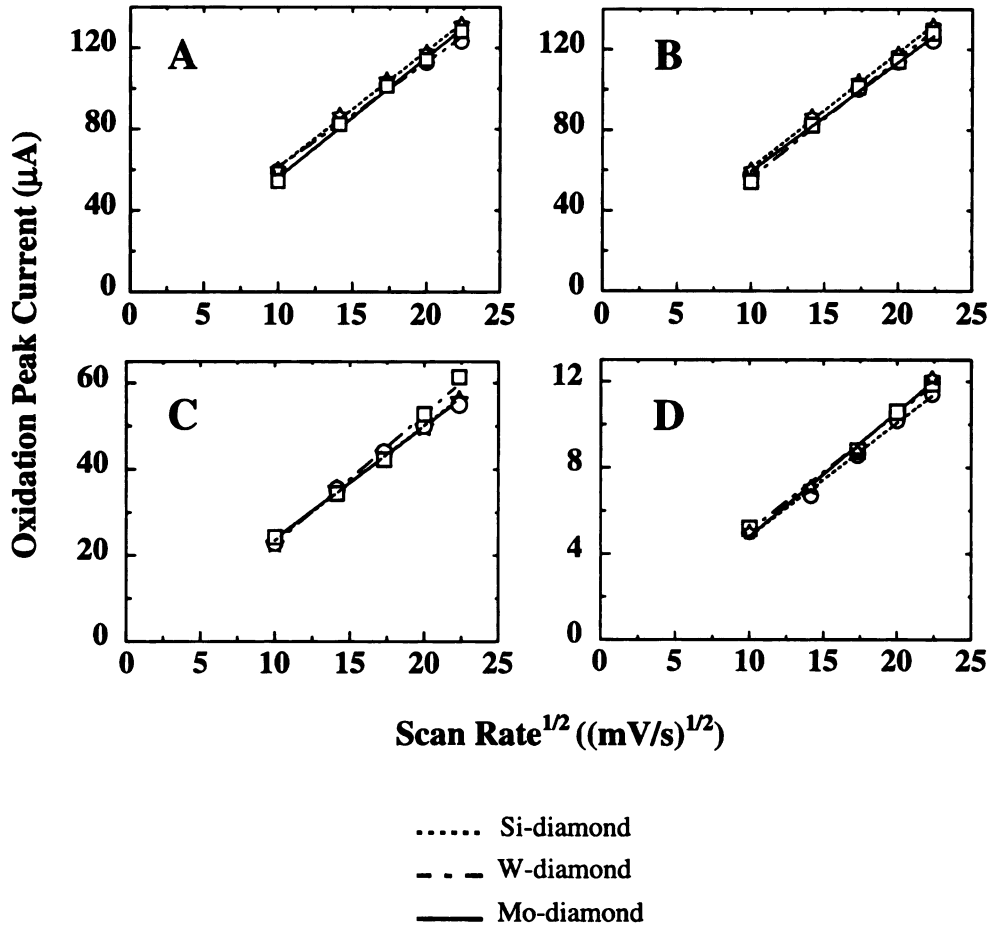

Figure 3.6 Plots of i_p^{ox} vs scan rate$^{1/2}$ for (A) $Fe(CN)_6^{-3/-4}$, (B) $Ru(NH_3)_6^{+2/+3}$,(C) $IrCl_6^{-2/-3}$, and (D) methyl viologen at diamond films deposited on Si, Mo, and W substrates.

A summary of the cyclic voltammetry data and the apparent heterogeneous electron transfer rate constants is presented in Table 3.1. It is important to note that the large rate constants were obtained without any conventional electrode pretreatment (e.g., mechanical polishing, laser activation, etc.). In general, all three diamond films are responsive for these redox systems. All the voltammetric data discussed herein support

the notion that the basic electrochemical properties of films deposited on the different substrates are similar. As long as there is complete film coverage, the substrate exerts, the substrate seems to exhibit negligible influence on the response.

Table 3.1 Summary of Cyclic Voltammetric Data and Apparent Heterogeneous Electron Transfer Rate Constants for Boron-Doped Microcrystalline Diamond Films

Analyte	Electrode	ΔE_p (mV)	i_p^{ox} (μA)	k^0_{app} (cm/s)
1.0 mM $Fe(CN)_6^{-3/-4}$	Si-diamond	72±3	57±2	0.018±0.008
	W-diamond	71±4	59±1	0.020±0.005
	Mo-diamond	71±3	59±1	0.027±0.003
1.0 mM $Ru(NH_3)_6^{+2/+3}$	Si-diamond	76±8	59±2	0.025±0.008
	W-diamond	74±5	57±1	0.037±0.019
	Mo-diamond	76±4	56±3	0.032±0.004
0.5 mM $IrCl_6^{-2/-3}$	Si-diamond	67±1	23±1	0.21±0.08
	W-diamond	68±8	24±2	0.12±0.07
	Mo-diamond	62±4	25±1	0.16±0.08
0.1 mM $MV^{+2/+1}$	Si-diamond	67±2	5.3±0.5	0.22±0.09
	W-diamond	66±8	4.8±0.2	0.12±0.01
	Mo-diamond	63±6	5.0±0.1	0.14±0.10

Note: Cyclic voltammetric ΔE_p and i_p^{ox} values are averages for a 0.1 V/s scan rate. k^0_{app} values are based on measurements performed on three Si-diamond, two Mo-diamond, and two W-diamond films over a narrow scan rate range from 0.1 V/s to 0.5 V/s. All solutions were prepared with 1 M KCl. Measurements were performed with 70 % iR compensation.

3.2.2. Material Characterization

Figure 3.7A-C, shows 6 x 6 μm^2 AFM images (force mode) of diamond films deposited on Si, Mo, and W, respectively. The images reveal that all the films are well faceted and polycrystalline with many randomly-oriented, octahedral and cubo-octahedral-shaped crystallites. The films are continuous over the substrate with no

obvious pin-holes or cracks. There is a sizeable number of secondary growths, mostly in the films deposited on Mo and W, as indicated by the arrows.

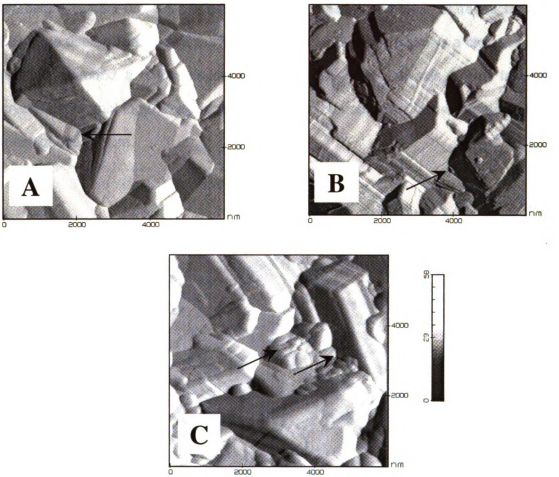

Figure 3.7 Atomic force microscope images (6 x 6 μm) of boron-doped, micro-crystalline diamond films deposited on (A)silicon, (B)molybdenum, and (C) tungsten.

These are the smaller grains that form in the grain boundaries and at defects on the facets of the primary crystallites. The increased fraction of secondary growths on the Mo and W films presumably results from a slightly higher inherent defect density. The higher number of secondary growths causes an increase in the fraction of exposed grain

boundary, and it is supposed this is the reason for the increased background voltammetric current. A nominal crystallite diameter of 3 μm is estimated from the image features for all three substrates. The roughness, as estimated from the change in the feature height, is 1.5 ± 0.2, 1.5 ± 0.3, 2.5 ± 0.3 μm for Si, W, and Mo films, respectively.

SEM was used also to probe the film morphology. Figure 3.8 shows a cross-section image of a diamond thin film deposited on Si. The image reveals a well faceted, polycrystalline morphology. The diamond film is continuous over the substrate, with a thickness of about 7 μm.

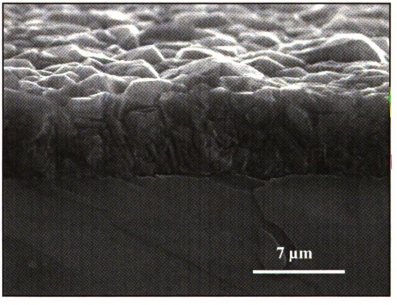

Figure 3.8 SEM image of a boron-doped microcrystalline diamond film deposited on Si.

Glancing angle XRD measurements (courtesy of Jennifer Spear, Philips Analytical) were made to examine the crystalline phases present near the surface and within the film bulk. Three angles of x-ray beam incidence (with respect to the surface)

were used: 0.5, 2.0, and 5.0 degrees. XRD analysis of the diamond film deposited on Si showed the major peaks expected for cubic diamond at 43.9, 75.3, and 91.5 degrees. These are assigned to the (111), (220), and (311) crystallographic orientations, respectively.[205] Figure 3.9 shows diffraction patterns for the film deposited on Si, at an incidence angle of 0.5 degrees. The intensity of all the peaks increased with increasing incidence angle (data not shown).

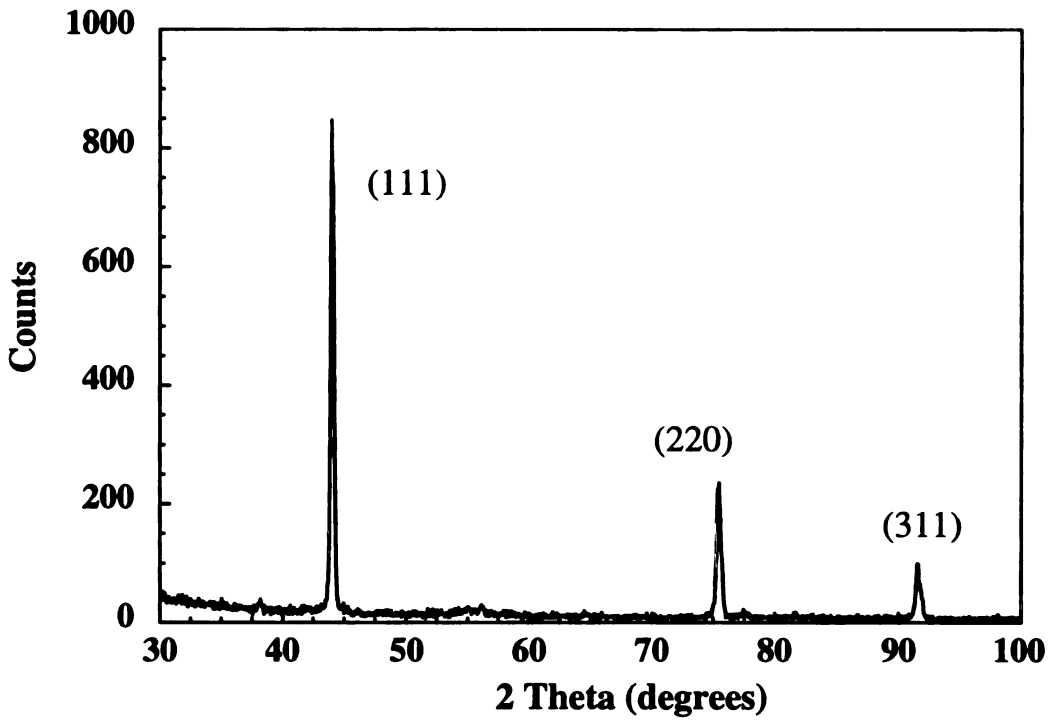

Figure 3.9 Grazing incidence XRD measurement of a boron-doped microcrystalline diamond film deposited on Si at a 0.5 degrees incidence angle.

The XRD analysis of the diamond films deposited on W and Mo showed that, in addition to the expected peaks for cubic diamond, both W and tungsten carbide (WC) phases are present (data not shown). The W reflections were at 40.3, 58.3, 73.2, 87.0, 100.6, and

114.9 degrees and are assigned to the (110), (220), (211), (220), (310), and (222) crystallographic orientations, respectively.[205] WC reflections were at 35.6, 48.3, 73.1, and 77.1 degrees. Since no electrochemical evidence was found for elevated levels of W metal impurities at the surface, the presence of these phases means that the x-rays were probing the interfacial region of the film, even at this shallow incidence angle.

In addition to cubic diamond, only a molybdenum carbide (Mo_2C) phase was detected on the Mo substrate. The Mo_2C reflections were at 34.5, 37.9, 52.2, 61.6, 69.6, 74.7, and 75.7 degrees and are assigned to the (100), (002), (102), (110), (103), (112), and (201) crystallographic orientations, respectively.[206] Again, since no electrochemical evidence was found for Mo metal impurities at the surface, the presence of these phases means that the x-rays are probing the interfacial region of the film, even at this shallow angle. For both metal substrates, the diamond peaks are shifted to slightly higher angles from where they are on Si. This is consistent with a contraction of the diamond lattice (i.e., compressive stress), which is likely caused by the higher thermal expansion coefficient of the two metal substrates, as compared to diamond, by a factor of 4 to 5. The FWHM of the (111) diamond line on Si was 0.33 degrees for the 0.5 degree incidence angle. The FWHM observed for diamond line on Mo and W was 0.40 and 0.49, respectively. The FWHM is indicative of the defect density in the films with a higher defect density corresponding to a larger peak width. The larger FWHM on the metal substrate is consistent with the higher fraction of exposed grain boundary due to the secondary growths, as evidenced in the AFM images.

Figure 3.10 presents Raman spectra for films deposited on Si, Mo, and W. The spectra consist of one intense band near 1332 cm^{-1} attributed to the first-order phonon scattering mode for diamond.[207] This peak is attenuated and shifted toward higher

wavenumbers for the Mo and W films. Peak positions of 1336.8 ± 0.6 cm^{-1} and 1334.04 ± 0.3 cm^{-1} are observed for the Mo and W substrates, respectively.

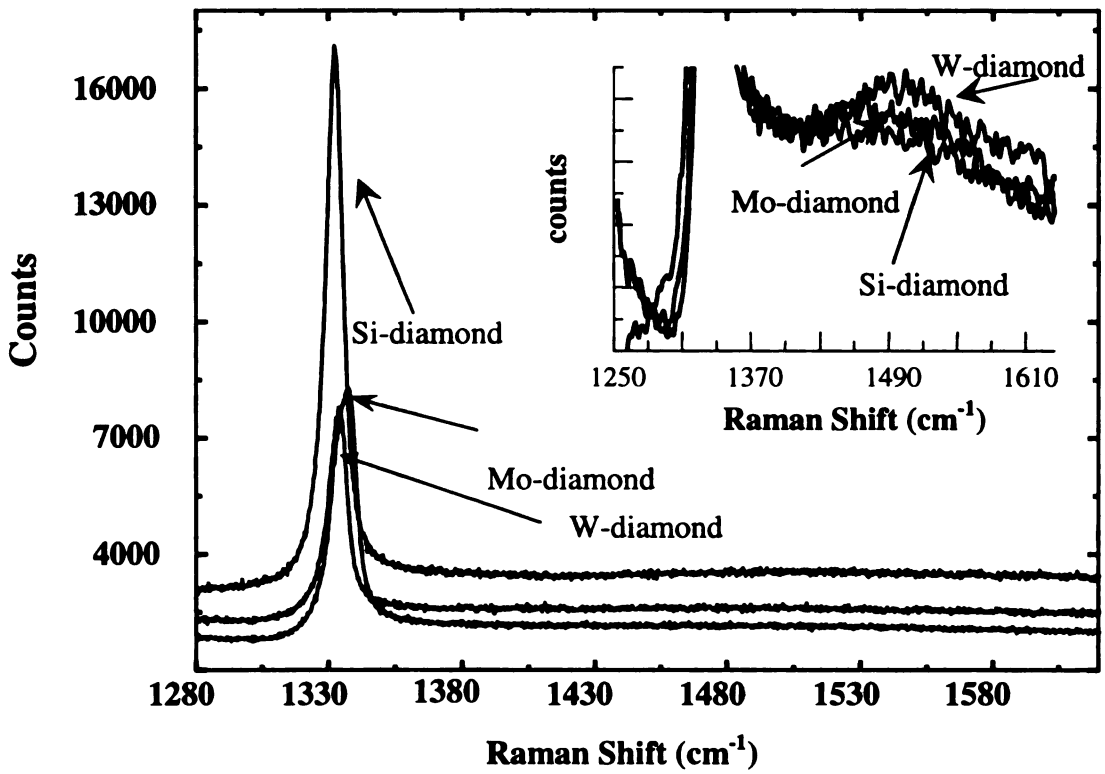

Figure 3.10 Macro-Raman spectra for boron-doped microcrystalline diamond films deposited on W, Mo, and Si. Enlargement of the spectra reveals the weak scattering intensity by non-diamond sp^2-bonded carbon impurity centered at ~1500 cm^{-1}.

The peak shift toward higher wavenumbers is indicative of a compressive stress within the film, due to the mismatch in thermal expansion coefficients. The results are in agreement with the XRD data. The line width (FWHM) of the diamond phonon on Mo is 10.4 ± 0.3 cm^{-1} and on W is 8.9 ± 0.5 cm^{-1}. These values are slightly higher than the line width on Si of 7.5±0.6 cm^{-1}. The line width for a peak of HPHT diamond was 2 cm^{-1}, for

comparison. The peak width provides information regarding the crystalline quality and, to a first approximation, is inversely related to the phonon lifetime (i.e., defect density).[207] In other words, the diamond films deposited on Mo and W possess a higher defect density than do the films on Si. This is in agreement with the AFM, SEM, XRD, and electrochemical data.

The increased number of secondary growths in the films grown on Mo and W contribute to a higher defect density. Non-diamond sp^2 carbon impurity is likely located at these defects. The expanded spectral region in the insert shows that the films deposited on Mo and W have slightly higher levels of sp^2-bonded carbon (1490 cm^{-1}). These impurities likely contain a mixture of sp^2 and sp^3 bonding, however, their concentration is low, considering that the peak intensity is weak and that the scattering cross-section for graphite (a model for sp^2-bonded carbon) is ca. 50 times larger than that of diamond.[207]

Raman spectroscopy can provide information regarding the residual stress in the diamond film.[208] At room temperature, the total film stress is the sum of two contributions: intrinsic and thermal stress.[201,208] The origins of the intrinsic stress are not well understood; however, the structural mismatch between the substrate and the film, or defects within the film, can be responsible. The thermal stress is caused by the difference in thermal expansion coefficients of the film and substrate, and can be evaluated from the expression:[200,201]

$$\delta_{therm.} = \left(\frac{E_d}{1-\nu_d}\right)\left(\alpha_d - \alpha_s\right)\delta T$$

in which E_d is the Young modulus of diamond (E_d=1210 GPa), ν_d is the Poisson ratio (ν_d = 0.1), α_d and α_s are the thermal expansion coefficients for diamond and the substrate, respectively, δT is the difference between the growth temperature and room

temperature.[200,201] At 25^{0}C, the thermal expansion coefficients for Si, W, Mo, and diamond are 3 x10^{-6}, 4.5 x10^{-6}, 5 x10^{-6}, and 1.1 x10^{-6} K^{-1}, respectively.[209] The thermal stress was calculated to be -1.7, -4.1, -3.3 GPa for Si, Mo, and W, respectively.

Secondary ion mass spectrometry (SIMS) was used to probe the chemical composition of the films, particularly in the near-surface region. A goal of this work was to determine if the surface contained higher levels of Mo and W, compared to the film bulk. Figure 3.11 presents depth profiles for the (A) Si, (B) Mo, and (C) W films. The ion profiles (raw intensities uncorrected for sputter yield) for C (m/z 11.99), C_2 (m/z 23.99), B (m/z 11.00) are shown for all films, as are the Si (m/z 27.97), Mo (m/z 97.90), and W (m/z 183.85) signals, depending on the substrate. The films were not acid washed and rehydrogenated, and were not used in any electrochemical measurements, prior to the SIMS analysis. In other words these were "as deposited". The profile for the diamond film deposited on Si shows intense signals for Si and C in the near-surface region. The intensities of these signals decrease significantly with depth. In fact, the C signal for films on all three substrates is very intense in the near-surface region and decays with depth into the film. This trend was very unexpected and uncharacteristic of other diamond films examined by SIMS. It is supposed that the intense C and Si signals are due to unintentional contamination layer on the surface.

Three possible sources of contamination are (i) pump oil condensation in the instrument, (ii) handling of the samples after deposition and during insertion into the vacuum chamber. Relatively high Si (m/z 27.97) signals were detected at the surface of all the films (profiles not shown in Fig 3.11 B and C). This supports the contamination layer cause. This contamination layer was apparently not present on those samples used in the electrochemical measurements, because its presence would have been

indirectly detected in either the background voltammograms, the capacitance profiles, or the voltammetric response for surface-sensitive redox analyte, like $Fe(CN)_6^{-3/-4}$.

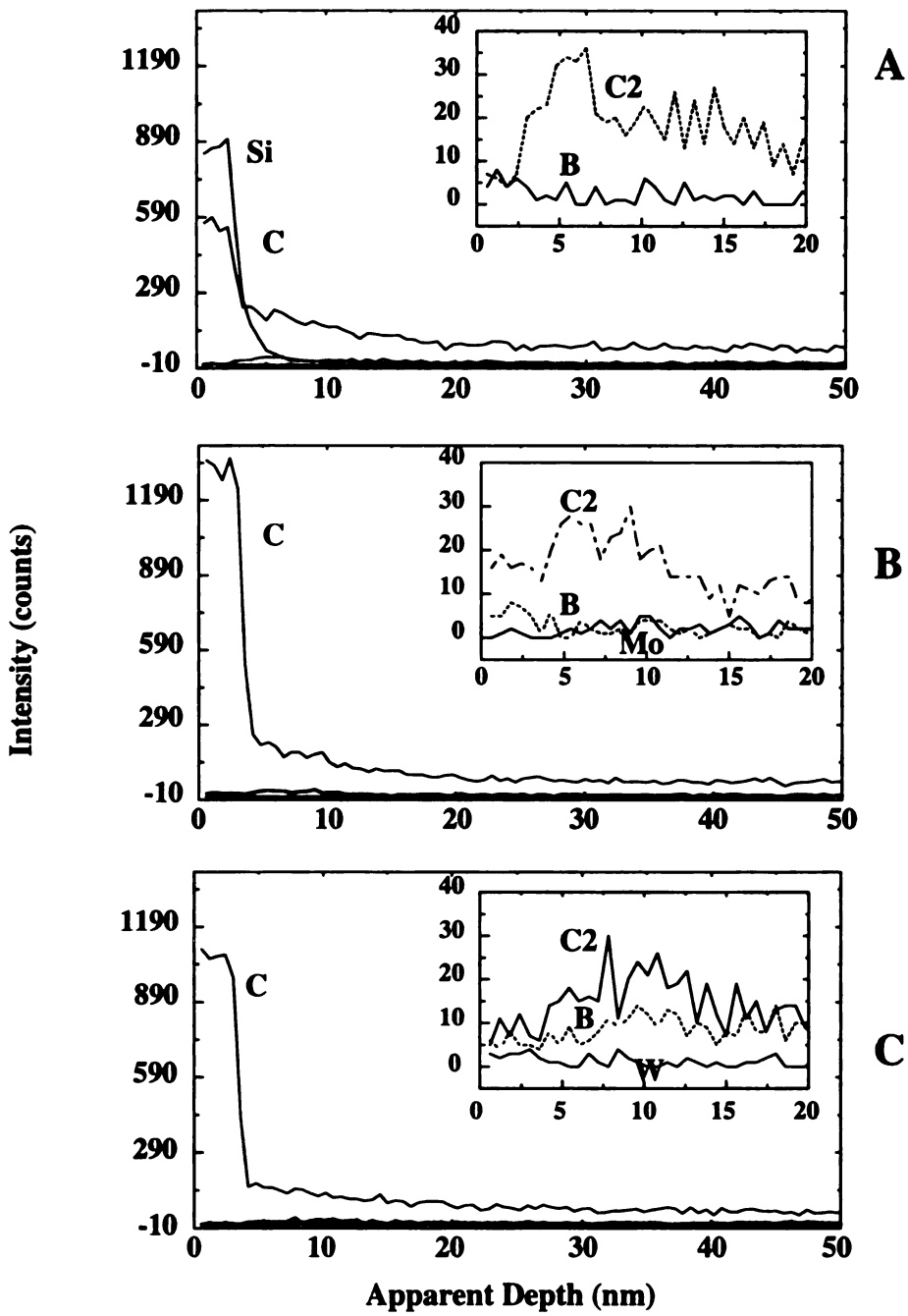

Figure 3.11 SIMS data for boron-doped microcrystalline diamond films deposited on (A) Si, (B) Mo, and (C) W.

For the diamond film deposited on Si, the Si, C, and B signals are relatively constant with depth after this suspected contamination layer is sputtered through. For the diamond films deposited on Mo and W, the B, Mo, and W ion intensities are constant with depth and are very near the background levels. Importantly, these SIMS results, even though apparently plagued by a contamination layer, do not reveal the presence of any elevated levels of metal impurities at the surface or in the bulk. Positive ion static SIMS measurements for all the diamond films prior to the depth profiling revealed the presence of a number of hydrocarbons: C_2H_3, C_3H_3, C_3H_4, C_4H_4, C_3H_4O, C_4H_8, C_2H_6O, C_5H_3, C_5H_4, C_5H_9, C_4H_5O. The O content on the surface was very low, based on ion intensities of the CHO fragments.

3.3. Conclusions

Good quality, boron-doped diamond thin films were deposited on three different substrates, Si, Mo, and W. The resulting films were characterized by electrochemical methods of analysis, atomic force microscopy, x-ray diffraction analysis, Raman spectroscopy, and dynamic secondary ion mass spectrometry. The goal for presented research was to learn how the substrate directly (e.g., chemical impurities) or indirectly (e.g., stress) affects the morphology, microstructure, chemical, and electrochemical properties.

A possible chemical contaminant during growth on metal substrates is metal impurity. Impurity at the surface could directly influence the electrochemical response by direct reaction with the analyte or electrolyte, or indirectly by creating more film defects (i.e., dislocations). It was observed that the electrochemical response of all films was independent of the substrate material. All films exhibited properties of high quality diamond – a wide working potential window; a low voltammetric background current and

capacitance; and good responsiveness for $Fe(CN)_6^{-3/-4}$, $Ru(NH_3)_6^{+2/+3}$, $IrCl_6^{-2/-3}$, and methyl viologen without any pretreatment. k^0_{app} values ranged from 10^{-2} to 10^{-1} cm/s for all four redox systems.

The films deposited on Mo and W did have some physical properties that were slightly different from those deposited on Si. For example, the Mo and W films have a higher defect density and more thermal stress (compression) than do films on Si. There is, however, no evidence of elevated levels of metal inclusions at the diamond surface or in the film bulk. The higher defect density is caused by a larger fraction of grain boundary resulting from secondary growths. Higher levels of sp^2-bonded carbon impurity appear to track the defect density, based on Raman spectroscopic measurements. The higher number of defects and the elevated fraction of non-diamond carbon seemingly lead to only a slight increase in the voltammetric background current.

In summary, the substrate appears to have little influence, directly or indirectly, on the electrochemical response of microcrystalline diamond films, at least for these four redox systems. It is possible that the higher internal film stress on the Mo and W substrates could affect their dimensional stability during the imposition of harsh electrochemical conditions. This remains for further investigation.

Chapter 4

THE CHARACTERIZATION AND ELECTROCHEMICAL RESPONSIVENESS OF BORON-DOPED NANOCRYSTALLINE DIAMOND THIN-FILM ELECTRODES

4.1. Introduction

High quality diamond films can be formed with two different morphologies and microstructures: microcrystalline and nanocrystalline. The distinction between these two structures arises from the nominal grain size, which for microcrystalline films is >1 μm and for nanocrystalline films is on the order of 15 nm. Conventional microcrystalline diamond CVD growth uses hydrocarbon-hydrogen (e.g., 1% CH_4/99% H_2) source gas mixtures, and it is known that under such growth conditions, hydrogen plays a number of critical roles.[111,146,147,210-214] Among these are stabilization of the diamond lattice and removal of sp^2-bonded carbon impurity, when formed, due to preferential gasification over sp^3-bonded diamond. Gruen and coworkers discovered that phase-pure nanocrystalline diamond can be deposited from CH_4/Ar gas mixtures containing very little or no added hydrogen.[146-148,151,182,213,214] There are two kinds of nanocrystalline

diamond films often reported on. The first are films deposited from high CH_4/H_2 (>5 %) gas mixtures. These films have nanometer-sized features, due to the high rate of nucleation, but are generally of low quality (so-called "dirty" diamond) with significant levels of secondary nucleation and sp^2-bonded carbon impurity phases. The second are films deposited from CH_4/Ar (~1 %) gas mixtures. These films consist of randomly oriented, nanometer-sized grains of phase-pure diamond and are generally of higher quality. The grains are on the order of 15 nm in diameter and the grain boundaries consist of π-bonded carbon atoms (2-4 atoms wide). The π-bonded grain boundaries have a profound effect on the mechanical, electrical, and optical properties of the films.[148,182]

The nanocrystalline diamond films reported on herein are of the second type. The most remarkable difference in films grown using hydrogen-poor Ar gas mixtures, compared with conventional hydrogen-rich mixtures, is the nanocrystallinity of the former compared with the microcrystallinity of the latter. The nanocrystallinity is a result of a new growth and nucleation mechanism that involves the insertion of C_2, carbon dimmer, into carbon-carbon and carbon-hydrogen bonds. The C_2 addition is believed to occur by a two-step growth mechanism.[213] In computational models, a C_2 molecule approaches the unreconstructed monohydride diamond surface and inserts into a C-H bond. The C_2 molecule then rotates to insert its other C into a neighboring C-H bond on the surface. A C_2 molecule then inserts into an adjacent C-H bond, parallel to the newly inserted C_2 dimer. The original state of the surface is recovered by a formation of a bond between carbon atoms in the adjacent surface dimers. Very high rates of heterogeneous nucleation are observed, on the order of 10^{10} cm^{-2}, and the resulting films consist of randomly oriented, phase-pure diamond grains with well-defined grain boundaries.[182] The smooth nanocrystalline films possess interesting mechanical, tribological, and

electrical properties, owing to the small grain size. For example, the films transition from an electrically insulating to an electrically conducting material with a reduction in crystallite size from the micrometer to the nanometer level.[151] This is largely due to the fact that the grain boundaries contain π-bonded carbon atoms (i.e., a high density of electronic states over a wide energy or potential range). The grain boundaries are conducting and, because their numbers vastly increase with decreasing crystallite size, the entire film becomes electrically conducting and functions as a good electrode material.[153] Theoretical calculations suggest that localized electronic states are introduced into the band gap due to the presence of sp^2-bonded dimers and sp^3-hybridzed dangling bonds in the grain boundaries.[182] There is a lack of spatial connectivity among the sp^2-bonded sites; therefore, the associated gap states do not form an extended π-system but remain localized.

Our group reported on the structural and electrochemical characterization of nitrogen-incorporated nanocrystalline diamond thin film electrodes, deposited from $CH_4/N_2/Ar$ gas mixtures.[153] The electrical conductivity of these nitrogen-containing films increases with increasing nitrogen content in the source gas mixture, up to about 5 %, and are generally more conductive than the early forms nanocrystalline diamond.[150,153] Recent Hall measurements (mobility and carrier concentration) for films deposited with 10 and 20% added N_2 revealed carrier concentrations of 2.0×10^{19} and 1.5×10^{20} cm^{-3}, respectively.[151] The room temperature carrier mobilities were 5 and 10 $cm^2/V\text{-}s$, respectively. A negative Hall coefficient indicated the electrons are the major charge carrier in these films. An explanation for the effect of nitrogen is that the impurity disrupts the microstructure by increasing the extent of sp^2-bonding. The increase in π-bonding causes an increase in the density of electronic states. Computational work indicated that

the incorporation of nitrogen into the grain boundaries is energetically favored by 3-5 eV, as compared to substitutional insertion into the grains.[182]

The electrical properties of the nitrogen-containing nanocrystalline diamond films are largely influenced by the π-bonded carbon atoms in the grain boundaries.[150,151,153,182,215] While these electrode materials possess good electrochemical properties, much like those for high quality microcrystalline diamond films, their electrical response is strongly linked to the physicochemical properties of the grain boundaries. Therefore, the electrochemical response can be strongly affected by changes in the π-bonded grain boundary carbon atoms. This is particularly true during exposure to chemically aggressive solutions conditions that can cause the oxidative etching of the grain boundary carbon atoms. *It would be better if the nanocrystalline diamond films exhibited a through-grain conduction mechanism as a result of impurity incorporation, such as boron doping. Such films should exhibit conductivity that scales with the doping level and possess electrochemical properties that are largely unaffected by changes in the physicochemical properties of grain boundaries.*

The objectives of this work were: (i) to determine the morphological, microstructural, chemical, and electrochemical properties of microwave-assisted CVD nanocrystalline diamond thin-film electrodes, deposited with and without boron dopant, (ii) to determine if the properties of the nanocrystalline film are similar to that of microcrystalline diamond.

4.2. Results and Discussion

4.2.1. Electrochemical Responsiveness

Figure 4.1 shows a background cyclic voltammetric i-E curve for a boron-doped nanocrystalline diamond thin film in 1.0 M KCl. The film was deposited from a $CH_4/H_2/Ar$ (1%/5%/94%) source gas mixture with 10 ppm of added B_2H_6. The deposition time was

2 h. The voltammetric background curve is largely featureless, over the potential range, and stable with cycling. There are no peaks present, associated with redox-active surface carbon-oxygen functionalities,[63,163] although there is a small anodic charge passed between 500-800 mV, just prior to the onset of chlorine evolution.

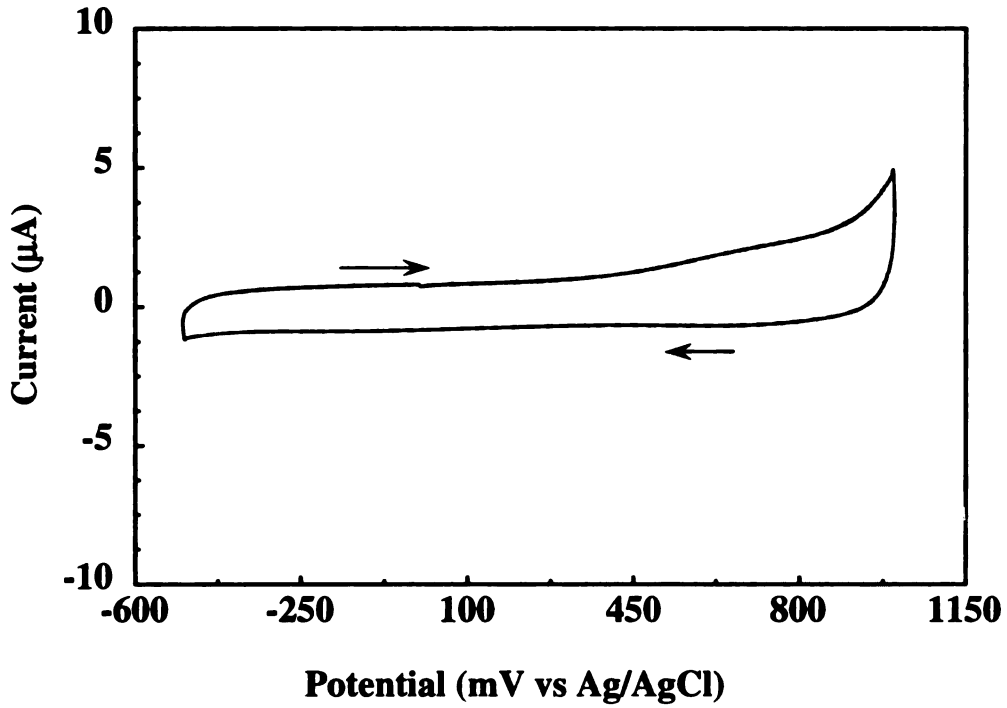

Figure 4.1 Background cyclic voltammetric i-E curve in 1.0 M KCl for a boron-doped nanocrystalline diamond film deposited on Si. Scan rate = 0.1 V/s. Electrode geometric area = 0.2 cm^2. Deposition time = 2h. Source gas mixture = CH_4/H_2/Ar (1%/5%/94%) (v/v) with 10 ppm B_2H_6 added. Power = 800 W. Pressure = 140 torr. Substrate temperature = ~800 ^oC.

The curve shape is similar to that for boron-doped microcrystalline diamond; however, the current magnitude of the former is slightly higher. For instance, at 250 mV, the anodic current for the nanocrystalline film is 0.96 μA (4.8 μA/cm^2), while the current for the microcrystalline films is about a factor of 1.5 less, 0.6 μA (3.0 μA/cm^2). The larger current is likely due to the higher fraction of exposed sp^2-bonded grain boundary. The

sp^2-bonded carbon in the grain boundaries is a source of charge carriers, along with the substitutional boron dopant atoms; hence, the overall carrier concentration is higher. A higher carrier concentration means greater excess surface charge at a given potential and a larger double layer charging current. The current for both diamond electrodes, however, is significantly less than that for freshly polished glassy carbon, 7-10 μA (35-50 $\mu A/cm^2$). The low background current is a characteristic feature of diamond electrodes and leads to improved SBR in electroanalytical measurements.[63,163]

Figure 4.2 shows a background cyclic voltammetric i-E curve for the same boron-doped nanocrystalline diamond in 1.0 M KCl over a much wider potential range. The working potential window is about 3.1 V (± 100 μA or 500 $\mu A/cm^2$) with a largely featureless response between the potential limits. The anodic current at 1200 mV is due to the oxidation of chloride to chlorine. The cathodic current flowing at -1800 mV is due to the reduction of water (hydrogen ion) to hydrogen. There is a current crossover at about -1700 mV, indicative of an activation overpotential necessary for the initiation of the hydrogen evolution reaction. A low background current and wide working potential window (3 to 3.5 V) are characteristic features of both high quality, boron-doped nanocrystalline, and microcrystalline diamond.[63,153,163]

The electrochemical responsiveness of the boron-doped nanocrystalline diamond thin film toward six redox systems was investigated using cyclic voltammetry. The influence of diamond's physical, chemical, and electronic properties on the electrode reaction kinetics and mechanism for each of these systems was tested. Figure 4.3 shows cyclic voltammetric i-E curves for (A) $Fe(CN)_6^{-3/-4}$, (B) $Ru(NH_3)_6^{+3/+2}$, (C) $IrCl_6^{-2/-3}$, (D) methyl viologen ($MV^{+2/+1/0}$) in 1 M KCl, and (E) 4-*tert*-butylcatechol, and (F) $Fe^{+2/+3}$ in 0.1 M $HClO_4$. The potential scan rate (ν) was 0.1 V/s. A summary of some of the cyclic voltammetric data is provided in Table 4.1.

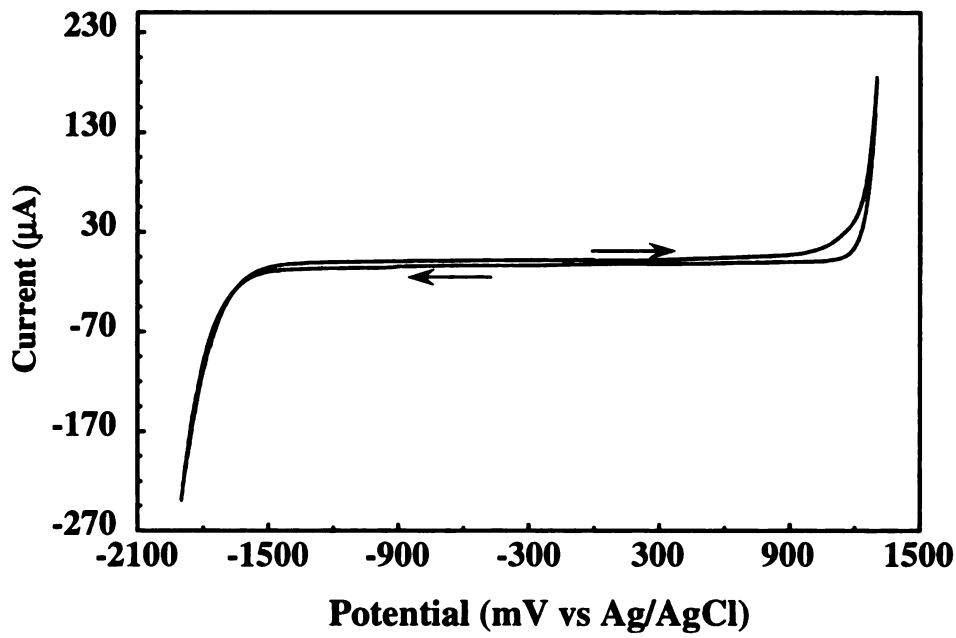

Figure 4.2 Background cyclic voltammetric i-E curve in 1.0 M KCl for a boron-doped nanocrystalline diamond film. Scan rate = 0.1 V/s. Electrode geometric area = 0.2 cm^2. The deposition conditions are the same as stated in Figure 4.1

Table 4.1 Cyclic Voltammetric Data for a Boron-Doped Nanocrystalline Diamond Film

Analyte	ΔE_p (mV)	$E_p^{ox.}$ (mV)	i_p^{ox} (μA)	i_p^{ox}/i_p^{red}
0.5 mM $MV^{+2/+1}$ in 1 M KCl	60	-633	34.5	1.1
1 mM $Ru(NH_3)_6^{+3/+2}$ in 1 M KCl	59	-135	62.7	0.99
1 mM $Fe(CN)_6^{-3/-4}$ in 1 M KCl	63	309	69.4	1.02
1 mM t-butylcatechol in 0.1 M $HClO_4$	419	655	112.2	1.8
0.5 mM $IrCl_6^{-2/-3}$ in 1 M KCl	61	823	22.7	0.98
1 mM $Fe^{+2/+3}$ in 0.1 M $HClO_4$	679	926	36.0	0.91

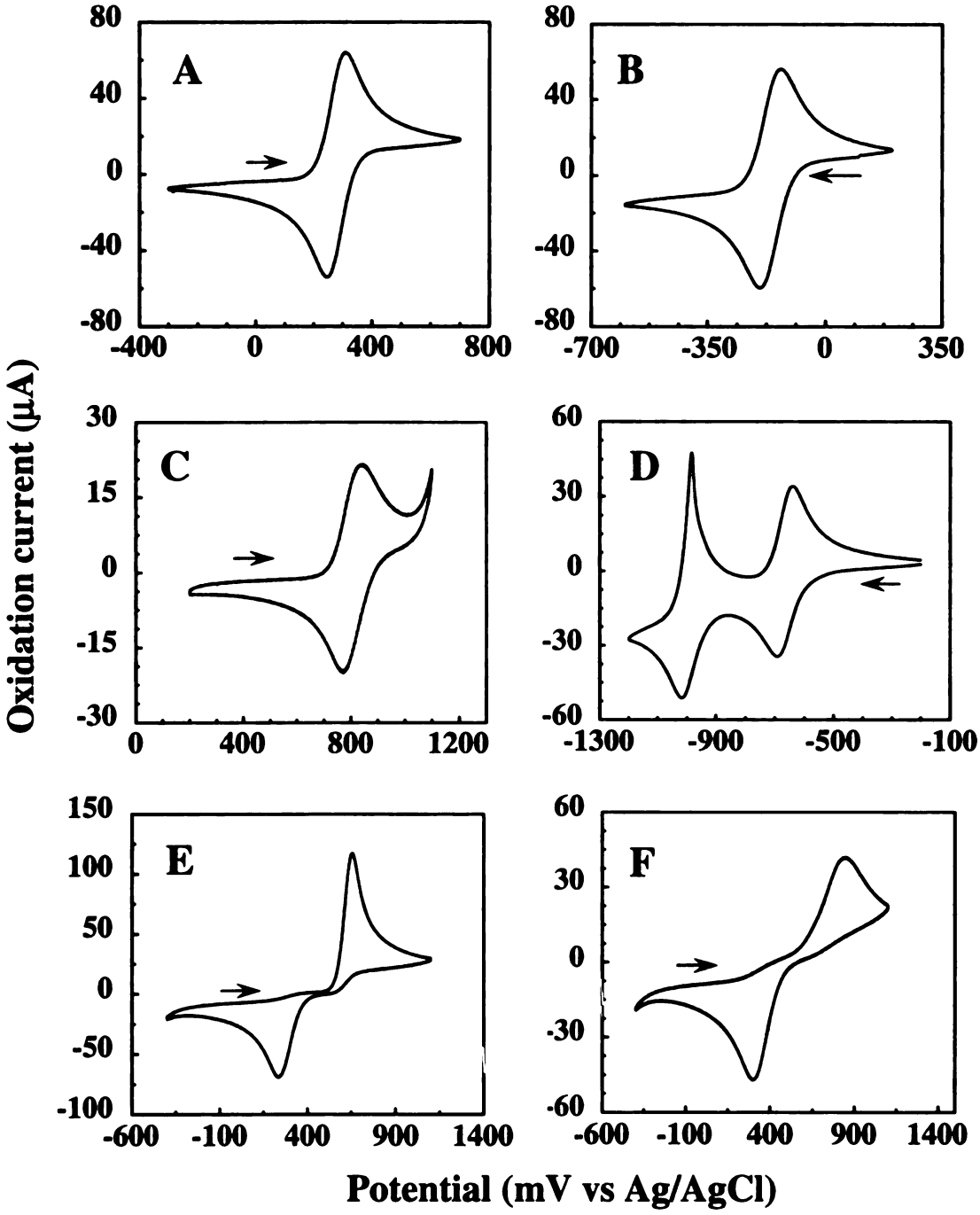

Figure 4.3 Cyclic voltammetric i-E curves for (A) $Fe(CN)_6^{-3/-4}$, (B) $Ru(NH_3)_6^{+3/+2}$, (C) $IrCl_6^{-2/-3}$, (D) methyl viologen ($MV^{+2/+1/0}$) in 1 M KCl, and (E) 4-*tert*-butylcatechol, and (F) $Fe^{+2/+3}$ in 0.1 M $HClO_4$ at a boron-doped nanocrystalline diamond thin film. Scan rate = 0.1 V/s. Electrode geometric area = 0.2 cm^2. The diamond deposition conditions are the same as stated in Figure 4.1

The $E^{o'}$ for these redox systems ranges from approximately +800 to -1100 mV, so they are very useful for probing the film's electronic properties over a wide potential range. A nearly reversible response is observed for $Fe(CN)_6^{-3/-4}$ with a ΔE_p of 63 mV and an i_p^{ox}/i_p^{red} of 1.0. $Fe(CN)_6^{-3/-4}$ is a surface-sensitive redox system at both glassy carbon and boron-doped microcrystalline diamond.[63,66,216] The electrode reaction kinetics for this couple are strongly influenced by the amount of exposed edge plane on sp^2–bonded carbon, as well as the surface cleanliness.[66] Granger et al. showed that surface carbon-oxygen functionalities on microcrystalline diamond significantly influence ΔE_p, with increasing oxygen content causing an increase in the peak potential separation.[187] Such an effect was also observed by Fujishima and coworkers.[217] The effect of the surface oxygen is reversed if the film is rehydrogenated in a hydrogen plasma.[187] The small ΔE_p seen for the boron-doped nanocrystalline diamond film is indicative of a high level of surface cleanliness and low surface oxide coverage. In other words, this result suggests the diamond surface is largely hydrogenated.[187]

A reversible response is seen for $Ru(NH_3)_6^{+2/+3}$ with a ΔE_p of 60 mV and an i_p^{ox}/i_p^{red} of 0.99. A nearly reversible response is also seen for $IrCl_6^{-2/-3}$ with a ΔE_p of 61 mV and an i_p^{ox}/i_p^{red} of 0.98. The electrode reaction kinetics for both of these redox systems are relatively insensitive to the physicochemical properties of both sp^2-bonded carbon and sp^3-bonded diamond electrodes.[63,66,216] The kinetics are mainly influenced by the density of electronic states at the formal potential for each couple. In other words, the nanocrystalline diamond electrode possesses a sufficient density of electronic states at both -200 mV, a potential that is negative of the apparent flatband potential (ca. 500 mV vs. Ag/AgCl) for hydrogen-terminated, semiconducting (*p-type*) diamond, and 800 mV, a potential that is positive of the flatband potential.[218-220]

A reversible response is seen for $MV^{+2/+}$ with a ΔE_p of 60 mV and an i_p^{ox}/i_p^{red} of 1.1. Like $Ru(NH_3)_6^{+2/+3}$ and $IrCl_6^{-2/-3}$, the electrode reaction kinetics for $MV^{+2/+}$ are relatively insensitive to the physicochemical properties of both sp^2-bonded carbon and diamond electrodes.[63,136,216] The kinetics are mainly influenced by the density of electronic states at the formal potentials. In fact, good responsiveness was also observed for the $MV^{+1/0}$ redox couple at an even more negative potential of -950 mV. The cathodic peak at -1025 mV is associated with the reduction of $MV^{+\bullet}$ to MV^0. The peak shape is consistent with a diffusion-limited reaction. However, the corresponding oxidation peak at -1010 mV for the MV^0 to $MV^{+\bullet}$ transition does not have the shape expected for a diffusion-limited process but, rather, is sharp and narrow, consistent with an oxidative desorption event. MV^0 has limited solubility in aqueous media and, depending on the solution conditions, methyl viologen concentration, and the electrode surface properties, MV^0 can adsorb and accumulate on the electrode surface.[68] This is the case at present. The sharp oxidation peak results from the oxidative desorption of surface confined MV^0.

The cyclic voltammetric i-E curves for 4-*tert*-butylcatechol (t-BC) and $Fe^{+2/+3}$ have much larger ΔE_p's and more asymmetric peak shapes than do the curves for the other redox systems. ΔE_p's of 419 and 679 mV are observed for t-BC and $Fe^{+2/+3}$, respectively. The i_p^{ox}/i_p^{red} ratios are 1.8 and 0.91 for t-BC and $Fe^{+2/+3}$. The larger peak separations, as compared to the other four redox analytes, are due to more sluggish electrode reaction kinetics.[63,216] The catechol redox reaction involves the transfer of both electrons and protons, and the electrode kinetics are highly sensitive to the surface microstructure, the presence of surface carbon-oxygen functionalities, and the surface cleanliness of sp^2-bonded carbon electrodes.[66] Surface adsorption catalyzes the reaction.[221] It is supposed that the slow kinetics for diamond result from a lack of

adsorption on the sp^3-bonded, hydrogen-terminated surface. Recent results have demonstrated a clear correlation between the fraction of exposed sp^2-bonded carbon in microcrystalline and nanocrystalline diamond films, and the surface coverage of adsorbed catechols.[222] The greater the coverage, the smaller the ΔE_p.

The electrode kinetics for $Fe^{+3/+2}$ are strongly influenced by the presence of surface carbon-oxygen functional groups, specifically carbonyl groups, which catalyze the reaction at sp^2-bonded electrodes.[223] The hydrogen-terminated diamond surface is void of such functionalities, so this is the postulated reason for the sluggish kinetics. Increasing the surface oxygen content on diamond has been observed to slightly decrease the ΔE_p.[217] Much work remains to understand why the kinetics of this analyte are so sluggish at diamond.

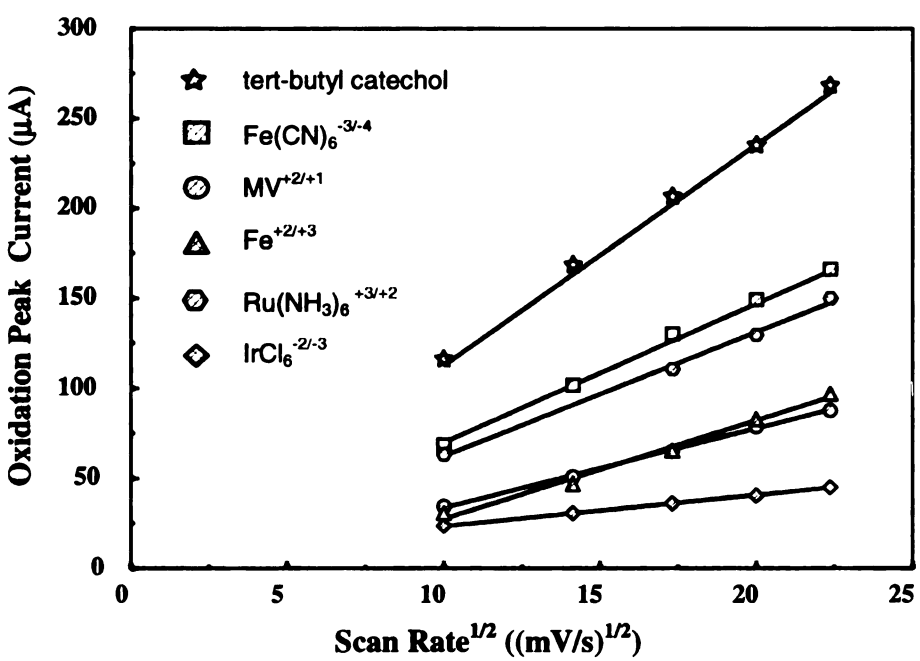

Figure 4.4 Plot of i_p^{ox} vs scan rate$^{1/2}$ for $Fe(CN)_6^{-3/-4}$, $Ru(NH_3)_6^{+3/+2}$, $IrCl_6^{-2/-3}$, methyl viologen ($MV^{+2/+}$), 4-*tert*-butylcatechol, and $Fe^{+2/+3}$ at a boron-doped nanocrystalline diamond film. The scan rate was varied from 100 to 500 mV/s. The diamond deposition conditions are the same as stated in Figure 4.1.

Figure 4.4 presents plots of i_p^{ox} versus $v^{1/2}$ for the different redox analytes. It can be seen that the oxidation peak current for each analyte varies linearly with the scan rate$^{1/2}$ with a near-zero y-axis intercept, indicative of reactions limited by semi-infinite linear diffusion of reactant to the electrode surface. The quasi-reversible to reversible voltammetry for all the couples indicates that the boron-doped nanocrystalline diamond has a sufficient density of electronic states over a wide potential range to support a rapid rates of electron transfer.

The electrical conductivity of previously reported nanocrystalline diamond thin film electrodes, both as deposited and as deposited with incorporated nitrogen, largely results from the π bonding in the intercrystalline grain boundaries.[153] If this π bonding is disrupted, then the localized density of electronic states is reduced, and the electrical conductivity decreases proportionally. *Hence the electrochemical responsiveness of these films depends, to a great extent, on the chemical and electronic properties of the grain boundaries.* The electrochemical responsiveness of the boron-doped nanocrystalline thin films should be much less influenced by the chemical and electronic properties of the grain boundaries. In other words, the diamond grains themselves should be highly conducting due to the carriers provided by the substitutionally-inserted boron dopant atoms. To test this, an acid washing and hydrogen plasma treatment was applied, which is very effective at oxidatively removing sp^2-bonded carbon.[63,187] The first step involved immersing the films in warm aqua regia for 30 min. The films were then rinsed with ultrapure water. The second step involved exposing the samples to a warm solution of H_2O_2 (30%) for 30 min. This was followed by rinsing with ultrapure water and drying. The films were then hydrogen plasma treated (microwave-assisted) for 6 h to remove the surface oxides formed during the acid washing and to terminate the surface with hydrogen.[63,187] The hydrogen was introduced into the reactor at a flow rate

of 200 sccm. The plasma power, system pressure, and temperature were 1 kW, 35 torr, and 800 ^{o}C, respectively.

The electrochemical response of two nanocrystalline films was evaluated before and after the acid washing/hydrogen plasma treatment. One was a nanocrystalline film deposited in the presence of the boron dopant source, and the other was a nanocrystalline film deposited without any intentionally added boron. Figure 4.5 shows a cyclic voltammetric i-E curves for $Ru(NH_3)_6^{+3/+2}$ in 1 M KCl at both films.

The response for the boron-doped nanocrystalline film is unaffected by the acid washing and hydrogen plasma treatment. A nearly reversible response is observed for $Fe(CN)_6^{-3/-4}$ with a ΔE_p of 78 mV before and 72 mV after treatment. A nearly reversible response was also observed for $Ru(NH_3)_6^{+3/+2}$, $IrCl_6^{-2/-3}$, and $MV^{+2/+1}$ with ΔE_p's of 74, 71, and 59 mV, respectively, after treatment. The response of the nanocrystalline film deposited without intentionally added boron was altered by the treatment. The ΔE_p for $Ru(NH_3)_6^{+3/+2}$ increases to 165 mV after treatment. The ΔE_p's for $Fe(CN)_6^{-3/-4}$, $IrCl_6^{-2/-3}$, and $MV^{+2/+1}$ all increased marginally after treatment to 166, 83, and 99 mV, respectively. The ΔE_p increases because of a decrease in the density of electronic states due to the oxidative etching and disruption of the π-bonded carbon in the grain boundary. The ΔE_p increases for this particular nanocrystalline film were not as dramatic as we have seen in tests of other films. The reason is that this film, even though deposited with no intentionally added boron, was doped with some boron because it was prepared in a reactor that is regularly used for depositing boron-doped films. In fact, recent boron nuclear reaction analysis measurements of an "undoped" film, deposited in the same reactor, revealed a doping level of ca. 50 ppm B/C. Previous tests have shown that the electrochemical response of a truly undoped nanocrystalline film can be almost completely inhibited after the same chemical/plasma treatment. These results suggest

that the electronic properties of the boron-doped films are dominated by the carriers (holes) concentration in the diamond lattice, rather than by the physicochemical properties of the grain boundaries.

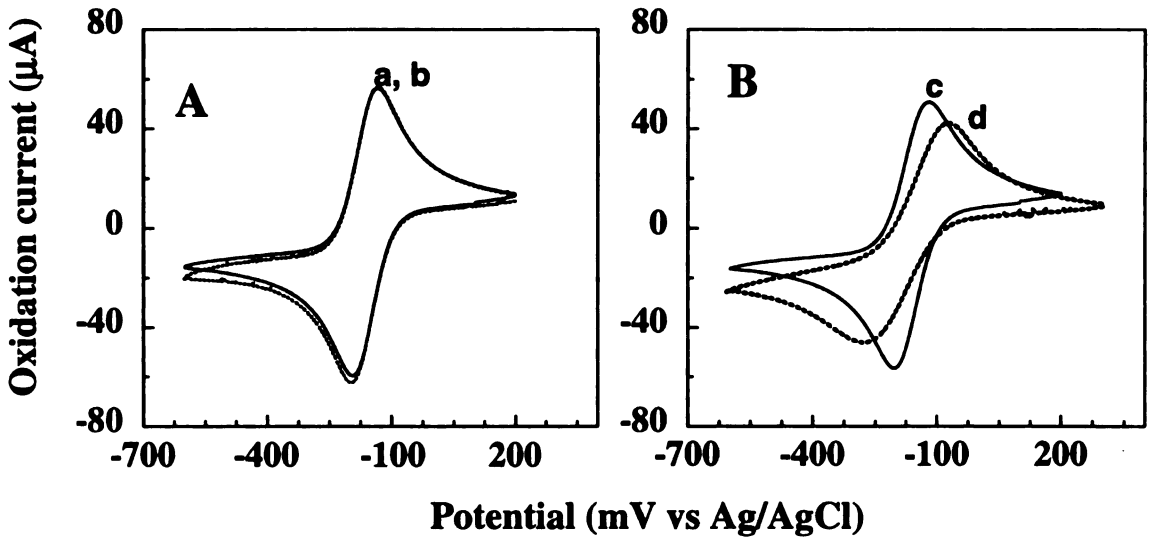

Figure 4.5 Cyclic voltammetric i-E curves for 1 mM $Ru(NH_3)_6^{+3/+2}$ in 1 M KCl for an (a) untreated $CH_4/H_2/Ar$ (1%/5%/94%) with 10 ppm B_2H_6 nanocrystalline diamond film, (b) the same electrode after treatment, (c) untreated $CH_4/H_2/Ar$ (1%/5%/94%) with 0 ppm B_2H_6 nanocrystalline diamond film, and (d) the same electrode after treatment. Scan rate = 0.1 V/s. Electrode geometric area = 0.2 cm^2.

4.2.2. Material Characterization

Figure 4.6 A and B shows a cross-section and top-view SEM image of a boron-doped nanocrystalline diamond thin-film electrode deposited for 2 h. The film was deposited from a $CH_4/H_2/Ar$ (1%/5%/94%) source gas mixture with 10 ppm of added B_2H_6. The smooth and uniformly coated film is composed of nodular features ~100 nm in diameter. No voids were found in the coating, and the thickness appeared uniform over the entire substrate.

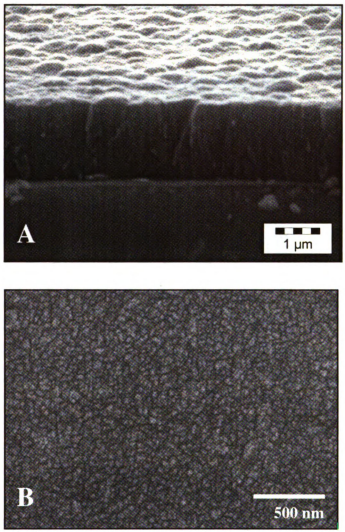

Figure 4.6 SEM images of a boron-doped nanocrystalline diamond film deposited on Si in (A) cross-section and (B) top-view image modes. The deposition conditions are the same as stated in Figure 4.1.

AFM images were also acquired to probe the film morphology. Figure 4.7 shows an AFM image for nanocrystalline diamond thin-film electrode. The root-mean-square surface roughness was found to be 34 nm over a 100 μm^2 area and was independent of the growth time (i.e., film thickness). The nodular features are actually clusters of

individual diamond grains formed as a result of the high nucleation rate, as evidenced by TEM images presented below.

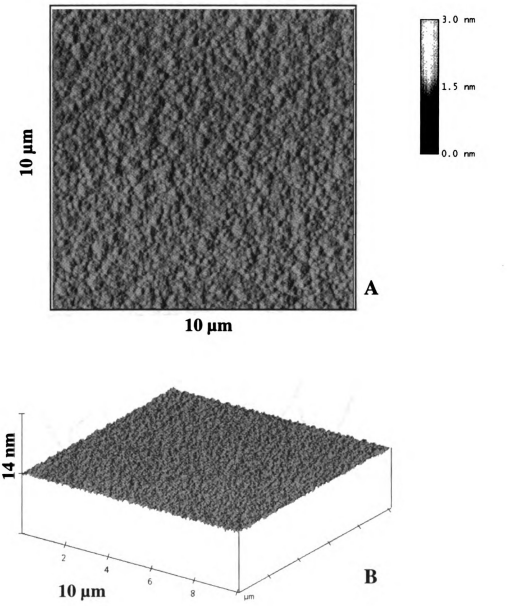

Figure 4.7 Atomic force microscope images (10x10µm) of a boron-doped, nanocrystalline diamond film deposited Si in the (A) deflection and (B) height image modes. The deposition conditions are the same as stated in Figure 4.1.

The individual grain size within the diamond clusters was revealed by TEM. Figure 4.8 shows a TEM image of the film. This image is representative of several that were collected. It can be seen that the film consists of diamond grains with diameters from 10 to 15 nm. These diamond grains make up the nodular features seen in Figure 4.6. Moreover, each diamond grain is a single crystal and randomly oriented in the film. This conclusion is based on the appearance of the lattice fringe patterns and their orientational differences from grain to grain.

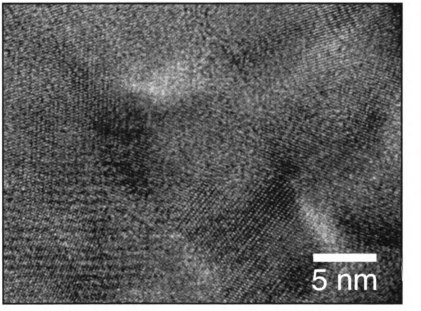

Figure 4.8 Transmission electron micrograph of a nanocrystalline boron-doped diamond film. The deposition conditions are the same as stated in Figure 4.1.

A rough estimate of the fringe spacing was made, even though this is not a high resolution image. The estimated spacing on at least a couple of the grains is ~ 0.20 nm. This is close to the 0.206 nm interplanar distance for diamond {111} planes. The transmission electron diffraction (TED) pattern from one of the grains, in Figure 4.9,

shows an intense ring pattern. This ring pattern also suggests atomically ordered, but randomly oriented grains. The diffraction pattern is indexed to the (111), (022), (113), (004), (133), (224), (115), and (333) planes of cubic diamond (ASTM 6-0675).

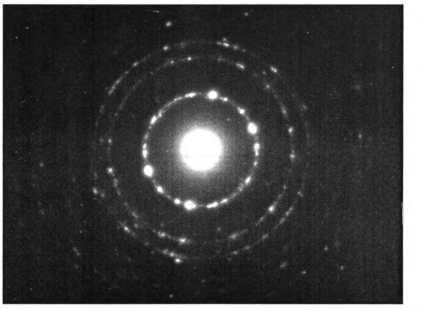

Figure 4.9 Transmission electron diffraction pattern for a grain in the boron-doped nanocrystalline diamond thin film. The deposition conditions are the same as stated in Figure 4.1

Figure 4.10 shows an XRD spectrum of the film. Three broad reflections are observed at 43.8, 75.5, and 91.5°. These reflections are assigned to the (111), (220), and (311) planes of the cubic diamond, respectively. The peaks are broader than they are for a microcrystalline film of the same approximate thickness, due to smaller diamond grain size in the nanocrystalline film. Table 4.2 summarizes the calculated lattice spacings and the relative peak intensities. Reference data for cubic diamond powder (ASTM 6-0675) are also presented, for comparison. The diffraction data reveal that the bulk structure of the film is sp^3-bonded diamond.

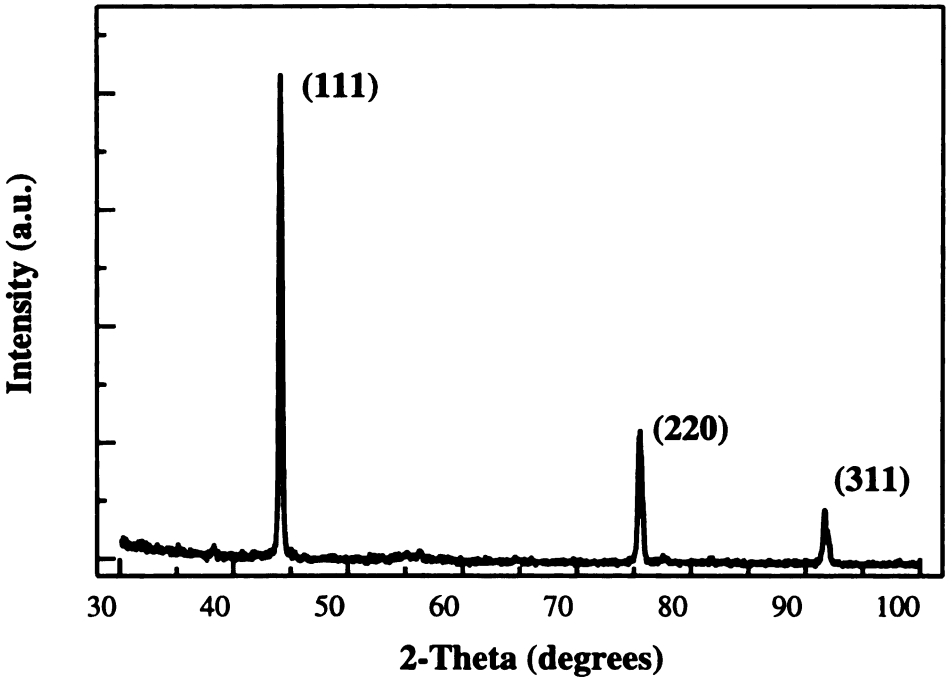

Figure 4.10 XRD pattern for a boron-doped nanocrystalline diamond film deposited on Si. The deposition conditions are the same as stated in Figure 4.1

Table 4.2 Lattice Spacings and Relative Peak Intensities Obtained from XRD Patterns of a Nanocrystalline Diamond Film and a Cubic Diamond Standard

Plane	Measured		ASTM (6-0675)	
	Spacing (Å)	Intensity	Spacing (Å)	Intensity
(111)	2.06	100	2.06	100
(220)	1.261	23	1.261	25
(311)	1.0747	13	1.0754	16

ASTM (6-0675) – American Society for Testing Material-reference data for cubic diamond powder.

Figure 4.11 shows a visible Raman spectrum of the film. This spectrum is characteristic of high-quality nanocrystalline diamond films. A single, sharp peak at 1332 cm^{-1} in the Raman spectrum is frequently used as a signature of high quality,

single crystal, or large-grained diamond.[215,224] The spectrum for the nanocrystalline films is quite different from this.

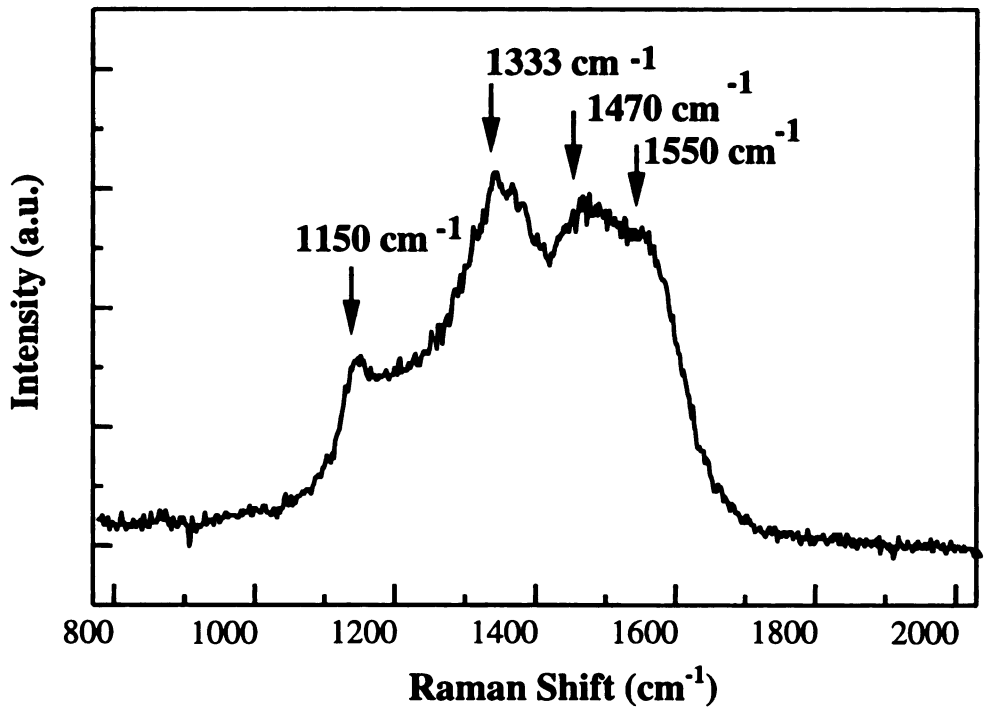

Figure 4.11 Visible Raman spectrum for a boron-doped nanocrystalline diamond film deposited on Si. The deposition conditions are the same as stated in Figure 4.1

Broad peaks are seen at 1150, 1333, 1470, and 1550 cm^{-1}. The peak at 1333 cm^{-1}, on top of a large background signal, is associated with the first-order phonon mode of sp^3-bonded diamond. Due to resonance effects, the Raman cross-section scattering coefficient (visible excitation) for sp^2-bonded carbon is larger (50x) than that for the sp^3-bonded carbon, and the scattering intensity for the former can often greatly exceed that for the latter.[225] The peak width (FWHM) is much broader than that for microcrystalline diamond, 140 cm^{-1} vs 10 cm^{-1}. This is due to the small grain size of the nanocrystalline film. Raman line broadening can result from several mechanisms. One possibility is the

well established confinement model.[226] This model states that the smaller the domain size, the larger the range of phonons modes (with different q vector and different energy) that are allowed to participate in the Raman process. Hence, the line width results from the spread in phonon energy. Another, and more likely, explanation for the line broadening is phonon scattering at impurities and defects (i.e., grain boundaries).[226] The scattering event shortens the lifetime of the phonons and thus broadens the Raman line. The peak at 1150 cm^{-1} is often used as a signature for high quality nanocrystalline diamond.[224] Prawer and coworkers, through the study of clean, nanocrystalline diamond particles (~5 nm diameter), have attributed this peak to a surface phonon mode of diamond.[227] On the other hand, Ferrari and Robertson have made arguments for this peak being associated with sp^2-bonded carbon, specifically transpolyactelylene segments at grain boundaries.[228] Their assignment of sp^2-bonded carbon, rather than sp^3-bonded carbon as has often been proposed,[228] is based on the observations that the peak position changes with excitation energy, the peak intensity decreases with increasing excitation energy, and the peak is always accompanied by another peak at ~1450 cm^{-1}, which behaves similarly with excitation energy. We, therefore, tentatively assign the peaks at 1470 and 1550 cm^{-1} to disordered sp^2-bonded carbon in the grain boundaries. The 1550 cm^{-1} peak is down-shifted from the expected 1580 cm^{-1} position for graphite. This shift results because the sp^2-bonded carbon is amorphous and is mixed with sp^3-bonded carbon. It is important to note that, very likely, the sp^2-bonded carbon is confined to the grain boundaries of the nanocrystalline film and yields a network of three- and four-fold coordinated carbon atoms.[144] Additional research is needed to confirm the origins of the 1150 and 1470 cm^{-1} bands.

The boron concentration in the film deposited with 10 ppm of added B_2H_6 was determined to be 810 ppm (1.43×10^{20} B/cm^3), by boron nuclear reaction analysis. One

preliminary Hall Effect measurement showed the major carrier to be the hole and the carrier concentration and the conductivity to be $6.4x10^{17}/cm^3$ and 10 $\Omega^{-1}cm^{-1}$, respectively. The carrier mobility was found to be 90.4 cm^2/V-s. More measurements are needed before these values can be established as being representation of the material.

4.3. Conclusions

A boron-doped nanocrystalline diamond thin film was deposited by CVD from a $CH_4/H_2/Ar$ source gas mixture. Boron doping was accomplished using B_2H_6 added to the source gas mixture. The films exhibited a wide working potential window, a low voltammetric background current and good responsiveness for $Fe(CN)_6^{-3/-4}$, $Ru(NH_3)_6^{+3/+2}$, $IrCl_6^{-2/-3}$, and methyl viologen without any pretreatment. The nearly reversible voltammetry for all four redox systems indicates that the boron-doped nanocrystalline diamond has a sufficient density of electronic states over a wide potential range. More sluggish kinetics were found for 4-*tert*-butylcatechol and $Fe^{+2/+3}$. The sluggish kinetics are attributed to weak surface adsorption for the former, and to the absence of catalyzing surface carbonyl groups for the latter.

XRD revealed that the bulk crystal structure of the film was cubic diamond. TEM indicated the film consists of 10-15 nm randomly oriented but atomically ordered diamond grains. SEM showed these grains form aggregates ~100 nm in size.

Unlike previously reported nanocrystalline diamond films that have electrical properties dominated by the high fraction of sp^2-bonded grain boundaries, the present film is doped with boron and the electrical properties are dominated by the charge carriers in the diamond (i.e., substitutionally insertedboron dopant atoms)..

Chapter 5

CYCLIC VOLTAMMETRIC STUDIES OF THE ELECTROOXIDATION OF ALIPHATIC POLYAMINE AT BORON-DOPED DIAMOND THIN FILMS

5.1. Introduction

Aliphatic alcohols and amines are usually observed to be electroinactive at most electrodes, at constant applied potential in aqueous media, and have been classified as such historically.[229] Despite favorable thermodynamics, the oxidation of aliphatic amines, for example, in aqueous media is kinetically limited because the reactions require transfer of oxygen from H_2O to the oxidation product(s), rather than only simple removal of an electron from the "lone pair" on the nitrogen atom. Conventional anode materials (e.g., Pt, Au, and C) lack the ability to support these O-transfer mechanisms[54,55,230] at constant applied potentials. A significant problem is fouling of the electrode by reaction intermediates and products. Attempts have been made to utilize metal oxides (i.e., copper oxide, nickel oxide, gold oxide, platinum oxides) or composites of metal oxides as anode materials.[35,231] For instance, anodized nickel

electrodes have been applied for amine oxidation. The anodic response has been proposed to involve a surface-mediated mechanism involving Ni(III) formed in the oxide film at positive potentials.[231] A disadvantage of using the anodized nickel, however, is the apparent need for the addition of $(NiOH^+)_4$ in the solution phase to minimize dissolution of the soluble metal oxide.[231] Amine oxidation in alkaline solution at glassy carbon has been reported by Masui et. al.[232] It was observed, however, that only secondary and tertiary amines could be oxidized stably. Recently, successful anodic oxidation of aliphatic polyamines was demonstrated at glassy carbon electrode modified with nickel particles.[34]

Silver electrodes have been used for the oxidation of primary and secondary amines as reported by Hampson et. al.[233-235] In alkaline media, the silver surface is oxidized to Ag_2O. Very soluble complexes between the amine and surface oxides form, causing electrode dissolution and as result, very slow kinetics for amine oxidation. However, at high positive potentials (≥0.6 V vs. NHE), where formation of AgO occurs, amines are rapidly oxidized in alkaline solution (pH12).

Amines can be detected at Au in alkaline media. However, the anodic response is quickly attenuated due to the adsorption of reaction intermediates and products. The electrodes can be restored to full activity by a series of positive and negative potential pulses, so called pulsed amperometric detection (PAD). The procedure accomplishes oxidation of amine, desorption of adsorbed carbonaceous species with regeneration of a clean and oxide-free surface.[31-33] The success of Au for amine oxidation is a result of electrocatalytic mechanisms believed to involve the anodic discharge of H_2O with generation of adsorbed hydroxyl radicals (OH•) as an intermediate product in the formation of surface oxide (AuO). The catalytically active gold surface is short-lived (ca. 1 s), and therefore, continuous detection is impossible. Only with the application of

multistep potential-time waveforms, which alternate the processes of electrocatalytic detection with subsequent cathodic reduction of surface oxide (i.e., regeneration of the gold surface), can the reproducible anodic oxidation can be accomplished.[31,32,56]

It was a premise of the research by Johnson and coworkers [41,54,55,236] that OH• is generated at the electrode surface through the anodic discharge of water. They proposed that OH• is adsorbed at specific surface sites, and transferred to the reactants via an electrocatalytic O-transfer reaction mechanism. O-transfer reactions can be catalyzed by increasing the surface concentration of adsorption sites, thereby, increasing the concentration of adsorbed OH•. The rate of O_2 evolution is also enhanced by increasing the coverage of OH• . It was proposed that there is an optimal low density of surface sites for which the desired O-transfer process can occur at near mass transport-limited rates without an unduly high background signal for O_2 evolution.[29,30,32,46,47,237]

The desire to achieve a significant improvement in electrooxidation of aliphatic amines has stimulated a search for new anode materials that retain their catalytic activity. Electrode characteristics suggested by researchers for these composite anodes include: (i) use of metal oxides with minimal solubility at the pH conditions of the application, (ii) existence of a low density of surface sites at which the anodic discharge of H_2O (evolution of O_2) occurs with lower potential than the surrounding matrix, and (iii) existence of surface sites that are effective for coordinating the analytes.[46,47,54] Adsorption/coordination of the analyte is believed to be important because of (i) a suspected need to "desolvate the electronic orbital", to which oxygen from adsorbed OH• is transferred, (i.e., oxygen transfer cannot occur by a tunneling mechanism), and (ii) a need for longer residence time of analyte at the electrode surface in order to observe O-transfer. [46,47]

Yeo et al., doped PbO_2 film electrodes with Bi(V) and observed significant activation for several O-transfer reactions.[49,238-241] Johnson et al. proposed silver as a dopant for PbO_2 films for amine oxidation, as it is known that Ag(I) forms complexes with amines in aqueous media.[54,55,57] The Ag-doped PbO_2 composite electrodes showed some activity for amine oxidation, however, at high analyte concentrations, some dissolution of the film occurred due to the high solubility of the amine-Ag(I) complex.[55] Similar drawbacks were observed for pure silver electrodes.[234,235] The partial success of electrodeposited Ag-PbO_2 electrodes led to examination of anodized Ag-PbO_2 alloy films.[55] These electrodes exhibited superior response stability for aliphatic amines in comparison to electrodeposited Ag-PbO_2 films. This was attributed to the presence of only AgO, not Ag_2O. Comparable voltammetric responses were observed for primary, secondary, and tertiary aliphatic amines. The catalytic activity of the anodized eutetic-phase Ag-PbO_2 alloy electrodes for oxidation of amines was observed in alkaline solutions of borate (pH 11) and phosphate buffers (pH 12). No response was observed in neutral phosphate buffer (pH 7), presumably because of protonation of the amine functional group which blocks adsorption at the silver sites in the Ag-Pb oxide surface.[55]

Johnson et. al. proposed the following reaction model for analyte oxidation at composite electrodes via anodic oxygen transfer reaction:[55]

$$S[\ ] + H_2O \rightarrow S[OH] + H^+ + e^- \text{ (OH radical generation at } Ag_2O)$$

$$S'[\ ] + R \leftrightarrow S'[R] \text{ (coordination of the amine at } Ag_2O \text{ surface sites)}$$

$$S[OH] + S'[R] \rightarrow S[\ ] + S'[\ ] + RO + H^+ + e^- \text{ (anodic oxygen transfer reaction)}$$

The authors indicated that silver, as a doping agent serves the following functions: (i) a low H_2O discharge overpotential compared to PbO_2, (ii) capability of adsorbing the

OH• generated during H_2O discharge, and (iii) capability of adsorbing the reactant species.[55]

The reports from the Johnson group provided the impetus for our efforts to fabricate and test diamond electrodes designed with the appropriate properties to support anodic oxygen-transfer reactions.[47,54,55,57,237,242] Applications of such electrocatalytic electrodes for electrosynthesis, as electroanalytical sensors, and in the anodic degradation of toxic chemical waste ("electrochemical incineration") are possible.[32,33,38,42,50,243-255]

Cyclic voltammetric studies of aliphatic polyamine oxidation at microcrystalline and nanocrystalline boron-doped diamond thin-film electrodes are reported herein. The goals of this research were to: (i) determine if the amines can be qualitatively and stably detected at boron-doped microcrystalline or nanocrystalline diamond thin-film electrodes, (ii) determine how the oxidation response varies with concentration, scan rate, and solution pH, (iii) determine the role of sp^2-bonded non-diamond carbon impurity on the oxidation response, and (iv) verify the role of surface boron sites on the oxidation response.

5.1.1. Model for Polyamine Oxidation at Polycrystalline Diamond

The proposed mechanism for polyamine oxidation at diamond is given below and is similar to the model for anodic oxygen-transfer reactions put forth by Johnson and coworkers.[46,54,55,57,230]

$$S_{ND}[\ ] + H_2O \rightarrow S_{ND}[OH] + H^+ + e^- \quad \text{(OH radical generation at a } sp^2 \text{ sites)}$$

$$S_B[\ ] + R \leftrightarrow S_B[R] \quad \text{(coordination of the amine at a boron surface site)}$$

$$S_{ND}[OH] + S_B[R] \rightarrow S_{ND}[\ ] + S_B[\ ] + RO + H^+ + e^- \quad \text{(oxygen-transfer reaction)}$$

The subscripts ND and B refer to non-diamond and boron, respectively. Boron-doped diamond thin film electrodes possess several properties important for anodic oxygen-transfer reactions. First, high-quality diamond films are stable and resistant to corrosion in strongly acidic and alkaline media.[61,109,256-258 and references therein] Therefore, at the anodic potentials used to detect the polyamines, the electrode structure is stable. Second, films may contain sp^2-bonded non-diamond carbon impurity distributed very locally over the surface. These impurities can exist at the grain boundaries or as extended defects within the diamond film. These surface impurities, which exhibit lower overpotential for oxygen evolution than does diamond, can also be intentionally introduced into the films by adjustment of the diamond deposition conditions.[63,163,259] This means that reactive OH• will be generated locally at these sites at low overpotential, and not to any appreciable extent on the diamond lattice. Third, boron dopant atoms located at the surface can serve as adsorption/coordination sites for the lone pair of electrons on the N atoms of the polyamines. Boron atoms can insert directly into the growing diamond lattice, but they can also cluster and accumulate in the grain boundaries. The distribution of boron atoms in the polycrystalline diamond film is not homogeneous as there is a growth sector dependence. For example, the boron dopant concentration in the (111) sector is a factor of 10 times higher than in (100) sector.[260-263 and references therein] The polyamine adsorption/coordination at the boron sites near the grain boundaries is important mechanistically, as these are sites very near where the OH • is being generated at lower overpotential.

5.2. Results and Discussion

5.2.1. Cyclic Voltammetry of Polyamines

Figure 5.1 shows typical cyclic voltammetric i-E curves for 1.0 mM (A) cadaverine (CAD) (B) putrescine (PUT), (C) spermidine (SPMD), and (D) 0.8 mM spermine (SPM),

in borax buffer pH 11(BBpH11) at a microcrystalline film deposited from a 0.5% CH_4/H_2 ratio and 10 ppm B_2H_6.

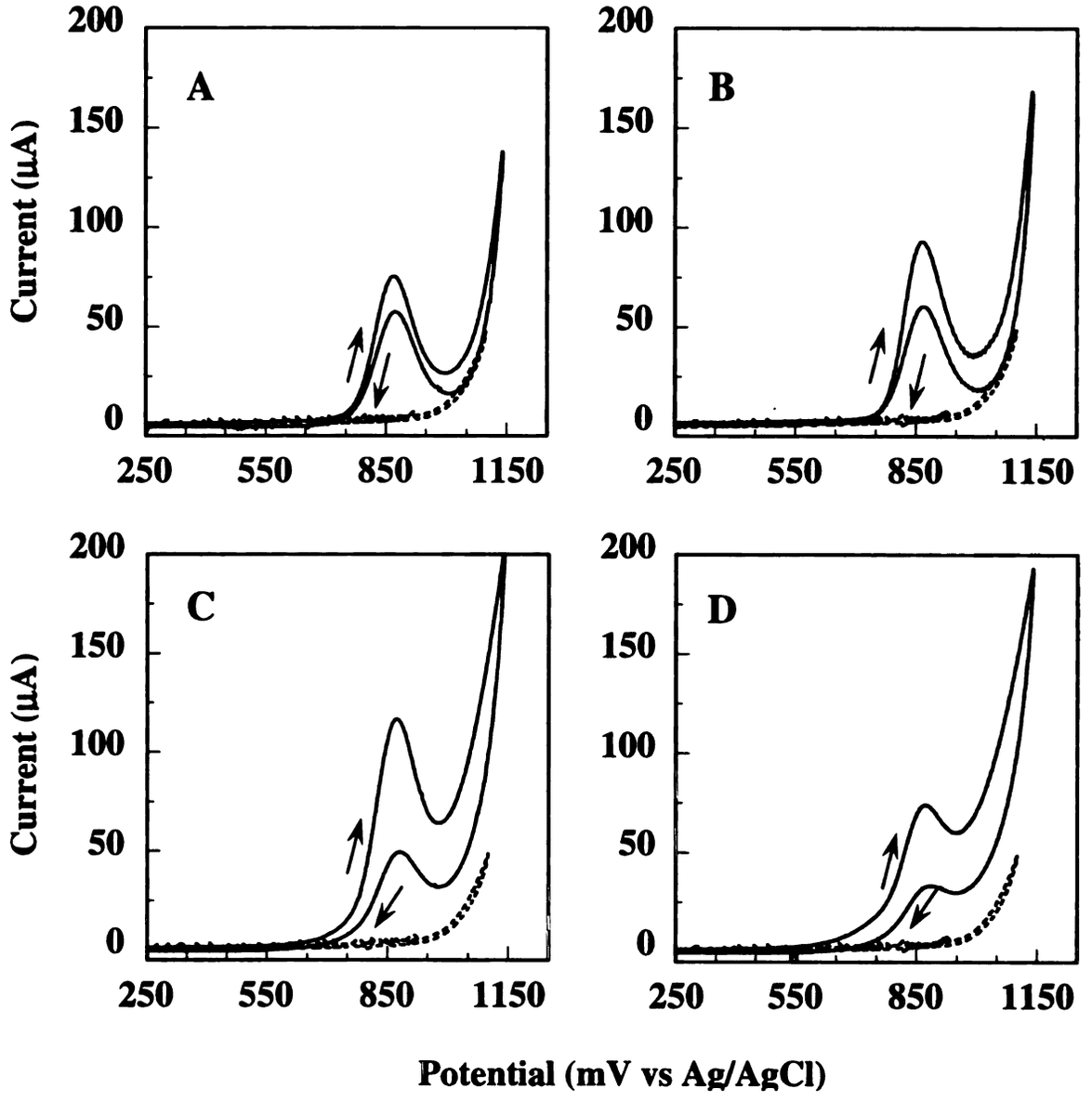

Figure 5.1 Cyclic voltammetric i-E curves, background (dashed line) and total current (solid line), for 1.0 mM (A) CAD (B) PUT, (C) SPMD, and (D) SPM in 0.01 M borax buffer/0.1 M NaCl, pH 11. The working electrode was a microcrystalline diamond film deposited from a 0.5% CH_4/H_2 ratio and 10 ppm B_2H_6. Scan rate = 0.1 V/s. Electrode geometric area = 0.2 cm^2.

Similarly shaped curves were observed for several other amines and polyamines (e.g., methylamine, ethylamine, propylamine, ethylenediamine, 1,3-diaminopropane, 1,6-hexamethylenediamine, and N-(3-aminopropyl)-1,3-propanediamine). The oxidation peak current for each of the amines is clearly discernible from the background current. The E_p^{ox} values are 872, 868, 876, and 872 mV, and the $E_{1/2}$ values are 821, 817, 820, and 815 mV for CAD, PUT, SPMD, SPM, respectively. The i_p^{ox} values are 75, 93, 116, and 76 μA for 1 mM CAD, PUT, SPMD, and 0.8 mM SPM, respectively. A summary of the cyclic voltammetric data for several amines and polyamines in BBpH11 are presented in Table 5.1.

Table 5.1 Cyclic Voltammetric Data for 0.1 mM Aliphatic Amine Oxidation

amine	E_p^{ox} (mV)	$E_{1/2}$ (mV)	wave shape
methylamine	865	801	peak
ethylamine	851	798	peak
propylamine	849	789	peak
ethylenediamine	848	780	peak
1,3-diaminopropane	860	797	peak
putrescine	851	770	peak
cadaverine	860	783	peak
spermidine	867	762	peak/wave
spermine	869	769	peak/wave

Note: Voltammetric data are for a 0.1 V/s scan rate. Reported potentials are versus a Ag/AgCl reference electrode. Analytes were prepared in 0.01 M borax buffer/0.1 M NaCl, pH 11. $E_{1/2}$ values correspond to the potential at half the peak current.

Whether a well defined peak shape is observed depends on the physicochemical properties of the electrode. The E_p^{ox} values are nearly the same, independent of the amine molecular structure, indicating the importance of OH• generation. The oxidation reaction all occur at potential near the onset of oxygen evolution. Very interestingly, there is an oxidation peak present during the reverse sweep, which is clearly associated with the oxidation of amine. The current goes through the maximum at about the same potential as on the forward sweep. At this potential, consumption of OH• by the oxygen evolution reaction is minimal, and these reactants are available for the oxygen transfer reaction. The current during reverse sweep is lower than that during the forward scan. This is partially due to the depletion of the amine during forward scan, and very likely at this scan rate there is not enough time for the new amine molecules to diffuse from the bulk solution and coordinate at the boron sites on the electrode surface. Hence, smaller number of molecules are available for oxidation and a lower current results. The lower current during the reverse sweep may also be limited by the availability of surface boron sites for adsorption. Some time is necessary for desorption of the oxidation products to free boron sites for amine coordination. Cyclic voltammograms obtained at lower scan rates (5-10 mV/s) confirm this supposition as it was observed that the current during reverse sweep tracked that obtained during forward sweep. The hysteresis depends on the scan rate with a larger hysteresis observed at higher scan rates.

Repetitive potential cycling in the amine solution led to progressive attenuation of the current. The voltammetric response could, however, be regenerated by vigorous mixing and/or inserting a time delay interval from 3 to 5 minutes between the cycles. This behavior indicates there is no permanent fouling of the electrode by the oxidation products, as in the case for other electrodes. The current recovery is consistent with

slow desorption of the product(s) from the surface. The absence of fouling and response recovery is demonstrated in Figure 5.2.

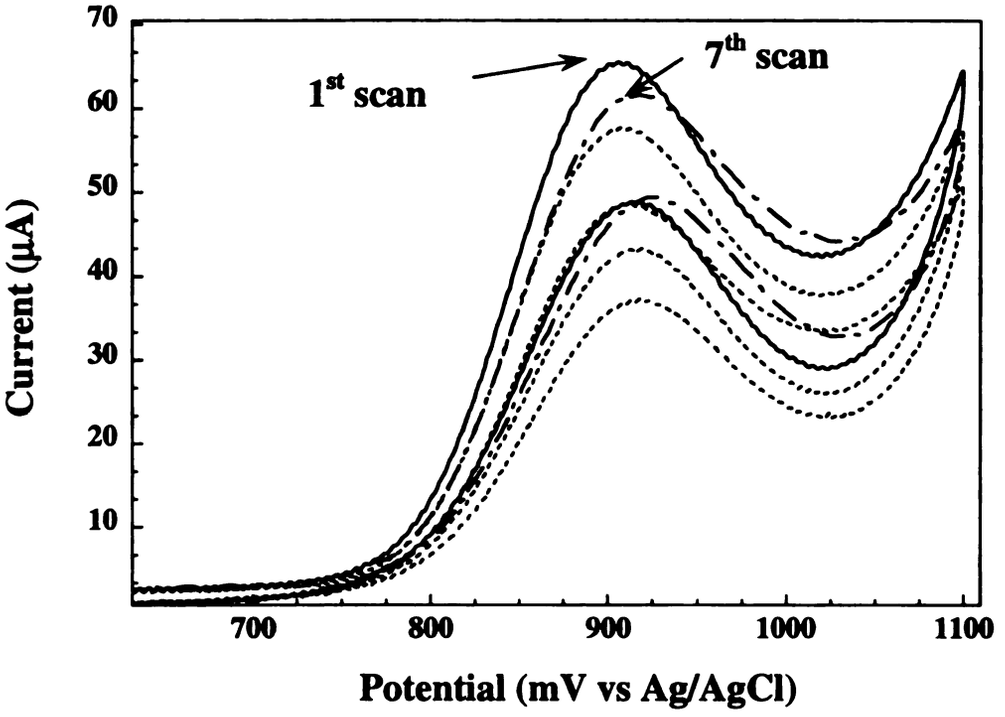

Figure 5.2 Cyclic voltammetric i-E curves for 1.0 mM CAD in 0.01M borax buffer/0.1 M NaCl, pH 11.2, at a nanocrystalline boron-doped diamond thin film. The nanocrystalline diamond electrode was deposited from a 0.5% $CH_4/H_2/Ar$ ratio and 1 ppm B_2H_6. Scan rate = 0.1 V/s. Electrode geometric area = 0.2 cm^2.

Figure 5.2 shows cyclic voltammetric i-E curves for 1.0 mM CAD in BBpH11 at the 0.5% $CH_4/H_2/Ar$ boron-doped nanocrystalline diamond film. There is a decrease in the peak current during each of the first six scans. This decrease is due to the formation of a depletion layer at the interface, as the oxidation reaction is irreversible, but also to slow desorption of the product(s) from the electrode surface. If a time delay of 3 min is applied between scans, with the potential poised at 0 V, then the peak current for the subsequent scan (cycle 7) is nearly the same as the initial scan. This indicates that the

electrode is not irreversibly fouled by reaction products, as is the case for other metallic electrodes, necessitating the need for pulsed waveforms or electrode pretreatment.

5.2.2. Effect of the Electrolyte on the Voltammetric Response

The influence of different supporting electrolytes on the voltammetric response for the polyamines was investigated. CAD was not detected in pH 7.2 phosphate buffer, very likely due to the protonation of the amine group. This probably could inhibits the coordination at surface boron sites, and makes the oxidation reaction more kinetically difficult. A signal was observed for amines with lower dissociation constants (e.g., EDA, SPM, SPMD). At pH 10.6, the voltammetric ressponse varied little with the supporting electrolyte. In general, for a given pH, the E_p^{ox} values for each amine were independent of the supporting electrolyte. The highest oxidation currents were observed for carbonate and borax buffers with supporting electrolytes present.

In pH 9 borax buffer, with $CuCl_2$ as the supporting electrolyte, it was observed that the amine oxidation current was attenuated compared with the response in borax buffer, pH 9 with NaCl as a supporting electrolyte. The amine oxidation current decreased proportionally as the $CuCl_2$ concentration increased because of Cu^{+2} and amino group complexation. This complexation prohibits the amine from coordinating at surface boron sites. It is expected that other cations (e.g., Mg^{+2}, Ca^{+2}) might also attenuate the oxidation current. This observation provides indirect evidence for the importance of amine adsorption in the oxidation reaction mechanism.

5.2.3. Effect of pH on the Voltammetric Response

The effect of pH on the voltammetric response for polyamines was tested in borax, phosphate, and carbonate buffers. Figure 5.3 shows cyclic voltammetric i-E curves for (A) the background response and (B) 1.0 mM CAD as a function of the electrolyte pH. The ionic strength of the electrolytes was maintained constant at 0.4M. A

negative shift in the onset potential for the background current (i.e., oxygen evolution) is observed with increasing pH.

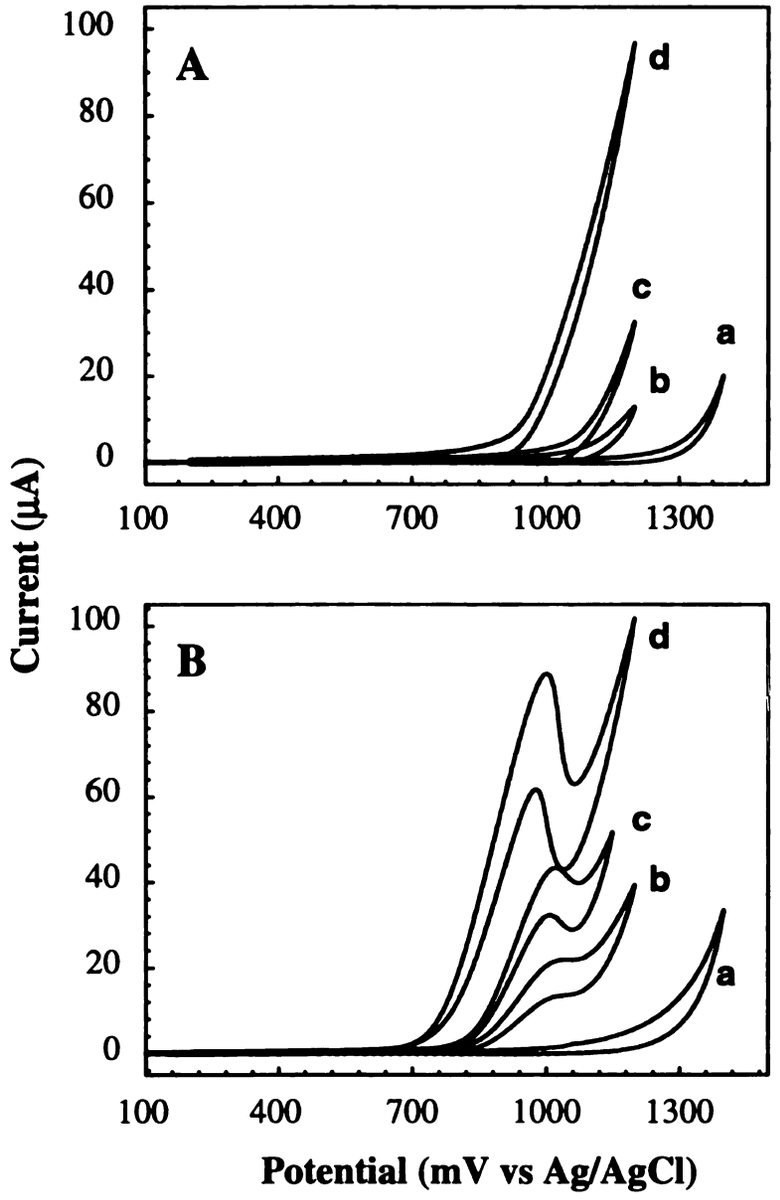

Figure 5.3 Cyclic voltammetric i-E curves for 1 mM cadaverine in (a) 0.01 M phosphate buffer, pH 7.2; (b) 0.01 M carbonate buffer/0.1 M $NaClO_4$, pH 9,; (c) 0.01 M carbonate buffer/0.1 M $NaClO_4$, pH 10, and (d) 0.01 M carbonate buffer/0.1 M $NaClO_4$, pH 11 at microcrystalline diamond film deposited from a 0.5% CH_4/H_2 ratio and 1 ppm B_2H_6. Scan rate = 0.1 V/s. Electrode area = 0.2 cm^2.

The onset potential shifts by ~60 mV/pH unit. The E_p^{ox} and $E_{1/2}$ values for all the polyamines also shifted negatively with increasing pH by ~60 mV/pH unit. These results confirm that the amine oxidation potential is dependent upon the potential at which OH• is generated.

As the pH of the electrolyte increased, i_p^{ox} and Q_p^{ox} for all the polyamines increased, as well. Table 5.2 summarizes the Q_p^{ox} data obtained at a microcrystalline diamond thin-film electrode deposited from 0.5 % CH_4/H_2 ratio. The charge was measured after background subtraction.

Table 5.2 Cyclic Voltammetric Charge Data for 1 mM Amines in 0.01 M Borax Buffer/0.1 M $NaClO_4$

0.01 M Borax Buffer	Charge (μC) for the forward scan			
	CAD	PUT	SPMD	SPM
pH 9	120	108	----	245
pH 10	192	163	273	378
pH 11	226	200	295	470

Note: Voltammetric data are for a 0.1 V/s scan rate.

At pH 7.2, there was no well resolved oxidation wave for either CAD and PUT. The lowest pK_a values for CAD and PUT are 9.13 and 9.35, respectively, and at pH below these values, most of the molecules are protonated. Therefore, they are not available for coordination and oxidation. The oxidation current for SPMD, SPM, and EDA was 2-3 times higher, compared with CAD or PUT, at pH 8.4. The pK_{a1} for SPMD, SPM, and EDA are 8.0, 7.9, and 6.8, respectively.[189] They are lower than the dissociation constant of CAD and PUT, and so the currents observed for SPMD, SPM and EDA are higher.

At pH 11, almost 97% of molecules have multiple amine groups unprotonated; therefore, the larger oxidation currents for each of the amine are observed at high pH. Since, the amine oxidation mechanism is thought to involve adsorption at surface boron sites via the non-bonding electron pair on the N atom, the higher oxidation peak current at higher pH is due to the limited protonation.

Figure 5.4 shows a diagram of the fractional composition of the protonated and unprotonated forms of (A) CAD and (B) SPM as a function of pH.

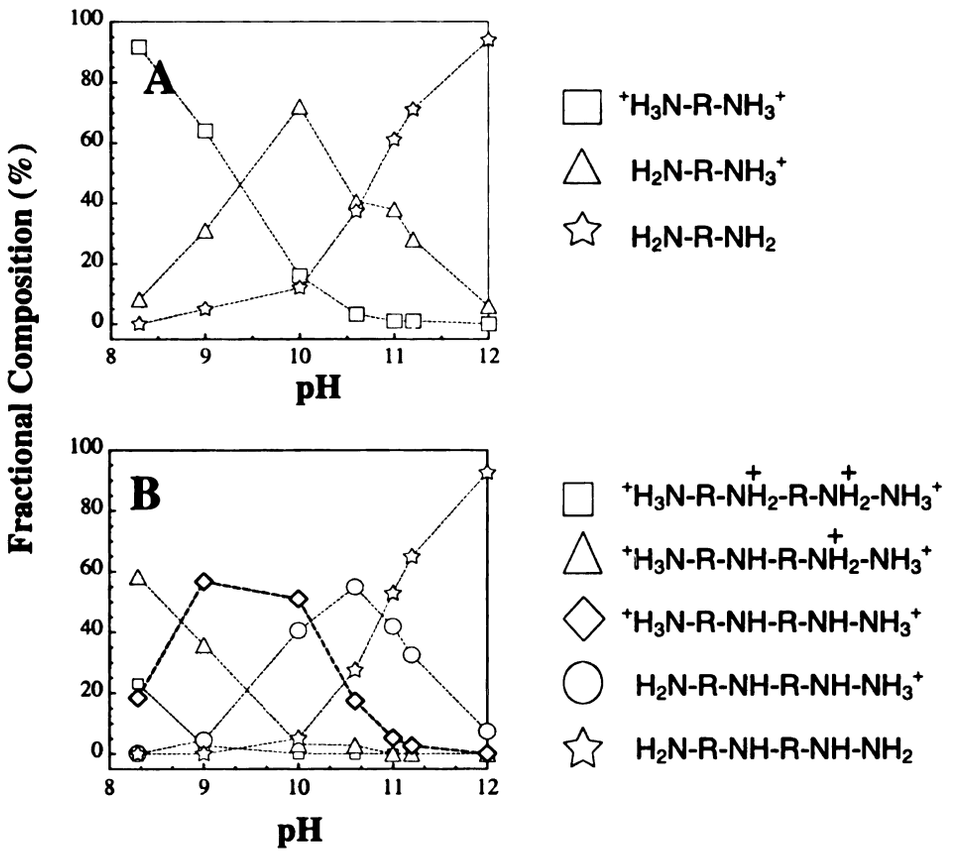

Figure 5.4 The fractional composition of protonate/unprotonated forms of (A) CAD and (B) SPM as a function of pH.

Polyamines, as polyprotic bases, can accept more than one proton. Depending upon the pH, amines are present at a different molar ratios of the protonated and

unprotonated forms. For pH < pKa_1, the fully protonated species is the predominant form $(H_nA)^{+n}$. For pKa_1< pH < pKa_2, the form $(H_{n-1}A)^{+(n-1)}$ is favored.[189] At pH values greater than the pKa_2, the fully basic, unprotonated form (A) is dominant.

The important point is that the pH of the electrolyte solution is critical for this reaction. The electrode response for the amine oxidation strongly depends on the molar ratio of the protonated and unprotonated forms. The maximum oxidation current is seen for the fully unprotonated form.

5.2.4. Effect of Scan Rate on the Voltammetric Response

The effect of scan rate on the cyclic voltammetric response for CAD, PUT, SPMD, and SPM in CBpH10.6, at a 0.5% CH_4/H_2 microcrystalline diamond film, is shown in Figure 5.5 A and B. The scan rate was varied from 10 to 400 mV/s. Examination of the data, using several heavily doped diamond films, revealed that the i_p^{ox} varied linearly with scan rate$^{1/2}$, with non-zero y-intercept. It was observed that the i_p^{ox} for moderately doped diamond electrodes was nearly independent of scan rate, particularly, above 0.1V/s. In general, more linear behavior was observed for the lower, ~0.1 mM, rather than the higher, 1.0 mM, amine concentrations. This is illustrated in Figure 5.5 A and B. For the higher amine concentrations, the reaction becomes surface site limited and, as a result, i_p^{ox} is nearly independent of scan rate. The unchanging peak current at higher scan rates is also attributable, at least in part, to slow desorption kinetics of the reaction product(s) from the surface sites. Therefore, as the scan rate is increased, the current becomes limited by the availability of open coordination sites.

The oxidation peak potential, E_p^{ox}, shifts positively with increasing scan rate. This is illustrated in Figure 5.5C. Johnson et al. attributed a similar positive shift in E_p^{ox} at

composite electrodes to an increased flux of the reactants (i.e., amine).[46] In order for the amine molecules to be oxidized via anodic oxygen transfer sites are required for the production of OH•. A higher amine flux will require a larger number of OH•, and higher concentration of these will be available at more positive potentials.[46]

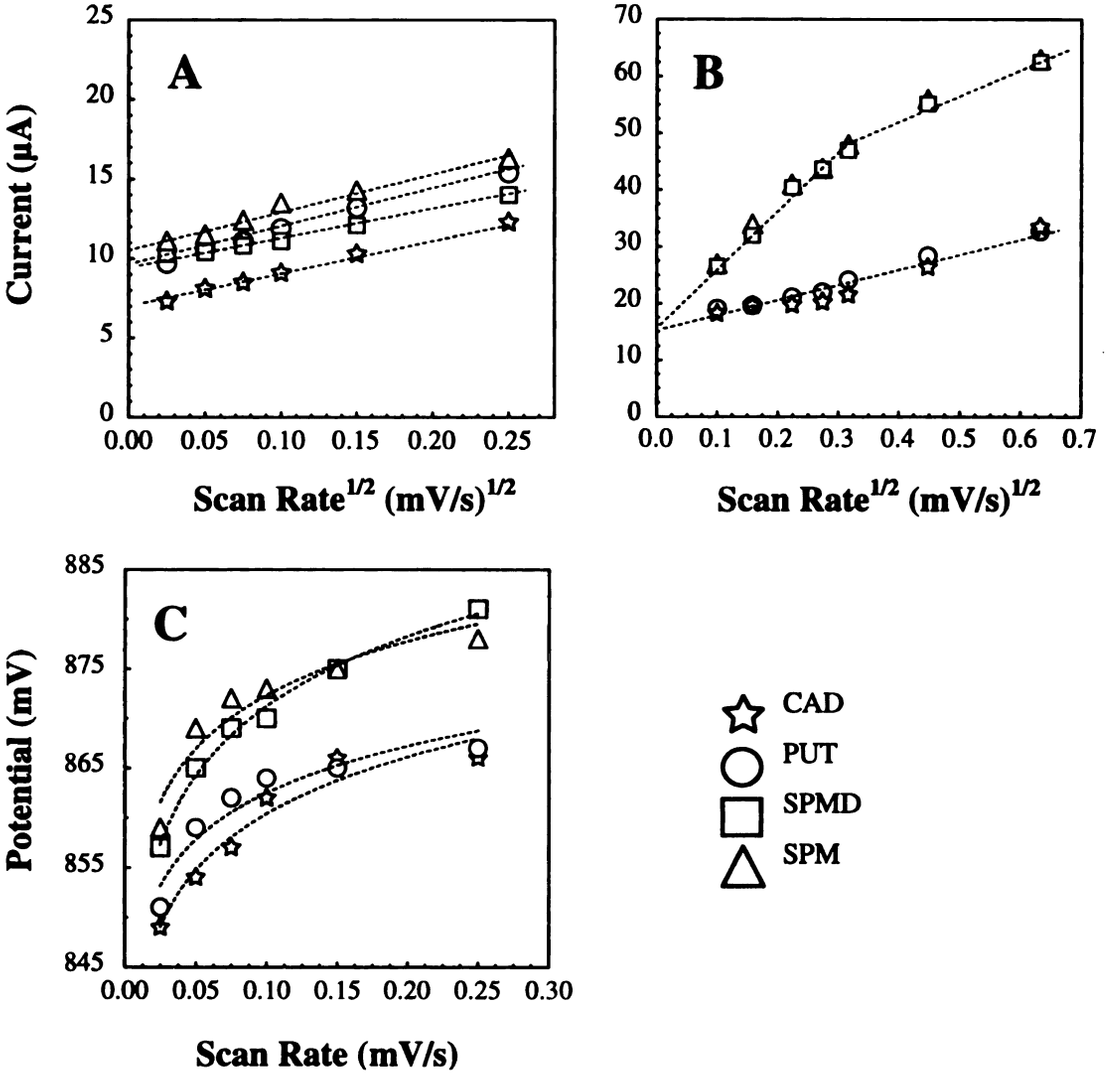

Figure 5.5 Plots of the cyclic voltammetric oxidation peak current, i_p^{ox} versus scan rate$^{1/2}$ for (A) 0.1 mM amines at moderately doped microcrystalline film, (B) 1 mM amines at highly doped microcrystalline film in CBpH10.6. (C) Plots of the oxidation peak potential, E_p^{ox}, versus scan rate for 0.1 mM amines in 0.01 M carbonate buffer, pH10.6.

5.2.5 Effect of Amine Concentration on the Voltammetric Response

The linear sweep voltammetric oxidation peak current was measured as a function of the amine concentration. Figure 5.6 shows cyclic voltammetric i-E curves for EDA in 0.01 M carbonate buffer, pH 10. The concentrations ranged from 0.10 to 5 mM.

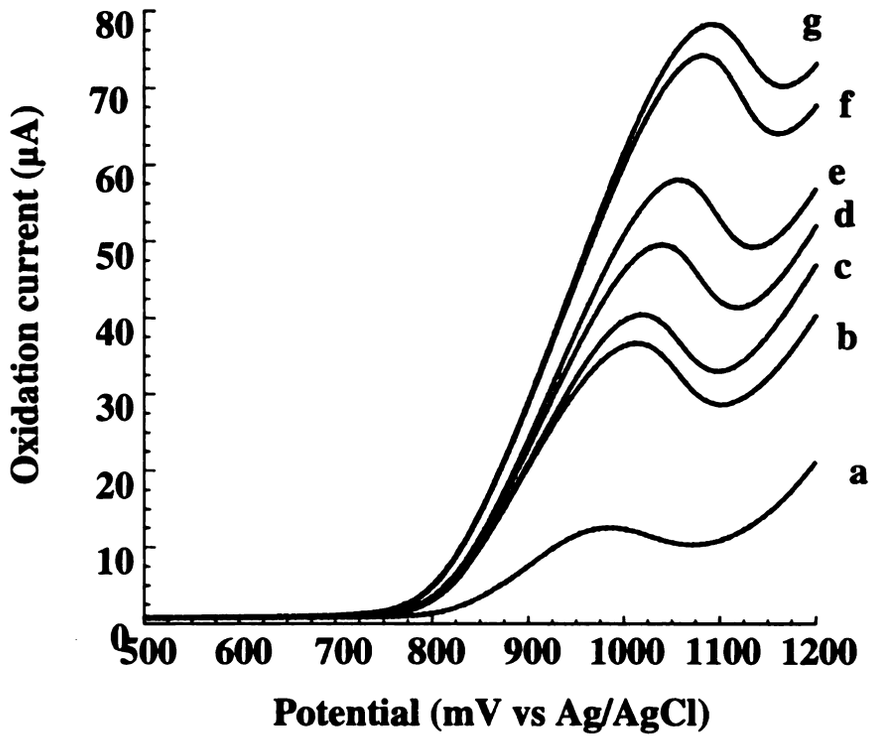

Figure 5.6 Linear sweep voltammetric i-E curves for ethylenediamine at concentrations of (a) 0.1, (b) 0.5, (c) 1, (d) 2, (e) 3, (f) 4, and (g) 5 mM at microcrystalline diamond film deposited from a 0.5% CH_4/H_2 ratio. Scan rate = 0.1 V/s. Electrode geometric area = 0.2 cm^2.

Increasing the amine concentration caused E_p^{ox} to shift toward more positive values, similar to the scan rate dependence. This is a consequence of the increased number of amine molecules available for oxidation, requiring a higher concentration of OH•. This is achieved at more positive potentials. A plot of i_p^{ox} vs concentration was linear up to a 1.0 mM concentration. The plot had non-zero intercept and different slopes (i.e.

sensitivities) for the different amines. Therefore, the analytical utility of the voltammetric and amperometric measurements would appear to be limited to concentrations below 1.0 mM. One possibility for the negative deviation from linearity at concentrations above 1mM could be a limited number of surface boron sites. Studies using films deposited with different boron concentrations support this supposition and will be presented further in this chapter.

5.2.6. Importance of Non-Diamond Carbon Impurities

Figure 5.7 shows cyclic voltammetric i-E curves for 1.0 mM CAD in CBpH10 at a 0.67% CH_4/H_2 microcrystalline diamond film. Figure 5.7 A shows the curve for the "as-deposited" film in the presence of 1 mM CAD along with the background response (dashed line). The onset potential for oxygen evolution at the "as-deposited" film begins at about 1020 mV. The oxidation response for CAD is well-resolved from the background with an E_p^{ox} of 990 mV, an $E_{1/2}$ of 920 mV, and an i_p^{ox} of 32 μA for a 10 mV/s scan rate.

If the film is acid washed (see Experimental Section) to remove the sp^2-bonded non-diamond carbon impurity from the surface and then hydrogen plasma hydrogenate the surface, then the voltammetric response in Figure 5.7 B is observed. Clearly, the removal of the non-diamond carbon impurity causes a total attenuation of the response.[259] The lack of an oxidation response is due to the removal of the non-diamond carbon impurity at which the OH• forms with lower overpotential than the surrounding diamond. It is important to note that the acid washing and rehydrogenation leads to a higher overpotential for oxygen evolution with an onset potential of about 1230 mV. The 200 mV difference in potential between the "as deposited" and rehydrogenated electrodes is evidence for the successful removal of sp^2-bonded non-diamond carbon impurity. This result provides compelling evidence for the importance of localized sp^2-bonded non-diamond carbon impurity sites in the amine oxidation reaction mechanism.

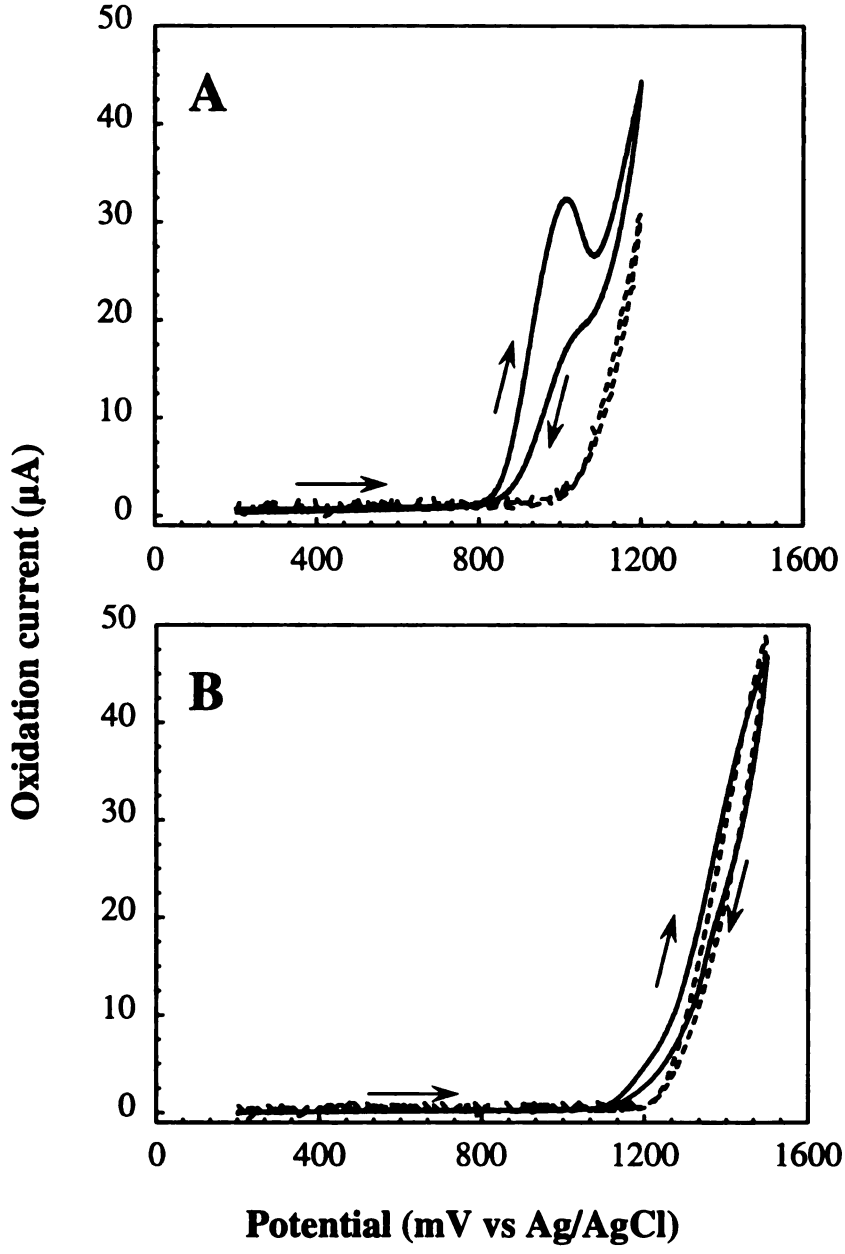

Figure 5.7 Cyclic voltammetric i-E curves for 1 mM cadaverine in 0.01 M carbonate buffer/0.1 M $NaClO_4$, pH10.6, at a microcrystalline diamond film deposited from a 0.67% CH_4/H_2 ratio. (A) "as deposited", and (B) acid washed and rehydrogenated diamond film. Scan rate = 10 mV/s.

5.2.7. Effect of CH_4/H_2 Ratio on the Voltammetric Response

Non-diamond sp^2-carbon impurity can be introduced into the diamond by adjusting the CH_4/H_2 ratio used for film deposition. Therefore, it is possible to optimize the amine oxidation response through manipulation of this ratio. In general, as the CH_4/H_2 ratio is increased, the film quality decreases with the highest quality films being deposited at a 0.33% CH_4/H_2 ratio. Non-diamond sp^2-carbon impurity and morphological defects tend to increase with increasing CH_4/H_2 ratio. Figure 5.8 shows AFM images of diamond films deposited with three different CH_4/H_2 ratios.

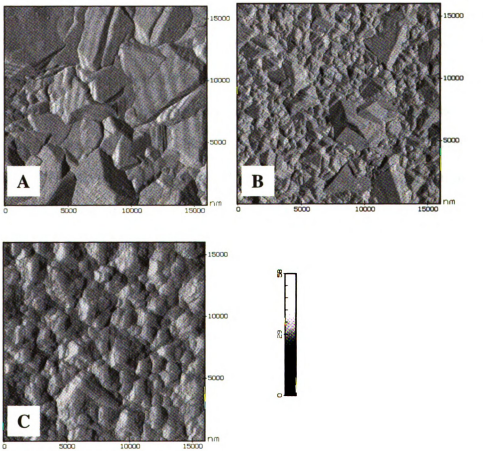

Figure 5.8 Contact-mode atomic force microscopy images of a microcrystalline diamond films deposited from a (A) 0.33%, (B) 0.67%, and (C) 1% CH_4/H_2 ratio. All images have the same x, y, z scales.

As the CH_4/H_2 ratio increases, the nominal crystallite size decreases and the extent of secondary nucleation increases. The decrease in crystallite size leads to an increase in the fraction of exposed grain boundary. It is at the grain boundary where non-diamond sp^2-carbon deposits form. [63 and references therein] The higher CH_4/H_2 ratio causes a higher rate of nucleation leading to the secondary growths and a reduction in grain size. As shown in Figure 5.8, the film surface for the 0.33% CH_4/H_2 ratio consists of large 1-5 μm crystals. The 0.67% CH_4/H_2 film has a large fraction of much smaller crystallites (0.1-0.5 μm) and few large grains (1-2 μm). The surface of the film deposited from 1% CH_4/H_2 ratio is not well faceted. Small crystallites <0.1 μm, are predominant. The small grain size results from the increased secondary nucleation rates.

Figure 5.9 shows corresponding visible Raman spectra for the films. The laser spot size was ca. 10 μm, meaning that several grains and grain boundaries were probed in the measurement. An intense first-order diamond phonon line is observed at 1332 cm^{-1} for the 0.33% CH_4/H_2 film. The full width at half-maximum (FWHM) of the band is 8 cm^{-1}. For comparison, the FWHM for a single-crystal diamond standard is 2-3 cm^{-1}. The FWHM is a measure of the film quality and, to a first approximation, is inversely related to the phonon lifetime.[207] In other words, grain boundary scatter decreases the phonon lifetime and increases the FWHM. There is minimal scattering intensity, observed between 1500 and 1600 cm^{-1}, associated with sp^2-bonded carbon impurity. The cross-sectional scattering coefficients (514.4 nm) for diamond and graphite (i.e., non-diamond carbon) are 9×10^{-7} and 500×10^{-7} cm^{-1}/sr, respectively.[207,225,264] Therefore, the technique is quite sensitive to the presence of non-diamond carbon impurity.

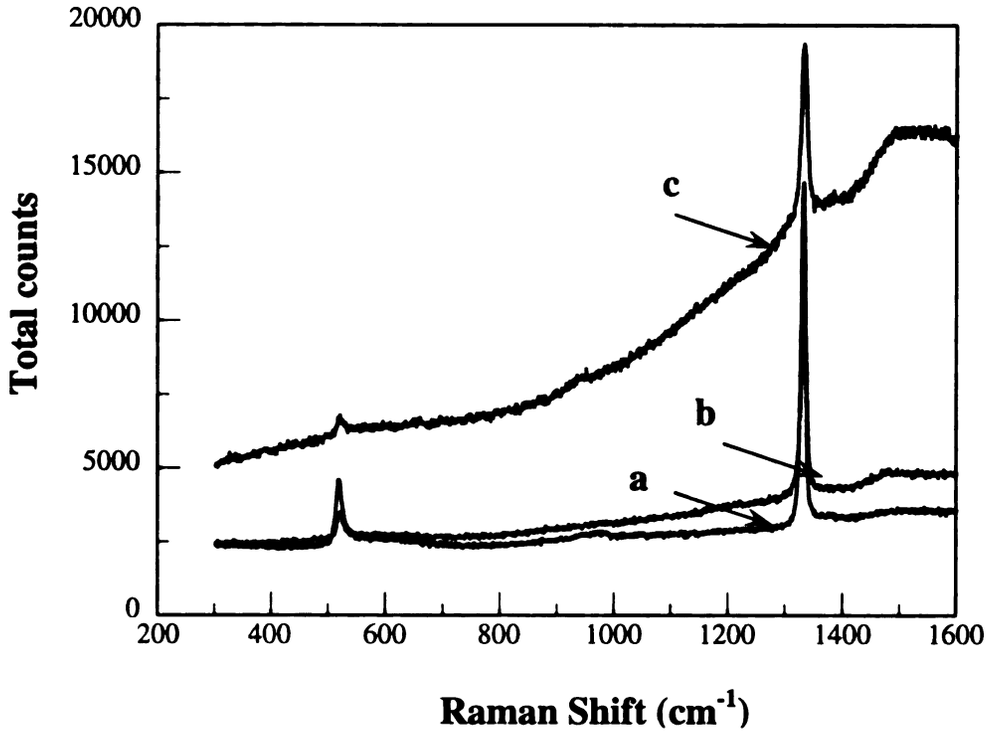

Figure 5.9 Visible Raman spectra for diamond films deposited using a (a) 0.33%, (b) 0.67%, and (c) 1% CH_4/H_2 ratio. 514.4 nm laser source and 10 s integration time.

Importantly, there is little photoluminescence background in the spectra for 0.33% and 0.67% CH_4/H_2 films, consistent with a low level of sp^2-bonded carbon impurity.[63 and references therein] Much larger photoluminescence background is observed in the spectrum for 1% CH_4/H_2 film.

As the CH_4/H_2 ratio increases, the diamond phonon line intensity decreases, and the FWHM, the scattering intensity between 1500 to 1600 cm^{-1} and the photoluminescence background all increase, consistent with an increased level of defects, in particular, grain boundaries and non-diamond carbon impurity. The band at 520 cm^{-1} is attributed to scattering by the underlying Si substrate. The intensity of this band decreases with increasing CH_4/H_2 ratio because of the increasing film thickness

and higher optical density due to non-diamond carbon. The presence of the sp^2-bonded non-diamond carbon impurity can also be detected using electrochemical measurements. The background cyclic voltammetric current and potential window in aqueous electrolytes are strongly affected by the presence of sp^2-bonded carbon.[63]

Background cyclic voltammetric i-E curves for the three different diamond films are shown in Figure 5.10 A-C. The background for each was recorded at different solution pH. For a given pH, the onset potential for oxygen evolution (i.e., OH• generation) decreases with increasing CH_4/H_2 ratio. For example, at pH 11, the onset potential, measured for a current of 7 μA is 1000, 940, and 870 mV, respectively, for films deposited from the 0.33, 0.50, and 1.0% CH_4/H_2 ratio. The non-diamond sp^2-carbon impurity exhibits a lower overpotential for oxygen evolution than does the surrounding diamond. As the concentration of this impurity increased, the onset potential decreases. Presumably, the lower overpotential results from the ability of certain sites on the sp^2 impurity to stabilize reaction intermediates. The onset potential also shifts negatively with increasing pH. The anodic current measured at 1050 mV (i.e., in the oxygen evolution regime) increases with increasing CH_4/H_2 ratio and pH. For instance, the current is 2.9, 7.3, 15.3, and 54.6 μA for the 0.33% CH_4/H_2 film at pH 9, 10, 11, and 12, respectively. Table 5.3 summarizes the voltammetric background current data.

Table 5.3 Cyclic Voltammetric Background Current Data for Boron-Doped Microcrystalline Diamond Films

Diamond Film	Current (μA) at 1050 mV vs Ag/AgCl			
	pH9	pH10	pH11	pH12
0.33% CH_4/H_2	2.9	7.3	15.3	54.6
0.50% CH_4/H_2	10.8	26.3	61.5	168.4
1.0% CH_4/H_2	22.1	42.4	91.2	188.9

Note: Voltammetric data are for a 0.1 V/s scan rate.

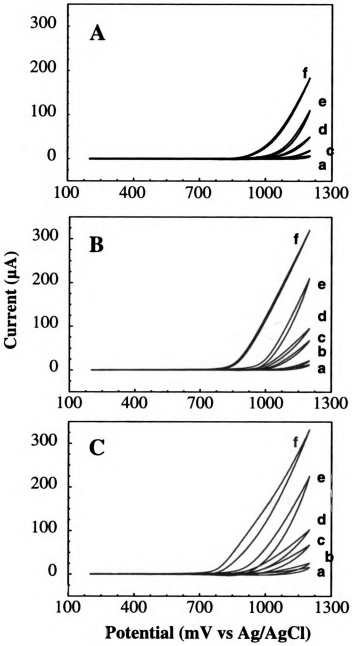

Figure 5.10 Background cyclic voltammetric i-E curves for a microcrystalline diamond films deposited using a (A) 0.33%, (B) 0.50%, and (C) 1% CH_4/H_2 ratio. The solution pH was (a) 8.4, (b) 9, (c) 10, (d) 10.6, (e) 11, and (f) 12. Scan rate = 0.1 V/s. Electrode geometric area = 0.2 cm^2.

The amine oxidation current also shows a dependence on the CH_4/H_2 ratio. Cyclic voltammetric i-E curves for 1.0 mM CAD in CBpH10.6, at microcrystalline diamond films deposited using three different CH_4/H_2 source gas ratios are shown in Figure 5.11.

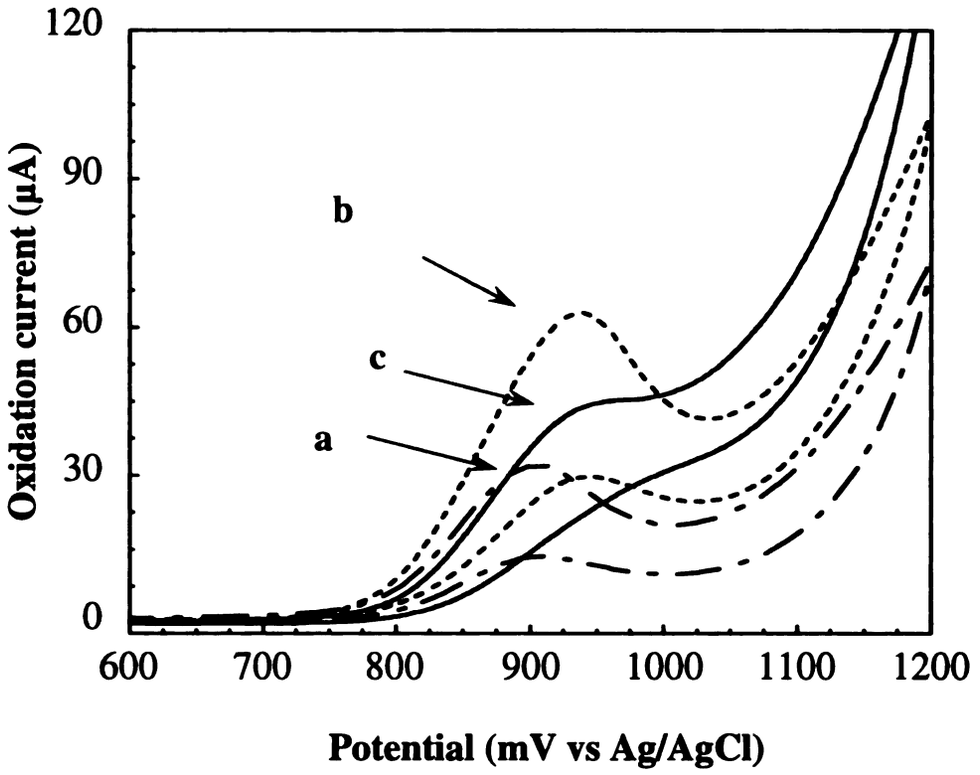

Figure 5.11 Cyclic voltammetric i-E curves for 1 mM cadaverine in 0.01 M carbonate buffer/0.1 M $NaClO_4$, pH10.6, at diamond films deposited using CH_4/H_2 source gas ratios of (a) 0.33%, (b) 0.5%, and (c) 1%. Scan rate = 0.1 V/s. Electrode geometric area = 0.2 cm^2.

The film deposited from the 0.5% CH_4/H_2 ratio exhibits the largest and most well-defined oxidation wave, with a peak current of ca. 60 μA. The 0.33% film was next best in performance, in terms of the peak current magnitude, with a value of ca. 20-30 μA. The 1.0% film exhibits a quantifiable response, with a peak current of ca. 45 μA, but it is superimposed on a larger background current. The reproducibility of the response was

best for the 0.5% film and worst for the 1% films. There is clearly an optimum electrode surface structure and chemical composition required for the polyamine oxidation reaction. Such a structure is achieved with films deposited from a 0.4-0.5% CH_4/H_2 source gas ratio. Table 5.4 shows a summary of some of the cyclic voltammetric data.

Table 5.4 Cyclic Voltammetric Peak Current and Potential Data for Amines Oxidation at Microcrystalline Diamond Films Deposited with Different CH_4/H_2 Ratios.

CH_4/H_2 ratio	$i_p^{ox.}$ (μA)/ $E_p^{ox.}$ (mV vs Ag/AgCl)							
	CAD		PUT		SPMD		SPM	
0.3 %	32.1	910	34.3	915	30.6	924	31.7	933
0.4 %	63.0	937	59.4	947	56.4	951	50.7	956
0.5 %	58.8	942	45.2	929	48.0	959	53.2	962
0.67 %	35.9	935	-----	-----	-----	-----	32.9	969
1.0 %	44.9	957	44.2	955	43.3	951	36.4	965

Note: Voltammetric data obtained at a scan rate = 0.1 V/s. Electrode area = 0.2 cm^2

5.2.8. Effect of Boron on the Voltammetric Response

An oxidation mechanism has been proposed whereby the amine functional group coordinates with a surface boron sites. This interaction is thought to take place near the grain boundaries where boron aggregates and sp^2-bonded carbon impurity is located. OH• is the primary oxidant with the surface boron interaction increasing the residence time of the amine at the electrode surface and weakening the C-N bond. The principal reaction is the transfer of O from adsorbed OH• species to the surface coordinated amine. The voltammetric results presented below support this supposition and provide compelling evidence for the importance of surface boron in the oxidation reaction mechanism.

Figure 5.12 shows cyclic voltammetric i-E curves for 1 mM CAD in 0.01 M borax buffer, pH 10.6, along with the corresponding background current at (A) a nanocrystalline diamond thin film deposited with intentionally added boron, and (B) a nanocrystalline film deposited without any intentionally added boron.

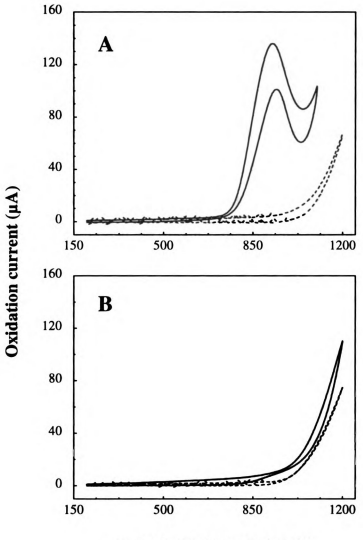

Figure 5.12 Cyclic voltammetric i-E curves for 1 mM CAD, along with the corresponding background current (dashed line), in a 0.01 M borax buffer, pH 11.2, at (A) a boron-doped nanocrystalline diamond thin-film electrode and at (B) a nanocrystalline diamond thin-film electrode deposited without intentionally added boron. Scan rate = 0.1V/s. Electrode geometric area = 0.2 cm^2

Figure 5.12 A shows a well defined oxidation wave, clearly distinguishable from the water electrolysis background current, for the boron-doped film. E_p^{ox} is 927 mV and i_p^{ox} is 136 μA. There is a second oxidation peak on the reverse sweep at about the same potential as on the forward sweep. This wave shape has been previously discussed and is consistent with a redox reaction that involves a competitive surface interaction.[35,54,55] Correspondingly, there is a poorly defined oxidation wave for the unintentionally doped film. During the forward and reverse sweeps, the current is slightly increased above the background, but there is no well-defined oxidation curve. The absence of an oxidation response for CAD is not due to poor film electrical conductivity, as the ΔE_ps for $Fe(CN)_6^{-3/-4}$, $Ru(NH_3)_6^{+2/+3}$, and $IrCl_6^{-2/-3}$ were 63, 68, 60 mV, and for methyl viologen, 4-tert-butyl catechol, and $Fe^{+2/+3}$ were 60, 764, 396 mV. [63] This result demonstrates the importance of surface boron in the oxidation reaction mechanism of aliphatic polyamines at diamond. [28] More detailed studies investigating the electrode activity for amine oxidation as a function of boron dopant concentration were performed for both nanocrystalline and microcrystalline films.

The characterization of a boron-doped nanocrystalline diamond thin-film electrode, deposited from a 1/94/5 $CH_4/Ar/H_2$ (v/v) ratio with 10 ppm B_2H_6 added for doping, was presented in Chapter 4. a set of nanocrystalline films were deposited with 1, 10, 20, and 30 ppm of added B_2H_6. This corresponds to a 200, 2000, 4000, 6000, and 10,000 ppm B/C ratio in the source gas mixture. The actual doping level was determined from BNR analysis measurements. Table 2.4 in Chapter 2 presents a summary of the doping levels and apparent resistivities for each film. The ultimate goal for the work was to study the effect of doping level on the polyamine oxidation response, but the first task was to perform a complete characterization of the films.

Figure 5.13 shows visible Raman spectra for the nanocrystalline films, deposited from a 1/94/5 $CH_4/Ar/H_2$ (v/v) ratio with 1, 10, 20, and 30 ppm B_2H_6 added, respectively. Broad peaks are seen near 1150, 1225, 1333, 1470 and 1550 cm^{-1}.

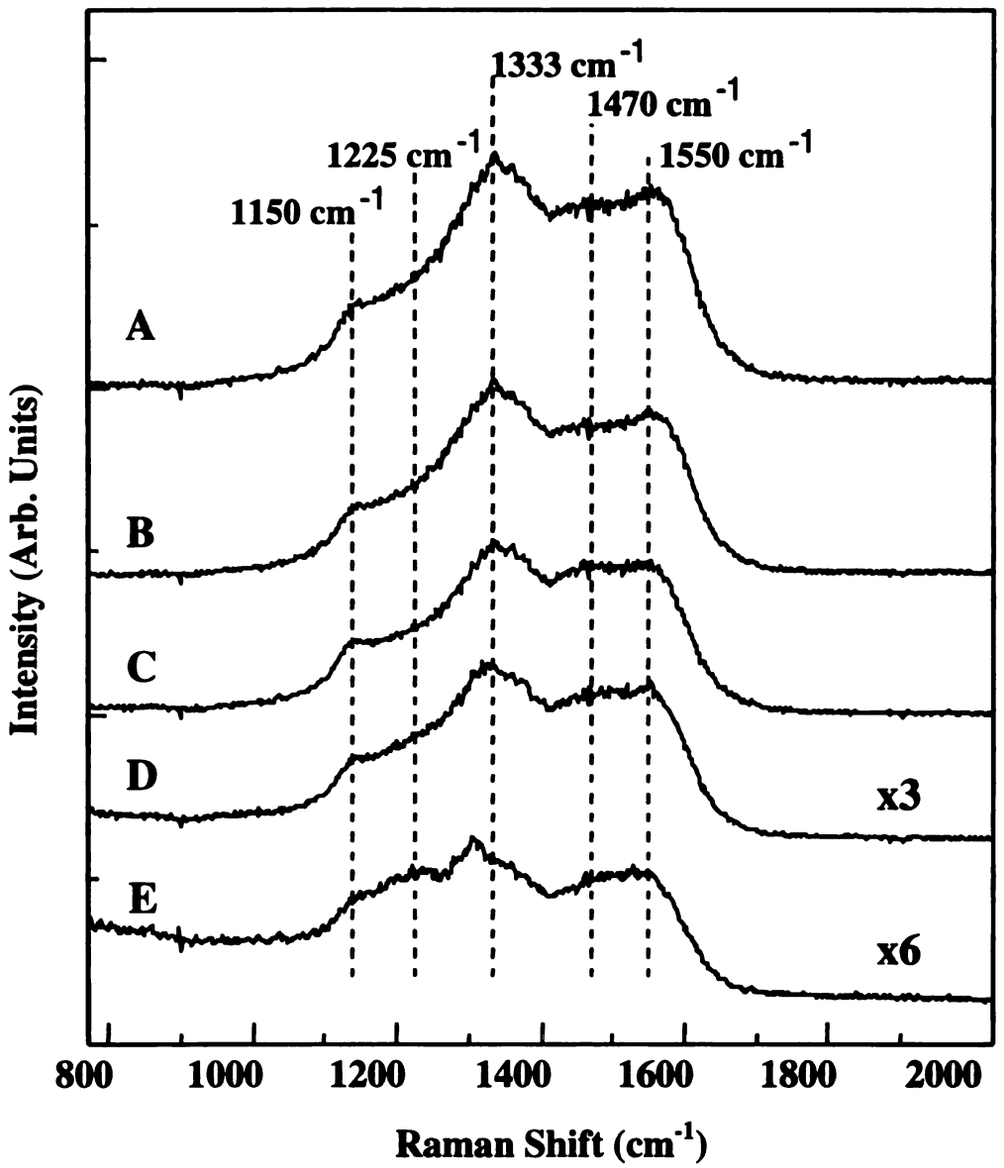

Figure 5.13 A-E Visible Raman spectra for boron-doped nanocrystalline diamond films deposited from a 1/94/5 $CH_4/Ar/H_2$ (v/v) source gas ratio with (A) 0, (B) 1, (C) 10, (D) 20, and (E) 30 ppm of added B_2H_6. 532 nm laser source and 10 s integration time.

The peak near 1333 cm^{-1} is attributed to the first-order phonon mode of diamond. The FWHM is much broader than that for a microcrystalline diamond film, due to the smaller grain size and higher grain boundary or defect density of the nanocrystalline film. All of the presented modes (i.e., 1150, 1225, 1333, 1470 and 1550 cm^{-1}), characteristic of nanocrystalline boron-doped diamond, are present in all the spectra. The band at ~1225 cm^{-1} is a signature of boron present in the film. Similarly to microcrystalline diamond, it is attributed to a disordered sp^3-carbon, due to distortion of diamond lattice by boron atoms. With increasing boron concentration, scattering intensity at this position becomes more pronounced. Another difference in the Raman spectra, especially in spectra D and E, is red-shift of the diamond line position from 1333 cm^{-1} to ~1325 cm^{-1}, very likely due to high boron concentration and possible defects developed because of it. The scattering intensity of the entire spectrum decreases with increasing doping level. This results from an increase in opacity (i.e., decreased sampling volume) with doping level.

The peak at 1150 cm^{-1} is used as a signature for high quality nanocrystalline diamond,[224] and is being associated with sp^2-bonded carbon, specifically transpolyactelylene segments at grain boundaries.[228]

Figure 5.14 A shows background cyclic voltammetric i-E curves for the boron-doped nanocrystalline diamond films in 1.0 M KCl, over a wide potential range. The working potential window (± 100 μA or 500 $\mu A/cm^2$) for each film decreases with increasing doping level. For example, the window is 3.1 V for film A, B, and C, and 3.0 for film D. The response is featureless for all films between the potential limits. The anodic current at positive potentials is due to the onset of chlorine evolution. The reduction of chlorine back to chloride is most pronounced at film D with a peak at 750 mV. The cathodic current at the negative potentials is attributed to hydrogen evolution.

Figure 5.14 B shows a background cyclic voltammetric i-E curves for a boron-doped nanocrystalline diamond films in 1.0 M KCl over a more limited potential range.

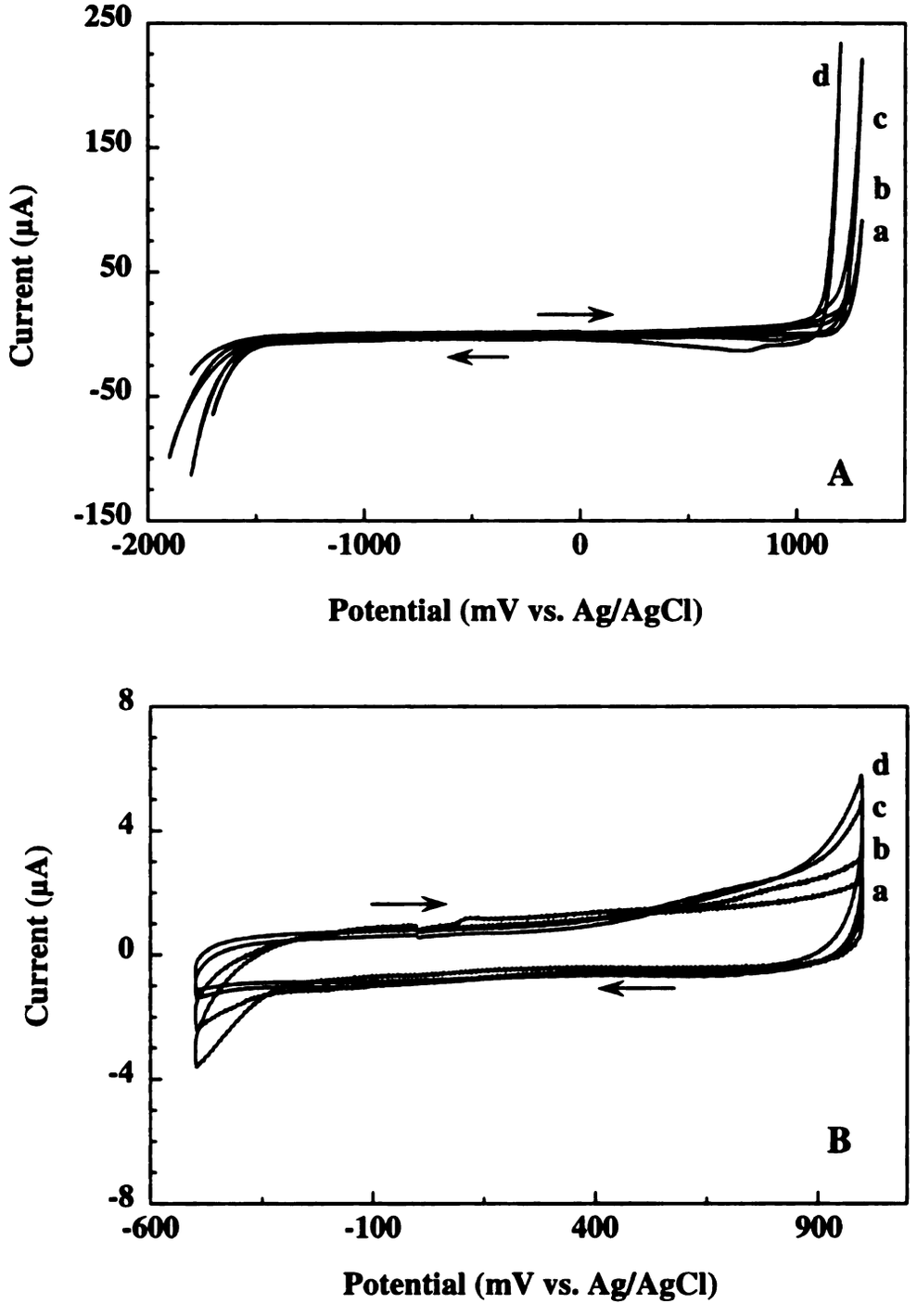

Figure 5.14 (A) Cyclic voltammetric i-*E* curves for boron-doped nanocrystalline diamond films in 1 M KCl over (A) wide potential range showing the working potential window and (B) a narrow potential range. Films deposited using a 1/94/5 CH_4/Ar/H_2 (v/v) source gas ratio and (a) 1, (b) 10, (c) 20, (d) 30 ppm of added B_2H_6. Scan rate = 0.1 V/s. Electrode geometric area = 0.2 cm^2

The curves are similar in shape and stable with cycling. There are no peaks present in the 0-500 mV range, associated with redox-active surface carbon-oxygen functionalities. There is anodic charge between 400 and 900 mV that increases with doping level. The cause of this current is unknown but may be related to oxidation of sp^2-bonded carbon in the grain boundaries and defects, which may increase with doping level. The current magnitude of the nanocrystalline diamond film is slightly higher, than the current for microcrystalline films. For example, the current for microcrystalline films is ca. 0.4-0.6 μA (2.0-3.0 μA/cm^2) at 250 mV vs Ag/AgCl in this medium, while the currents for the nanocrystalline films are 0.7, 0.9, 1.0, and 1.1μA (3.5-5.5 μA/cm^2) for films A, B, C, and D, respectively. The larger current, is likely due to the higher fraction of exposed sp^2-bonded carbon in grain boundaries.

The electrochemical responsiveness of the boron-doped nanocrystalline diamond film toward five redox systems was next investigated using cyclic voltammetry. A summary of the cyclic voltammetric data is given in Tables 5.5 and 5.6.

Table 5.5 Cyclic Voltammetric Data for $Fe(CN)_6^{-3/-4}$, $Ru(NH_3)_6^{+3/+2}$, $IrCl_6^{-2/-3}$ at Boron-Doped Nanocrystalline Diamond Films

Film (ppm)	1 mM $Fe(CN)_6^{-3/-4}$			1 mM $Ru(NH_3)_6^{+3/+2}$			0.25 mM $IrCl_6^{-2/-3}$		
	E_p^{ox} (mV)	i_p^{ox} (μA)	ΔE_p (mV)	E_p^{ox} (mV)	i_p^{ox} (μA)	ΔE_p (mV)	E_p^{ox} (mV)	i_p^{ox} (μA)	ΔE_p (mV)
1	309	73.1	**65**	-132	63.2	**67**	821	13.6	**66**
10	309	69.4	**63**	-135	62.7	**59**	833	21.6*	**63**
20	311	74.2	**67**	-131	64.9	**59**	824	14.4	**64**
30	310	70.1	**62**	-131	67.8	**59**	830	14.6	**64**

Note: Voltammetric data obtained at scan rate=0.1V/s, electrode geometric area=0.2 cm^2, and * concentration of $IrCl_6^{-2/-3}$ was 0.5 mM.

For all of three systems a nearly reversible voltammetric response was observed for all the films. ΔE_ps were in the range of 59-67 mV. The small ΔE_ps observed for the boron-doped nanocrystalline diamond films are indicative of a high level of surface cleanliness, low surface oxide coverage and high electrical conductivity for all four films. Cyclic voltammetric i-E curves for 4-*tert*-butylcatechol (t-BC) and $Fe^{+2/+3}$ have much larger ΔE_ps and more asymmetric peak shapes. ΔE_p's of 419-487 mV and 632-735 mV are observed for t-BC and $Fe^{+2/+3}$, respectively. The larger peak separations, as compared to the other redox analytes, result from more sluggish electrode reaction kinetics.[17,18]

Table 5.6 Cyclic Voltammetric Data for $Fe^{+2/+3}$ and t-Butyl Catechol at Boron-Doped Nanocrystalline Diamond Films

Film (ppm)	1 mM $Fe^{+2/+3}$			1 mM t-butyl catechol		
	E_p^{ox} (mV)	i_p^{ox} (μA)	ΔE_p (mV)	E_p^{ox} (mV)	i_p^{ox} (μA)	ΔE_p (mV)
1	920	32.3	**632**	690	118.3	**439**
10	926	36.0	**679**	655	112.2	**419**
20	960	33.6	**735**	680	117.5	**487**
30	940	31.7	**716**	669	115.5	**477**

Note: Voltammetric data obtained at a scan rate = 0.1 V/s.
Electrode geometric area = 0.2 cm^2

In general, as discussed in Chapter 3, the electrode kinetics for these two analytes are more sluggish at both microcrystalline and nanocrystalline diamond, as compared to glassy carbon. The ΔE_p for t-butyl catechol shows little variation with doping

level and the values are smaller than the 600-800 mV observed for microcrystalline diamond. It is supposed that the slow kinetics for nanocrystalline diamond result from a lack of adsorption on the sp^3-bonded, hydrogen-terminated surface.

The ΔE_p for $Fe^{+2/+3}$ increases with increasing doping level. The reason for this is unclear. ΔE_p for this redox system at both microcrystalline and nanocrystalline diamond is larger than that for glassy carbon. This has been attributed at least in part, to the absence of catalyzing surface carbon-oxygen functional groups on the diamond surface, specifically carboxyl groups.[63,66]

Plots of i_p^{ox} versus $v^{1/2}$ for all five redox analytes were linear (r^2=0.998), with y-axis intercepts near zero. This trend is indicative of reactions limited by semi-infinite linear diffusion of reactants to the electrode surface. In summary, the nanocrystalline films, with different doping levels, all show a high degree of electrochemical responsiveness for $Fe(CN)_6^{-3/-4}$, $Ru(NH_3)_6^{+3/+2}$, and $IrCl_6^{-2/-3}$ without any pretreatment. Over this doping range, the density of electronic states in the films is not significantly different. This is an important observation because it proves that the differences in voltammetric response for the polyamines discussed below are not due to variations in the electrical conductivity.

Figure 5.15 shows cyclic voltammetric i-E curves for nanocrystalline diamond film electrodes in borax buffer, pH 10.6. At potentials less than 900 mV, the current for all three electrodes have a similar shape. The main difference in the voltammograms is that the onset potential for oxygen evolution, which shifts toward negative potentials with increasing doping level. This trend may indicate that surface boron sites are involved in the oxygen evolution reaction (i.e., stabilization of OH•).

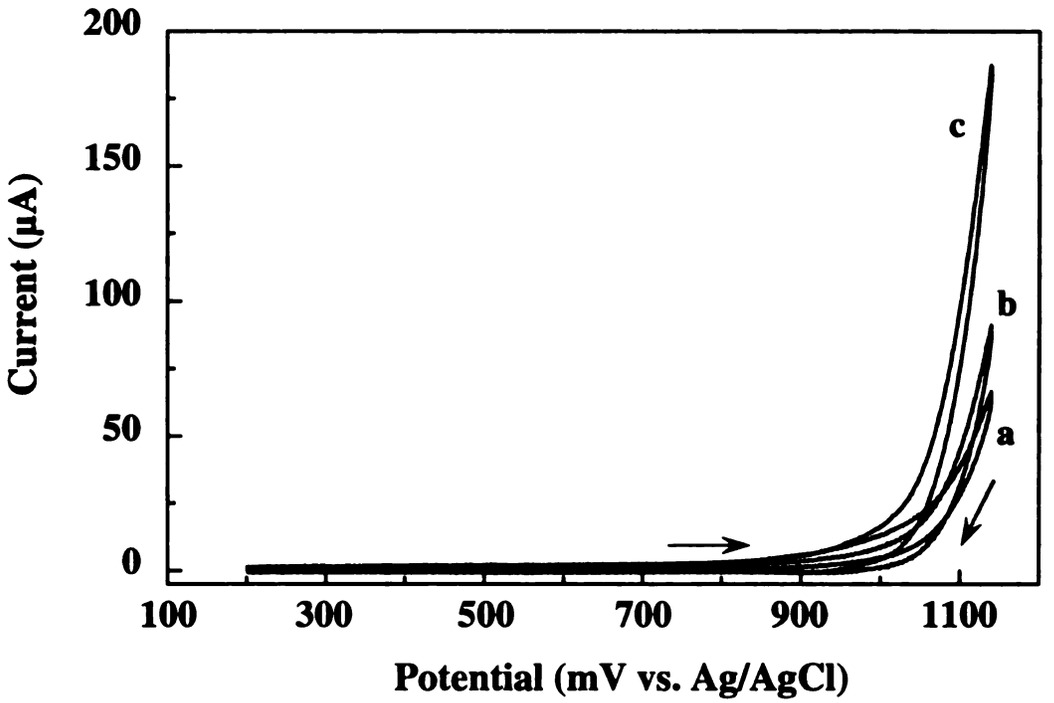

Figure 5.15 Cyclic voltammetric i-E curves for boron-doped nanocrystalline diamond films in borax buffer pH 10.6. The films were deposited with (a) 1, (b) 20, (c) 30 ppm B_2H_6. Scan rate = 0.1 V/s. Electrode geometric area = 0.2 cm^2.

This trend may also reflect an increased level of sp^2-bonded carbon present at the surface, caused by the increased doping level. It is known, as shown in Chapter 5, that sp^2-bonded carbon exhibits a lower overpotential for oxygen evolution than does sp^3-bonded diamond.

Figure 5.16 shows cyclic voltammetric i-E curves for the oxidation of PUT, CAD, SPMD, and SPM at nanocrystalline films with different doping levels.

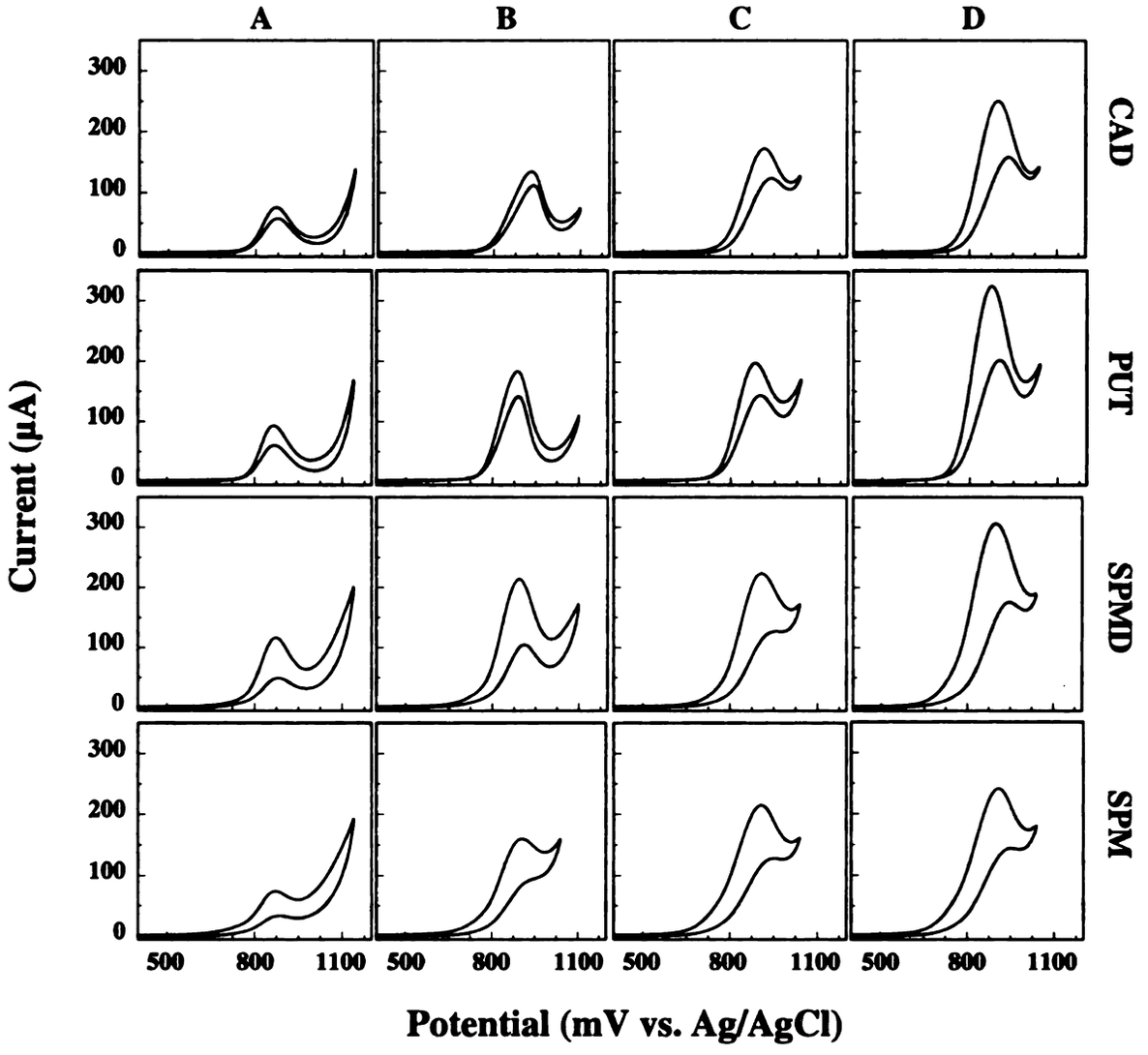

Figure 5.16 Cyclic voltammetric i-E curves for 1.0 mM cadaverine, putrescine, spermidine, and 0.8 mM spermine in BBpH10.6 at boron-doped nanocrystalline diamond films deposited with (A) 1 ppm (B) 10 ppm , (C) 20 ppm, and (D) 30 ppm of added B_2H_6.

A well-defined voltammetric wave is observed for each of the amines at all films. Most important is the fact that the peak current increases with increasing boron level for all four amines. This is direct evidence for the effect of surface boron on the oxidation

reaction. An increasing doping level leads to a higher number of surface boron sites available for the reaction.

The cyclic voltammetric peak current and potential data are summarized in Tables 5.7 and 5.8, respectively. It is clear that the oxidation peak current for each amine increases with increasing doping level. It is also clear that the oxidation peak potentials are largely invariant with doping level. At low doping level, the currents for SPMD and SPM are larger than those for PUT and CAD. However, as the doping level increases this trend changes, with the largest currents observed for CAD and SPMD.

Table 5.7 Summary of Cyclic Voltammetric Peak Current Data for Boron-Doped Nanocrystalline Diamond Electrodes

Film	Oxidation Peak Current i_p^{ox} (μA)			
	1 mM CAD	1 mM PUT	1 mM SPMD	0.8 mM SPM
0 ppm	no oxidation	no oxidation	no oxidation	no oxidation
1 ppm	32.4 ± 4.9	32.5 ± 1.4	51.0 ± 2.4	50.1 ± 1.7
10 ppm	124.5 ± 11.5	115.2 ± 39.2	153.7 ± 2.4	167.1 ± 6.9
20 ppm	261.8 ± 62.7	220.2 ± 38.9	264.6 ± 41.4	198.6 ± 26.4
30 ppm	304.5	251	306	225

Note: Voltammetric data obtained at a scan rate = 0.1 V/s.
Electrode geometric area = 0.2 cm^2.
Data are averages for two or three electrodes at each doping level

Table 5.8 Summary of Cyclic Voltammetric Peak Potential Data for Boron-Doped Nanocrystalline Diamond Electrode

Film	Oxidation Peak Potential E_p^{ox} (mV)			
	1 mM CAD	1 mM PUT	1 mM SPMD	0.8 mM SPM
0 ppm	no oxidation	no oxidation	no oxidation	no oxidation
1 ppm	874 ± 19	884 ± 12	896 ± 1	895 ± 2
10 ppm	880 ± 25	882 ± 12	889 ±15	896 ± 27
20 ppm	880 ± 4	905 ± 5	906 ± 4	910 ± 2
30 ppm	876	900	902	910

Note: Voltammetric data obtained at a scan rate = 0.1 V/s.
Electrode geometric area = 0.2 cm^2.
Data are averages for two or three electrodes at each doping level

Studies investigating the microcrystalline electrode activity for amine oxidation as a function of boron dopant concentration were performed as well. All the microcrystalline films were deposited from 0.5 % CH_4/H_2 volumetric ratio with 1, 10, and 20 ppm of added B_2H_6. The concentration of boron in the film is proportional to the boron concentration introduced into CVD reactor. Measured resistivities of the films appear to track the boron concentration. They were 0.38, 0.17, and 0.12 Ω-cm, for 1 ppm, 10 ppm, and 20 ppm films, respectively.

High quality microcrystalline films, lightly doped with boron possess a Raman spectrum resembling that observed for high quality HPHT synthetic diamond. The only spectral feature is the first- order diamond phonon line at about 1332 cm^{-1} with a narrow FWHM of about 6 cm^{-1}. Very heavily doped films (>10^{20} B/cm^3) have a more complex

spectrum. The diamond phonon line position is usually downshifted from the expected 1332 cm^{-1} position and possesses a larger FWHM. The increased FWHM is due to the larger number of defects caused by inserted boron dopant atoms.[260] The phonon line shape is asymmetric with an upward shift in intensity on the high wavenumber side of the peak. This asymmetric shape is attributed to a Fano-type interference between the scattering by the zone-center optical phonon and the scattering by an electronic continuum caused by the formation of a B impurity band above 10^{19} B/cm^3 whose energy overlaps that of the phonon.[260] A band around 1200 cm^{-1} is also observed and is attributed to the presence of disordered sp^3 – bonded carbon, due to high concentration of boron atoms in diamond lattice. [260-263] The 1200 cm^{-1} band arises from scattering by phonons outside the center of the Brillouin zone, hence a breakdown of the Raman selection rules associated with the loss of long range periodicity in the lattice. This loss can be related to an amorphous state or very small, discrete crystalline regions of diamond. [260-263]

Figure 5.17 (A-C) shows Raman spectra for three microcrystalline films. The doping levels are in the range of 10^{19} to 10^{20} B/cm^3. For 1 ppm, 10 ppm, and 20 ppm films respectively, the FWHM values are 9.7, 11.6, and 13.5 cm^{-1}. The diamond line intensity also decreases with increasing doping level as the films become more opaque. The first-order diamond phonon line is downshifted about the 2 cm^{-1} from the expected 1332 cm^{-1} position. All the films showed the diamond peak asymmetry and scattering intensity around 1200 cm^{-1}. The intensity of this mode was the highest for film 20 ppm.

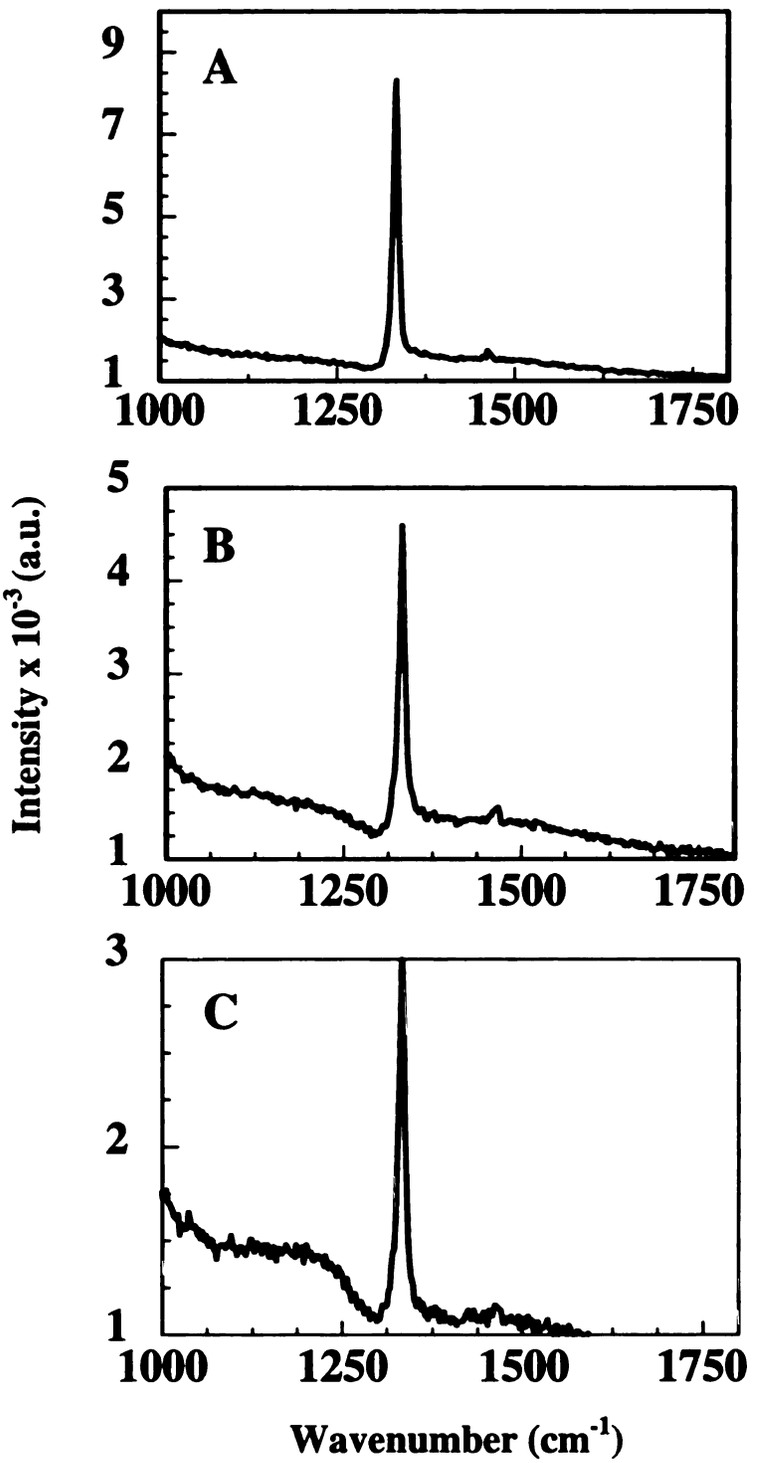

Figure 5.17 A-C Raman spectra for three microcrystalline films, deposited from a 0.5 % CH_4/H_2 volumetric ratio with (A) 1, (B) 10, and (C) 20 ppm B_2H_6 added. The doping level was in the range of 10^{19} to 10^{20} B/cm^3.

Background voltammetric i-E curves, which are extremely useful for evaluating the diamond film quality, were recorded in 1 M KCl.[32] The voltammetric i-E curves were all flat and featureless. The scans were stable with multiple sweeps. The potential windows were 3.1, 3.0, and 3.0 for the 1 ppm, 10 ppm, and 20 ppm films, respectively.

The electrochemical responsiveness of a boron-doped diamond thin film toward four redox systems was first investigated using cyclic voltammetry to verify that all three electrodes exhibit a good electrochemical responsiveness. The redox systems were $Fe(CN)_6^{-3/-4}$, $Ru(NH_3)_6^{+2/+3}$, and $IrCl_6^{-2/-3}$ in 1 M KCl, and $Fe^{+2/+3}$ in 0.1 M $HClO_4$ .The influence of diamond's physical, chemical and electronic properties on the electrode reaction kinetics for each of these systems was discussed in Chapter 3.

Table 5.9 summarizes some of the cyclic voltammetric data for the four redox systems. All films exhibited a good responsiveness for $Fe(CN)_6^{-3/-4}$, $Ru(NH_3)_6^{+2/+3}$, and $IrCl_6^{-2/-3}$ without any kind of pretreatment.

Table 5.9 Summary of Cyclic Voltammetric Data for Boron-Doped Microcrystalline Diamond Electrode

Film ID	$Fe(CN)_6^{-3/-4}$		$Ru(NH_3)_6^{+3/+2}$		$IrCl_6^{-2/-3}$		$Fe^{+2/+3}$	
	ΔE_p (mV)	i_p^{ox} (μA)	ΔE_p (mV)	i_p^{ox} (μA)	ΔE_p (mV)	i_p^{ox} (μA)	ΔE_p (mV)	i_p^{ox} (μA)
A	**73**	62.9	**72**	57.5	**64**	20.7	**852**	33.9
B	**82**	61.5	**68**	61.8	**63**	22.2	**782**	32.6
C	**74**	61.2	**63**	59.9	**64**	21.7	**824**	31.7

Note: Voltammetric data obtained at a scan rate = 0.1 V/s, Electrode geometric area = 0.2 cm^2

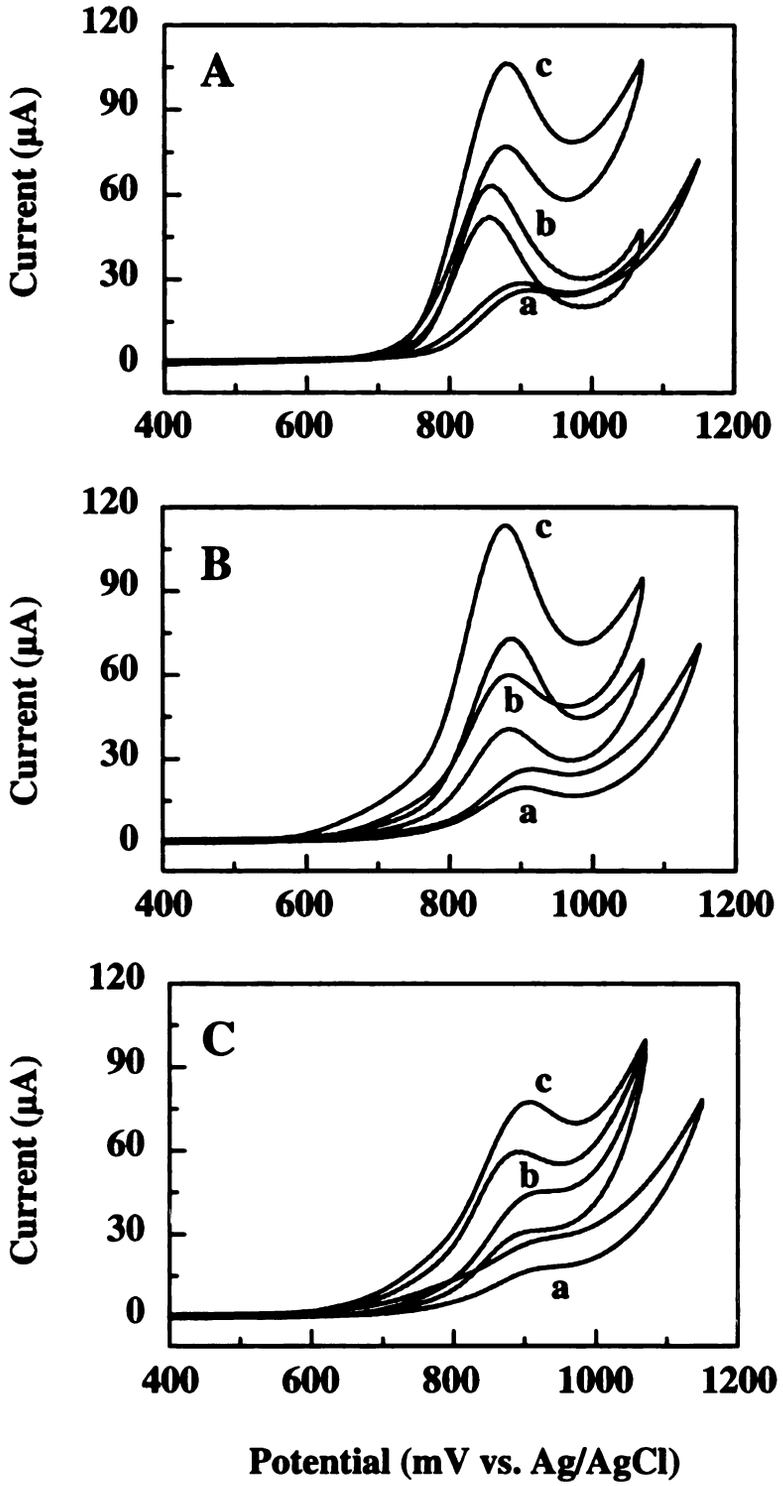

Figure 5.18 Cyclic voltammetric i-E curves for (A) 1.0 mM PUT, (B) 1.0 mM SPMD, and (C) 0.8 mM SPM, in the BBpH10.6 at three microcrystalline diamond films deposited from a 0.5 % CH_4/H_2 volumetric ratio with (A) 1, (B) 10, and (C) 20 ppm B_2H_6 added.

The only redox systems that sluggish kinetics were observed for was $Fe^{+2/+3}$, presumably due to a lack of catalytic surface carbon-oxygen functionalities.[63,66] The oxidation peak current for each electrode varied linearly with the scan rate$^{1/2}$ up to 1000 mV/s (r^2=0.998). The ΔE_p values are between 60-75 mV for $Fe(CN)_6^{-3/-4}$, $Ru(NH_3)_6^{+2/+3}$, and $IrCl_6^{-2/-3}$.

Figure 5.18 shows cyclic voltammetric i-E curves for 1.0 mM (A) CAD, (B) SPMD, and (C) 0.8 mM SPM in the BBpH10.6 electrolyte at the three microcrystalline diamond films with different boron doping levels. A well defined oxidation peak current is seen for all three amines at each electrode. However, the highest oxidation currents are observed for the most heavily doped film (i.e., highest surface concentration of boron sites). The i_p^{ox} and E_p^{ox} values are summarized in Table 5.10.

Table 5.10 Summary of Cyclic Voltammetric Data for Aliphatic Amines at Boron-Doped Microcrystalline Diamond Electrode

Film	1 mM PUT		1 mM CAD		1 mM SPMD		0.08 mM SPM	
	E_p^{ox} (mV)	i_p^{ox} (μA)	E_p^{ox} (mV)	i_p^{ox} (μA)	E_p^{ox} (mV)	i_p^{ox} (μA)	E_p^{ox} (mV)	i_p^{ox} (μA)
A	915	28.3	891	22.1	916	26.3	919	28.8
B	861	63.1	854	58.5	889	73.0	887	59.6
C	896	105.1	872	90.9	879	113.4	907	77.4

Note: Voltammetric data obtained at a scan rate = 0.1 V/s. Electrode area=0.2 cm^2

Several observations can be made from the voltammetric data. First, the oxidation potentials show no clear trend with doping level. One might expect there to be a trend of more positive oxidation potential with doping level as the surface coverage of the polyamine should increase with doping level. Second, the oxidation current for each

amine increases with increasing doping level. This is consistent with the nanocrystalline film data showing a direct correlation between the surface boron content and the oxidation current. Third, the oxidation current for each amine is nearly the same at the lowest doped film, with value of approximately 27μA, but shows some variation for each amine at the higher doping levels.

5.3. Conclusions

The results clearly show that the polyamines can be qualitatively and stably oxidized at both boron-doped microcrystalline and nanocrystalline diamond thin-film electrodes. The oxidation current is highly dependent on the physicochemical properties of the diamond surface, in particular, the sp^2-bonded non-diamond carbon impurity and surface boron concentration. A CH_4/H_2 source gas ratio of 0.4-0.5% produces the optimum structure and leads to the largest peak currents. Both boron-doped microcrystalline and nanocrystalline diamond film provide a quantifiable and stable response.

The oxidation response also depends on the solution pH. In order to be oxidized, the amines need to be unprotonated. This means that the maximum oxidation currents are observed at pHs above the pK_a of the amines. A solution pH of 11 was found to be the optimum. The onset potential for oxygen evolution (OH• formation) shifts toward less positive potentials with increasing pH (~60 mV/pH unit). The E_p^{ox} values for the amines also shift toward less positive potentials with increasing pH. For a given pH, the oxidation response, both E_p^{ox} and i_p^{ox}, were relatively independent of the electrolyte type.

At low amine concentrations and low scan rates, the oxidation peak currents vary linearly with the scan rate $^{1/2}$. Increasing the amine concentration caused E_p^{ox} to shift toward more positive values, similar to the scan rate dependence. This is a

consequence of an increased number of amine molecules available for oxidation, requiring a higher concentration of OH•. This is achieved at more positive potentials. Plots of i_p^{ox} vs concentration were linear up to a 1.0 mM concentration. The plot had non-zero intercept and different slopes (i.e. sensitivities) for the different amines.

Evidence was presented for the importance of (i) sp^2-bonded non-diamond carbon impurity and (ii) surface boron sites in the amine oxidation reaction mechanism. The amine oxidation current shows a dependence on the CH_4/H_2 ratio with a maximum signal seen for films deposited from a 0.5 % CH_4/H_2. If a film is rehydrogenated to remove all the sp^2-bonded non-diamond carbon impurity, then a total attenuation of the amine response, prior to oxygen evolution, is observed.

The film deposited from the 0.5% CH_4/H_2 ratio exhibited the largest and most well-defined waves. The reproducibility of the response was also best for the 0.5% film. It is important to point out again that the prerequisite for the anodic oxygen transfer reaction (OTR) is the anodic discharge of H_2O to produce adsorbed OH• as shown in Eq.1.

$$H_2O \rightarrow S[\bullet OH_{ads}] + H^+ + e^- \quad (1)$$

Evolution of O_2 can diminish the current efficiency for OTR, by consumption of adsorbed OH•, as shown in Eq.2.

$$S[\bullet OH] + H_2O \rightarrow S[\ ] + O_2 + 3H^+ + 3e^- \quad (2)$$

There is a competition between the O_2 evolution (OER) and OTR for the adsorbed OH• and any increase in the rate of OER will result in decrease in the rate of OTR. However, the proper fraction of sp^2-bonded non-diamond impurity exposed at the surface catalyzing discharge of water at lower overpotential is extremely important for achieving the optimum electrode response for amine oxidation. Such a structure is achieved with

films deposited from a 0.4-0.5% CH_4/H_2 source gas ratio. Figure 5.19 shows a simplified model of the competition between the OER and amine oxidation via OTR.

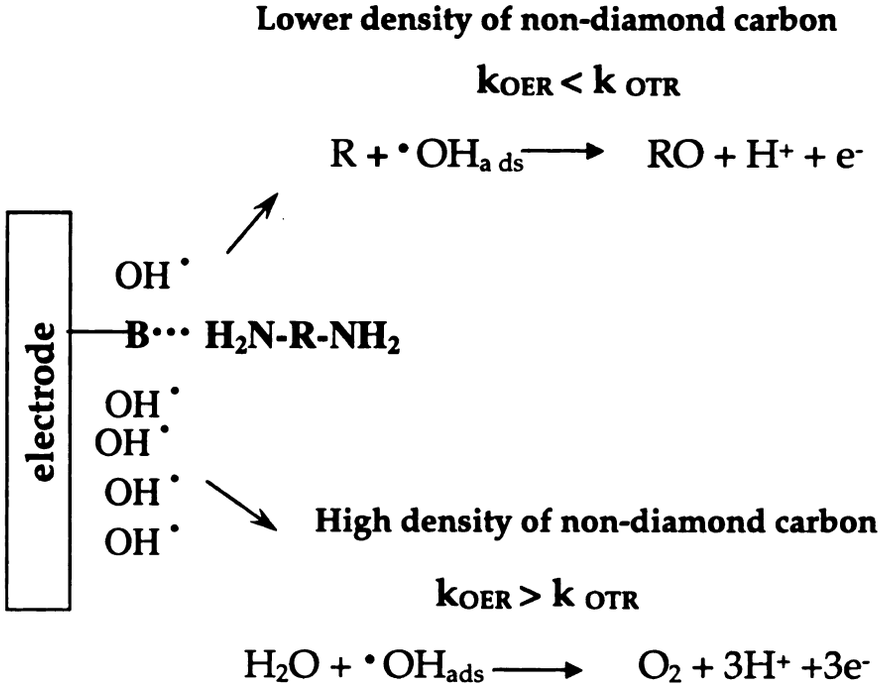

Figure 5.19 Model of the competition between the O_2 evolution (OER) and O-transfer reaction (OTR).

We presented compelling evidence regarding the importance of surface boron sites in the reaction model. At nanocrystalline conductive diamond film deposited without boron, signal for amine oxidation was attenuated. The absence of a well defined oxidation response for cadaverine was not due to poor film electrical conductivity since the high fraction of grain boundary, containing π-bonded atoms, gives film sufficient electrical conductivity, even in the absence of intentional boron-doping.

A set of boron-doped nanocrystalline and microcrystalline boron-doped diamond deposited with different dopant level was probed. All microcrystalline films exhibited a good responsiveness and fast kinetics for $Fe(CN)_6^{-3/-4}$, $Ru(NH_3)_6^{+2/+3}$, and $IrCl_6^{-2/-3}$. The ΔE_ps of the redox probes studied were independent on doping level. Even the film

deposited with the lowest doping level (1 ppm B_2H_6) had high carrier concentration, adequate to support fast electron transfer.

Very fast kinetics for redox systems were observed at nanocrystalline boron-doped diamond electrode, regardless the doping level.

A well-defined voltammetric waves for amine oxidation were observed for both types of films. For both, microcrystalline and nanocrystalline diamond films the anodic signal increased with the increasing dopant level. The differences in anodic oxidation response for amines were not due to poor films electrical conductivity, as it was shown that all the films possessed high density of carriers to support rapid electron transfer for other tested redox systems. This is direct evidence of a surface boron on the oxidation reaction mechanism. Increasing doping level leads to a higher number of surface boron sites available for the reaction.

Polycrystalline boron-doped diamond thin film electrodes possessed the requisite surface structure and chemical composition to support and sustain the oxidation of aliphatic amines. Because of the synthetic nature of the film deposition, the appropriate structure and composition can be fabricated into a film.

A model is proposed whereby the non-diamond carbon impurity sites, presumably located in the grain boundaries or crystal defects, generate reactive OH• at lower overpotential, than the surrounding diamond matrix. The radicals then attack the polyamine molecules adsorbed/coordinated at surface boron sites near the grain boundaries.

Chapter 6

INVESTIGATIONS OF ALIPHATIC POLYAMINE OXIDATION REACTION MECHANISM AT BORON-DOPED DIAMOND THIN-FILM ELECTRODES

6.1. Introduction

Recently a number of reviews have been written about the chemical and electrochemical oxidation of amines.[265, 266-268] The mechanism and kinetics of the two types of oxidations have been reported on and, in some cases, studies have shown that the mechanisms are similar for the two routes.[269] Evidence for a two-electron transfer reaction has been reported for amine oxidation by H_2O_2, peroxy acids, and ozone.[269 and references therein] Hydroxylamine was found to be the primary product for these oxidants. Other oxidation reactions, such as the reaction of an aliphatic tertiary amine with chlorine dioxide, produced a secondary amine and an aldehyde.[270] It was proposed that the reaction involved abstraction of an electron from the amine in the rate-determining step, followed by rapid loss of a proton and a second electron. The same reaction mechanism was also reported for the oxidation of amines with dibenzoyl peroxide,[271] manganese

dioxide,[272] potassium permanganate,[273] and N-bromosuccinimide.[274] Ag (II), Ni (III), Co (III), and Cu (II) oxides are all known oxidants,[275,276] with Ag (II) oxide being particularly efficient for amine oxidation.[277,278] Heterogeneous reactions with transition-metal oxides are often considered to occur via adsorption of the organic compound on the surface of the oxide, followed by a chemical reaction, commonly hydrogen abstraction.

The interest in amine electrooxidation dates back to the mid 1800s, when aniline oxidation was first studied.[266 and references therein] Recently, the mechanistic aspects of aromatic and aliphatic amine electrooxidation have received considerable attention.[232,265,279,280 and references therein] It was found that the electrooxidation of aromatic amines depends on several factors:[266] (i) the presence of hydrogen at the α-carbon, (ii) the presence of hydrogen on the nitrogen atom, and (iii) the presence and type of substituent groups on the aromatic ring. The oxidation of aromatic aliphatic amines is generally easier than aliphatic ones, due to the strong electron donating aromatic ring.[265,266] This is evidenced electrochemically by more positive aliphatic amine oxidation potentials.

The electrooxidation reaction strongly depends on anode material.[281,282] A survey performed by Cañizares et al. [281] shows that the type of electrode material used has a great influence on the oxidation reaction mechanism. Two types of anode behavior have been identified. The first type is called *active behavior* in which the electrode surface undergoes chemical and structural changes (i.e., oxidation) that promote the amine oxidation. The second type is called *non-active behavior* in which the electrode surface undergoes no change and simply acts as a sink for electrons. Pt, IrO_2, and stainless steel electrodes are examples of the active type. These electrodes are not fully oxidized and, consequently, are transformed into higher oxides. Fully oxidized metal oxides, such as PbO_2, SnO_2, or boron-doped diamond are examples of the non-active

type. A similar classification of anode materials for the electrooxidation of amines was proposed by Chow et. al.[265] The authors assigned Ag, Cu, Co, Ni, Fe, and Au to the *active type*, and PbO_2 and glassy carbon to the *non-active type*. Interestingly, Pt electrode was classified by them as an inert material for amine oxidation.

In general, the electrochemical oxidation of amines is considered to involve the removal of an electron from the N atom.[265] The formation of a cation radical via a one electron transfer reaction is the first step of oxidation process for both types of electrodes.[265] In simple cases, at inert electrodes, oxidative dealkylation processes dominate because the amine radical cation deprotonates at the α-carbon, and the α-amino radical formed is oxidized to the immonium salt. The immonium salt then hydrolyzes to the dealkylated amine and a carbonyl compound.

The detection of amine oxidation intermediates has received considerable study. In only a few cases, however, has the initially formed cation radical been sufficiently long-lived to allow its detection.[265 and references therein.] For example, the radical cations of conjugated amines are sufficiently stable to be detected. In those cases, the esr data has contributed to an understanding of the electronic structure and spin distribution in non-aromatic aminium radicals, and the electrochemistry yielded information on the ease of formation and stability of these intermediates. To evaluate the ease of formation of aminium radical in solution, the E^o value for amine $\leftrightarrow$ amine$^{+\bullet}$ + e$^-$ couple is required. Voltammetry is often used to obtain E^o values experimentally. For the reversible process, E^o for the system is equal to $E_{1/2}$. If the electron transfer is irreversible, the oxidation potential is shifted anodically from the "reversible" position of the E^o, and the value of the shift depends on the heterogeneous rate constant for the electron transfer. A reliable E^o value may be obtained only when the cation radical is sufficiently long lived for a reversible reaction to occur amine$^{+\bullet}$ + e$^-$ $\leftrightarrow$ amine and oxidation/reduction are

observed. Usually, however, the cation radical for simple aliphatic amines is so reactive that only an oxidation wave is observed in voltammetry. In spite of these limitations, it was suggested [265] that for irreversible oxidation of amine to cation radical shift of E_p^{ox} from E^o would be similar for all aliphatic amines, so that the differences in E_p^{ox} for different amines would reflect differences in E^o, and the same provide information on ease of formation of cation radical. From these studies it was found that in general, primary amines oxidize much slower than secondary or tertiary amines. The order of reactivity among aliphatic amines is: tertiary>secondary>primary.[265] This is as to be expected for electron transfer from nitrogen atom, since the alkyl groups are electron-donating substituents.

A short review on inert and active anode materials and mechanistic aspects of amine oxidation on those electrodes is presented below.

6.1.1. Non-Active Electrodes

Mann and coworkers investigated the electrochemical oxidation of primary and tertiary amines at Pt in alkaline medium.[269,280,283,284] The rate limiting step was concluded to be loss of the first electron from the N atom, followed by rapid loss of proton from the α-carbon to form radical (II), as shown in Eqs. 1 and 2.

In the next step, the radical (II) may either lose a second electron to form the iminium ion (III) or may undergo disproportionation to form the enamine. It has not been determined which of these intermediates is actually formed. The aldehyde and dealkylated amine were found, however, as the final products.

$$R_2\ddot{N}CH_2R' \rightleftharpoons R_2\dot{N}^{+}CH_2R' + e^- \quad (1)$$
(I)

$$R_2\dot{N}^{+}CH_2R' \xrightarrow{fast} R_2N\dot{-}CHR' + H^+ \quad (2)$$
(II)

$$R_2N\dot{-}CHR' \xrightarrow{fast} R_2N^{+}=CHR' + e^- \quad (3)$$
(III)

$$R_2N^{+}=CHR' \xrightarrow[fast]{+H_2O} R_2\text{-}NH + R'CHO + H^+ \quad (4)$$

Anodic oxidation of amines has been studied by Masui et. al. [232] at glassy carbon (GC). The first step in the anodic oxidation of aliphatic tertiary amines at GC electrode in aqueous solution was considered to be the abstraction of an electron from the lone-pair on the nitrogen. The increasing difficulty of oxidation of amines with increasing electron-withdrawing power of the substituents was observed. It was stated that overall reaction involved transfer of 2 electrons and a proton. The transfer of the first electron was suggested as limiting step, similarly to studies by Mann et. al. at Pt electrode.[280] It was proposed that the intermediate aminium cation radical is converted into a quaternary Schiff base, which rapidly hydrolyzes to the amine (ammonia) and the aldehyde. The secondary amine and aldehyde were shown to be produced by anodic oxidation of a tertiary amine. The electrode reaction for amine was deduced to be as in Eq. 5:

$$R_2\ddot{N}CH_2R' \xrightarrow[slow]{-e^-} \{R_2\dot{N}^{+}CH_2R' \xrightarrow[fast]{-H^+} R_2N\dot{-}CHR' \xrightarrow[fast]{-e^-} R_2N^{+}=CHR'\} \quad (5)$$

$$R_2N^{+}=CHR' \xrightarrow[fast]{+H_2O} R_2\text{-}NH + R'CHO$$

6.1.2. Active Electrodes

Oxidation of primary and secondary amine compounds on Ag electrodes in alkaline medium has been studied by Hampson et al.[233-235] The authors reported that the initial step in the reaction sequence corresponds to oxidation of amine to the corresponding imine, as indicated by Eq.6. The imine can undergo hydrolysis to form acetaldehyde and ammonia, as indicated by Eq.7, or it can undergo further oxidation to form acetonitrile as indicated by Eq.8. The ratio of aldehyde to nitrile was determined to be dependent on potential, hydroxide ion concentration and amine concentration.

$$(CH_3CH_2NH_2)_{ads} \rightarrow CH_3CH{=}NH + 2H^+ + 2e^- \quad (6)$$

$$CH_3\text{-}CH{=}NH + H_2O \rightarrow CH_3\text{-}CHO + NH_3 \quad (7)$$

$$CH_3\text{-}CH{=}NH \rightarrow CH_3CN + 2H^+ + 2e^- \quad (8)$$

In general, electrochemical studies have shown that primary amines are readily oxidized by AgO in aqueous electrolytes. The oxidation mechanism of secondary amines at AgO was found to be different from that of primary amine. Mechanism according to Hampson et al. is proposed in Eq. 9-13.[234]

Detected products (II) and (III) of the oxidation were explained by oxidative fission of (I). The product (III) was further responsible for the appearance of alcohols (IV) and olefins (V). It was proposed that Schiff base may also be oxidized at silver electrode to produce aldehydes (VII) and nitriles (VIII). The products of oxidation were the same as products of hydrolyzed Schiff base. It was also proposed that Schiff base $RCH_2N{=}CHR$ produced from secondary amine (quasi (VI)) can be oxidized to primary amine (RCH_2NH_2) and aldehyde (RCHO) and the product primary amine can be further oxidized to RCN or RCHO.

$$RCH_2CH_2NHCH_2R \xrightarrow{-e^-} \underset{(I)}{RCH_2CH_2\overset{\bullet+}{N}HCH_2R} \quad (9)$$

$$RCH_2CH_2\overset{\bullet+}{N}HCH_2R \xrightarrow{-e^-} \underset{(II)}{R\text{-}CH_2\text{-}\overset{\bullet\bullet+}{N}H} + \underset{(III)}{RCH_2\overset{+}{C}H_2} \quad (10)$$

$$\underset{(III)}{RCH_2\overset{+}{C}H_2} + OH^- \longrightarrow \underset{(IV)}{RCH_2CH_2OH} + \underset{(V)}{RCH_2{=}CH_2} \quad (11)$$

$$\underset{(II)}{R\text{-}CH_2\text{-}\overset{\bullet\bullet+}{N}H} \xrightarrow{-H^+} \underset{(VI)}{RCH{=}NH} + OH^- \longrightarrow \underset{(VII)}{RCHO} \quad (12)$$

$$\underset{(II)}{R\text{-}CH_2\text{-}\overset{\bullet\bullet+}{N}H} \xrightarrow{-H^+} \underset{(VI)}{RCH{=}NH} \xrightarrow[-2H^+]{-2e^-} \underset{(VIII)}{RC{\equiv}N} \quad (13)$$

The kinetics and mechanism of the oxidation of amines were studied at oxide-covered Ni, Cu, Co electrodes by Fleischmann et. al.[35] The oxidation potentials for the primary and secondary amines were the same and oxidation occurred at potentials where the oxide transition takes place (i.e., Ni(II)→Ni(III), Co(II) →Co(III)). It was stated that the electrode reaction takes place by a mechanism involving a rate determining chemical reaction between higher oxide and amine intermediate. The nature of the chemical step was investigated, and it was concluded that the rate-determining step is hydrogen abstraction from α-carbon. The authors indicated that adsorption of the amine is required before the chemical reaction can occur. They based their conclusion on the fact that tertiary amines did not oxidized at metals oxides. The rate of oxidation of secondary amine oxidation was much slower than the rate of oxidation of primary amines.

Recently the anodic oxidation of aliphatic amines has been reported at two relatively new electrode materials: nickel-based chemically modified glassy carbon electrode (active) [34] and an anodized eutectic-phase Ag-PbO_2 (inert).[54,55,57,285]

At a nickel-based chemically modified glassy carbon electrode (Ni-CME) the electrocatalytic function of the electrode was attributed to the formation of β-NiOOH.[34] Electrode exhibited activity toward mono- and polyamine oxidation and the mechanism was proposed involving adsorption of amine at Ni and a concerted oxidation of the intermediates on the catalytic sites (i.e. β-NiOOH). The radical hydrogen abstraction from the organic compound was considered rate determining step, however, it was pointed out that adsorption played an important role on the overall kinetic mechanism. It was concluded that the oxidation of amino compounds on Ni-CME is under a mixed control of both adsorption and chemical process leading to cleavage of N-H and C-H bonds in α-position. It was stated that the energy released in the formation of adsorption bonds between analytes and catalytic sites partially compensates the activation energy barrier associated with the abstraction of hydrogen atoms and bond cleavage.

The primary, secondary, and tertiary aliphatic amines were oxidized at the anodized eutectic-phase Ag-PbO_2 in alkaline media.[54,55,57,285] Acetaldehyde and ammonia were detected as the product of the electrolysis of ethylamine. The overall reaction is presented as in Eq. 14

$$CH_3\text{-}CH_2\text{-}NH_2 + 2OH^- \rightarrow CH_3\text{-}CHO + NH_3 + H_2O + 2e^- \qquad (14)$$

The reaction mechanism was suggested to be electrocatalytic in nature. The authors proposed that hydroxyl radicals can be adsorbed at specific surface sites, and transferred to the reactants via an electrocatalytic oxygen transfer reaction mechanism.

Oxygen transfer reactions can be catalyzed by increasing the surface concentration of adsorption sites, thereby, increasing the concentration of adsorbed OH radicals. It was proposed that there is an optimal low density of surface sites for which the desired O-transfer process can occur at near mass transport – limited rates without high background signal for O_2 evolution.

At Ag-PbO_2 electrode, silver as doping agent serves the function of H_2O discharge and capability of adsorbing the •OH species, and adsorbing the amine molecules via the non-bonded electron pair of the nitrogen atom. The authors presented following mechanistic sequence, describing oxygen transfer at Ag-PbO_2 electrode: (i) anodic discharge of water to produce an adsorbed (•OH), (ii) adsorption of the amine, (iii) cleavage of the carbon-nitrogen bond with transfer of oxygen to the carbon radical.

In present chapter the mechanism of amine oxidation was investigated in details by use of different electrochemical measurements. First, the number of electrons transferred in the limiting step was determined from the measurements of Tafel slopes, and the ratio between number of protons and electrons taking part in the oxidation process was evaluated from the pH dependence of the $E_{p/2}$ of amine oxidation peak. Then the adsorption behavior of amines was studied by evaluating how amine concentration and the temperature influence the amine oxidation current. Finally, results of a rotating disc electrode studies were used to determine the heterogeneous electron transfer rate constant and total number of electrons per amine group characteristic for amine oxidation reaction.

6.2. Results and Discussion

6.2.1. Irreversibility of the Process

Voltammetric investigations of aliphatic amine oxidation at diamond reveal that the overall reaction is irreversible with a single anodic peak observed ~100mV prior to oxygen evolution. The overall irreversibility of the amine oxidation process may be caused by (i) *an irreversible electron transfer step,* (Eq. 15)

$$A \xrightarrow{-e^-} B \qquad (15)$$

or (ii) *an irreversible electron transfer step followed by a chemical reaction,* (Eq.16)

$$A \xrightarrow{-e^-} B \longrightarrow C \qquad (16)$$

Other possible reaction scheme can involve (iii) *a reversible electron transfer followed by a fast irreversible chemical step* or (iv) *a reversible electrochemical step, followed by a fast reversible chemical step.*

Literature data indicate that electron transfer involved in amine oxidation is irreversible. Cation radicals found from saturated aliphatic amines, are usually short-lived,[265] and the equilibrium of the consecutive step is shifted very far toward the chemical step and product formation. Hence, the mechanism (iii) and (iv) with a reversible electron transfer for amine oxidation can be rule out.

We have shown that amine did not oxidize at hydrogenated boron-doped diamond electrodes,[259] at which simple electron transfer reactions occur (i.e., $Fe(CN)_6^{-3/-4}$, $Ru(NH_3)_6^{+2/+3}$,[163] azides[286]). Yet, at "as deposited" diamond film we observed amine oxidation reaction. Those results strongly suggest that mechanism of amine oxidation does not involve only electron transfer. This suggests the type of mechanism, where electron transfer is followed by chemical process (EC) as it is shown in Eq.16. The nature of the chemical step then, needs to be considered.

Recent studies of the electrooxidation of organic compounds suggest that the oxidation of the amine is assumed to be mediated and performed by hydroxyl radicals.[54,55,230,242,244,281,287-289] A model for the amine oxidation strongly suggests involvement of those species and their function in chemical part of the mechanism (i.e., oxygen transfer). Hydroxyl radical generation at lower potentials, occurs primarly at sp^2-bonded non-diamond carbon. If sp^2-bonded non-diamond carbon is removed (i.e., hydrogenation of the diamond electrode), then the OH• generation occurs at higher overpotential at diamond surface. Amine upon adsorption at electrode surface assumes the same charge as the electrode and as result it may as well rapidly desorb from the electrode surface. This may very likely occur when the following, chemical reaction is very slow. This effect was observed for high quality diamond films where amount of sp^2-bonded non-diamond carbon is low . In extreme case, for hydrogenated boron-doped diamond electrodes,[259] the chemical reaction was shut by lack of hydroxyl radicals. These observations suggest that amine oxidation can be indeed classified as EC mechanism, with involvement of hydroxyl radical in chemical step. Fast reaction rates are observed only for diamond electrodes, at which the discharge of water had appreciable rate.

6.2.2. Reaction of the Primary and Secondary Amine Groups

In Chapter 5, it was shown that oxidation potentials (E_p^{ox}) are similar for all tested amines, regardless of their molecular structure, indicating similar oxidation kinetics. Figure 6.1A shows typical cyclic voltammetric i-E curves for 1.0 mM PUT (dashed line) and 0.8 mM SPM (solid line), in borax buffer, pH 11, at a boron-doped nanocrystalline film. Similarly shaped voltammograms are observed for PUT and SPM. However, close inspection of the voltammograms reveals a difference in the shapes of

the curves at low potentials (700-750 mV vs Ag/AgCl). In this potential range, the current for SPM is larger than that for PUT. The voltammogram for PUT was subtracted from that for SPM, and the resulting difference voltammogram is presented in 6.1B. There are two peaks observed at 740 and 870 mV. The difference between these two polyamines is the presence of the two secondary amine groups in SPM. It is expected that the secondary amines will oxidize at lower potential compared to primary amines. To test this supposition the voltammograms were obtained in phosphate buffer pH 7.2. At this pH, all primary amine functional groups are protonated and this reduces the oxidation current response due to the fact that adsorption is inhibited.

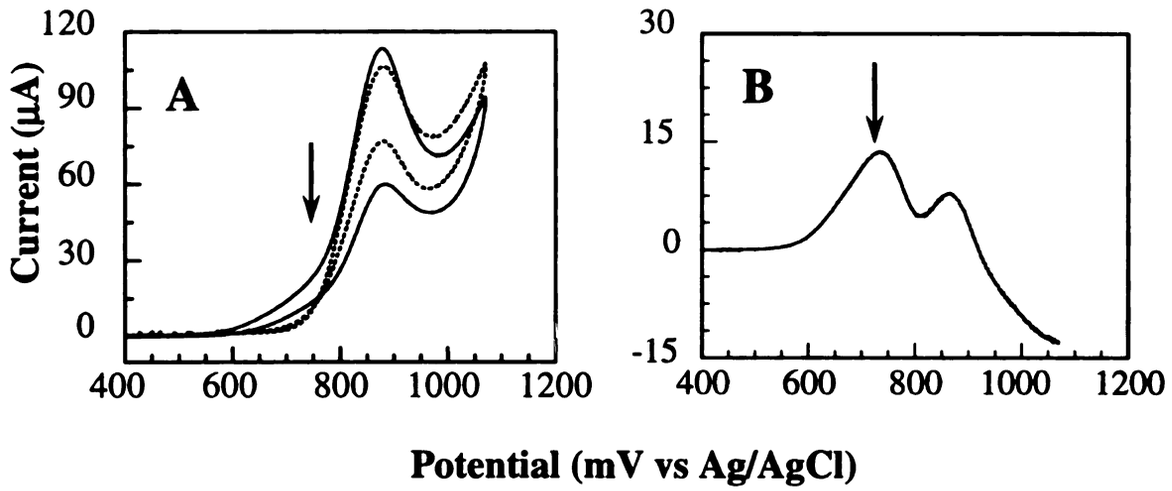

Figure 6.1 (A) Cyclic voltammetric i-E curves for 1.0 mM PUT (dashed line) and 0.8 mM SPM (solid line) in borax buffer pH 11 at a boron-doped nanocrystalline film. Scan rate=0.1 V/s. Electrode area = 0.2 cm^2. (B) Subtracted SPM-PUT voltammogram.

Figure 6.2 shows cyclic voltammetric i-E curves for (A)1.0 mM PUT, (B) 1.0 mM EDA and (C) 1.0 mM SPM in phosphate buffer, pH 7.2, at a boron-doped nanocrystalline film. There is no net oxidation current electrode response for the PUT at pH 7.2. There was also no net oxidation current for DAP at this pH. This can be explained by the fact

that the lowest dissociation constant value for PUT is 9.3 and DAP is 8.5.[189] At the same pH for EDA, however, there is a net oxidation current observed at 1200 mV (p2) with a current of 16 μA (S/B=4). The lowest pK_a for EDA is 6.9 which explains observed oxidation current.[189]

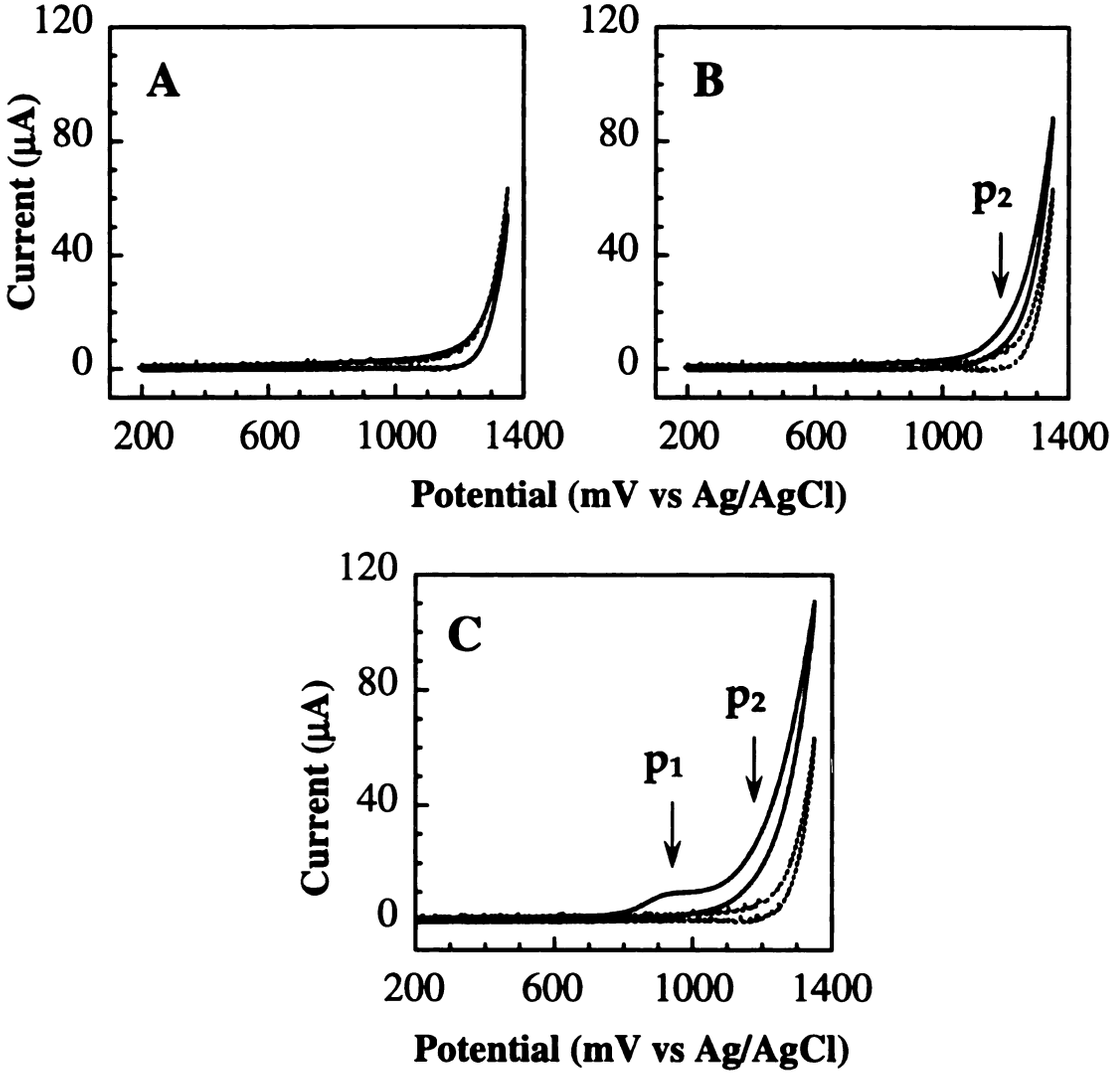

Figure 6.2 Cyclic voltammetric i-E curves, background (dashed line) and total current (solid line) for (A) 1.0 mM PUT, (B) 1.0 mM EDA, and (C) 1 mM SPM in phosphate buffer, pH 7.2 at a boron-doped nanocrystalline film. Scan rate = 0.1 V/s. Electrode area = 0.2 cm^2.

In contrast, the voltammogram for SPM shows an oxidation peak **p1** at a much lower potential (940 mV) with the current of 11 μA (S/B=5). This oxidation peak is followed by an increased oxidation current at 1200 mV, (**p2**). This is the same potential at which oxidation of the primary amine group of EDA is observed. The peak p1 is observed at much lower potential than the p2 wave for EDA. The lowest pKa value for SPM is 7.9[189] and corresponds to one of the two secondary amine groups. At this pH only this secondary amino group is in partially deprotonated form, and thus available for oxidation. This result indicates that oxidation of secondary amine occurs at lower potential.

Interestingly, at the 1200 mV (p2), significant current for oxidation of SPM is also observed. It is twice as large as current for EDA at this potential. This is interesting since the electrooxidation of the secondary amine groups of SPM would lead to formation of a primary amine with the structure resembling that of PUT or DAP. Both PUT and DAP do not oxidize at pH 7.2 due to protonation of the amino group, what makes them unlikely to be adsorbed and oxidized. So why would the primary amino groups, resulted from secondary amine oxidation, undergo oxidation? This observation can be explained by the mechanism in which produced primary amine does not desorb rapidly from the boron surface site on the time scale of experiment, and it is available oxidation.

These results suggest that the oxidation potentials for primary and secondary amine vary slightly at diamond. Secondary amine groups oxidize at less positive potentials than primary amine groups, although the rate of the oxidation is much lower than that for the primary amines. This is because at lower potentials, where the p1 for SPM is observed, the rate of hydroxyl radical generation is low. At higher potentials, OH• generation is much faster. SPM molecule may be coordinated at ~940 mV, at the surface, however, the overall process is limited by concentration of •OH present. Since

amine oxidation is performed by hydroxyl radicals, the step of their generation is the limiting one. The fact that secondary amine oxidize at diamond at lower potential suggests that the mechanism with rate determining electron-transfer step (i.e., amine adsorption onto electrode) is rather unlikely.

6.2.3. Determination of the Ratio Between Number of Protons and Number of Electrons.

In order to determine whether the amine oxidation reaction involves transfer of protons, the effect of pH on the voltammetric response was tested. For a reaction:

$$\mathbf{Red \rightarrow Ox + mH^{+} + ne} \qquad (17)$$

the Nernst equation is presented as follows:

$$E_p^{ox} = E^o + \frac{0.059}{n} \log \frac{[ox][H^+]^m}{[red]} \qquad (18)$$

where R is the molar gas constant (8.314 J/mol-K), T is the temperature [K], F is the Faraday constant (96,485 C/eq), n is number of electrons, and m is number of protons. At room temperature (298 K) and knowing that pH=-log[H^+] this equation can be rewritten as:

$$E_p^{ox} = E^o - \frac{m\ 0.059}{n}[pH] \qquad (19)$$

Equation 19 indicates a linear relationship between E_p^{ox} and pH with a slope of to -0.059 m/n. Such a plot is commonly used to determine the ratio of protons and electrons involved in the electrochemical reaction.[290] For instance, for a slope

of -59 mV/pH unit, m/n=1, indicating an equal number of protons and electrons involved in the reaction, whereas the slope of -118 mV/pH unit (m/n=2) indicates twice as many protons as electrons.

Voltammetric investigations revealed that the E_p^{ox} and $E_{p/2}$ values for all the polyamines shifted negatively with increasing pH. This trend indicates that, indeed, electron transfer is accompanied by proton transfer. Plots of $E_{p/2}$ vs pH revealed slopes of ca. -60 mV/pH unit. This indicates an even number of protons and electrons are transferred during the oxidation reaction. Table 6.1 summarizes the results obtained at different electrodes.

Table 6.1 Aliphatic $E_{p/2}$ values as a Function of Solution pH

amine	$\partial E_{p/2}/\partial pH$ slope		
	0.3% CH_4/H_2	0.5% CH_4/H_2	1.0% CH_4/H_2
cadaverine	-68.4	-56.7	-52.8
spermidine	-63.9	-64.7	-59.2
putrescine	-75.4	---	-51.7
spermine	-54.8	---	-48.7

6.2.4. Quantification of Adsorption

Our oxidation model indicates that amine adsorption occurs at surface boron sites as an initial step in the oxidation reaction.[259,291] Data presented in Chapter 5 demonstrated the importance of surface boron, as without it, even for electrically conducting films, a quantifiable amine oxidation signal is not observed. The simplest type of adsorption - the Langmuir-type[292,293] can be characterized by the relationship between peak current (i_p) and concentration (C) is given

$$i_p = \frac{C}{b + aC} \quad (20)$$

$$\frac{1}{i_p} = a + \frac{b}{C} \quad (21)$$

where a and b are specific constants of the amine oxidation. They are determined experimentally by linear regression of a plot of 1/i vs 1/C. a and b are concluded to correspond to fundamental chemical and electrochemical constants according to equations 22 and 23.[292]

$$a = 1/nFAk\Gamma_{max} \quad (22) \quad \text{and} \quad b = 1/nFAkK\Gamma_{max} \quad (23)$$

where K is the equilibrium constant for adsorption, k is the heterogeneous rate constant (s^{-1}) for the faradaic reaction, Γ_{max} is the maximum surface coverage (mol/cm^2) of adsorbed analyte at high solution concentration, and n, F, and A have their usual electrochemical meanings. Equation 20 has the form of the Langmuir isotherm and applies in cases of relatively low surface coverage where lateral interactions between the adsorbed molecules are negligible and the adsorption sites are fully equivalent.

Figure 6.3A shows current-concentration profiles for CAD at a boron-doped microcrystalline diamond film deposited with (a) 1 ppm and (b) 10 ppm B_2H_6. The current for both films rises with concentration at low values before reaching a plateau. The limiting current is higher for the more heavily doped film. This is consistent with a higher surface boron site density. The plateau is reached at 0.5 mM for the 1ppm film and 1.0 mM for the 10 ppm B_2H_6 film.

Figure 6.3 B presents reciprocal plots of the peak current vs concentration for CAD at the same diamond electrodes grown with (a) 1 ppm and (b) 10 ppm B_2H_6.The plots are linear over a wide concentration range (0.2 mM to 3.7 mM) with correlation

coefficients greater than 0.996. The linear relationship indicates that the amine adsorption at boron sites follows Langmuir-like type behavior. Since there is only a limited number of surface boron sites, a low surface coverage is expected with one amine molecule interacting with one surface boron sites.

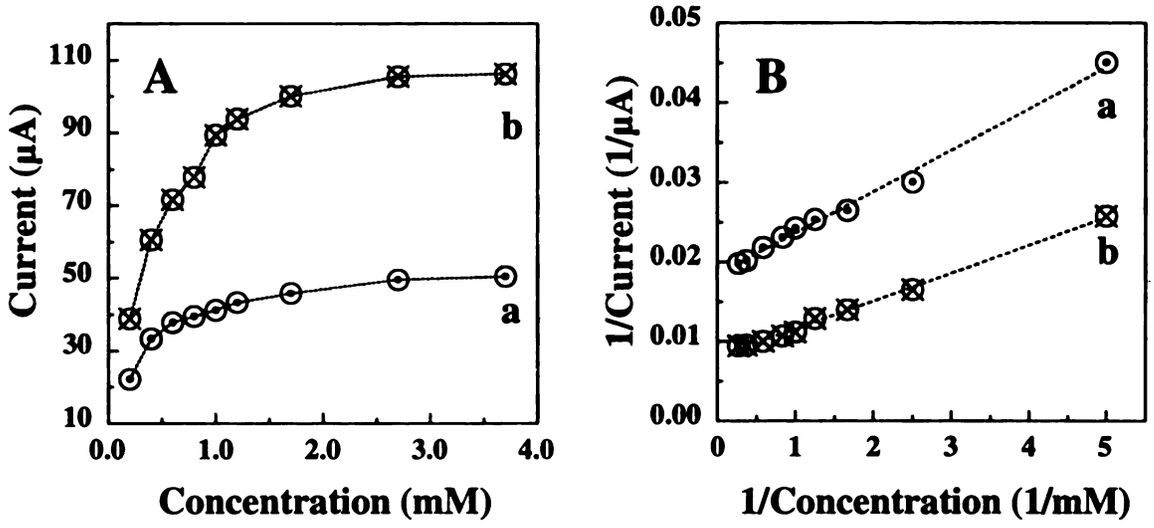

Figure 6.3 (A) Peak current vs concentration profiles for 1 mM cadaverine at boron-doped microcrystalline diamond electrodes deposited in a 0.5 % CH_4/H_2 ratio with (a) 1 ppm B_2H_6, and (b) 10 ppm B_2H_6. (B) Reciprocal plots of peak current versus cadaverine concentration at (a) 1 ppm B_2H_6, (b) 10 ppm B_2H_6 diamond electrode.

6.2.5. Rotating Disk Voltammetric Studies

The use of rotating disk voltammetry for the study of electrode kinetics and reaction mechanisms is well known.[294 and references therein] The technique is useful because the rate of mass transport of reactants to electrode surface is controlled by fixing the rotational velocity of the electrode. The number of electrons (n, eq/mol) transferred per reactant molecule can be estimated from the slope of plots of the reciprocal current (1/i) versus the reciprocal square root of rotational velocity ($1/\omega^{1/2}$).

This is known as a Koutecký-Levich plot derived for a one step electron transfer mechanism, according to Eq. 25.[294]

$$\frac{1}{i} = \frac{1}{i_k} + \frac{1}{i_l} = \frac{1}{n_{app}FAk_{app}C_o} + \frac{1}{0.62n_{app}FAD_o^{2/3}\omega^{1/2}\upsilon^{1/6}C_o} \quad (24)$$

$$\text{or} \quad \frac{1}{i_l} = a + \frac{b}{\omega^{1/2}} \quad (25)$$

where i_K represents the kinetically-controlled current in the absence of mass transfer, $n_{app.}$ is apparent number of electrons transferred, $k_{app.}$ is the apparent heterogeneous rate constant (cm/s), F is Faraday constant, A is geometric electrode area (cm^2), D_o is diffusion coefficient (cm^2/s), ω is rotational velocity (rad/s), υ is kinematic viscosity (7-10x10^{-3} cm^2/s for aqueous solutions), and C_o is the bulk concentration of the redox species (mol/cm^3). The apparent number of electrons transferred during the redox reaction ($n_{app.}$ [eq./mol]) and the apparent heterogeneous rate constant ($k_{app.}$) can be estimated from the slope and intercept, respectively, of the plot.

The diamond disk electrodes were characterized using $Fe(CN)_6^{-3/-4}$ and $Ru(NH_3)_6^{+3/+2}$ to verify that the limiting currents were observed and that the limiting current varied with the rotation rate according to theory. Results for rotating rates ranging from 52.2 to 314.2 rad/s, at scan rate of 0.1 V/s, are presented in Figures 6.4 and 6.5, respectively. For both couples, steady state i-E voltammetric curves are observed for each rotation rate. Plots of 1/I vs $1/\omega^{1/2}$ were linear (r^2=0.999) with slopes of 0.065 and 0.072 for $Fe(CN)_6^{-3/-4}$ and $Ru(NH_3)_6^{+3/+2}$, respectively. The diffusion coefficients (D) for each analyte were determined from the slopes, according to Eq.24, where n=1 and electrode area=0.2 cm^2. The calculated values were 7.3 (±0.3) x10^{-6}

cm^2/sec and 6.8 (±0.4) x10^{-6} cm^2/sec for $Fe(CN)_6^{-3/-4}$ and $Ru(NH_3)_6^{+3/+2}$, respectively. These values correspond well to the reported values of 7.6 x 10^{-6} cm^2/s for $Fe(CN)_6^{-3}$ and 5.5 x 10^{-6} cm^2/s for $Ru(NH_3)_6^{+3/+2}$.[204]

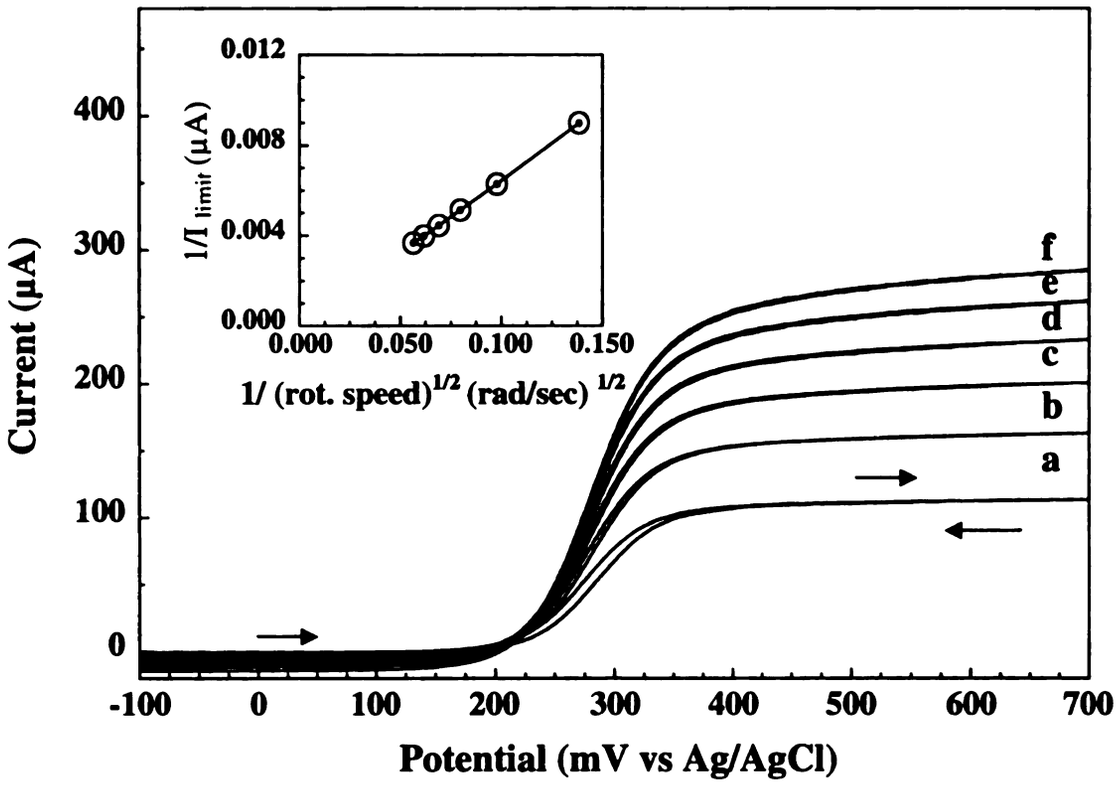

Figure 6.4 Voltammetric response for 1 mM $Fe(CN)_6^{-3/-4}$ in 1 M KCl at a rotating microcrystalline diamond disk electrode as a function of rotation speed. The electrode was deposited with a 0.5 % CH_4/H_2 ratio and 10 ppm B_2H_6. Scan rate = 0.1 V/s. Rotational velocites (rad/s) = (a) 52.2, (b) 104.7, (c) 157.1, (d) 209.4, (e) 261.8, and (f) 314.2.

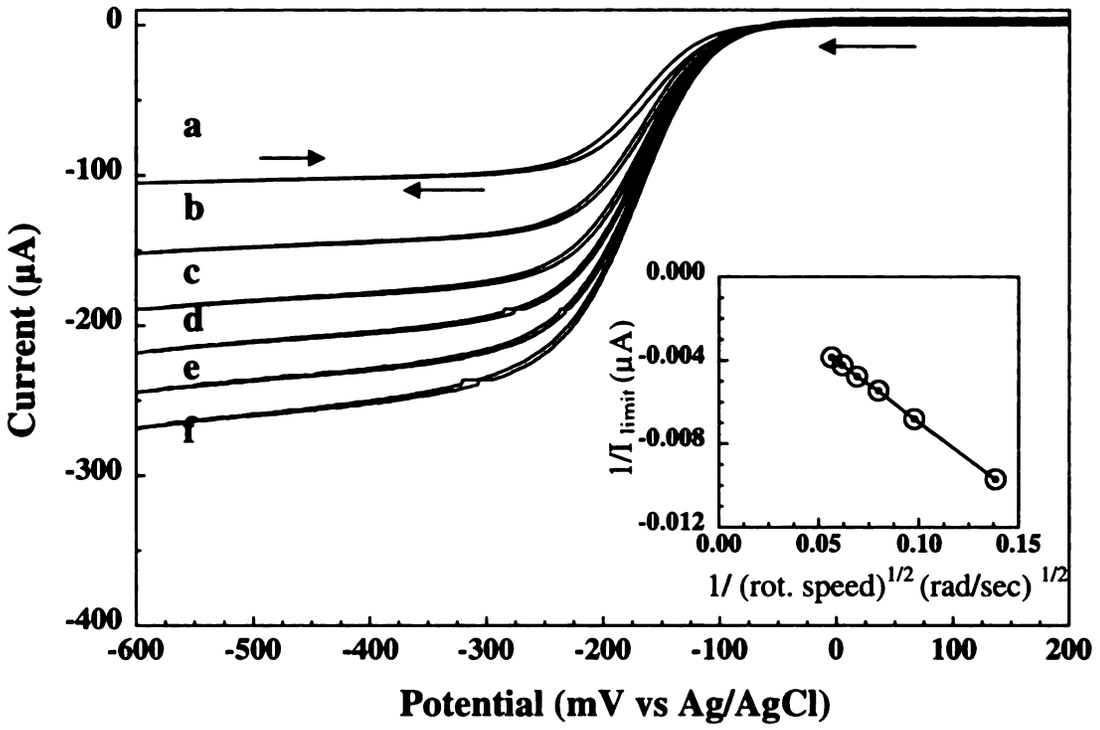

Figure 6.5 Voltammetric response for 1 mM $Ru(NH_3)_6^{+3/+2}$ in 1 M KCl at rotating microcrystalline diamond disk electrode as a function of rotation speed. The electrode was deposited with 0.5 % CH_4/H_2 ratio and 10 ppm B_2H_6.Scan rate = 0.1 V/s. Rotational velocites (rad/s): (a) 52.2, (b) 104.7, (c) 157.1, (d) 209.4, (e) 261.8, and (f) 314.2.

Figure 6.6 shows the voltammetric response for 0.2 mM CAD (forward scan) in borax buffer, pH 11, at different rotational rates. The film was deposited with 0.5% CH_4/H_2 and 1 ppm B_2H_6. The current is independent of the rotation rate, at least at this scan rate, and a limiting current plateau is not observed as it is expected for mass transport controlled reactions (Figure 6.4 and 6.5). Similarly, the oxidation peak currents for PUT, SPMD, and SPM were independent of rotation velocity. These results indicate that the oxidation reaction, at this scan rate, is not limited by mass transport of the amine to the electrode surface. It is supposed that the amine flux to the surface, under these

conditions, is too high compared to the rate of adsorption (coordination of the amine at surface boron sites). It could also be that the rate of adsorption is high but the number of surface sites is limiting the current. Such behavior was reported by Johnson et al. for ethylamine oxidation at Au-Ag composite electrodes.[295]

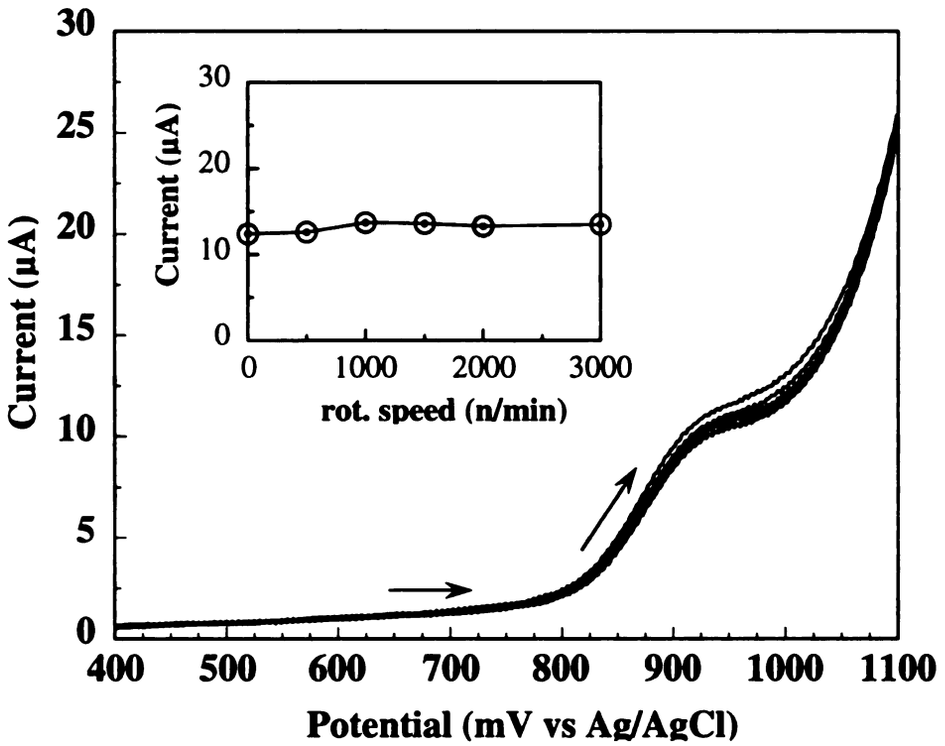

Figure 6.6 Voltammetric response for 0.2 mM CAD (forward scan) in borax buffer pH 11 at a boron-doped microcrystalline diamond disk electrode as a function of rotational speed. The electrode was deposited with 0.5 % CH_4/H_2 and 1 ppm B_2H_6. Scan rate = 0.1 V/s. Rotational velocities (rad/s) = (a) 52.2, (b) 104.7, (c) 157.1, (d) 209.4, (e) 261.8, and (f) 314.2.

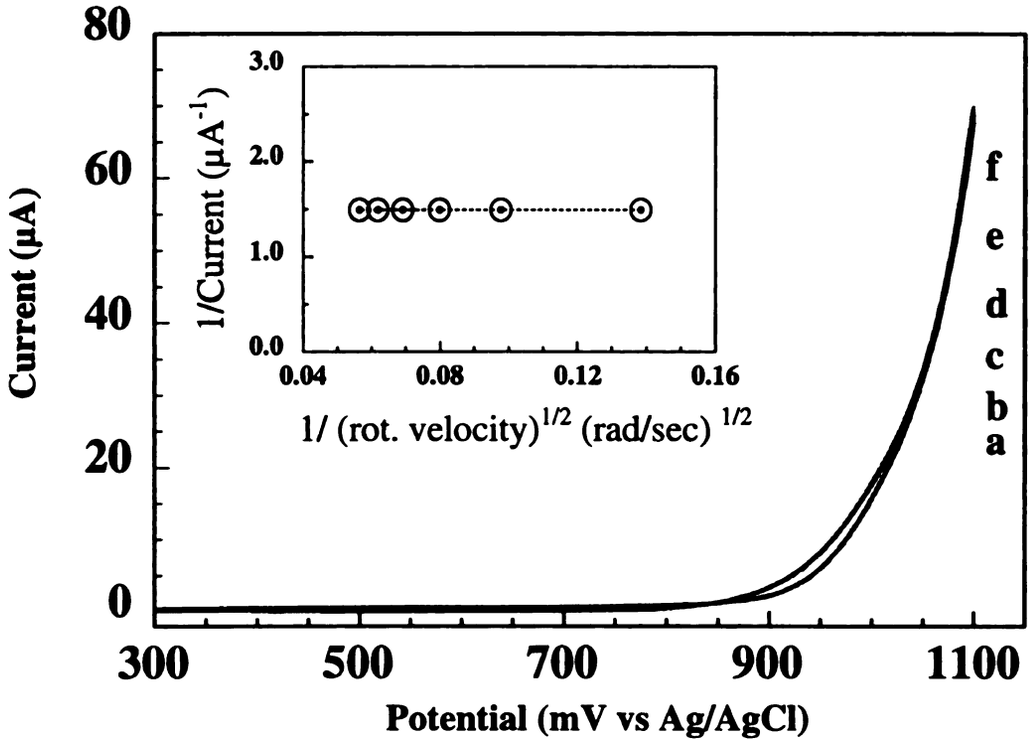

Figure 6.7 Voltammetric response for borax buffer, pH 11, at a boron-doped microcrystalline diamond disk electrode as a function of rotational speed. The electrode was deposited with 0.5% CH_4/H_2 and 20 ppm B_2H_6. Scan rate = 0.05 V/s. Rotational velocities (rad/s) = (a) 52.2, (b) 104.7, (c) 157.1, (d) 209.4, (e) 261.8, and (f) 314.2.

Figure 6.7 shows the voltammetric response for borax buffer, pH 11, at different rotational rates. The film was deposited from 0.5% CH_4/H_2 and 20 ppm B_2H_6. The background current is independent of rotational velocity. The oxygen evolution current is not limited by mass transport but rather by the generation of OH• at the electrode surface.

Figure 6.8 shows the voltammetric response for 0.2 mM SPM (forward scan) in borax buffer, pH 11, at different rotation rates. The film was deposited from 0.5% CH_4/H_2 and 20 ppm B_2H_6.

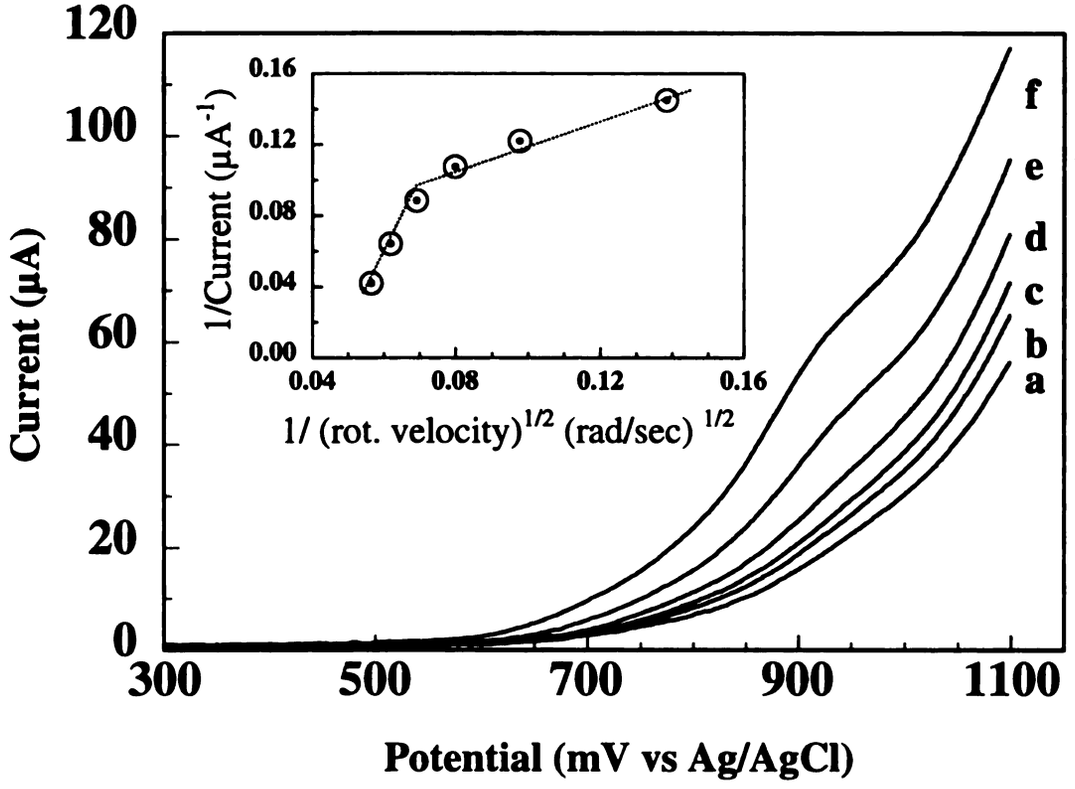

Figure 6.8 Voltammetric response for 0.2 mM SPM (forward scan) in borax buffer, pH 11, at a boron-doped microcrystalline diamond disk electrode as a function of rotational speed. The electrode was deposited with 0.5% CH_4/H_2 and 20 ppm B_2H_6. Scan rate = 0.05 V/s. Rotational velocities (rad/s) = (a) 52.2, (b) 104.7, (c) 157.1, (d) 209.4, (e) 261.8, and (f) 314.2.

For this higher doped film, the current increases with increasing rotation rate, however a limiting current plateau is not observed. Similar observations were made for CAD, PUT, and SPMD. The fact that the current showed some increase with rotation rate indicates that, at this lower scan rate, the reaction rate is influenced by mass transport of the amine. Koutecký-Levich plots were constructed from the data and are shown in Figure 6.9. The plots show a dependence of reciprocal current on the reciprocal rotation velocity$^{1/2}$ with two regions of linearity. Interestingly, one region with a steep slope is

observed at fast rotation rates and a second region with a shallower slope at low rotation rates. Such behavior, although not typical, was previously observed by Treimer et al.[48] for oxidation of toluene at Fe(III)-doped PbO_2 electrodes. It was attributed to the shift in the rate-controlling step in anodic oxygen-transfer reactions from that of reactant transport at low rotational velocities, to OH• generation at fast rotation velocities.[48]

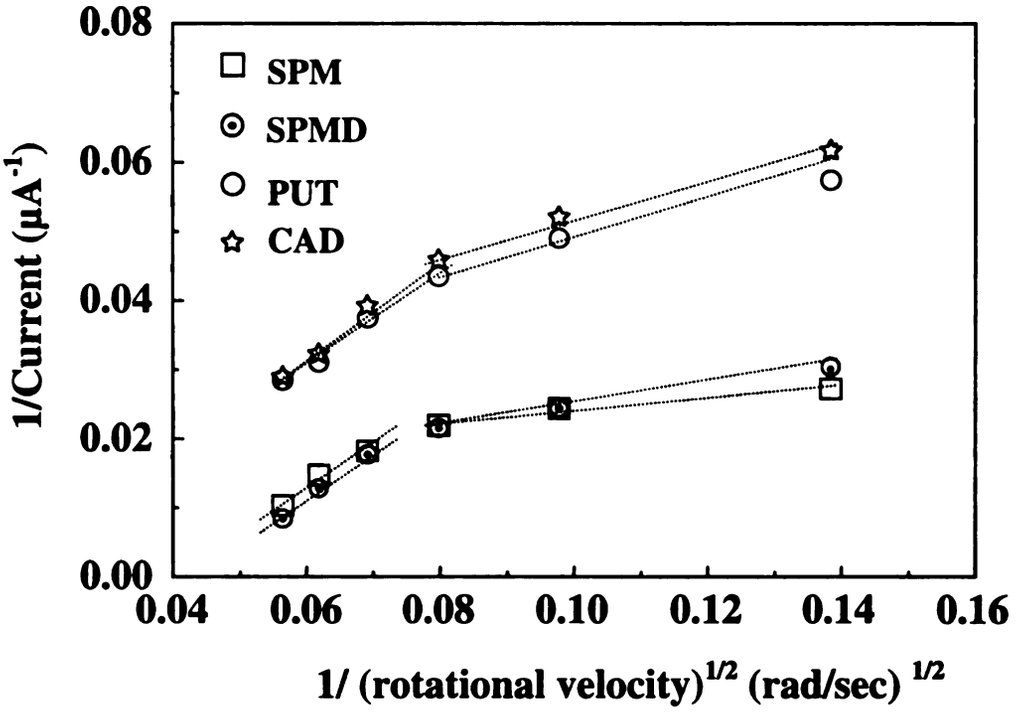

Figure 6.9 Koutecký-Levich plots for the oxidation of 0.2 mM amines at a boron-doped microcrystalline diamond disc electrode deposited with 0.5% CH_4/H_2 and 20 ppm B_2H_6. Scan rate = 0.05 V/s. Potential: 0.7 V vs Ag/AgCl

Values for the number of electrons transferred (n_{app}) and the heterogeneous rate transfer (k_{app}) for the amine oxidation were calculated from the slopes and intercepts, respectively. The kinetic parameters calculated at 0.7 V vs Ag/AgCl are presented in Table 6.2. Results presented in the Table 6.2 were calculated for *low rotational velocities* (i.e., low flux region). The apparent number of electrons n_{app} transferred for CAD, PUT is

1.9, and for SPMD and SPM n_{app} is higher, at 3.6 and 5.6, respectively. The n_{app} values are close to 2 eq/mol for CAD and PUT, 4 eq/mol for SPMD, and 6 eq/mol for SPM. The reaction rates were calculated using the n_{app} and they were found to be $6.6 \pm 0.1 \times 10^{-3}$ cm/s for CAD and PUT and $7.4 \pm 0.2 \times 10^{-3}$ cm/s for SPMD and SPM. The measured overall rate constants contain the rate constant for the adsorption and desorption steps, and for the OH• generation, and the anodic oxygen transfer electron transfer chemical reaction.

Table6.2 Kinetic Parameters for Amines Oxidation (pH11) at 20 ppm Microcrystalline Boron-Doped Diamond

0.2 mM amine BBpH11	$1/i = a + b\,\omega^{-1/2}$			
	b ($mV^{-1}rad^{-1/2}s^{1/2}$)	n_{app}/eq	a (μA^{-1})	k_{app} (cm/s)
CAD	244	1.9	20.3	6.7×10^{-3}
PUT	232	1.8	22.3	6.5×10^{-3}
SPMD	134	3.6	9.6	7.6×10^{-3}
SPM	90	5.6	6.4	7.3×10^{-3}

Note: Electrode geometric area = 0.2 cm^2, $D = 1 \times 10^{-5}$ cm^2/s for CAD and PUT, $D = 0.8 \times 10^{-5}$ cm^2/s for SPMD and SPM. $C = 0.2 \times 10^{-3}$ M, $\nu = 10 \times 10^{-3}$ cm^2/s.

The kinetic parameters calculated for microcrystalline diamond are compared for other electrodes in Table 6.3. The k_{app} values for the polyamine oxidation at diamond are approximately an order of magnitude higher than those for the oxidation of EDA at Ni, Cu, Co, and Ag. They are smaller than the values for EA at Ag-PbO_2, and similar to the value at Cu-Mn alloy electrodes.

Table 6.3 Kinetic Parameters for Anodic Oxidation of Amines

Amine	Electrode	Kinetic parameters		Reference
		n_{app} (eq/mol)	k_{app} (cm/s)	
EDA (pH10)	Cu	5.2	5.6×10^{-3}	43
EDA (pH10)	Cu-Mn (95:5)	7.7	6.7×10^{-3}	43
EDA (pH10)	Cu-Mn (90:10)	8.6	8.0×10^{-3}	43
EA (pH12)	Ni	4	7.0×10^{-5}	35
diethylamine (pH12)	Ni	6	2.4×10^{-6}	35
EA (pH12	Cu	4	1.4×10^{-4}	35
diethylamine (pH12)	Cu	6	5.6×10^{-5}	35
EA (pH12	Co	4	9.0×10^{-6}	35
diethylamine (pH12)	Co	6	$<10^{-6}$	35
EA (pH12)	Ag	4	1.4×10^{-4}	35
diethylamine (pH12)	Ag	4	3.6×10^{-6}	234
EA (pH10)	Ag-PbO_2	1.9	1.3×10^{-2}	54,55,57
CAD (pH11)	Diamond	1.8	6.7×10^{-3}	This work
PUT(pH11)	Diamond	1.8	6.5×10^{-3}	This work
SPMD(pH11)	Diamond	3.6	7.6×10^{-3}	This work
SPM (pH11)	Diamond	5.6	7.3×10^{-3}	This work

Secondary amine (e.g., diethylamine) oxidation studies at Ag revealed an overall mechanism involving transfer of $4e^-$ and $3H^+$ to form a nitrile, $2e^-$ and $2H^+$ to form an aldehyde, and $2e^-$ and 1 H^+ to form an alcohol and alkene (Eqs. 9-13 in the introduction of this chapter).[234] Our studies show the involvement of $4e^-$ and 4 H^+, and $6e^-$ and $6H^+$ for SPMD and SPM, respectively. Fleischmann et al. proposed transfer of $6e^-$ for secondary amine oxidation.[35]

The n_{app} values for the polyamines at diamond are smaller when compared with the values for EA at Ni, Cu, Cu-Mn, Co, and Ag. For the transition-metal and Ag-PbO_2 electrodes, the primary amine oxidation mechanism involves $4e^-$ and $4H^+$ with the nitrile formation, and for secondary amine $2e^-$ and $2\ H^+$ to form a primary amine. The mechanism for Ag-PbO_2 suggests involvement of hydroxyl radicals and overall transfer of $2e^-$ and $2H^+$.

6.3. Conclusions

The investigations presented in this chapter suggest the following:

(i) Amine oxidation can be classified as mechanism, where electron transfer is followed by chemical process (EC), with involvement of hydroxyl radical in chemical step. Fast reaction rates (i.e., high currents) are observed only for diamond electrodes at which the discharge of water has appreciable rate.

(ii) The oxidation potentials for primary and secondary amines vary at diamond. Secondary amine groups oxidize at less positive potentials than primary amine groups, although the rate of the oxidation is much lower for the former.

(iii) A primary amine is likely formed during the oxidation of a secondary amine remaining adsorbed at the surface boron sites, and available for further oxidation at higher potentials.

(iv) E_p^{ox} and $E_{p/2}$ values for all the polyamines shifted negatively with increasing pH. This observation indicates that electron transfer is accompanied by proton transfer. Plots of $E_{p/2}$ vs pH had slopes of ca. -60 mV/pH unit. This indicates that an even number of protons and electrons are involved in oxidation reaction.

(v) The adsorption or coordination of the amines follows a Langmuir-type isotherm.

(vi) The oxidation peak current for the amines at boron-doped microcrystalline films deposited with 0.5% CH_4/H_2 and 1 ppm B_2H_6 was independent of the rotation velocity in rotating disc voltammetric measurements at a scan rate of 0.1 V/s. This indicates that either the adsorption kinetics are rate limiting or that the current is limited by the number of available surface boron sites.

(vii) The Koutecký-Levich plots constructed for the amine oxidation at boron-doped microcrystalline films deposited with 0.5% CH_4/H_2 and 20 ppm B_2H_6 show a peak current dependence with the rotational velocity, with two regions of linearity. It was attributed to the shift in the rate-controlling step in O-transfer reactions from that of reactant transport at low rotational velocities, to OH• generation at fast rotational velocities.

(viii) The apparent number of electrons n_{app} transferred, at pH 11, during the oxidation of CAD and PUT was 2. For SPMD and SPM, n_{app} is 4 and 6, respectively. The reaction rates were calculated using n_{app} and were found to be $6.6 \pm 0.1 \times 10^{-3}$ cm/s for CAD and PUT and $7.4 \pm 0.2 \times 10^{-3}$ cm/s for SPMD and SPM.

Based on these findings we propose the mechanism of amine oxidation at boron-doped diamond electrode (Eq.26-28)

$$CH_3\text{-}CH_2\text{-}NH_2 \rightarrow (CH_3\text{-}CH_2\text{-}^{+}NH_2)_{ads} + e^- \quad (26)$$

$$H_2O \rightarrow (\bullet OH)_{ads} + e^- + H^+ \quad (27)$$

$$(CH_3\text{-}CH_2\text{-}^{+}NH_2)_{ads} + (\bullet OH)_{ads} \rightarrow CH_3\text{-}CHO + NH_3 + H^+ \quad (28)$$

It is our opinion that at highly doped diamond films, chemical process of radical formation and oxygen transfer to the amine molecule is the limiting step. Adsorption process at boron sites itself is not limiting, but the number of those sites can influence the overall kinetics of oxidation. This can be observed for low doped films for which reaction is kinetically limited by surface sites available. The results presented in this chapter and Chapter 5 strongly support it.

It is anticipated that the step in Eq.28 proceeds by the surface equivalent of a SN2-type mechanism. The proposed mechanism is presented in Figure 6.10.

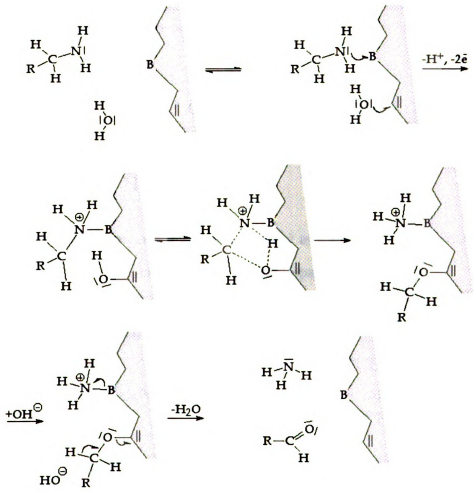

Figure 6.10 Proposed surface SN2-type mechanism of aliphatic amine oxidation at boron-doped diamond electrode

Such mechanism was proposed by Johnson. et al.[54,55,57] In the mechanism a non-bonded electron pair on $\bullet OH_{ads}$ interacts with the anti-bonding orbital of the α-carbon atom. This is followed by oxidative dissociation of the H-atom from •OH, and cleavage of the C-N bond with formation of NH_3 (for primary group) and primary amine (for secondary groups). It was stated [54,55,57] that such surface mechanism requires the proximate location of adsorption sites for •OH and NH_2, as well as significant vibrational motions of these adsorbed species along an axis passing through the O and C atoms.

Although the amine oxidation reaction products were not examined, it is our supposition that the products of primary amine oxidation are aldehyde and ammonia. Two electron and two proton process is proposed and presented below.

$$H_2N(CH_2)_4NH_2 + H_2O \xrightarrow[-2H^+]{-2e^-} H_2N(CH_2)_3CHO + NH_3$$

$$\begin{matrix} RCH_2CHO \\ NH_3 \end{matrix} \xrightarrow{pH\ 11} \textbf{No oxidation}$$

Oxidation of polyamines involves secondary amine group. The SPMD oxidation products may be: 4-aminobutanal (II) and diaminopropane (DAP).

SPERMIDINE

$$\underset{(I)}{H_2N(CH_2)_3NH(CH_2)_4NH_2} + H_2O \xrightarrow[-2H^+]{-2e^-} \begin{matrix} H_2N(CH_2)_3NH_2\ (II) \\ \text{and} \\ H_2N(CH_2)_3CHO \end{matrix}$$

$$\underset{(II)}{H_2N(CH_2)_3NH_2} + H_2O \xrightarrow[-2H^+]{-2e^-} H_2N(CH_2)_2CHO + NH_3$$

The DAP can be further oxidized at higher potential, resulting 3-aminopropanal and ammonia. It was found during investigations that ammonia and aldehydes were not electroactive in the studied potential range (0.2-1.2 V vs. Ag/AgCl). SPMD oxidation process involves 4 e^-. The mechanism of SPM oxidation is similar. Overall process may involve both secondary amino groups and overall transfer of 6 e^-.

SPERMINE

(I)

$$H_2N(CH_2)_3NH(CH_2)_4NH(CH_2)_3NH_2 + H_2O \xrightarrow[-2H^+]{-2e^-} \underset{\text{(II)}}{H_2N(CH_2)_3NH_2} \text{ and } \underset{\text{(III)}}{OHC(CH_2)_3NH(CH_2)_3NH_2}$$

$$\underset{\text{(II)}}{H_2N(CH_2)_3NH_2} + H_2O \xrightarrow[-2H^+]{-2e^-} NH_2(CH_2)_2CHO + NH_3$$

$$\underset{\text{(III)}}{OHC(CH_2)_3NH(CH_2)_3NH_2} + H_2O \xrightarrow[-2H^+]{-2e^-} OHC(CH_2)_3NH_2 + OHC(CH_2)_2NH_2$$

Chapter 7

FLOW INJECTION ANALYSIS INVESTIGATIONS OF ALIPHATIC POLYAMINE OXIDATION AT BORON-DOPED DIAMOND THIN-FILM ELECTRODES

7.1. Introduction

A key finding from the work presented in previous chapters is the fact that aliphatic polyamines can be electrooxidized at boron-doped microcrystalline and nanocrystalline diamond films.[169,188,259,291,296] Voltammetry was employed to study the diamond electrode response for amine oxidation. The objective for the work reported on presently was to use diamond films for the oxidative detection of aliphatic amine in a flowing system, (i.e., in flow injection analysis (FIA) and liquid chromatography (LC)).[291,296]

FIA was originally designed for analysis of homogeneous samples and the development of single component assays.[297-302] The FIA was first developed almost 30 years ago, and since that time the perception of it has changed. Chromatogaphic techniques are aimed to determine many analytes in a single injected sample, by resolving them through separation. FIA is aimed at detection of a single (or several)

analyte(s) within a single dispersion zone.[301] Selective chemical or enzymatic conversion is used to minimize matrix effect. In FIA, a sample is injected into a flowing non-segmented stream of the mobile phase. FIA serves as a convenient means for the analysis of small volumes (μL) of sample.[301] The injected sample forms a zone that disperses on its way to the detector and the magnitude of the resulting readout peak reflects the concentration of the injected analyte. In FIA or LC with electrochemical detection, the supporting electrolyte of the system acts as a mobile phase. Since the supporting electrolyte is in motion over the electrode surface, mass transfer is assisted by forced convection. Hence, all electrochemical techniques applied for LC or FIA detection are classified as hydrodynamic techniques.[303] The most commonly used electrochemical detectors in FIA or LC are thin-layer cells, in which the working electrode is positioned in a thin channel through which the mobile phase flows.[303] Schematic of the cell used in these studies was presented in Chapter 2. The thin-layer detector in these studies was operated at constant potential (amperometric detection) so-called dc amperometry.[303] The current or charge passed was measured as a function of time. Usually, the active volume of the cell is about 0.1-1μL, and typically about 5% of the analyte is electrolyzed as it is swept past the electrode.[303] A well-designed FIA system yields the detector readout within 15 s from the moment of sample injection. Approximately the same time is required for the dispersed sample to clear out of the detector, so that the next sample can be injected.[299] Considering it, a big number of samples, in a short period of time, can be analyzed and detector tested. Compared with cyclic voltammetric techniques in which the potential is scanned, the amperometry provides a major advantage. By operating at a fixed potential, the charging current is minimized.

Flow injection analysis with amperometric detection was used to evaluate the polycrystalline diamond electrode performance for detection of aliphatic amines in the hydrodynamic mode. The electrode performance was tested as a function of the linear dynamic range, limit of quantitation, response variability, and response stability.

7.2. Results and Discussion

7.2.1. Hydrodynamic Voltammetric i-E Curves

Hydrodynamic background i-E curves in carbonate buffer pH 10, for microcrystalline boron-doped diamond thin-film electrodes, deposited using 0.33%, 0.50%, and 0.67% CH_4/H_2 ratios, are shown in Figure 7.1.

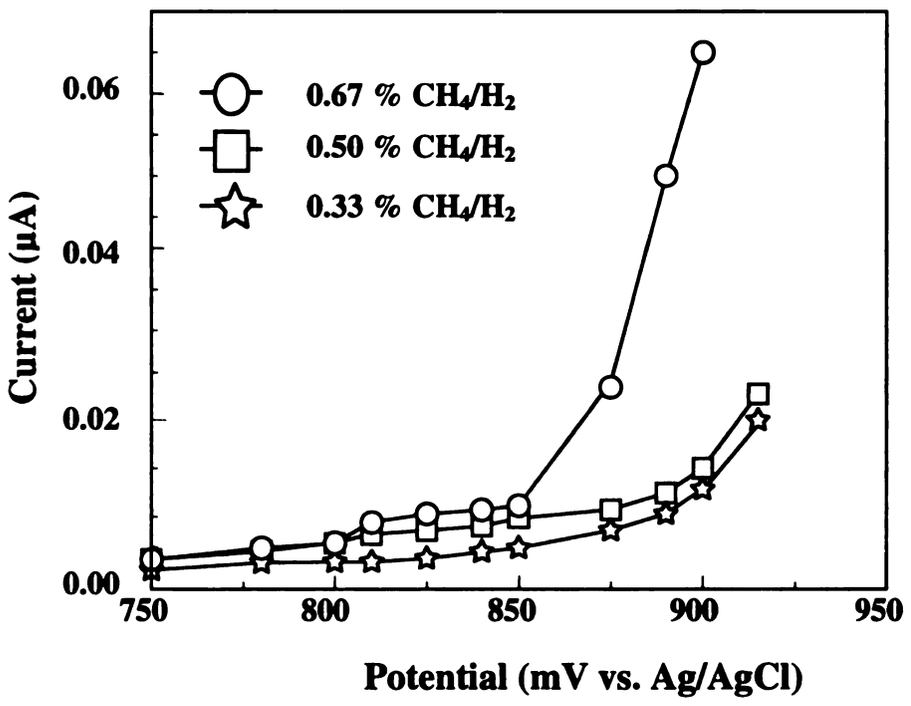

Figure 7.1 FIA-EC hydrodynamic voltammetric background i-E curves for a microcrystalline diamond film deposited using 0.33%, 0.50% and 0.67% CH_4/H_2 ratio in carbonate buffer, pH 10. Flow rate = 1.0 mL/min.

The voltammogram was obtained by incrementally changing the detection potential. Once a stable baseline was observed at a given potential, the background and noise signal were measured and higher potential was applied. The measurements were made at a flow rate of 1.0 mL/min. The background current increases with increasing CH_4/H_2 ratio. For example, the background current at 815 mV was 3, 6, and 9 nA, respectively for the 0.33 %, 0.5 % and 0.67 % CH_4/H_2 film. Three films for each of the type of electrode were evaluated. The onset potential for oxygen evolution is least positive for the 0.67 % CH_4/H_2 film. Table 7.1 shows comparison of the background current and noise signal magnitude for three electrodes at a given potential.

Table 7.1 FIA-EC Background and Noise Signal for Microcrystalline Diamond Film in Carbonate Buffer pH10

Diamond film deposited from CH_4/H_2 ratio	Applied Potential vs Ag/AgCl			
	815 mV		870 mV	
	Background current	Noise	Background current	Noise
0.33%	2-10 nA	230 pA	10-20 nA	200 pA
0.50%	8-12 nA	190 pA	12-25 nA	200 pA
0.67%	10-20 nA	200 pA	30-60 nA	400 pA

The higher background current for films deposited at higher CH_4/H_2 ratio is associated with a higher faction of exposed grain boundary where non-diamond carbon exists. Non-diamond sp^2-bonded carbon exhibits a lower overpotential for oxygen evolution than does diamond and is more reactive (i.e., susceptible to oxidation) than does diamond. The carbon in the grain boundary is also a source of charge carriers, along with the substitutional boron dopant atoms. This leads to a greater excess surface charge at a

given potential and a larger double-layer charging current. The peak to peak noise for all the tested films ranged from 200-230 pA at 815 mV. At a more positive potential of 870 mV, the noise increased to 200-400 pA.

As was the case in cyclic voltammetric measurements, nanocrystalline films possessed slightly higher background current than microcrystalline diamond films. Similar results were observed in FIA, when hydrodynamic current was measured in the same electrolyte at the same potential. Nanocrystalline films were deposited from a 1/94/5 $CH_4/Ar/H_2$ (v/v) ratio with 1, 10 and 20 ppm of added diborane. The measurements were made at a flow rate of 1.0 mL/min. The background current varied only slightly at these electrodes, and was generally about 10-30 nA at 730 mV. The onset potential for oxygen evolution at pH 11 was similar for all the films. The peak to peak noise ranged from 150-250 pA at 730 mV. The hydrodynamic voltammetric background current for boron-doped nanocrystalline diamond films, in borax buffer, pH 11, are shown in Figure 7.2. Table 7.2 shows comparison of background current and noise signal magnitude for nanocrystalline electrodes at a given potential.

Table 7.2 FIA-EC Background and Noise Signal for Nanocrystalline Diamond Film in Borax Buffer pH 11.

Diborane (B_2H_6) concentration	Applied Potential vs Ag/AgCl			
	675 mV		730 mV	
	Background current	Noise	Background current	Noise
1 ppm	3-5 nA	120 pA	10-15 nA	150 pA
10 ppm	3-6 nA	200 pA	20-30 nA	150 pA
20 ppm	5-7 nA	150 pA	25-30 nA	250 pA

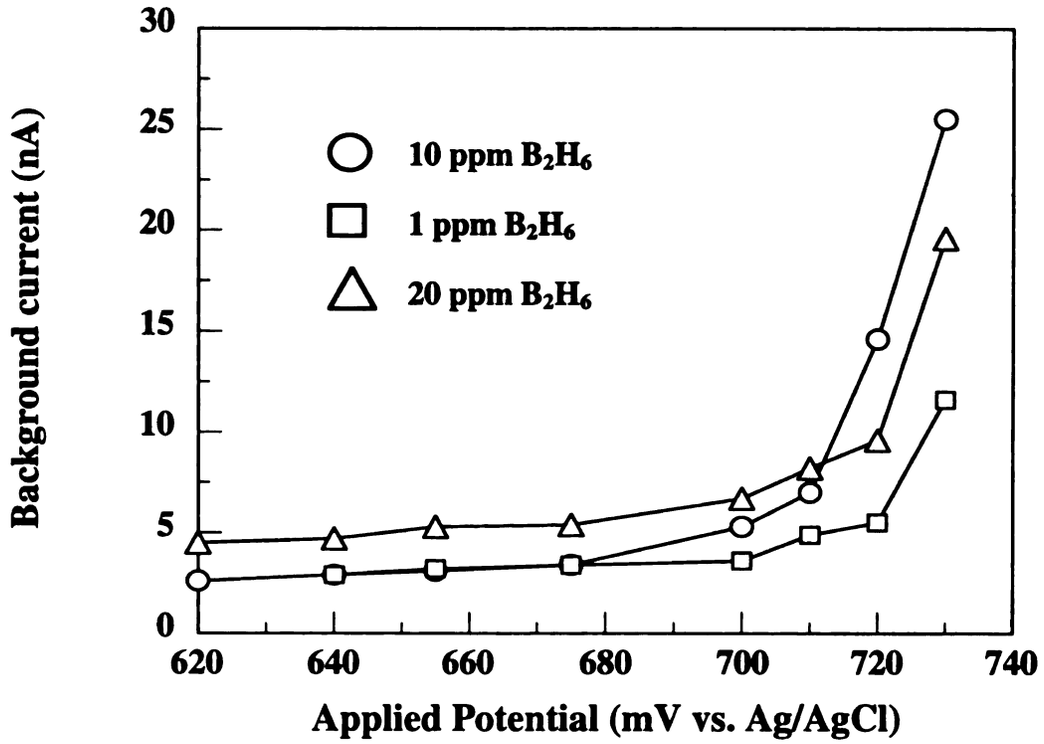

Figure 7.2 FIA-EC hydrodynamic voltammetric background i-E curves for boron-doped nanocrystalline diamond films deposited with 1 ppm, 10 ppm, and 20 ppm of added B_2H_6 in borax buffer, pH 11. Flow rate = 1.0 mL/min.

At more positive potentials (>740 mV) in this medium, the background current becomes unstable due to the oxygen evolution reaction. The background current for "as deposited" nanocrystalline and microcrystalline films stabilizes quickly after detector turn-on, reaching a constant value in about 10 min. The background current for films in use (conditioned), stabilizes in less than 2 minutes, after detector turn-on. A rapid stabilization time and a low and stable background current are characteristic features of diamond electrodes.[163,188] Figure 7.3 presents a background current-time plot for a diamond thin-film electrode in borax buffer, pH 11.

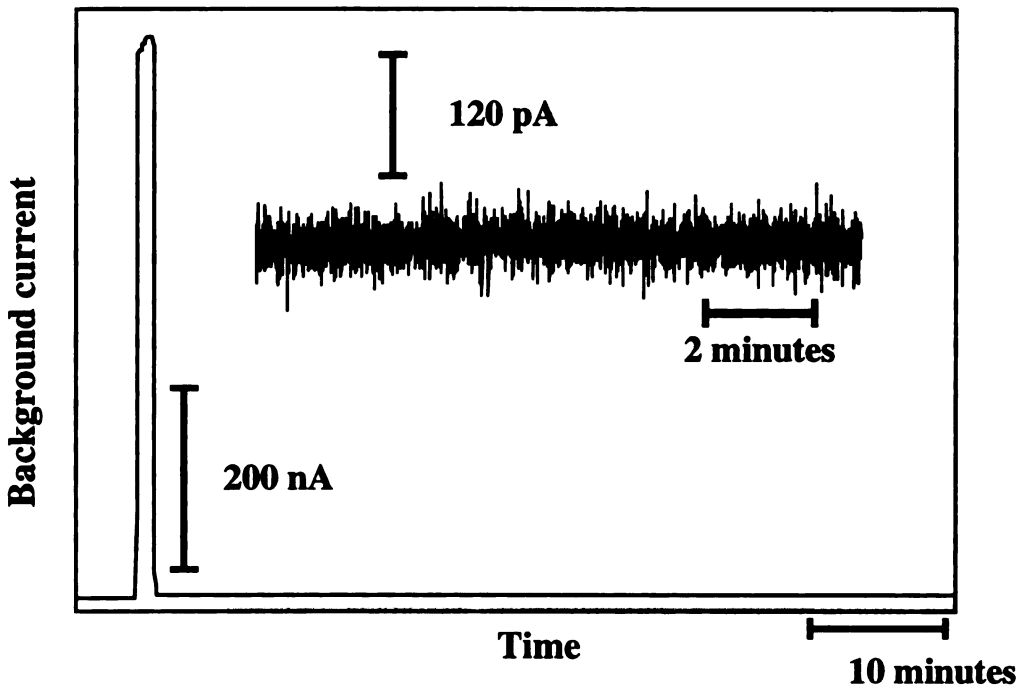

Figure 7.3 Background current-time profile in FIA after detector turn-on in borax buffer, pH 11, for a nanocrystalline diamond film deposited from 1/94/5 $CH_4/Ar/H_2$ (v/v) ratio and 1 ppm B_2H_6. Detection potential = +695 mV vs Ag/AgCl. Electrode area = 0.08 cm^2. Flow rate =1 mL/min.

Figure 7.4 A and B shows hydrodynamic voltammetric i-E curves for 20 µL injections of (A) 1.0 mM SPMD and (B) CAD at boron-doped microcrystalline diamond thin-film electrodes, deposited using CH_4/H_2 gas source ratio of 0.33%, 0.50%, and 0.67%. The hydrodynamic voltammogram was obtained by making repetitive injections of each amine while incrementally increasing the detection potential. Each datum shown represents an average of at least six injections. Error bars are within the size of the marker. Generally, the largest current for CAD and SPMD is observed for the 0.5% CH_4/H_2 film. Similar results were observed for PUT and SPM, with the largest current obsrved for SPM. The total current response for the polyamines is larger by about a factor of ca. 4 than that for the diamines. For instance, for a 0.5% CH_4/H_2 film, at 850

mV, the current for 1 mM SPMD is 4.5 μA and for 1 mM CAD is 1.0 μA. The larger current for SPMD, compared to CAD, is an observation that has been made previously in cyclic voltammetric studies for highly doped diamond films and reflects a larger number of electrons being transferred per equivalent of analyte.

Well-defined, sigmoidally-shaped hydrodynamic i-E profiles are not observed for either analyte. This is because the oxidation reaction is not limited by mass transport but is strongly influenced by the generation and transport of reactive OH• and the adsorption/desorption of the reactant/product. The thin-layer electrochemical flow cell used did give well-defined sigmoidal hydrodynamic voltammograms for other less mechanistically complicated oxidation reactions (e.g., azide oxidation).[286]

Figure 7.4 C and D show plots of the signal-to-background (S/B) ratio, as a function of the applied potential for SPMD (C) and CAD (D), at the same three diamond films. The S/B ratio was calculated as $I_{total} - I_{bakground} / I_{background}$. Such plots are particularly useful for determining the optimum detection potential in situations where a mass-transport limited process is not observed in the hydrodynamic voltammogram. The largest S/B ratios are seen for the 0.5% CH_4/H_2 film. The maximum ratio was observed at about 820-840 mV. Similar observations were made for PUT and SPM.

The boron doping level in all three films discussedin the previous figure was approximately the same, ~$1x10^{19}$ B/cm^3. The doping level was estimated in boron nuclear reaction analysis of other films deposited in a similar manner. Before performing FIA of the polyamines, all the electrodes were tested using other redox systems (i.e., $Fe(CN)_6^{-3/-4}$, $Ru(NH_3)_6^{+2/+3}$) to ensure that the electrode possessed good responsiveness and adequate electrical conductivity. The tested couples showed near-reversible behavior, therefore, one can conclude that the differences in response toward polyamine

oxidation are due to differences in the electrode surface structure and chemical composition and not electronic property variations.[259]

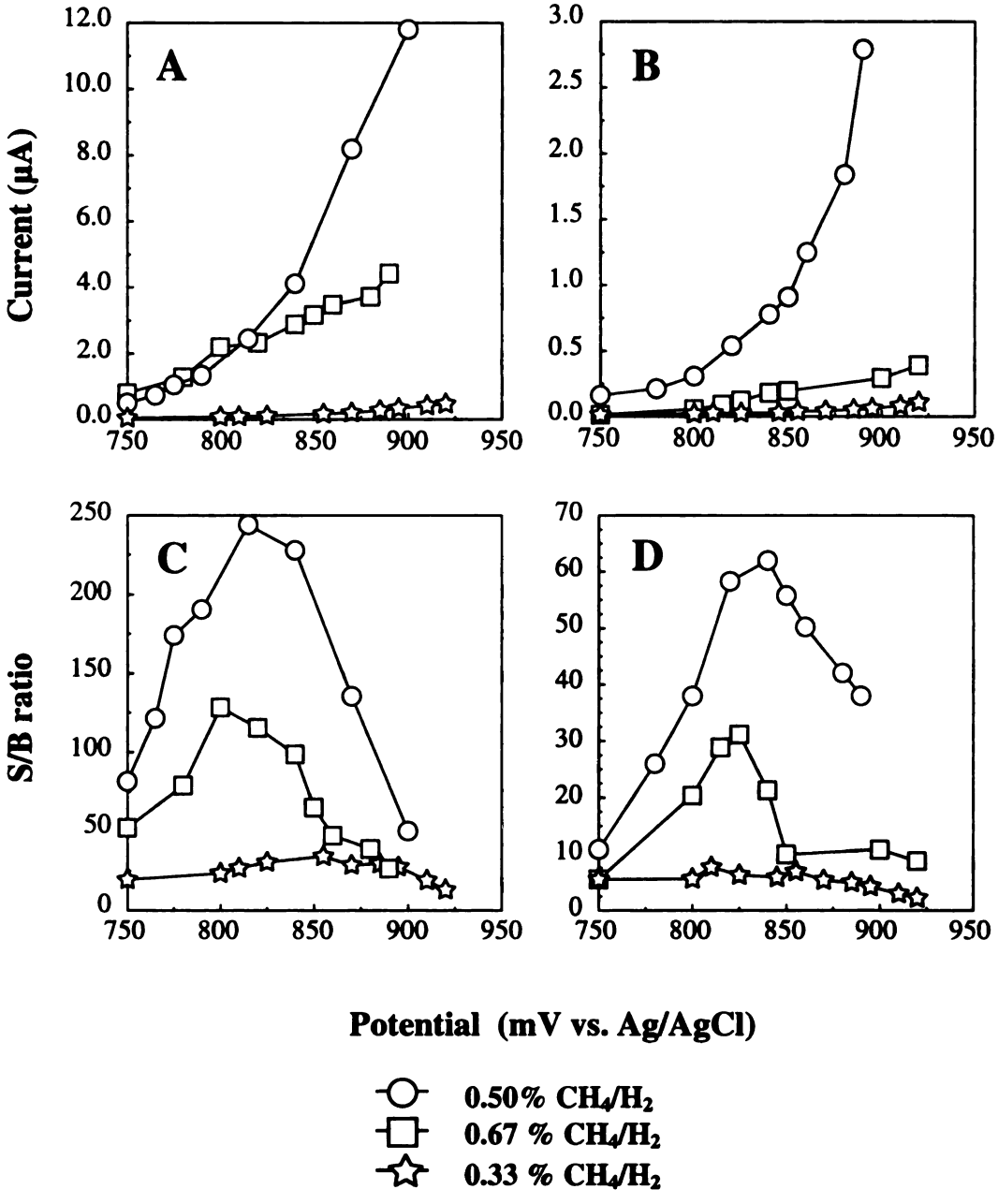

Figure 7.4 Hydrodynamic voltammetric i-E curves for 20 μL injections of (A) 1.0 mM SPMD and (B) 1.0 mM CAD. The carrier solution was 0.1M $NaClO_4$ + 0.01 carbonate buffer, pH 10. Plots of the S/B ratio versus the applied potential are shown for (C) SPMD and (D) CAD. Flow rate =1.0 mL/min.

It was disscussed in Chapter 5 that the amine oxidation response depends on the sp2-bonded non-diamond carbon impurity and boron concentration. The oxidation current increases with increasing boron concentration in the film. Similar results were observed in FIA-EC. Figure 7.5 shows hydrodynamic voltammetric i-E curves for 20 µL injections of 0.1 mM PUT, CAD, SPMD, and SPM obtained at nanocrystalline diamond thin-film electrodes deposited using a 1/94/5 $CH_4/Ar/H_2$ source gas ratio with (A) 1 ppm B_2H_6, (B) 10 ppm B_2H_6, and (C) 20 ppm of added B_2H_6. Each datum shown represents an average of four injections. Error bars are within the size of the marker. Relative standard deviations of the response were in the range of 0.4-1.0 %. As was the case for microcrystalline films, well-defined, sigmoidal hydrodynamic i-E curves were not observed for any analyte. The largest oxidation currents are seen for the highest doping level.

Figure 7.5 D-F show plots of the signal-to-background (S/B) ratio, as a function of the applied potential for 0.1 mM amines at the same electrodes. The oxidation currents and S/B ratios were similar for PUT and CAD, and SPMD and SPM. The S/B ratios for all four amines increased with increasing boron doping level in the film. For instance at 720 mV, the current for 0.1 mM SPMD was 270, 384, and 1678 nA at 1 ppm, 10 ppm, and 20 ppm B_2H_6 films, respectively. For 0.1 mM PUT, the current was 44, 57, and 458 nA for thet 1 ppm, 10 ppm, and 20 ppm B_2H_6 films, respectively. The S/B ratio for the polyamines at 720 mV was larger by about a factor of 7 than that for the diamines at all three nanocrystalline films. The optimum detection potential for all polyamines, regardless of the film was determined to be about 700-720 mV vs Ag/AgCl.

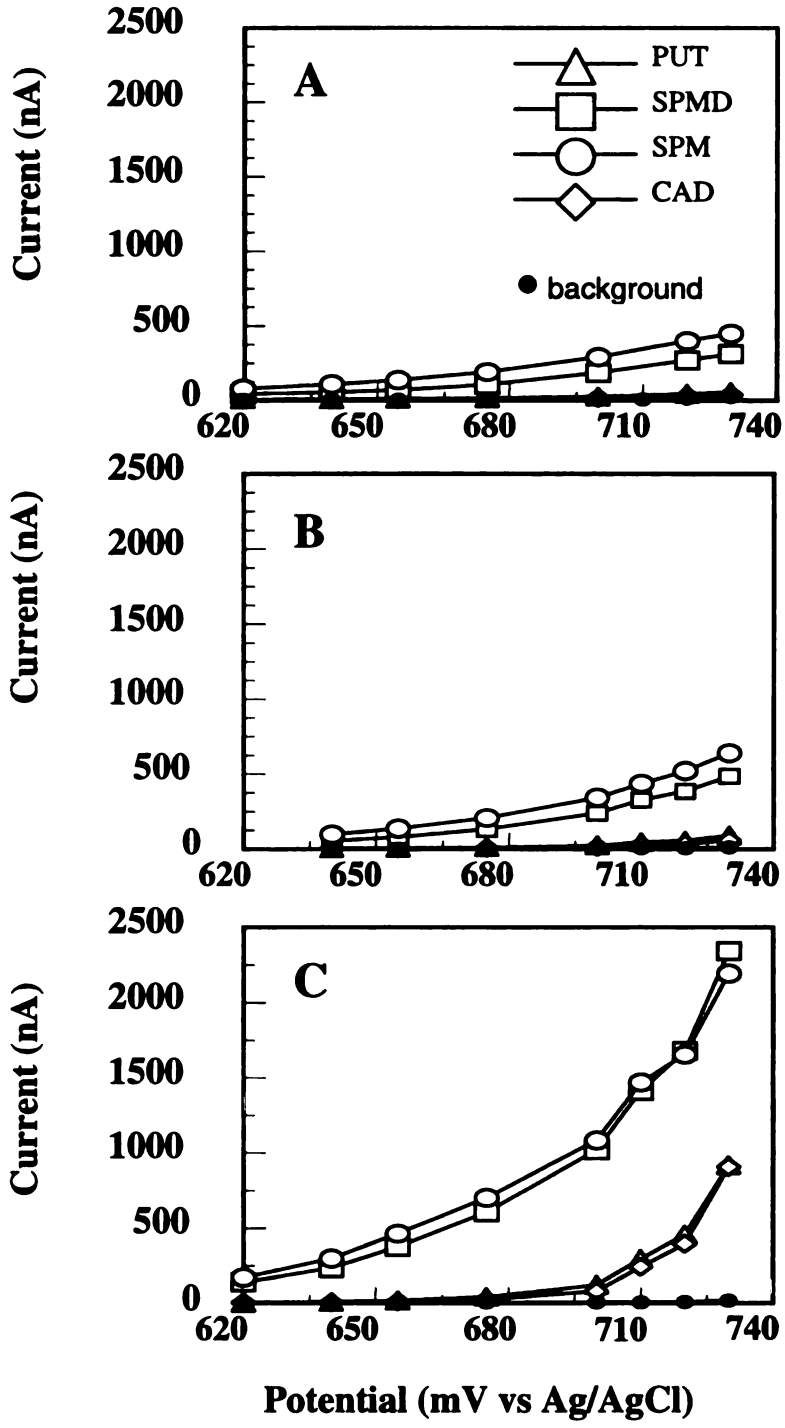

Figure 7.5 Hydrodynamic voltammetric i-E curves for 20 µL injections of 0.1 mM amines. The carrier solution was 0.1M NaCl + 0.01 borax buffer, pH 11. Nanocrystalline diamond films were deposited from a 1/94/5 CH_4/Ar/H_2 (v/v) ratio with (A) 1 ppm, (B) 10 ppm, and (C) 20 ppm of added B_2H_6. Flow rate=1.0 mL/min.

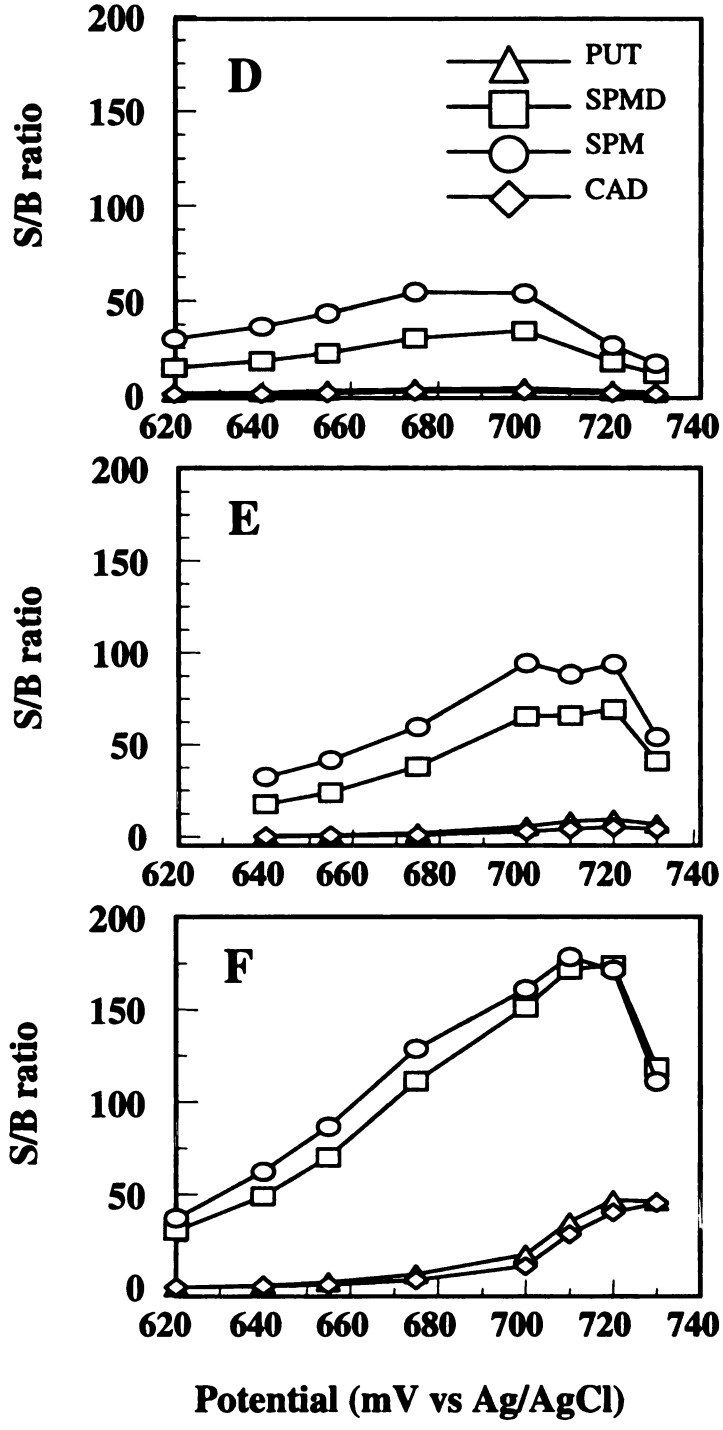

Figure 7.5 Plots of the S/B ratio versus the applied potential for 0.1 mM amines. The carrier solution was 0.1M NaCl + 0.01 borax buffer, pH 11. Nanocrystalline diamond film were deposited from a 1/94/5 CH_4/Ar/H_2 (v/v) ratio with (D) 1 ppm, (E) 10 ppm, and (F) 20 ppm of added B_2H_6. Flow rate = 1.0 mL/min.

A lower onset potential for SPMD and SPM oxidation was observed which is the most pronounced in Figures 7.5 C and F for the 20 ppm B_2H_6 film. Table 7.3 presents a summary of numerical values of the current as a function of the potential. It can be seen that the oxidation current for SPMD and SPM is much greater than that for CAD and PUT at lower potentials (550 mV-620 mV). For example at 550 mV, the current for SPMD, SPM, PUT, and CAD is 17, 33, 3 and 3 nA, respectively.

Table 7.3 Amperometric Data Obtained During FIA of Aliphatic Amines at pH 11

Applied Potential (mV vs. Ag/AgCl)	Current response (nA)			
	PUT	CAD	SPMD	SPM
550	3.2 ± 0.1	3.0 ± 0.1	17.3 ± 0.3	32.5 ± 0.4
570	4.4 ± 0.1	4.0 ± 0.1	33.8 ± 0.5	57.4 ± 0.8
595	4.5 ± 0.1	4.0 ± 0.1	41.9 ± 0.4	71.0 ± 1.3
605	4.8 ± 0.2	4.1 ± 0.1	53.5 ± 0.9	95.8 ± 1.2
615	5.4 ± 0.2	4.3 ± 0.1	79.5 ± 1.7	133.9 ± 2.1
620	6.3 ± 0.1	5.9 ± 0.2	145.8 ± 2.8	171.4 ± 3.6
640	9.4± 0.3	7.3 ± 0.1	235.6 ± 2.5	297.4 ± 3.8
655	19.1 ± 0.3	11.6 ± 0.2	375.8 ± 3.8	464.3 ± 2.2
675	42.1 ± 0.8	25.2 ± 0.8	604.8 ± 2.4	700.7 ± 2.3
700	123.6 ± 2.2	81.8 ± 1.2	1018.2 ± 2.5	1084.5 ± 6.4
710	294.4 ± 4.2	240.3 ± 2.9	1413.5 ± 2.8	1470.7 ± 5.4
720	457.9 ± 3.3	395.3 ± 2.5	1678.3 ± 3.1	1654.5 ± 9.6
730	919.1 ± 3.9	906.2 ± 4.1	2324.4 ±30.3	2192.8 ± 2.1

Another observation is that the signal for SPM is approximately twice as big as that of SPMD up to 615 mV. The cyclic voltammetric data shown in Chapter 6, for 1 mM SPM at pH 7.2, showed an oxidation wave at 940 mV with a peak current of 11 μA. The lowest pKa value for SPM is 7.9 and corresponds to one of the two secondary amine groups.[189] At this pH only this secondary amino group is in partially deprotonated form, and thus available for oxidation. This result indicates that oxidation of secondary amine occurs at lower potential. It is harder to oxidize primary amine group, hence, the oxidation potential is more positive. This would also suggests, that the higher currents, for SPMD and SPM, at low potentials are due to oxidation of secondary amino groups. Furthermore, the current for SPM is approximately twice as large as that for SPMD, presumably because SPM possesses two secondary amine groups while SPMD has only one.

Hydrodynamic voltammogramms for 0.1 mM CAD and 0.1 mM SPMD were obtained as a function of the carrier solution pH. Figure 7.6 shows the SPMD/CAD current ratio at pH 9, 10.6, and 11.4. The first observation is that the optimum oxidation potential shifts toward less positive values as the pH increases. This is due to a negative shift in the onset potential for the background current (i.e., oxygen evolution) observed with increasing pH. The second observation is that the magnitude of the SPMD/CAD current ratio (as well the SPM/PUT ratio) increases with increasing pH. For example, at pH 9 and 10 the current for SPMD is about 4 times larger than that for CAD. However, at pH 10.6 and 11.4 the current for SPMD is 8 and 17 times larger than that for CAD. This is associated with higher number of electrons transferred per equivalent for SPMD due to oxidation of both primary (from the SPMD and the reaction products) and secondary (from the SPMD only) amine group, while for CAD only one primary group is involved in reaction. The current for SPMD is becoming much larger than that for CAD or PUT at

higher pH because the primary amine groups of polyamines (i.e., SPMD and SPM) have high pK_a values, and only at high pH they are available for oxidation (i.e., in a unprotonated form).

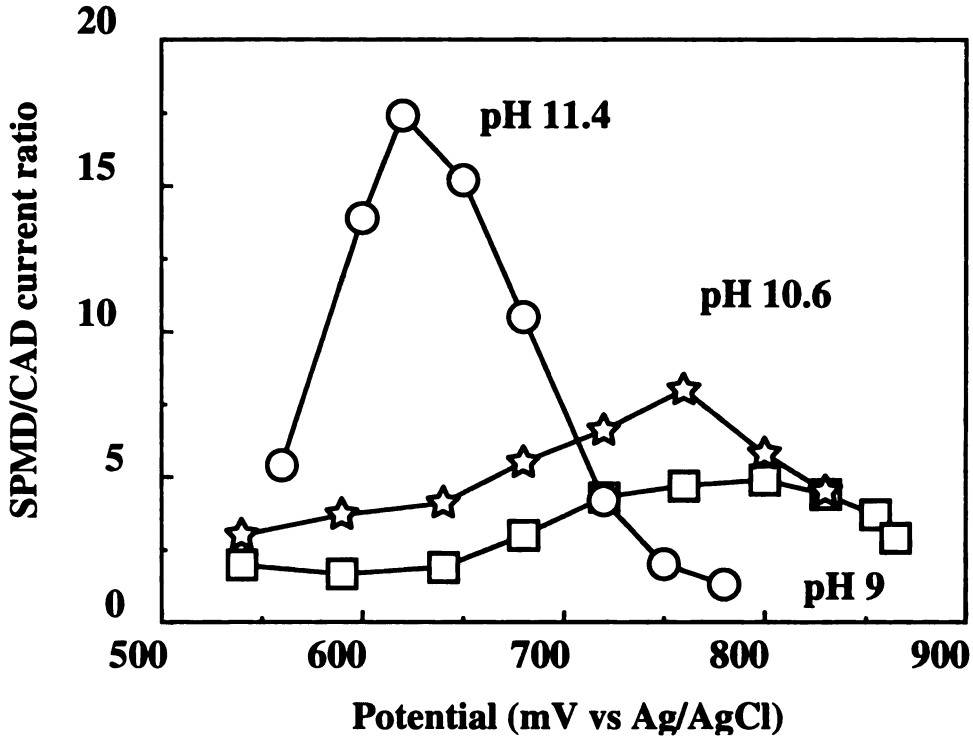

Figure 7.6 Variation of the SPMD/CAD current ratio, as a function of pH of the mobile phase. The carrier solution was 0.01 borax buffer/0.1M NaCl. Microcrystalline diamond films deposited with 0.5% CH_4/H_2 source gas mixture. Flow rate = 1.0 mL/min.

The effect of flow rate on the response magnitude and stability for CAD, PUT, SPMD and SPM was investigated. In the flow rate range between 0.3 and 1.5 mL/min, the background current was insensitive to the flow rate changes at the detection potential of 665 mV (pH 11). The amperometric response, however, for all the amines

was inversely related to the flow rate. The current for 100 μM amine decreased by 30-38 % when increasing the flow rate from 0.5 to 1.5 mL/min. The reproducibility was poorest at the highest and lowest flow rates of 1.5 and 0.3 mL/min (2-4% based on 5 injections). The best reproducibility was obtained at 0.8-1 mL/min (0.5-0.8 % also based on 5 injections). These observations can be explained by slow adsorption of the reactants at the surface or desorption of the reaction product(s).

7.2.2. Calibration Curves

The working curves for each amine were obtained in carbonate buffer, pH 10, as a function of the injected analyte concentration. Plots of log peak height versus log concentration for (A) SPMD and (B) CAD are shown in Figure 7.7. The calibration curves are based on 7 concentrations between 0.32 μM and 1000 μM or 1 μM and 1000 μM. The iInjected volume was 20 μL and flow rate was 1.0 mL/min. The current response at pH 10 increases linearly with the concentration for all four amines. The linear dynamic range for all four polyamines, at all three films, is at least three orders of magnitude ranging from 1.0 to 1000 μM (r^2 > 0.99). A slightly wider dynamic range, down to 0.32 μM was seen for SPM at 0.5% CH_4/H_2. The nominal y-axis intercept of the calibration plots for all four analytes was less than 0.02 μA. The average limits of detection for CAD and PUT are 0.8± 0.05 μM and for SPMD and SPM are 0.30 ± 0.1 μM. The lowest LODs were obtained for films deposited using 0.5% CH_4/H_2.

The working curves for each amine were also obtained in borax buffer, pH 11, using microcrystalline films deposited from a 0.50% CH_4/H_2 ratio with 10 ppm of B_2H_6. Table 7.4 presents summary for the FIA-EC data.

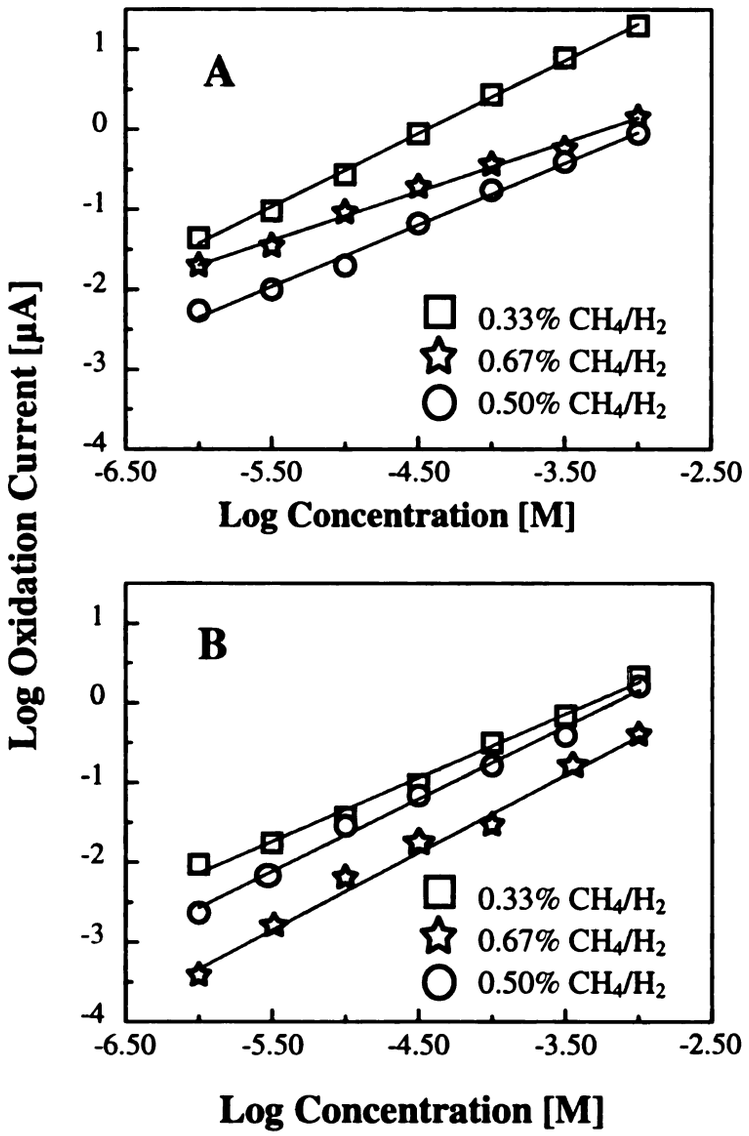

Figure 7.7 Calibration curves obtained for (A) SPMD and (B) CAD at boron-doped microcrystalline diamond films deposited withdifferent CH_4/H_2 source gas ratios. The carrier solution was 0.01M carbonate buffer/0.1M $NaClO_4$, pH 10. Injected volume = 20 μL. Flow rate =1.0 mL/min. Applied potential = +700 mV

Table 7.4 FIA-EC Data for Aliphatic Polyamines Detection at Microcrystalline Diamond Thin-Film Electrode in Borax Buffer, pH 11.2

Polyamine	Linear Dynamic Range	LOD at S/N≥3	Sensitivity (μA/mM)
Cadaverine (CAD)	0.5 μM-1000 μM (r^2= 0.9985)	0.4 μM	0.53
Putrescine (PUT)	0.5 μM-1000 μM (r^2= 0.9992)	0.4μM	0.61
Spermidine (SPMD)	0.5 μM-1000 μM (r^2= 0.9993)	0.1μM	2.97
Spermine (SPM)	0.5 μM-1000 μM (r^2= 0.9994)	0.1μM	4.68

Note:The calibration curves are based on 7 concentrations between 0.5 and1000 μM. Injected volume=20 μL.Flow rate=1.0 mL/min.

The current response and peak charge both varied linearly with the concentration. The linear dynamic range for all four polyamines ranged from 0.5 to 1000 μM (r^2 > 0.99). The limits of detection were lower at pH 11 than at pH10. For example, the average limits of detection for CAD and PUT are about 0.4 μM, and for SPMD and SPM are 0.1 μM. The mass detection limits are 0.8 ng for CAD, 0.7 ng for PUT, 0.3 ng for SPMD, and 0.4 ng for SPM.

The calibration curves were also obtained using boron-doped nanocrystalline diamond films, deposited from a 1/94/5 CH_4/Ar/H_2 (v/v) source gas ratio with 20 ppm of added B_2H_6. Working curves were built at pH 11 for 7 different amines (mono-, di- and polyamines). The results are summarized in Table 7.5, and Figure 7.8 shows the plots of peak heights versus concentration.

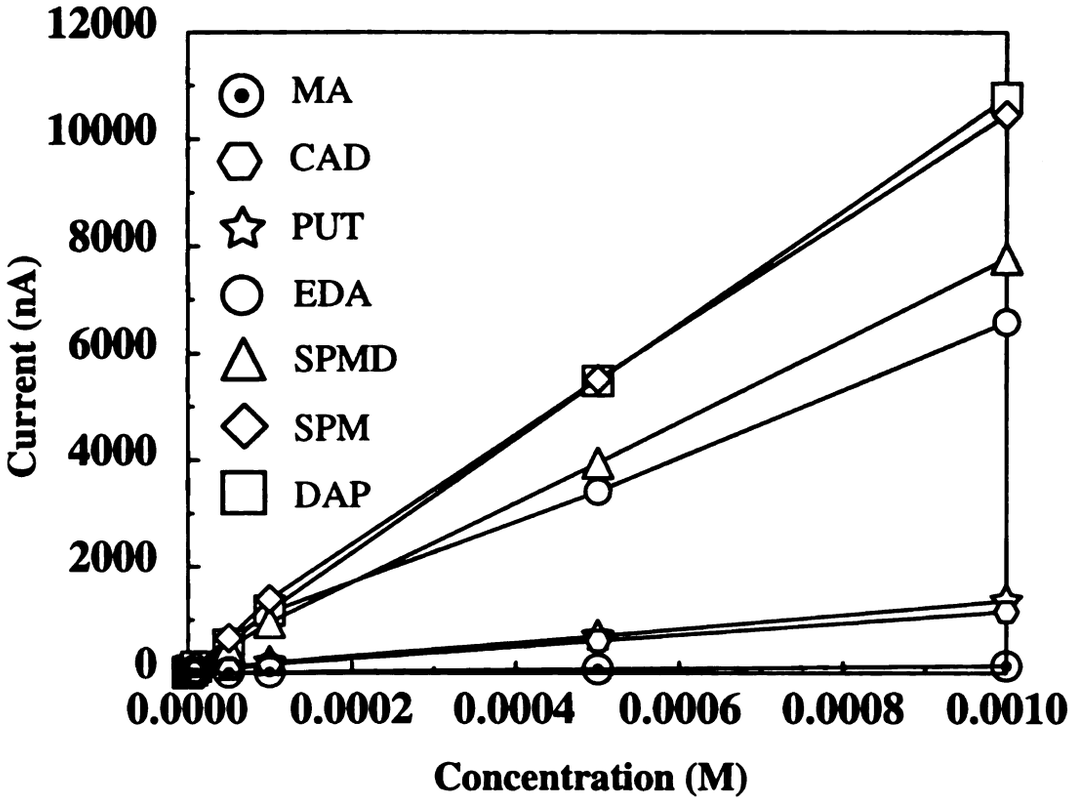

Figure 7.8 Calibration curves for aliphatic amines at a boron-doped nanocrystalline diamond electrode deposited from a 1/94/5 $CH_4/Ar/H_2$ (v/v) source gas ratio with 20 ppm B_2H_6. Injected volume = 20μL. Flow rate = 1.0 mL/min.

The peak current and charge varied linearly with the concentration for all the amines. The LOD for MA is 10μM. The LODs for EDA and DAP are 100 times lower at 0.1μM. The same 0.1 μM LODs are achieved for SPMD and SPM. CAD and PUT would be detectable at 0.3 μM. The mass detection limits are 6 ng for MA, 0.12 ng for EDA, 0.15 ng for DAP, 0.6 ng for CAD, 0.5 ng for PUT, 0.3 ng for SPMD and 0.4 ng for SPM.

Table 7.5 FIA-EC Data for Aliphatic Polyamines at a Nanocrystalline Diamond Thin Film Deposited from a 1/94/5 $CH_4/Ar/H_2$ source gas ratio with 20 ppm B_2H_6.

Polyamine	Linear Dynamic Range	LOD at S/N≥3	Mass Detected	Sensitivity μA/mM
methylamine (MA)	10 μM-1000 μM (r^2= 0.9997)	10 μM (300 ppb)	6.2 ng	0.13
ethylenediamine (EDA)	0.1 μM-1000 μM (r^2= 0.9975)	0.1μM (6 ppb)	0.12 ng	6.37
diaminopropane (DAP)	0.1 μM-1000 μM (r^2= 0.9999)	0.1μM (7.4 ppb)	0.15 ng	10.7
Cadaverine (CAD)	0.5 μM-1000 μM (r^2= 0.9992)	0.3μM (30 ppb)	0.61 ng	1.2
Putrescine (PUT)	0.5 μM-1000 μM (r^2= 0.9988)	0.3μM (26 ppb)	0.53 ng	1.3
Spermidine (SPMD)	0.1 μM-1000 μM (r^2= 0.9998)	0.1μM (15 ppb)	0.29 ng	7.7
Spermine (SPM)	0.1 μM-1000 μM (r^2= 0.9993)	0.1μM (20 ppb)	0.40 ng	10.5

Note:The calibration curves are based on 7 concentrations between 0.1 and 1000 μM. Injected volume = 20 μL. Flow rate = 1.0 mL/min.

The values of sensitivity were analyzed for both types of electrodes: boron-doped nanocrystalline (20 ppm) and microcrystalline (10 ppm). Interestingly, there is a vast difference in the sensitivity factor for each of the polyamines at microcrystalline film. The average sensitivities for CAD and PUT in borax buffer, pH 11, measured at microcrystalline film; are similar, (0.5-0.6 μA/mM see Table 7.4). The sensitivity for SPMD is ~3 μA/mM, and for SPM is 4.7 μA/mM. At pH 11 the response factors at nanocrystalline film deposited with 20 ppm B_2H_6 are about twice larger than that for the microcrystalline film deposited from gas mixture containing 10 ppm B_2H_6. They are 1.2, 1.3, 7.7, 10.5 μA/mM for CAD, PUT, SPMD, and SPM, respectively.

The response factor for nanocrystalline film at pH 11 is the highest for amines: SPMD (3,4), SPMD (3,3), SPMD (2,2), SPM, DAP, EDA, DEP. The lowest is observed for monoamines: MA, PA, EA. For diamine as CAD, PUT, HA, DA sensitivity factor was somewhat in between the highest and the lowest value.

Figure 7.9 shows FIA-EC responses for a multiple injections of 0.1μM amine (a) CAD, (b) EDA, (c) DAP, (d) DA, (e) DEP, (f) SPM, (g) PUT, and (h) SPMD in 0.01 borax buffer/ 0.1 M NaCl, pH11.2. For the same concentration of the amine injected, the diamond responses are dramatically different. The oxidation current obtained at pH11.2 for the different amines, at three different diamond electrodes, was plotted versus the first pK_a value of each amine.

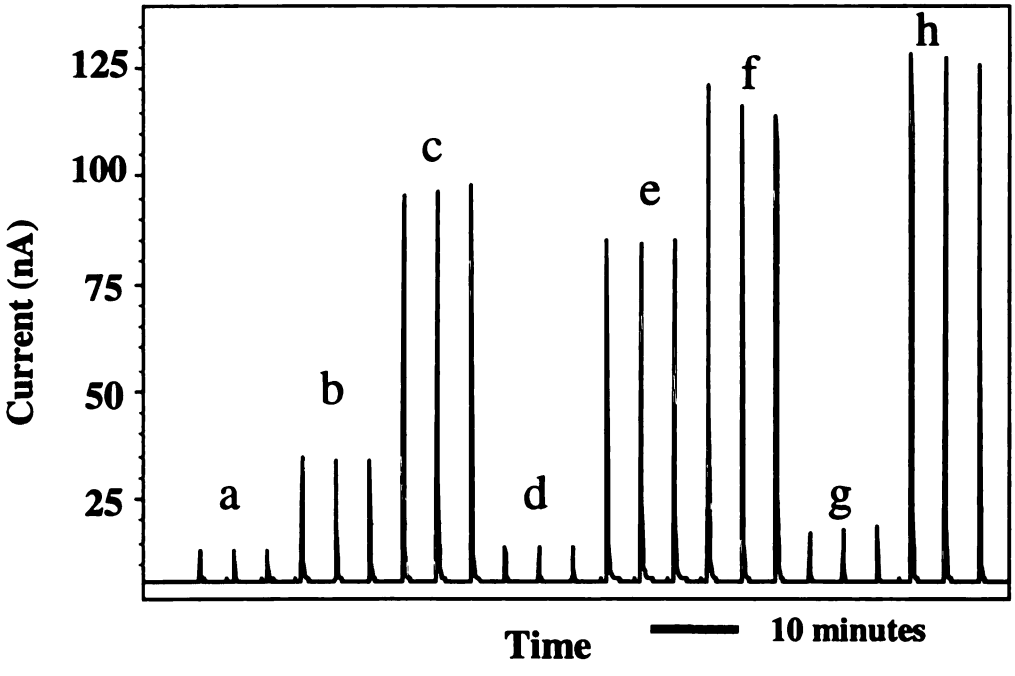

Figure 7.9 FIA-EC responses for a series of 10 μL injections of 0.1μM amine: (a) CAD, (b) EDA, (c) DAP, (d) DA, (e) DEP, (f) SPM, (g) PUT, and (h) SPMD. The carrier solution was 0.01 borax buffer/0.1 M NaCl, pH 11.2. Detection potential=+ 660 mV.

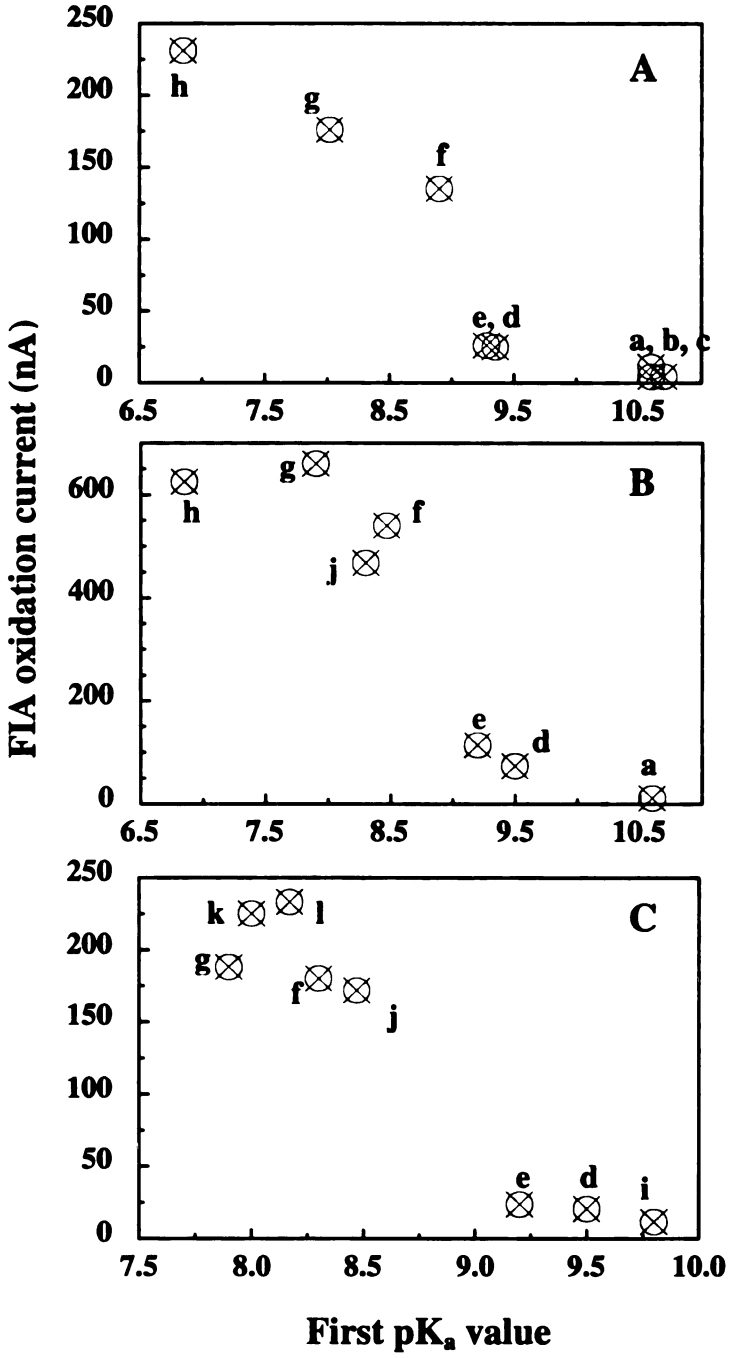

Figure 7.10 Relationship between the FIA peak current and first pK_a for (a) MA, (b) EA, (c) PA, (d) CAD, (e) PUT, (f) SPMD, (g) SPM, (h) EDA, (i) HA, (j) DAP, (k) SPMD (2,2), (l) SPMD (3,3). Data collected at two microcrystalline films for 0.1 mM amines (Fig.A and C), and a nanocrystalline film for 0.5 mM amines (Fig. B).

Figure 7.10 shows relation between the current and first pK_a at (A) and (C) microcrystalline films for 0.1 mM amines, and (B) nanocrystalline film for 0.5 mM amines. A good relationship was observed for all amines, suggesting that for analytes with the lowest dissociation constant, the highest electrode response is observed. It was observed for microcrystalline and nanocrystalline diamond films. The discrepancies in the electrode response may be partially explained based on differences in fraction of amine present in unprotonated form, available for oxidation. For instance, at pH 11, there will be 60, 65, 61, 91, and 92 % of deprotonated MA, PUT, CAD, DAP, and EDA, respectively. For polyamines it will be even more complicated, because both, primary and secondary amines will be available for oxidation.

The FIA results show, also that the amine oxidation current decreases with increasing molecular size, within the same classification group. For example, for monoamines (MA, EA, and PA) the amperometric response for a 0.1 mM concentration was 11.5 ± 0.3, 4.7 ± 0.3, 4.5 ± 0.4 nA, respectively. Even more significant differences were observed for diamines. The signal was 231.3 ± 1.2, 26.3 ± 0.1, and 25.1 ± 0.1 nA for EDA, PUT and CAD. Another possible explanation for observed differences in sensitivity factors may be related to steric differences of amine (i.e. amine orientation, nature and number of amino-group). Different energies required for amine-boron complex formation, as well as stability of these complexes. The nature and stability of the boron-amine complexes was not studied, though and will remain for future considerations.

7.2.3. Response Variability and Stability

A major weakness of the assay in the preliminary studies we conducted was the unacceptably large response variability of 15-25% at electrodes deposited from a 1% CH_4/H_2.[188,259] We also observed, that when injections of the aliphatic polyamine were

made with high frequency (every 1 minute), the amperometric response decreased by as much as 30-50% during the initial 10 injections. Thereafter, the response stabilized. The magnitude of the attenuation tended to be similar for each of the polyamines. It was generally much less at a 0.50% than at a 1% or 0.33% CH_4/H_2 film. Figure 7.11 shows an extreme example of this at as "deposited" 0.33% CH_4/H_2 film.

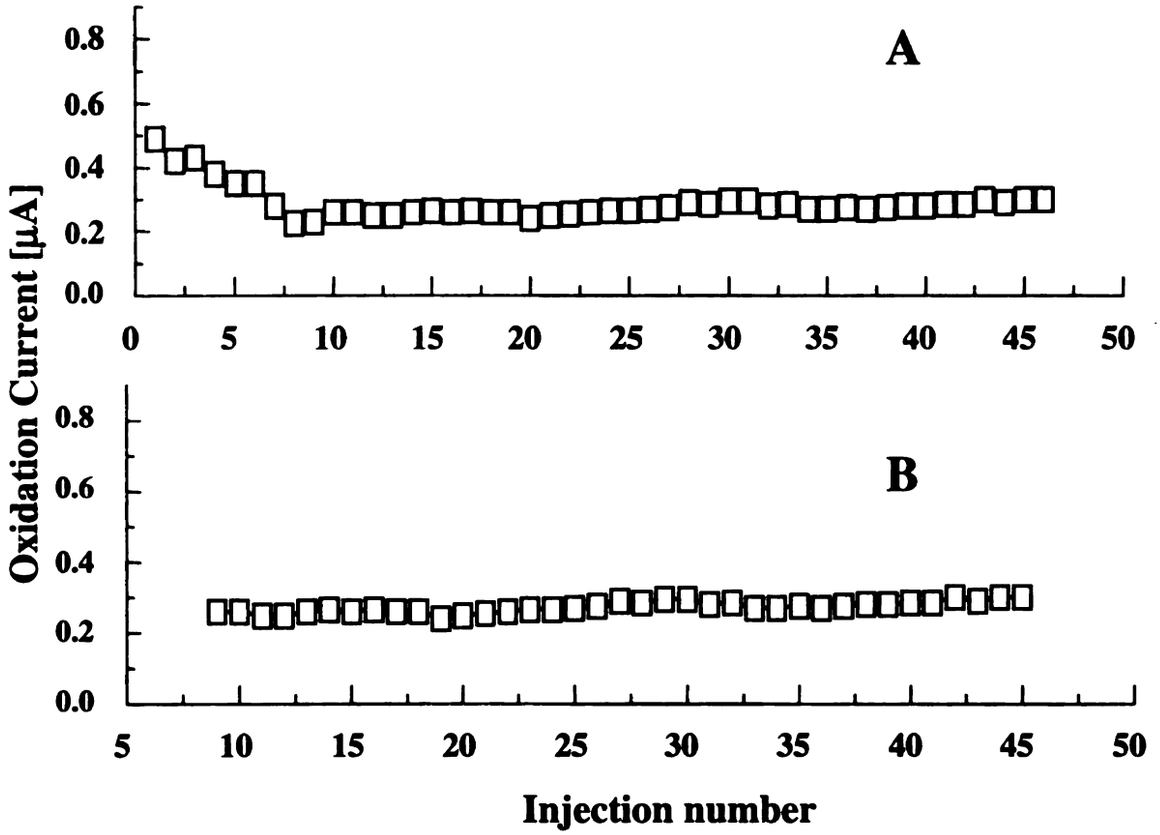

Figure 7.11 FIA-EC responses for a multiple injections of 1.0 mM CAD at as "deposited" 0.33% CH_4/H_2 diamond film. The carrier solution was carbonate buffer pH10. Detection potential=+ 810 mV. Injection volume=20 μL. Flow rate=1.0 mL/min.

The response for 1.0 mM CAD is attenuated during the first eight injections by about 60%. The peak height variability for all 46 injections is 18%. However, after the first eight injections the response stabilizes. Thereafter, the peak height variability is 5.6%.

The response variability at all types of diamond films was significantly reduced simply by adding a 3-6 min delay period between injections. It is supposed that this time allows for desorption of the reaction product from surface boron-sites, making these sites available for adsorption/coordination of new reactant molecules. Nominally at the films deposited from a 0.5% CH_4/H_2 ratio the response variability ranges from 2 to 8% for all injections made with a 3-6 min delay. The largest variability of 8% is seen for PUT. Films deposited from 0.33% and 0.67% CH_4/H_2 ratios show greater variability, but well-controlled delay times between injections were not used to obtain the presented data. With controlled delay periods of 3-6 minutes the variability was in the range of 7-10 %. Table 7.6 presents a summary of the response variability for aliphatic amines obtained at microcrystalline diamond electrodes. The number of injections used in the statistical analysis is shown in parentheses.

Table 7.6 FIA-EC Response Variability Data for Aliphatic Polyamines at a Microcrystalline Diamond Thin Film

Polyamine	Response Variability (% RSD)		
	0.33% CH_4/H_2	0.50% CH_4/H_2	0.67 % CH_4/H_2
Cadaverine (CAD)	6.7% (70)	5.0% (90)	20.8% (131)
Putrescine (PUT)	15.0% (80)	7.5% (118)	9.7% (50)
Spermidine (SPMD)	7.3% (50)	5.0% (104)	15.9% (39)
Spermine (SPM)	13.1% (90)	3.0% (40)	-----

Figure 7.12 A and B shows a series of responses of 1.0 mM CAD and SPMD, respectively, at an extensively used 0.50% CH_4/H_2 film. By extensively, we mean use over many days and hundreds of injections. Detection was made at 855 and 780 mV,

respectively in carbonate buffer, pH 10. The first important observation is that the response is quite stable with no progressive response attenuation. This is because the decrease only seems to occur during the first few injections at a new electrode, not at a used one.

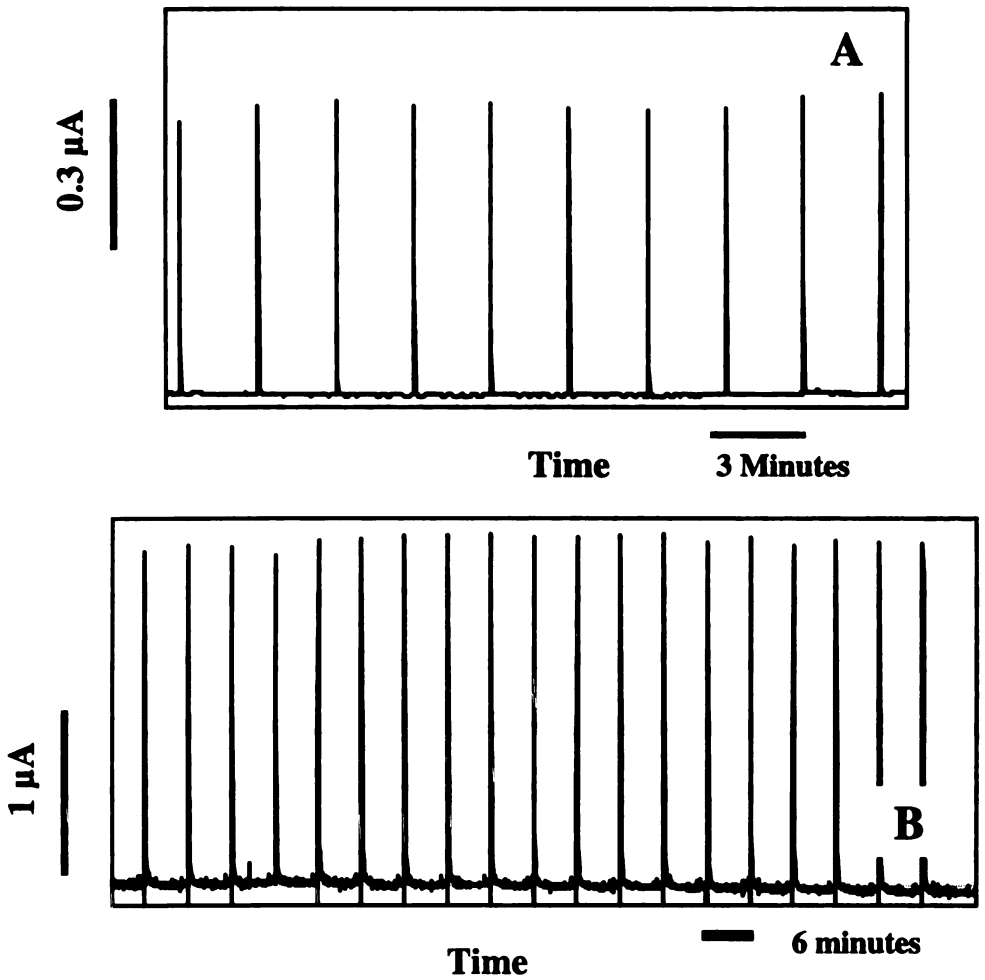

Figure 7.12 FIA-EC responses for a multiple injections of **(A)** 1.0 mM CAD and **(B)** 1.0 mM SPMD at a well "conditioned" 0.50% C/H film. The carrier solution was CBpH10. A detection potential=855 mV and 3-minute delay between injections was used for CAD. A detection potential=780 mV and a 6-minute delay between injections was used for SPMD. Injection volume = 20 µL. Flow rate = 1.0 mL/min.

A second observation is that a delay time of 3 min between injections gives an acceptable response variability of 3.2% (n=17 injections) for CAD and a delay time of 6 min gives a slightly improved value of 2.8% (n=16 injections) for SPMD. These variabilities are lower than those reported in Table 7.6, because these electrodes were extensively used and there was no response attenuation during the first few injections. Values of 2-4% were commonly observed for all four polyamines at extensively used electrodes. In general, there was not a significant improvement in the response variability for any of the analytes when increasing the delay time between injections from 3 to 6 min. At best, the variability was improved by 0.5-1.0%.

For comparison the amine oxidation response at highly oriented pyrolytic graphite (HOPG) and glassy carbon (GC) electrodes was also studied. Figure 7.13 shows the response variabilities for these two electrodes and a diamond electrode at the detection potential of 655 mV. The first observation is that the signal for 1 mM CAD and SPMD at HOPG and GC is much smaller than that for boron-doped nanocrystalline diamond. The currents are about 150 nA and 260 nA at HOPG, and 50 nA and 150 nA at GC for 1 mM CAD and 1 mM SPMD, respectively. The current at diamond is about 30 nA and 50 nA for 0.1 mM CAD and 0.025 mM SPMD, respectively. The differences in current are due to couple of factors. First, the surface boron sites are not present on either HOPG or GC. The absence of these sites is leading to a short residence time for attack by OH•. Second, most of the OH• generated probably reacts with the surface of the electrode (i.e., edge plane sites) or is consumed in oxygen evolution reaction. The increasing background current may very likely suggest that. Even if some interactions of the amine with carbon-oxygen functional groups are possible, the driving force for the OER at GC and oxidation of the GC surface at this potential are much greater than OTR.

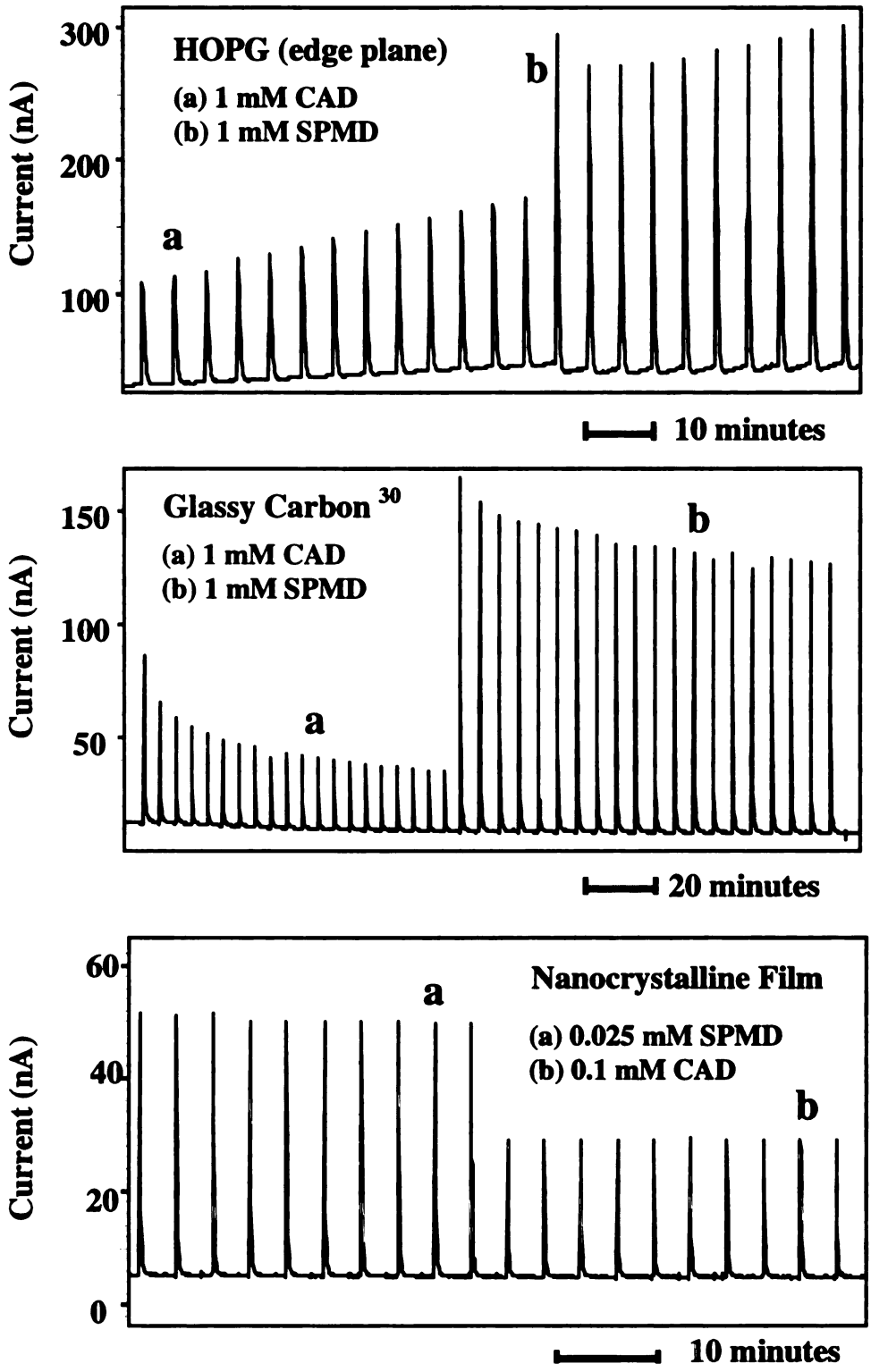

Figure 7.13 FIA-EC responses for a multiple injections of CAD and SPMD at a HOPG, GC and a nanocrystalline boron-doped diamond thin-film electrode. Applied potential=655 mV vs Ag/AgCl. Flow rate = 1.0 mL/min.

The second observation is the attenuation and variability in the signal at GC and HOPG electrodes. Both of these electrode microstructures are unstable in alkaline media at these detection potentials, and are easily oxidazed.[62] What is interesting though is the dramatic difference in the oxidation response variability for each electrodes. For HOPG the amine response increases with the injection number at HOPG, but for GC, the response decreases. It was shown that electrochemically induced corrosion occurs at HOPG in acidic medium.[62,304] HOPG undergoes oxidation, intercalation, delamination, and exfoliation.[304,305,62] These processes can result in alteration of the surface microstructure and an increase of the active area. GC does not undergo as much microstructural changes as HOPG so the active area remains fairly constant. The response at GC likely decreases, due to fouling by reaction products. Reaction products likely adsorb on HOPG as well, but since the active area increases with time, the response does not decrease but actually shows an increase. The boron-doped diamond films possessed the proper structure-function relationship for stable and reproducible oxidation of aliphatic amines.

The long-term response stability of an extensively used 0.50% CH_4/H_2 film was examined. For this specific test, injections of 1.0 mM CAD were made over a 10 h period of continuous use. The background signal during this period remained low and unchanging even at this positive detection potential. This is due to the excellent morphological and microstructural stability of the material. The peak height changed by less than 8% (n = 100 injections) over the period. Also, there was no progressive loss of signal due to any kind of permanent electrode fouling, as is the case for other electrodes.

The reproducibility and stability studies of amine oxidation were also performed for boron-doped nanocrystalline diamond electrodes. Figure 7.14 shows a series of

responses of 0.1 mM CAD, PUT, SPMD and SPM at a nanocrystalline film deposited from 1/94/5 $CH_4/Ar/H_2$ (v/v) ratio and 1 ppm B_2H_6.

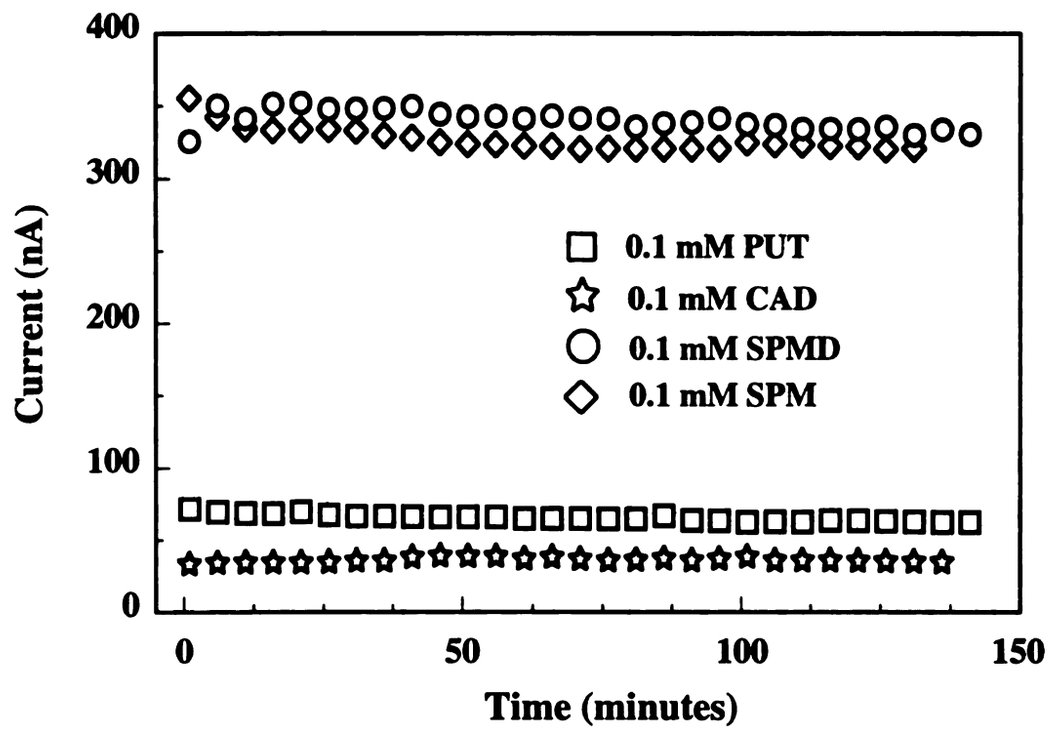

Figure 7.14 FIA-EC responses for a multiple injections of 0.1 mM CAD, PUT, SPMD and SPM at a boron-doped nanocrystalline film deposited from 1/94/5 $CH_4/Ar/H_2$ (v/v) ratio with 1 ppm of added B_2H_6. The carrier solution was borax buffer pH 11. Applied potential=+665 mV. Injection volume of CAD and PUT = 30μL, and SPMD and SPM = 10μL. Flow rate = 1.0 mL/min.

The response is quite stable with no progressive response attenuation. The decrease only seems to occur during the first few injections for SPM. The response variability of the peak height was 3.5, 3.1, 2.1, and 3.3% for PUT, CAD, SPMD, and SPM respectively, based on 30 injections. Similar results were observed for other nanocrystalline films, deposited from 10 and 20 ppm B_2H_6. Response varied by 3-5%

during 20-30 injections. The response stability was measured for 0.05 mM DAP during a 7-h period of use. The background signal during that period remained low and stable. Figure 7.15 shows a series of 11 responses. The peak variability was 5%.

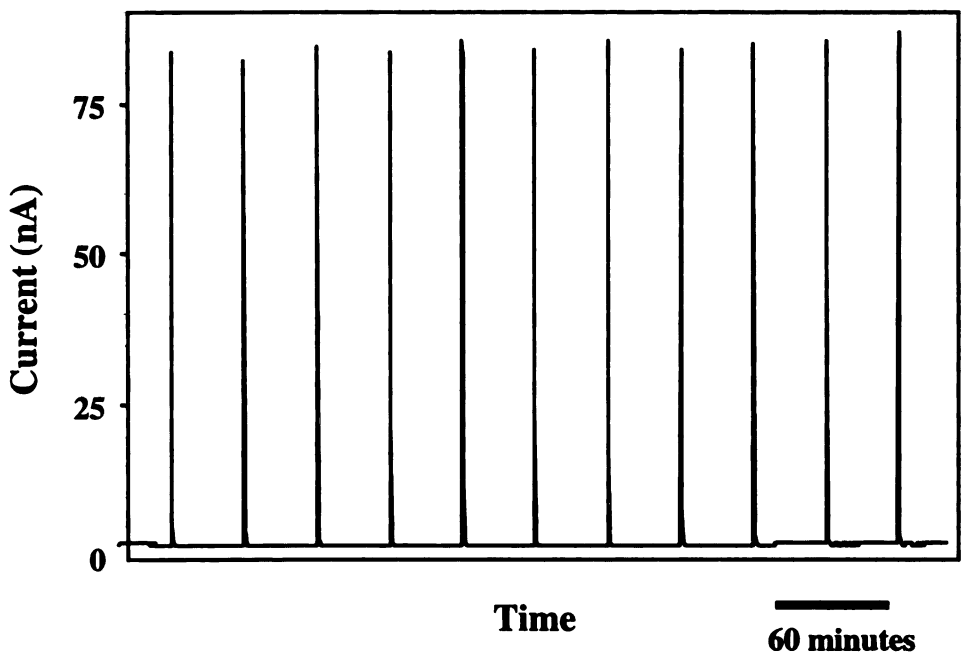

Figure 7.15 FIA-EC series of responses for 0.05 mM DAP at a boron-doped nanocrystalline thin film deposited from a 1/94/5 $CH_4/Ar/H_2$ (v/v) ratio and 10 ppm B_2H_6. The carrier solution was borax buffer, pH 11. Applied potential=+665 mV. Injection volume = 10 µL.

7.3. Conclusions

It has been shown that aliphatic polyamines can be quantitatively electrooxidized and detected at boron-doped nanocrystalline and microcrystalline diamond thin-film electrodes. FIA-EC results indicate that cadaverine, putrescine, spermidine, and

spermine can be detected stably and reproducibly at constant potential in alkaline media. The reproducibility of the assay, in terms of the linear dynamic range, limit of quantitation and response variability, was best for microcrystalline films deposited from 0.50% CH_4/H_2 ratio (i.e., films with the optimum balance of localized non-diamond sp^2-carbon impurities and surface boron sites). There was correlation observed between amine oxidation electrode response (current) and the boron-doping level (i.e., surface boron-sites) in the microcrystalline and nanocrystalline diamond film. The highest signals and sensitivity values in FIA were observed for highly boron doped nanocrystalline diamond films (20 ppm). Therefore, these films or films with even higher boron-doping are the best performing for the aliphatic amine detection assay. The linear dynamic range for most of the amines was 4 orders of magnitude. In general, the limits of detection (LOD) for EDA, DAP, SPMD, and SPM were 0.1μM. A 0.3 μM LODs were observed for CAD and PUT. Monoamine (methylamine) was detected at 10 μM level, however, an increase in the electrolyte pH would likely increase the sensitivity and improve the LOD for this analyte. The response variability was vastly improved over previous work by introducing a 3 to 6 minute delay period between injections. Typical peak height variabilities were in the 2 to 4 % range for both microcrystalline and nanocrystalline diamond. The long-term stability was excellent over a 7 or 10-h period of continuous use with no evidence for permanent electrode fouling by the reaction product(s) for nanocrystalline and microcrystalline films.

The advantage of using diamond electrode is that no derivatization, pH adjustment of the carrier solution or pulsed waveform is necessary for detection. The detection figures of merit at diamond are as good or superb to data for other electrode materials reported in the literature. Table 7.7 summarizes some of the literature FIA-EC and LC-EC results for aliphatic amines. A limited amount of data has been reported for

CAD, PUT, SPMD, and SPM. There are examples of these analytes being separated and detected, but to the best of our knowledge, there has been no complete set of FIA-EC or LC-EC data published. Most of the data are for EA and DAP.

Table 7.7 FIA-EC Data for Aliphatic Mono- and Diamine

Material	Detection Method	Amine	Limit of Detection (μM)	Response Variability (RSD %)	Reference
Anodized Ag-PbO_2	amperometric detection	DAP	0.3 (6 pmol)	4.7 % 45 hrs, (540 inj.)	54
Gold	PAD	DAP	0.1 (4 pmol)	not given	31
Gold	ISWD	DAP	0.01 (0.5pmol)	0.5% (7 inj.)	31,32
Ni-GC	amperometric detection	CAD	0.8 (3.8 pmol)	4 % (7 hrs) 2% (22 inj)	34
Copper	amperometric detection	EA	0.4 (8 pmol)	3.0 % (5 inj.) short term stability	231
Nickel	amperometric detection	EA	1.0 (20 pmol)	3.0 % (5 inj.) short term stability	231
Platinum	amperometric detection	EA	60 (1.2 nmol)	3.0 % (5 inj.) short term stability	231
Cobalt	amperometric detection	EA	70 (1.4 nmol)	very short-lived	231
diamond	amperometric detection	CAD PUT	0.3 (6 pmol)	3-5% 20 inj.	This work
diamond	amperometric detection	DAP SPMD SPM	0.1 (4 pmol)		This work

Diamond provides comparable detection figures of merit to those reported for DAP.[31-33,54] Data for the amperometric detection of EA (pH 11) at diamond provide

higher LOD than that for copper and nickel electrodes. They are better than that for platinum and cobalt oxide electrodes. Diamond, however, provides superior stability. The limits of detection for diamond are very much the same, or better than what has been achieved for Ag-PbO_2 alloy electrode.[54] The pulsed amperometric detection (ISWD) [32] mode using gold provides one orders of magnitude lower limits of detection for DAP, however detection of CAD and PUT has been shown to be much lower at diamond.[29,33]

The key finding from these studies is that aliphatic polyamines can be electrooxidized and detected at boron-doped microcrystalline and nanocrystalline diamond films. Both of these materials provide stable and reproducible response for amine oxidation in alkaline medium. Both of these materials provide good limits of quantitation for diamines and polyamines. Electrochemical detection using diamond provides advantage of direct assay for monitoring of amines. Amine can be detected without need of derivatization or pH adjustment of the mobile phase. Simple amperometric detection mode is a suitable technique for this assay, no pulsed waveform is necessary as is the case of gold electrode.

Chapter 8

REVERSED-PHASE HPLC SEPARATION AND AMPEROMETRIC DETECTION OF ALIPHATIC POLYAMINES AT BORON-DOPED DIAMOND THIN-FILM ELECTRODES

8.1. Introduction

Few electrochemical assays for aliphatic amine detection have been reported in literature. The most successful ones involved noble and transition metal electrodes, alloy composite electrodes, and chemically modified electrodes.[34] The Johnson group demonstrated the effective separation and detection of several polyamines with a detection limit of 200 pmole for putrescine, using an ion exchange-liquid chromatography coupled with pulsed amperometric detection (PAD).[29,31,33] PAD at Au electrodes, while highly useful, is somewhat complicated to implement and, even though the detector is commercially available, detection at constant applied potential is rather the method of choice for many routine analyses. Stable amperometric detection of aliphatic polyamines was observed at metal alloy composite electrodes (e.g., Ag-PbO_2).[54,55]

The results described herein constitute the last phase of the polyamine assay development at diamond electrodes – liquid chromatographic separation and amperometric detection. The first phase of the work involved a cyclic voltammetric study of the electrooxidation of PUT, CAD, SPMD and SPM at boron-doped diamond electrodes. An oxidation reaction mechanism was proposed and some of the electrode properties influencing the amine oxidation response were highlighted. Clearly, boron-doped, polycrystalline diamond thin-film electrodes possess the requisite properties for stable, sensitive, and reproducible detection of aliphatic polyamines at constant applied potential. The next phase of the work involved a detailed flow-injection analysis investigation of the amperometric detection, at constant applied potential, of the four polyamines.

The reversed-phase liquid chromatographic separation of the polyamines coupled with amperometric detection is described herein. The goals were to: (i) optimize the reversed-phase separation (isocratic) of PUT, CAD, SPMD, and SPM, and (ii) complete a comprehensive evaluation of the analytical detection figures of merit for the four polyamines in the amperometric detection mode.

8.2. Results and Discussion

8.2.1. Cyclic Voltammetry and Flow Injection Analysis

Figure 8.1 shows cyclic voltammetric i-E curves in borax buffer, pH 10.6 at microcrystalline diamond film deposited from a 0.4% CH_4/H_2 ratio. There is anodic current passed between 550 and 950 mV during the first scan, which is not present in subsequent scans. This current is likely associated with the irreversible oxidation of the diamond surface, involving replacement of some surface hydrogen atoms with chemisorbed oxygen functionalities (e.g., OH).[185,306,307] The current at 1100 mV is due

to oxygen evolution. After the initial one, the scans are stable with multiple sweeps between 200 and 1100 mV. The low and steady background current results from the morphological and microstructural stability of diamond.[163]

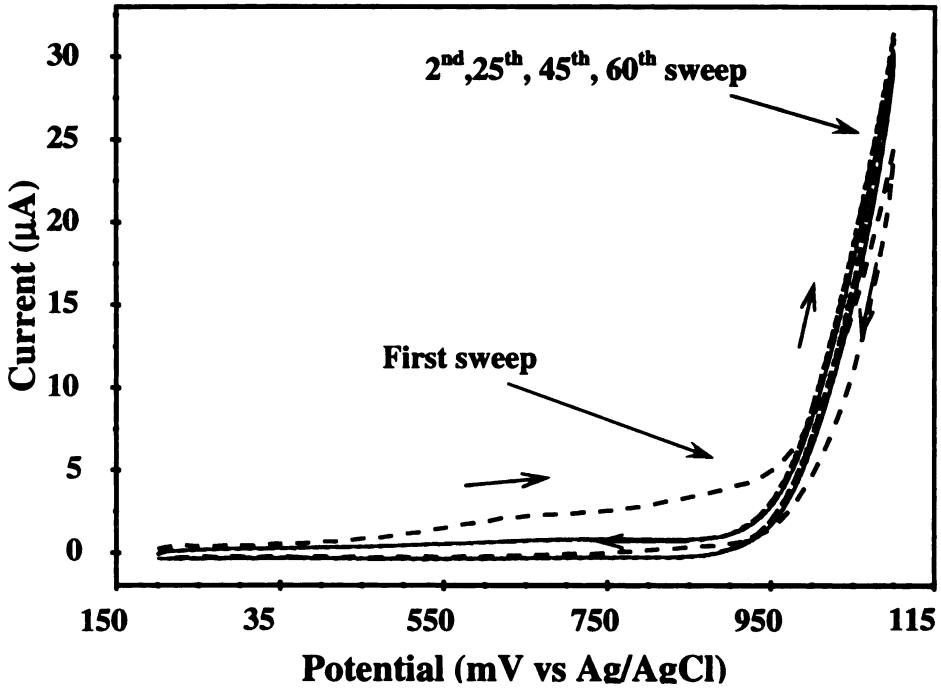

Figure 8.1 Background cyclic voltammetric i-E curves in 0.01 M borax buffer, pH 10.6, for a boron-doped microcrystalline diamond film deposited from a 0.4% CH_4/H_2 ratio. Presented are the 1st, 2nd, 25th, 45th, 60th scans. Scan rate = 0.1V/s. Electrode area = 0.2 cm^2.

Figure 8.2A presents a background current-time plot for a diamond thin-film electrode in borax buffer, pH 11.2, and acetonitrile (93/7 v/v) at 665 mV. The flow rate was 1 mL/min. The measurements were made in the thin-layer flow cell and the plot reveals the time dependence of the background current after detector turn-on. The background current stabilizes quickly, reaching a constant value in less than 2 min. The mean value of the current after stabilization is about 11 nA and the peak-to-peak

variation is less than 120 pA. The background current for diamond is lower than that for glassy carbon, and remained low and stable with time. By way of comparison, the

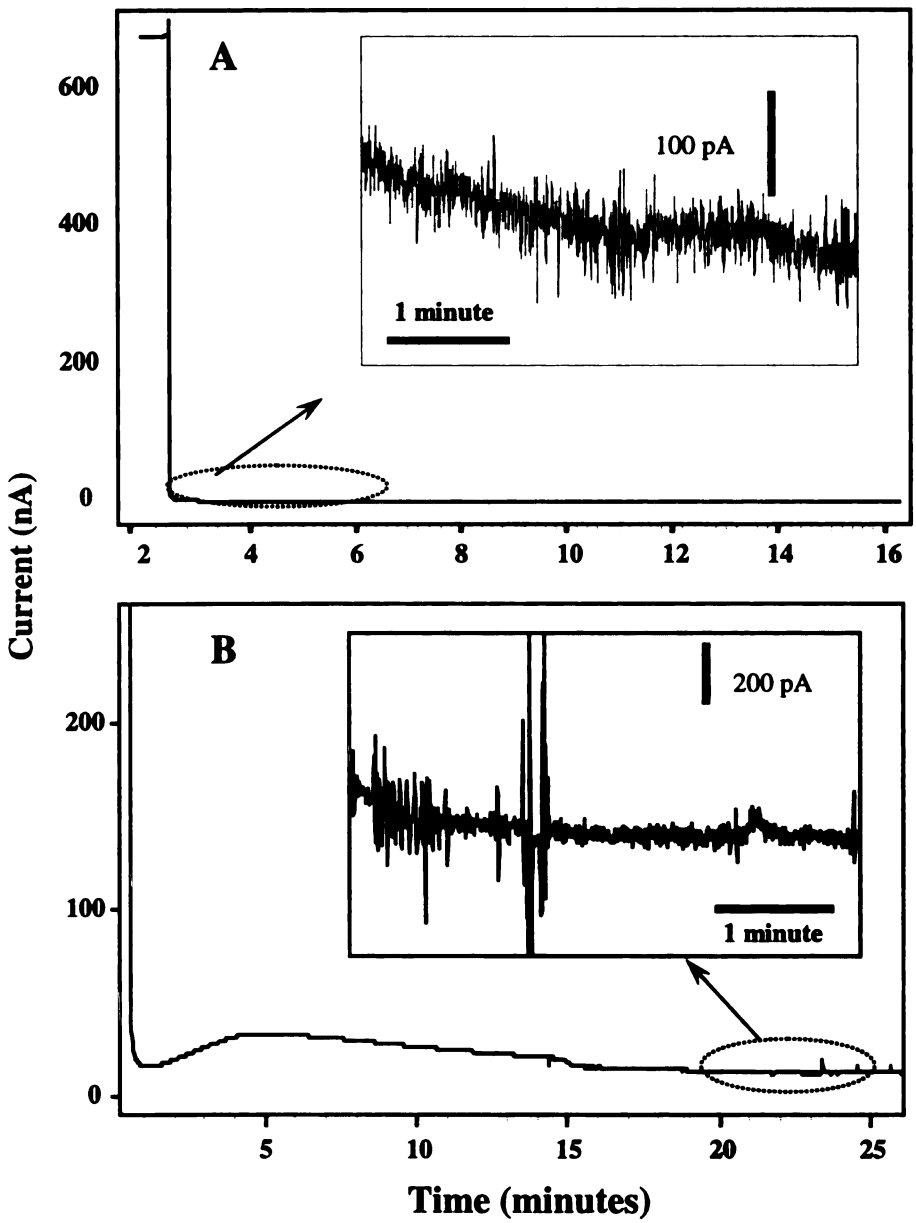

Figure 8.2 Background current-time profile in FIA after detector turn-on for (A) a microcrystalline diamond and (B) glassy carbon.[30] The carrier solution for diamond was 7/93 (v/v) acetonitrile/borax buffer, pH 11.2. The carrier solution for GC was borax buffer, pH 11.2. Detection potential = 665 mV vs Ag/AgCl. Electrode area = 0.08 cm^2. Flow rate = 1 mL/min.

stabilization time for glassy carbon, under similar conditions (in borax buffer, pH 11.2 only), is about 20 min, as seen in Figure 8.2B. The current initially decreases as the double layer charging reaches completion. This is followed, however, by an increase in the current reaching a maximum at about the 5-min mark. The current then slowly decays over a 15 min period before stabilizing at approximately 20 nA after 20 min. The peak-to-peak variation in the signal ranges from a low 200 pA to a high of 800 pA. A rapid stabilization time, and a low and stable background current are characteristic features of diamond electrodes.[163]

Figure 8.3 shows cyclic voltammetric i-E curves for 1 mM solutions of CAD and SPMD (0.01M borax buffer, pH 11.2) at a boron-doped microcrystalline diamond thin film.

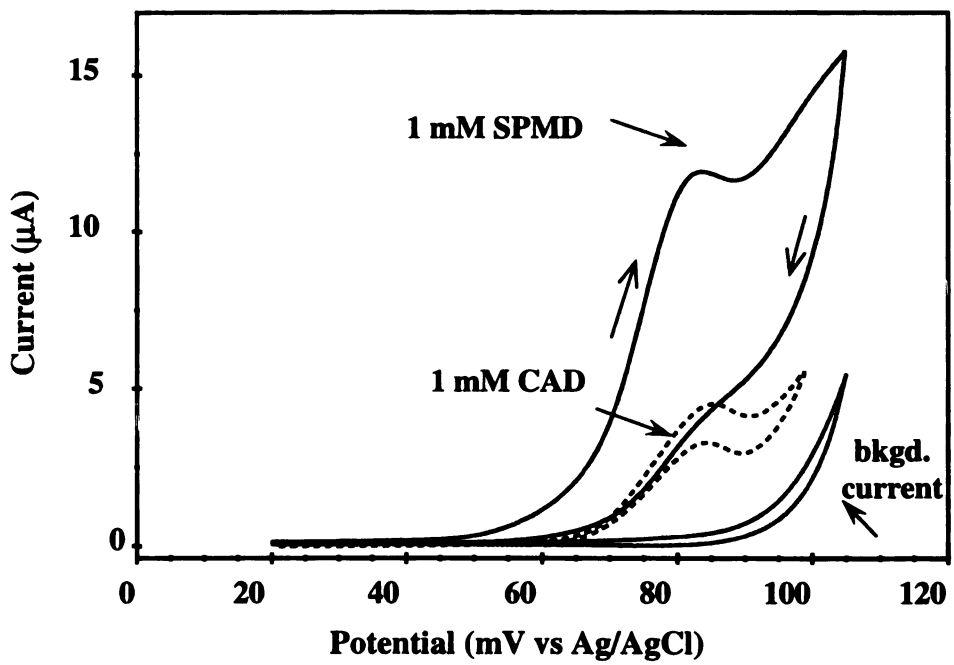

Figure 8.3 Cyclic voltammetric i-E curves for 1 mM CAD and 1 mM SPMD in 0.01 M borax buffer, pH 11.2, along with the corresponding background current, for a boron-doped microcrystalline diamond film deposited from a 0.4% CH_4/H_2 ratio. Scan rate = 0.1 V/s.

The corresponding background voltammogram is also shown, for comparison. The background current is low at potentials negative of 850 mV (1.6 μA at 700 mV and 3.3 μA at 850 mV). At about 850 mV, the current sharply increases due to the onset of oxygen evolution. The background current at potentials negative of 850 mV is associated with charging of the electric double layer and surface faradaic processes.

An irreversible anodic oxidation wave near 800 mV is observed for both CAD and SPMD, as was seen for the other two aliphatic polyamines (data not shown). The well-defined peak is typical for the oxidation of aliphatic polyamines in alkaline media, pH≥10, for boron-doped diamond thin-film electrodes.[188,259] E_p^{ox} is 855 and 845 mV, respectively, for CAD and SPMD, with corresponding i_p^{ox} values of 45 and 118 μA. The signal-to-background ratio is about 14 for CAD and 36 for SPMD. Most interesting is the fact that i_p^{ox} for SPMD is ~2.5 times greater than for CAD. The higher current is presumably due to a larger number of electrons being transferred per molecule.

The electrode response for amines was also studied in the presence of acetonitrile as this solvent was used as the organic modifier for the reversed-phase separation discussed below. Cyclic voltammetry was employed to confirm that the organic modifier had no adverse effect on the amine oxidation response. The voltammograms were recorded in a 7% acetonitrile/borax buffer solution (v/v). Figure 8.4 shows cyclic voltammetric i-E curves for 0.1 mM solutions of CAD for a microcrystalline boron-doped diamond film in (A) 0.01 M borax buffer, pH 10.6, and (B) 93/7 (v/v) 0.01 M borax buffer, pH 10.6 /CH_3CN. The E_p^{ox} values are 960 and 930 mV without and with added CH_3CN, respectively. Most importantly, the i_p^{ox} values, 15-17 μA, are unchanged, indicating that the organic modifier does not adversely affect the response. The background current, however, was slightly higher with the added acetonitrile.

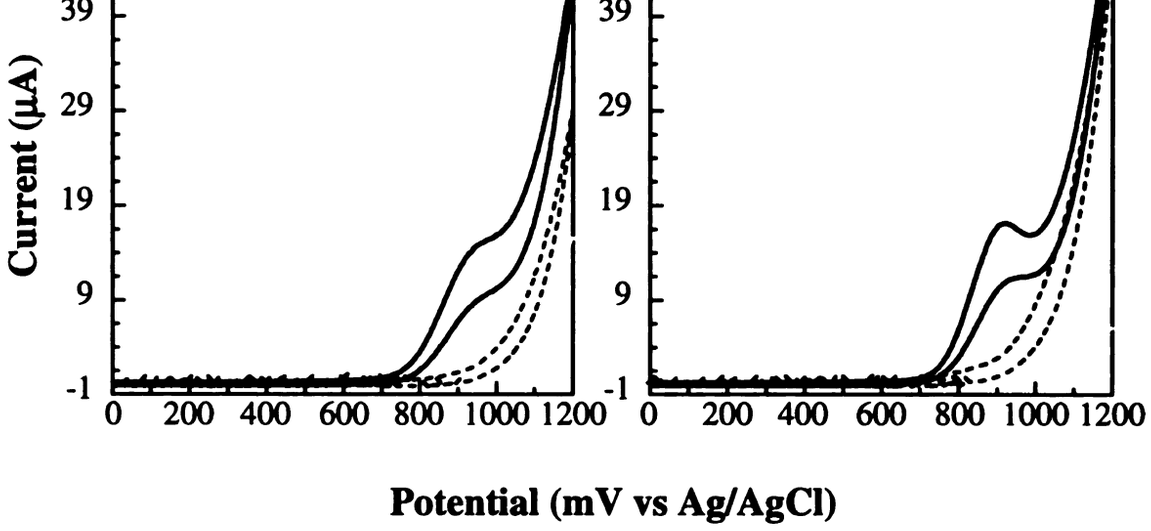

Figure 8.4 Cyclic voltammetric i-E curves in 0.1 mM CAD plus (A) 0.01 M borax buffer, pH 10.6, and (B) 93/7 (v/v) 0.01 M borax buffer, pH 10.6 / CH_3CN, for a boron-doped microcrystalline diamond film deposited from a 0.4% CH_4/H_2 ratio. Scan rate =0.1 V/s.

Flow injection analysis with electrochemical detection (FIA-EC) was used to initially evaluate the electrode performance in (7/93 v/v) acetonitrile/borax buffer, pH 11.2. The flow rate was 1 mL/min. Figure 8.5 A shows hydrodynamic voltammograms for the four different polyamines. The background current at the different potentials is also shown, for comparison. Each marker represents the average signal for 4 injections, and the standard deviations are within the size of the marker. The response increases for all the polyamines as the potential is made more positive. As discussed previously, the curves do not exhibit a limiting current as the reactions are not purely mass transport limited, but rather are controlled by the adsorption of the polyamine and reaction with electrogenerated OH•. The signal for PUT is 6.1 nA at 565 mV and increases to 80.7 nA at 665 mV. The background current is 2.9 nA at 565 mV and increases to only 7 nA at

665 mV. The background current at potentials higher than 695 mV was somewhat unstable, due to the water discharge reaction.

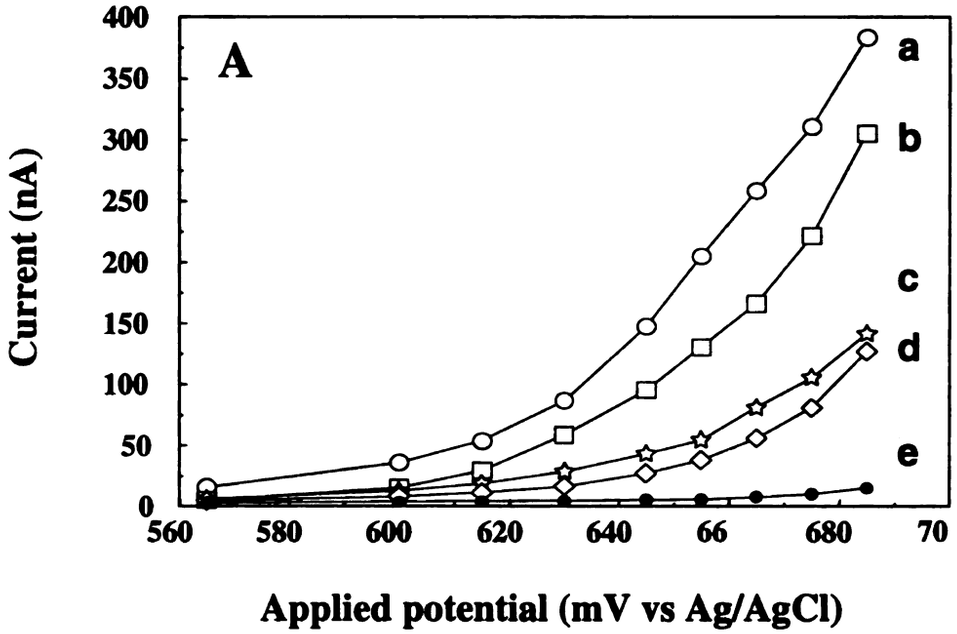

Figure 8.5 A Hydrodynamic voltammetric i-E curves for a boron-doped microcrystalline diamond film (0.4% CH_4/H_2 ratio), in 100 μM (a) SPM, (b) SPMD, (c) PUT, and (d) CAD. The carrier solution was 7/93 (v/v) acetonitrile/borax buffer, pH 11.2 (e). Injection volume = 20μL.

Figure 8.5 B shows plots of the signal-to-background (S/B) ratio as a function of the potential. These plots are useful for determining the optimum detection potential in cases, like this one, where a well-defined sigmoidal hydrodynamic voltammogram is not observed.[259,291] The maximum S/B for CAD, PUT, SPMD, and SPM is 9.2, 10.6, 24.8, and 38.7, respectively, all at 665 mV. The S/B ratio for CAD and PUT is approximately the same, ~10, while the value for SPMD is approximately two times (~20), and for SPM

is approximately four times greater (~40). This reflects a greater number of electron transferred per molecule for SPMD and SPM.

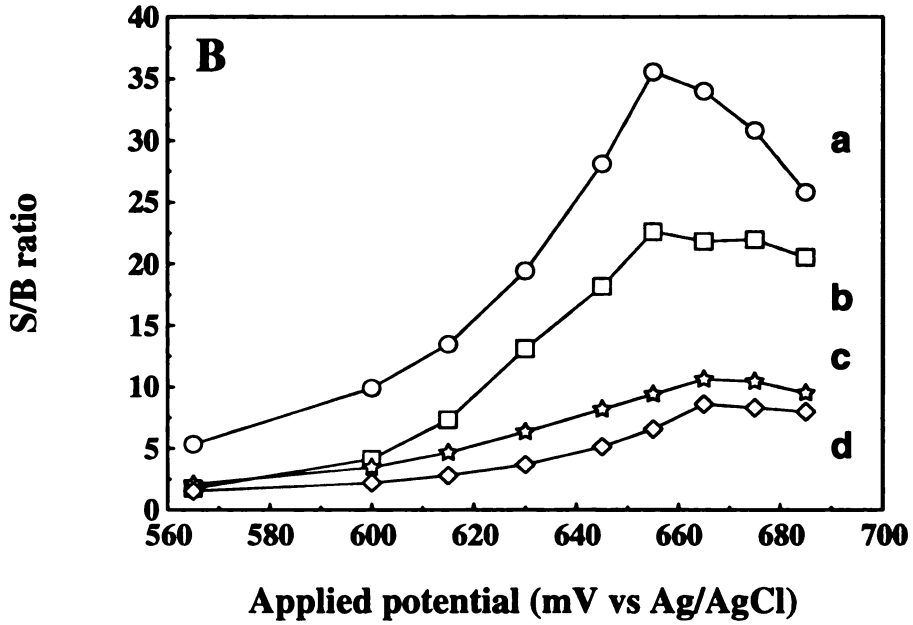

Figure 8.5 B Plots of the S/B ratio versus the applied potential for a boron-doped microcrystalline diamond film (0.4% CH_4/H_2 ratio), in 100 μM (a) SPM, (b) SPMD, (c) PUT, and (d) CAD. The S/B ratio was calculated as $I_{total} - I_{background} / I_{background}$.

Figure 8.6 A and B show the FIA-EC responses for multiple injections of 5 μM PUT and 2 μM SPMD at a detection potential of 665 mV. The carrier solution was (7/93 v/v) acetonitrile/borax buffer, pH 11.2, and the flow rate was 1 mL/min. For 40 injections of PUT and 60 injections of SPMD, the response variability was 2.6 and 4.3 %, respectively. A 4 min delay time was used between injections, which resulted in an improvement in the precision.[291]

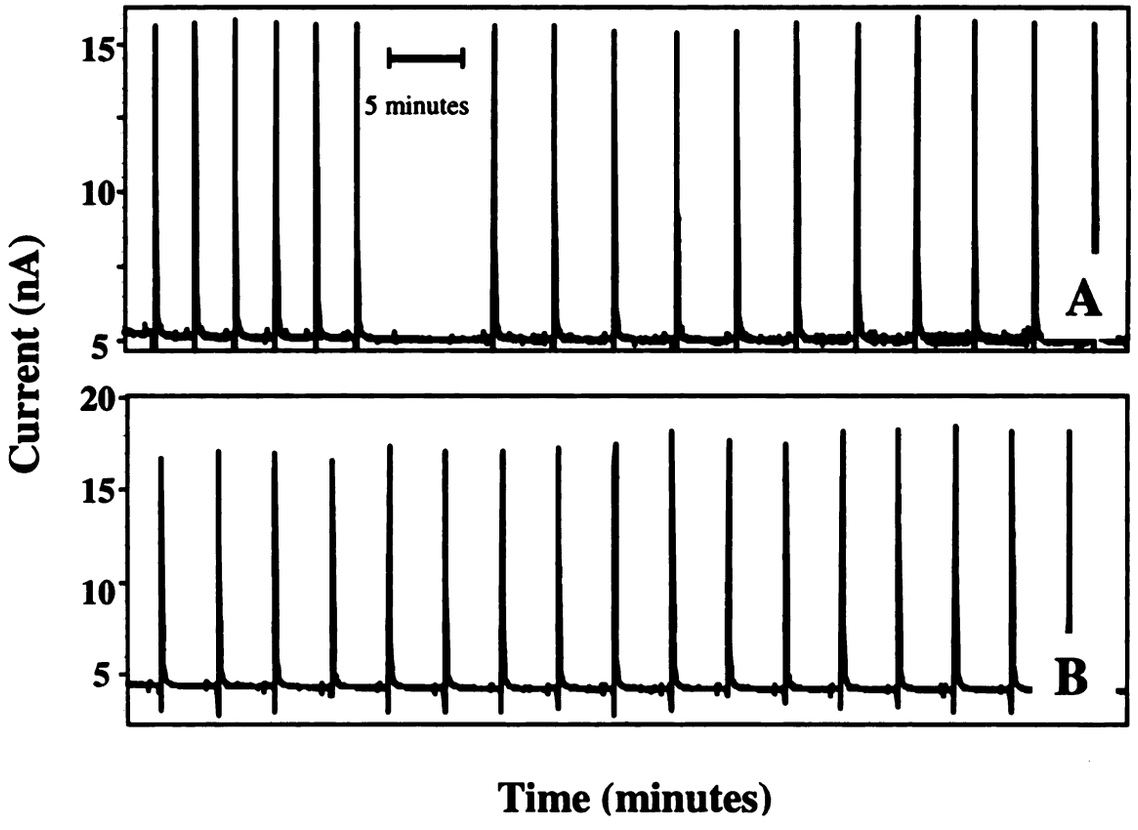

Figure 8.6 FIA-EC responses for a boron-doped microcrystalline diamond film (0.4% CH_4/H_2) during a multiple injections of **(A)** 5 μM PUT and **(B)** 2 μM SPMD. The carrier solution was a 7/93 (v/v) acetonitrile/borax buffer, pH 11.2. Detection potential = 665 mV vs. Ag/AgCl. Injection volume = 20 μL. Flow rate = 1.0 mL/min.

Figure 8.7 shows a series of FIA-EC responses for 50 μM SPM at a detection potential of 665 mV. The carrier solution was 7/93 (v/v) acetonitrile/ borax buffer, pH 11.2, and the flow rate was 1 mL/min. The response curve was generated by varying the injected volume from 2 to 20 μL (a-h). Both the peak current and charge change linearly with the injected mass of each analyte ($r^2 \geq 0.998$). Such was the case for the other three polyamines. Linear regression statistics for a plot of current vs. mass injected (r^2 = 0.998) had a slope of 0.18 μA/ng and an intercept of 0.5 nA.

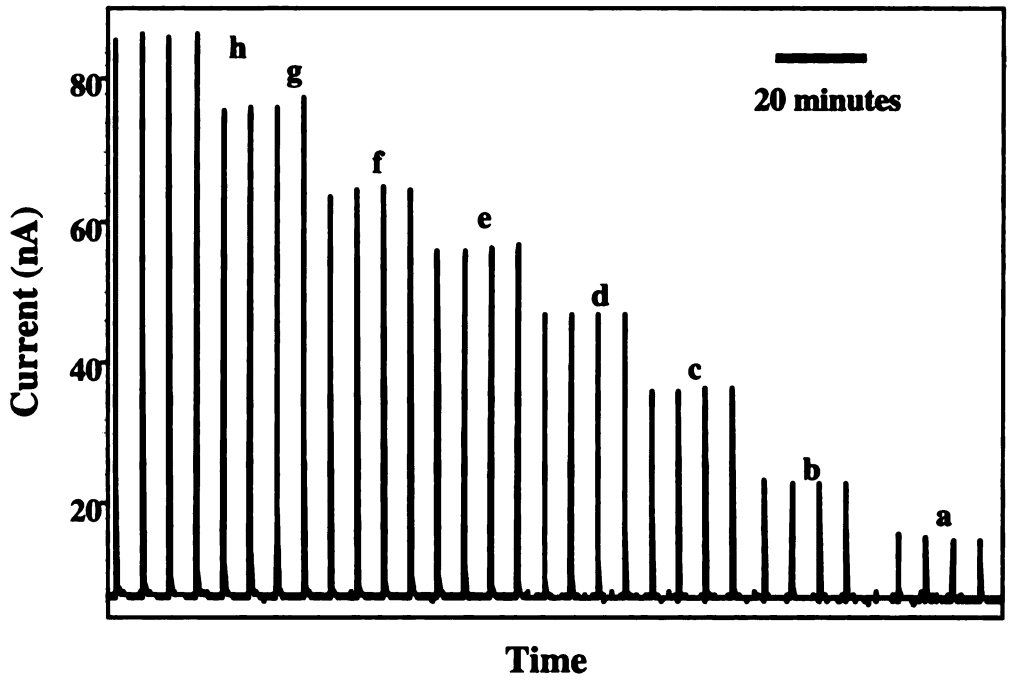

Figure 8.7 FIA-EC calibration responses for a boron-doped microcrystalline diamond film (0.4% CH_4/H_2) during multiple injections of 5 µM SPM. Injected volumes were (a-h) 2 to 20 µL. The carrier solution was a 7/93 (v/v) acetonitrile/borax buffer, pH 11.2. Applied potential = 665 mV vs Ag/AgCl. Flow rate = 1.0 mL/min.

In summary, the addition of acetonitrile to the supporting electrolyte had no adverse effect on the voltammetric or FIA-EC response for any of the polyamines. A linear response was observed with injected mass, and good response precision was seen.

8.2.2. Liquid Chromatography

The reversed-phase HPLC separation of a mixture of the four aliphatic polyamines, coupled with amperometric detection, was investigated. The maximum oxidation response is obtained in alkaline solution, at pH values above the pK_a, therefore

the separation was investigated using different mobile phase compositions consisting of borax buffer and acetonitrile at pH values of 10.0, 10.5, and 11.2. For the most part, all of the amines are unprotonated at these pHs. Peak assignments were made based on the retention times of the individually injected analytes using identical separation and detection conditions.

Much work was performed in an effort to optimize isocratic separation of the polyamines. Acetonitrile was selected as the organic modifier, and after examing the separation with modifier concentrations (v/v) from 0 to 20%, a 7 % concentration was found to be optimum in terms of the efficiency of the separation (capacity factor, peak width, and resolution). Figure 8.8 shows a typical chromatogram for a mixture of 47 μM CAD, PUT, SPMD, and SPM. A chromatogram for 0.50 μM PUT, CAD and SPMD is presented in the inset. In both cases, amperometric detection was made at 665 mV vs. Ag/AgCl, and the mobile phase composition was (7/93 v/v) acetonitrile/borax buffer, pH 11.2. Variations in retention time during a 7-h period of testing were 1.4, 1.2, 2.8, and 2.9% for PUT, CAD, SPMD, and SPM, respectively. The capacity factors, k', are 0.40, 1.0, 1.5, and 4.2 for PUT, CAD, SPMD, and SPM, respectively. The selectivity coefficients, α, for PUT/CAD, CAD/SPMD, and SPMD/SPM are 2.5, 1.5, and 2.8, respectively. The total number of theoretical plates, N, for the separation is 188, based on retention time and peak width of the SPM peak.

All four peaks are asymmetrically shaped with the most significant tailing seen for the late eluting solutes, SPMD and SPM. The peak asymmetry is calculated as the distance from the leading to the tailing edge of the peak, measured at 5% of the peak height, divided by the distance from the leading edge to the peak maximum. The asymmetry values are 3.8, 2.8, 5.1, and 6.9 for PUT, CAD, SPMD, and SPM,

respectively. The tailing appears to be mainly caused by interactions of the amine functional group with the stationary phase, not with the electrode surface as no such tailing is seen in the FIA –EC results. The tailing seemed to get worse with column use. This was because of stationary phase dissolution which creates silanol sites. The interaction of the amine functional groups with the silanol sites is believed to be the cause of the tailing. Obviously, the low number of theoretical plates for the separation is due to the excessive peak tailing.

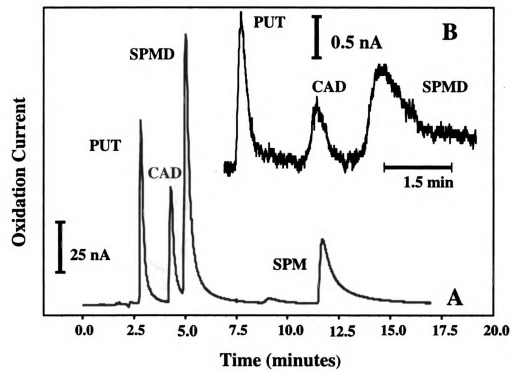

Figure 8.8 Reversed-phase liquid chromatographic separation of (A) 47 μM PUT, CAD, SPMD, and SPM, and (B) 0.5 μM PUT, CAD, and SPM on a C_{18} column (X-Terra, 5 μm particle size, 4.6 x 150 mm). The mobile phase was a 7/93 (v/v) acetonitrile/borax buffer, pH 11.2. Detection potential = 665 mV vs. Ag/AgCl. Injection volume = 20 μL. Flow rate = 1.0 mL/min. The boron-doped microcrystalline diamond film was deposited from a 0.4% CH_4/H_2 ratio.

The most essential biogenic aliphatic polyamines, and those found at significant concentrations in biological fluids, are PUT, SPM, and SPMD. Figure 8.9 shows a typical chromatogram for the three amines at 20 μM concentration. The separation was achieved using 16/84 (v/v) acetonitrile/borax buffer, pH 11.2, mobile phase, and the detection was made at 665 mV vs Ag/AgCl.

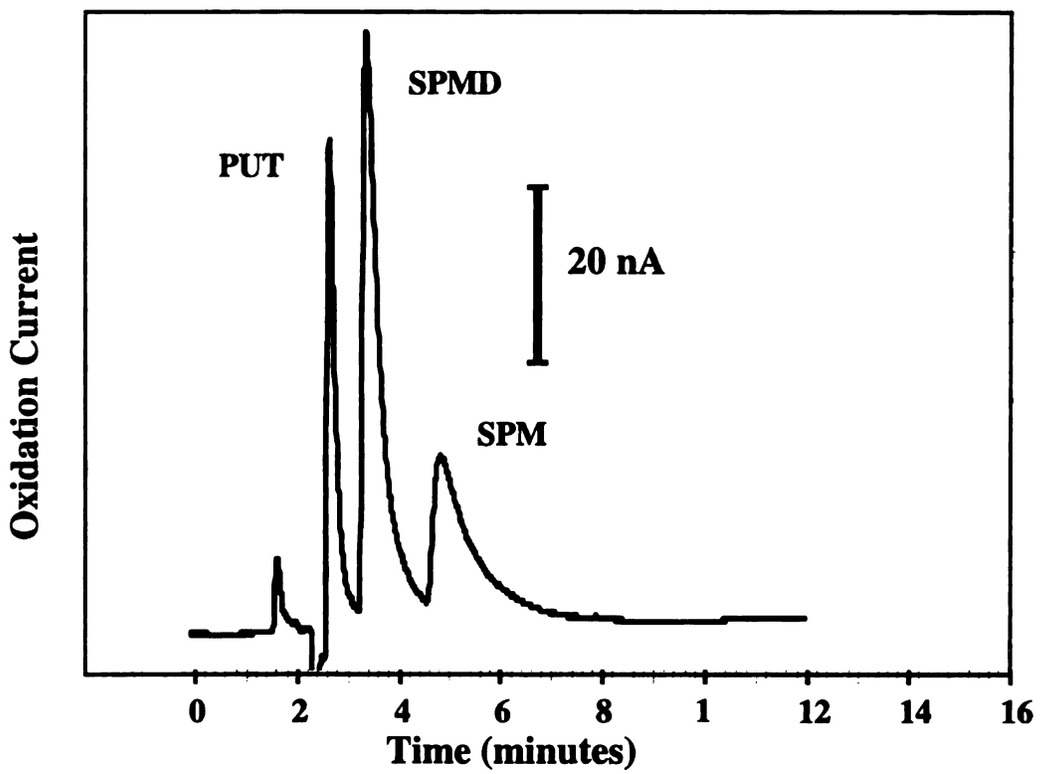

Figure 8.9 Reversed-phase liquid chromatographic separation of PUT, SPMD, and SPM on a C_{18} column. The solution mixture contained 20 μM of each amine. The mobile phase was a 16/84 (v/v) acetonitrile/borax buffer, pH 11.2. Detection potential = 665 mV vs. Ag/AgCl. Injection volume = 20 μL. Flow rate = 1.0 mL/min. The boron-doped microcrystalline diamond film was deposited from a 0.4% CH_4/H_2 ratio

The retention times for all three analytes decreased with the addition of the organic modifier between 7 and 20% (refer to Fig.8.9) with the total separation taking about 8 minutes for the 16/84 composition. The reduced retention times lessen the peak asymmetry, although the tailing for SPM on this column is still significant. The retention times are 2.2, 3.9, and 5.6 minutes for PUT, SPMD, and SPM, respectively. Further additions of acetonitrile to the mobile phase lead to insufficient peak resolution and an increase in the background current.

Amperometric detection analytical figures of merit were determined for the HPLC separation and detection of the aliphatic polyamines. The electrode response for PUT, CAD, SPMD, and SPM were examined as a function of the injected concentration. The results are summarized in Table 8.1.

Table 8.1 Amperometric Detection Figures of Merit for the HPLC Separation of the Aliphatic Polyamines

Amine	LDR	Concentration LOQ (S/N ≥3)	Molar LOQ	Mass LOQ
Putrescine PUT	0.5 -500 μM (r^2=0.998)	0.5 μM	10 pmol	0.88 ng
Cadaverine CAD	0.5 -500 μM (r^2=0.998)	0.5 μM	10 pmol	1.02 ng
Spermidine SPMD	0.5 -500 μM (r^2=0.998)	0.5 μM	10 pmol	1.45 ng
Spermine SPM	5 -500 μM (r^2=0.998)	5 μM	100 pmol	31.2 ng

Note:The calibration curves were constructed with concentrations (4 injections at each) from 0.5 to 500 μM. Injection volume=20 μL. Flow rate=1 mL/min. Detection potential=665 mV. LOQ=limits of quantitation.

The calibration curves were constructed from the response for 8 different injected concentrations ranging from 0.5 to 500 μM. A linear relationship between both the peak current and charge, and the concentration was observed for PUT, CAD, and SPMD, with

a linear regression correlation coefficient >0.998. A smaller dynamic range was observed for SPM ranging from 5 to 500 μM with a regression coefficient of > 0.998. The nominal y-axis intercept for all the calibration plots was less than 5 nA for CAD, SPMD, and SPM and about 10 nA for PUT. The limits of quantitation for PUT, CAD, and SPMD were 0.5 μM or 10 pmol injected, while the limit for SPM was 5 μM or 100 pmol injected (S/N≥3). The mass limits of quantitation were 1.0 ng for CAD, 0.9 ng for PUT, 1.5 ng for SPMD, and 31 ng for SPM. The LOD observed for SPM are the highest. It is because calibration curves were constructed based on peak height and the broadness observed for SPM peak reduces LOD. The theoretical limits of detection, obtained by extrapolating the linear calibration plots to the concentration at which the S/N=3, were 0.3 μM for PUT and SPMD, 0.5 μM for CAD, and 3 μM for SPM.

Table 8.2 presents a summary of the LC-EC amperometric detection reproducibility and stability data. The reproducibility was tested at different concentrations. The highest response variability was observed for the highest concentration of each analyte. For 170 μM PUT, the current variation is about 6%, while for the 20 and 0.5 μM solutions, variations are about 3% for six injections. A similar trend is observed for all four amines. Generally, the reproducibility data based on the peak charge are much better than those based on peak height, due to the broadened and assymetric peaks. The long-term response stability was examined over a 7-h period of continuous use. Twelve injections of all four amines (47 μM ea.) were periodically made. The background signal, during this period, remained low and unchanging. The peak height varies by 3.0% for PUT and CAD, 6.3% for SPMD and 11.0% for SPM. The peak charge varies much less over this period with values of 2.0% for PUT and SPM, 4.2% for CAD, and 3.9% for SPMD. Most importantly, there is no progressive loss of signal due to permanent electrode fouling.

Table 8.2 Amperometric Detection Reproducibility and Stability for the HPLC Separation of the Aliphatic Polyamines

Amine	Concentration [μM]	Reproducibility RSD %	Stability RSD % (47 μM)	
		Current	Charge	Current
Putrescine PUT	170	6.1	2.1	3.0
	20	3.0		
	0.5	3.1		
Cadaverine CAD	150	7.0	4.2	3.0
	20	n/a		
	0.5	3.6		
Spermidine SPMD	108	6.1	3.9	6.3
	20	2.0		
	0.5	2.5		
Spermine SPM	100	12.0	2.1	11.0
	20	6.0		
	5	5.8		

Reproducibility conditions: n=15 (170, 150, 108, 100 μM), n=11 (20 μM), n=7 (0.5 μM). Stability conditions: n=16 (7 hrs). Separation and detection conditions are the same as in Table 8.1.

Diamond provides comparable or better detection figures of merit to those reported in the literature for Au, anodized Ag-PbO_2, Cu, Ni, Pt. The limit of detection at conductive diamond is better than that achieved so far using Au (~200 pmole for PUT) in LC-EC[33] and comparable to or better than those in flow injection studies with chemically modified electrodes, e.g., nickel-modified glassy carbon[34] or Ag-PbO_2 (0.1 and 0.3 μM amine, respectively).[54,58] In terms of response reproducibility and stability, diamond provides superior figures of merit to those for Cu, Ni, Pt [231] and comparable to those of Au, Ag-PbO_2 and nickel-modified glassy carbon.[31-34,54]

8.3. Conclusion

Four important aliphatic polyamines were separated isocratically by reversed-phase liquid chromatography and detected amperometrically using boron-doped diamond electrodes. Diamond electrodes are unique within the carbon electrode family for their ability to stably and sensitively detect aliphatic polyamines. Detection was made at a constant potential of 665 mV vs. Ag/AgCl using microcrystalline diamond electrodes deposited from a 0.4% CH_4/H_2 ratio. The analytes were isocratically separated in a 7/93 (v/v) acetonitrile/0.01 M borax buffer, pH11.2, mobile phase. Good separation and peak resolution for all four analytes was achieved within 14 minutes. There was extensive peak tailing for the last eluting components, SPMD and SPM. The peak broadening is presumably due to interaction of the amines with the residual silanol groups on the stationary phase. A linear dynamic range from 0.5 to 500 μM was observed for cadaverine (CAD), putrescine (PUT) and spermidine (SPMD), with a theoretical limit of detection (S/N=3) of 0.3 μM for PUT and SPMD and 0.5 μM for CAD. The linear dynamic range for SPM was 5 to 500 μM and limit of detection was 3 μM. The mass detection limits were 0.88 ng for PUT, 1.02 ng for CAD, 1.45 ng for SPMD, and 31.2 ng for SPM. Typical response variabilities (n=6) for a 0.5 μM injected concentration were ~3%. Excellent long-term stability was found with no progressive loss of signal due to permanent electrode fouling. The major advantage of using diamond is that no pre- or post-column analyte derivatization, pH adjustment of the mobile phase, or pulsed detection waveform is necessary for detection.

Chapter 9

SUMMARY

1) Good quality, boron-doped diamond thin films were successfully deposited on three different substrates: Si, Mo, and W. The resulting films were characterized by electrochemical methods of analysis, AFM, XRD, Raman spectroscopy, and dynamic SIMS. It was observed that the electrochemical response of the films was independent of the substrate material. All films exhibited properties of high quality diamond – a wide working potential window, a low voltammetric background current and capacitance, and good responsiveness for $Fe(CN)_6^{-3/-4}$, $Ru(NH_3)_6^{+2/+3}$, $IrCl_6^{-2/-3}$, and methyl viologen without any pretreatment. k^0_{app} values ranged from 10^{-2} to 10^{-1} cm/s for all four redox systems.

2) Boron-doped nanocrystalline diamond thin films were deposited by CVD from $CH_4/H_2/Ar$ source gas mixture. XRD revealed that the bulk crystal structure of the films was cubic diamond. TEM indicated the films consist of 10-15 nm randomly oriented but atomically ordered diamond grains. SEM showed these grains form

aggregates ~100 nm in size. Electrochemically, these films exhibited a wide working potential window, a low voltammetric background current and good responsiveness for $Fe(CN)_6^{-3/-4}$, $Ru(NH_3)_6^{+3/+2}$, $IrCl_6^{-2/-3}$, and methyl viologen without any pretreatment. The quasi-reversible voltammetry for all the couples indicates that the boron-doped nanocrystalline diamond has a sufficient charge carrier density over the wide potential range to support a rapid electron transfer. More sluggish kinetics were found for 4-*tert*-butylcatechol and $Fe^{+2/+3}$. The sluggish kinetics are attributed to weak surface adsorption for the former, and to the absence of catalyzing surface carbonyl groups for the latter.

3) Aliphatic amines can be quantitatively oxidized at both boron-doped microcrystalline and nanocrystalline diamond thin-film electrodes. *The oxidation response is highly dependent on the physicochemical properties of the diamond surface, in particular, the sp^2-bonded non-diamond carbon impurity and surface boron concentration. High doping level and moderate amount of sp^2-carbon impurities were found to be the optimal parameters for amine detection.* The oxidation response depends on the solution pH. In order to be oxidized the amines need to be unprotonated.

4) FIA-EC results indicate that aliphatic amines can be stably and reproducibly detected at constant potential in alkaline media at boron-doped diamond thin films. *The highest signals and sensitivity values in FIA were observed for highly boron-doped nanocrystalline diamond films (20 ppm). Therefore, these films or films with even higher boron-doping are the best performing for the aliphatic amine detection assay.* The linear dynamic range for most of amines was 4 orders of magnitude. The limits of

detection (LOD) achieved for EDA, DAP, SPMD, and SPM were 0.1μM, for CAD and PUT 0.3 μM, and for MA 10 μM.

5) Aliphatic polyamines (cadaverine, spermine, spermidine, and putrescine) can be isocratically separated by reversed-phase liquid chromatography and amperometrically detected using boron-doped diamond electrodes. Detection was made at a constant potential of 665 mV vs Ag/AgCl using microcrystalline diamond electrodes deposited from a 0.4% CH_4/H_2 ratio. The analytes were separated in a 7/93 (v/v) acetonitrile/0.01 M borax buffer, pH11.2. Good separation and peak resolution for all four analytes was achieved within 14 minutes. A linear dynamic range from 0.5 to 500 μM was observed for CAD, PUT and SPMD, with a theoretical limit of detection (S/N=3) of 0.3 μM for PUT and SPMD and 0.5 μM for CAD. The linear dynamic range for SPM was 5 to 500 μM and limit of detection was 3 μM. The mass detection limits were 0.88 ng for PUT, 1.02 ng for CAD, 1.45 ng for SPMD, and 31.2 ng for SPM. Typical response variability (n=6) for a 0.5 μM injected concentration were ~3%. Excellent long-term stability was found, with no progressive loss of signal due to permanent electrode fouling.

References

1. Pegg, A. E. *Cancer Res.* **1988**, *48*, 759-774.

2. Tabor, C. W.; Tabor, H. *Annu. Rev. Biochem.* **1984**, *53*, 749-790.

3. Tabor, C. W.; Tabor, H. *Microbiol. Rev.* **1985**, *49*, 81-99.

4. Russell, D. H. D., B. G. M. *Polyamines as Biochemical Markers of Normal and Malignant Growth.*; Raven Press, 1978.

5. Aikens, D.; Bunce, S.; Onasch, F.; Parker, R., III; Hurwitz, C.; Clemans, S. *Biophys. Chem.* **1983**, *17*, 67-74.

6. Grant, G.; Bardocz, S.; Brown, D. S.; Watt, W. B.; Stewart, J. C.; Pusztai, A. *Biochem. Soc. Trans.* **1990**, *18*, 1009-1010.

7. Bardocz, S. *Eur. J. Clin. Nutr.* **1993**, *47*, 683-690.

8. Bardocz, S.; Grant, G.; Brown, D. S.; Ralph, A.; Pusztai, A. *J. Nutr. Biochem.* **1993**, *4*, 66-71.

9. Tabor, C. W.; Tabor, H. *Faseb J.* **1995**, *9*, A1389-A1389.

10. Bardocz, S. *Trends Food Sci. Technol.* **1995**, *6*, 341-346.

11. Bardocz, S.; Duguid, T. J.; Brown, D. S.; Grant, G.; Pusztai, A.; White, A.; Ralph, A. *Br. J. Nutr.* **1995**, *73*, 819-828.

12. Nagy, G.; Xu, C. X.; Cosofret, V. V.; Buck, R. P.; Lindner, E.; Neuman, M. R.; Sprinkle, R. H. *Talanta* **1998**, *47*, 367-376.

13. Marzouk, S. A. M.; Xu, C. X.; Cosofret, B. R.; Buck, R. P.; Hassan, S. S. M.; Neuman, M. R.; Sprinkle, R. H. *Anal. Chim. Acta* **1998**, *363*, 57-65.

14. Seiler, N.; Sarhan, S.; Knodgen, B.; Gerhart, F. *J. Cancer Res. Clin. Oncol.* **1988**, *114*, 71-80.

15. Seiler, N.; Sarhan, S.; Grauffel, C.; Jones, R.; Knodgen, B.; Moulinoux, J. P. *Cancer Res.* **1990**, *50*, 5077-5083.

16. Simon, P.; Lemacon, C. *Anal. Chem.* **1987**, *59*, 480-484.

17. Tabor, C. W.; Tabor, H. *Methods Enzymol.* **1983**, *94*, 29-36.

18. FDA, U. S.; Nutrition, Center for Food Safety and Applied Nutrition, 2001.

19. Roig Sagues, A. X.; Hernandez Herrero, M. M.; Rodriguez Jerez, J. J.; Quinto Fernandez, E. J.; Mora Ventura, M. T. *Alimentaria (Madrid)* **1998**, *294*, 59-66.

20. Petaja, E.; Eerola, S.; Petaja, P. *European Food Research and Technology* **2000**, *210*, 280-285.

21. Eerola, S.; Sagues, A. X. R.; Lilleberg, L.; Aalto, H. *Zeitschrift Fur Lebensmittel-Untersuchung Und-Forschung a-Food Research and Technology* **1997**, *205*, 351-355.

22. Yen, G. C. *Chung-kuo Nung Yeh Hua Hsueh Hui Chih (Abstract)* **1986**, *24*, 211-227

23. Su, S. C.; Chou, S. S.; Chang, P. C.; Hwang, D. F. *J. of Chrom. B* **2000**, *749*, 163-169.

24. Hungerford, J. M.; Arefyev, A. A. *Anal. Chim. Acta* **1992**, *261*, 351-359.

25. Khuhawar, M. Y.; Qureshi, G. A. *J. of Chrom. B* **2001**, *764*, 385-407.

26. Khuhawar, M. Y.; Memon, A. A.; Bhanger, M. I. *Journal of the Chemical Society of Pakistan* **2000**, *22*, 115-118.

27. Ma, Y., Zhang, R. , Cooper, C. L. *J. Chrom. A* **1992**, *608*, 93.

28. Muskiet, F. A. J.; Dorhout, B.; Vandenberg, G. A.; Hessels, J. *J. of Chrom. B* **1995**, *667*, 189-198.

29. Dobberpuhl, D. A.; Hoekstra, J. C.; Johnson, D. C. *Anal. Chim. Acta* **1996**, *322*, 55-62.

30. Dobberpuhl, D. A.; Johnson, D. C. *Electroanalysis* **1996**, *8*, 726-731.

31. Hoekstra, J. C.; Johnson, D. C. *Anal. Chim. Acta* **1999**, *390*, 45-54.

32. Hoekstra, J. C.; Johnson, D. C. *Anal. Chem.* **1998**, *70*, 83-88.

33. Pineda, R.; Knapp, A. D.; Hoekstra, J. C.; Johnson, D. C. *Anal. Chim. Acta* **2001**, *449*, 111-117.

34. Casella, I. G.; Rosa, S.; Desimoni, E. *Electroanalysis* **1998**, *10*, 1005-1009.

35. Fleischmann, M.; Korinek, K.; Pletcher, D. *J. Chem. Soc., Perkin Trans. 2* **1972**, 1396-1403.

36. Hansen, E. H.; Ruzicka, J.; Ghose, A. K. *Soil Nitrogen Fert. Pollut. Proc. Rep. Res. Coord. Meet.* **1980**, 77-91.

37. Hughes, S.; Johnson, D. C. *J. Agric. Food Chem.* **1982**, *30*, 712-714.

38. Hughes, S.; Meschi, P. L.; Johnson, D. C. *Anal. Chim. Acta* **1981**, *132*, 1-10.

39. Jensen, M. B.; Johnson, D. C. *Anal. Chem.* **1997**, *69*, 1776-1781.

40. Johll, M. E.; Williams, D. G.; Johnson, D. C. *Electroanalysis* **1997**, *9*, 1397-1402.

41. Feng, J.; Johnson, D. C. *J. Electrochem. Soc.* **1990**, *137*, 507-510.

42. LaCourse, W. R.; Hsiao, Y. L.; Johnson, D. C. *J. Electrochem. Soc.* **1989**, *136*, 3714-3719.

43. Mho, S. i.; Johnson, D. C. *J. Electroanal. Chem.* **2001**, *495*, 152-159.

44. Mho, S. I.; Johnson, D. C. *J. Electroanal. Chem.* **2001**, *500*, 524-532.

45. Pamplin, K. L.; Johnson, D. C. *J. Electrochem. Soc.* **1996**, *143*, 2119-2125.

46. Popovic, N. D.; Cox, J. A.; Johnson, D. C. *J. Electroanal. Chem.* **1998**, *456*, 203-209.

47. Popovic, N. D.; Cox, J. A.; Johnson, D. C. *J. Electroanal. Chem.* **1998**, *455*, 153-160.

48. Treimer, S. E.; Feng, J.; Scholten, M. D.; Johnson, D. C.; Davenport, A. J. *J. Electrochem. Soc.* **2001**, *148*, E459-E463.

49. Yeo, I. H.; Johnson, D. C. *J. Electrochem. Soc.* **1987**, *134*, 1973-1977.

50. Allen, R. E.; Johnson, D. C. *Talanta* **1973**, *20*, 799-809.

51. Chang, H.; Johnson, D. C. *J. Electrochem. Soc.* **1990**, *137*, 2452-2457.

52. Chang, H.; Johnson, D. C. *J. Electrochem. Soc.* **1990**, *137*, 3108-3113.

53. Feng, J.; Johnson, D. C. *J. Electrochem. Soc.* **1991**, *138*, 3328-3337.

54. Ge, J.; Johnson, D. C. *J. Electrochem. Soc.* **1995**, *142*, 1525-1531.

55. Ge, J.; Johnson, D. C. *J. Electrochem. Soc.* **1995**, *142*, 3420-3423.

56. Dobberpuhl, D. A.; Johnson, D. C. *J. Chrom., A* **1995**, *694*, 391-398.

57. Ge, J.; Johnson, D. C. *J. Electrochem. Soc.* **1996**, *143*, 2543-2548.

58. Ge, J. J., D. C. *J. Electrochem. Soc.* **1995**, *142*, 1525.

59. Swain, G. M. *J. Electrochem. Soc.* **1994**, *141*, 3382-3393.

60. Swain, G. M. *Adv. Mater.* **1994**, *6*, 388-392.

61. Swain, G. M.; Anderson, A. B.; Angus, J. C. *MRS Bull.* **1998**, *23*, 56-60.

62. Granger, M. C., USU, Logan, 2000.

63. Granger, M. C.; Witek, M.; Xu, J.; Wang, J.; Hupert, M.; Hanks, A.; Koppang, M. D.; Butler, J. E.; Lucazeau, G.; Mermoux, M.; Strojek, J. W.; Swain, G. M. *Anal. Chem.* **2000**, *72*, 3793-3804.

64. Arihara, K.; Kitamura, F.; Nukanobu, K.; Ohsaka, T.; Tokuda, K. *J. Electroanal. Chem.* **1999**, *473*, 138-144.

65. Edstrom, K.; Herranen, M. *J. Electrochem. Soc.* **2000**, *147*, 3628-3632.

66. Chen, P.; McCreery, R. L. *Anal. Chem.* **1996**, *68*, 3958-3965.

67. Duebgen, R. *Can. Chem. News* **1987**, *39*, 13-16.

68. Engelman, E. E.; Evans, D. H. *Langmuir* **1992**, *8*, 1637-1644.

69. Kamau, G. N. *Anal. Chim. Acta* **1988**, *207*, 1-16.

70. Angus, J. C.; Argoitia, A.; Gat, R.; Li, Z.; Sunkara, M.; Wang, L.; Wang, Y. *Philos. Trans. R. Soc. Lond. Ser. A-Math. Phys. Eng. Sci.* **1993**, *342*, 195-208.

71. Angus, J. C.; Collins, A. T. *Nature* **1994**, *370*, 601-601.

72. Angus, J. C.; Gardner, N. C.; Chem. Eng. Div.,Case West. Reserve Univ. Cleveland,Ohio,USA., 1973, pp 53 pp.

73. Angus, J. C.; Martin, H. B.; Landau, U.; Evstefeeva, Y. E.; Miller, B.; Vinokur, N. *New Diamond and Frontier Carbon Technology* **1999**, *9*, 175-187.

74. May, P. W. *Philosophical Transactions of the Royal Society of London, Series A: Mathematical, Physical and Engineering Sciences* **2000**, *358*, 473-495.

75. Sakharova, A. Y. P., Y. V.;Quarto, F. D.; Piazza, S.; Sunseri, C.; Teremetskaya, I. G.; Varnin, V. P. *J. Electrochem. Soc.* **1995**, *142*, 2704.

76. Pleskov, Y. V. *Uspekhi Khimii* **1999**, *68*, 416-429.

77. Pleskov, Y. V. *J. Anal. Chem.* **2000**, *55*, 1045-1050.

78. DeClements, R.; Swain, G. M.; Dallas, T.; Holtz, M. W.; Herrick, R. D.; Stickney, J. L. *Langmuir* **1996**, *12*, 6578-6586.

79. Ramesham, R.; Rose, M. F. *Diamond Relat. Mater.* **1997**, *6*, 17-27.

80. Ramesham, R.; Rose, M. F. *Thin Solid Films* **1997**, *300*, 144-153.

81. Ramesham, R.; Roppel, T.; Ellis, C.; Loo, B. H. *J. Electrochem. Soc.* **1991**, *138*, 2981-2984.

82. Strojek, J. W.; Granger, M. C.; Swain, G. M.; Dallas, T.; Holtz, M. W. *Anal. Chem.* **1996**, *68*, 2031-2037.

83. Chen, Q. Y.; Granger, M. C.; Lister, T. E.; Swain, G. M. *J. Electrochem. Soc.* **1997**, *144*, 3806-3812.

84. Terashima, C.; Rao Tata, N.; Sarada, B. V.; Tryk, D. A.; Fujishima, A. *Anal. Chem.* **2002**, *74*, 895-902.

85. Rao Tata, N.; Loo, B. H.; Sarada, B. V.; Terashima, C.; Fujishima, A. *Anal. Chem*, **2002**, *74*, 1578-1583.

86. Patel, K.; Hashimoto, K.; Fujishima, A. *Denki Kagaku oyobi Kogyo Butsuri Kagaku* **1992**, *60*, 659-661.

87. Fujishima, A.; Popa, E.; Wu, Z.; Rao, T. N. *Novel Trends in Electroorganic Synthesis, [Papers presented at the International Symposium on Electroorganic Synthesis], 3rd, Kurashiki, Japan, Sept. 24-27, 1997* **1998**, 421-424.

88. Ohta, N.; Nakabayashi, S.; Fujishima, A. *Chem. Lett.* **1999**, 1147-1148.

89. Rao, T. N.; Yagi, I.; Miwa, T.; Tryk, D. A.; Fujishima, A. *Anal. Chem.* **1999**, *71*, 2506-2511.

90. Rao, T. N.; Sarada, B. V.; Tryk, D. A.; Fujishima, A. *J. Electroanal. Chem.* **2000**, *491*, 175-181.

91. Sarada, B. V.; Rao, T. N.; Tryk, D. A.; Fujishima, A. *Proceedings - Electrochemical Society* **2000**, *99-32*, 502-506.

92. Chailapakul, O.; Aksharanandana, P.; Frelink, T.; Einaga, Y.; Fujishima, A. *Sens. Actuators B* **2001**, *B80*, 193-201.

93. Notsu, H.; Fukazawa, T.; Tatsuma, T.; Tryk, D. A.; Fujishima, A. *Electrochemical and Solid-State Letters* **2001**, *4*, H1-H3.

94. Tsunozaki, K.; Einaga, Y.; Rao, T. N.; Fujishima, A. *Chem. Lett.* **2002**, 502-503.

95. Abaturov, M. A.; Elkin, V. V.; Krotova, M. D.; Mishuk, V. Y.; Sakharova, A. Y.; Pleskov, Y. V. *Russ. J. Electrochem.* **1995**, *31*, 1119-1124.

96. Pleskov, Y. V.; Mishuk, V. Y.; Abaturov, M. A.; Elkin, V. V.; Krotova, M. D.; Varnin, V. P.; Teremetskaya, I. G. *J. Electroanal. Chem.* **1995**, *396*, 227-232.

97. Pleskov, Y. V.; Elkin, V. V.; Abaturov, M. A.; Krotova, M. D.; Mishuk, V. Y.; Varnun, V. P.; Teremetskaya, I. G. *J. Electroanal. Chem.* **1996**, *413*, 105-110.

98. Pleskov, Y. V.; Sakharova, A. Y.; Churikov, A. V.; Varnin, V. P.; Teremetskaya, I. G. *Russ. J. Electrochem.* **1996**, *32*, 1075-1079.

99. Modestov, A. D.; Evstefeeva, Y. E.; Pleskov, Y. V.; Mazin, V. M.; Varnin, V. P.; Teremetskaya, I. G. *J. Electroanal. Chem.* **1997**, *431*, 211-218.

100. Pleskov, Y. V.; Mishuk, V. Y.; Abaturov, M. A.; Elkin, V. V.; Krotova, M. D.; Varnin, V. P.; Teremetskaya, I. G. *Russ. J. Electrochem.* **1997**, *33*, 61-68.

101. Pleskov, Y. V. *J. Chem. Vap. Deposition* **1997**, *5*, 126-132.

102. Evstefeeva, Y. E.; Krotova, M. D.; Pleskov, Y. V.; Mazin, V. M.; Elkin, V. V.; Mishuk, V. Y.; Varnin, V. P.; Teremetskaya, I. G. *Russ. J. Electrochem.* **1998**, *34*, 1352-1357.

103. Pleskov, Y.; Tameev, A.; Varnin, V.; Teremetskaya, I. *J. Solid State Electrochem.* **1998**, *3*, 25-30.

104. Pleskov, Y. V.; Evstefeeva, Y. E.; Krotova, M. D.; Elkin, V. V.; Mazin, V. M.; Mishuk, V. Y.; Varnin, V. P.; Teremetskaya, I. G. *J. Electroanal. Chem.* **1998**, *455*, 139-146.

105. Mazin, V. M.; Evstefeeva, Y. E.; Pleskov, Y. V.; Varnin, V. P.; Teremetskaya, I. G.; Laptev, V. A. *Russ. J. Electrochem.* **2000**, *36*, 580-585.

106. Pleskov, Y. V.; Krotova, M. D.; Evstefeeva, Y. E.; Ral'chenko, V. G.; Vlasov, II; Khomich, A. V. *Russ. J. Electrochem.* **2001**, *37*, 1123-1127.

107. Bouamrane, F.; Tadjeddine, A.; Butler, J. E.; Tenne, R.; Levy-Clement, C. *J. Electroanal. Chem.* **1996**, *405*, 95-99.

108. Bouamrane, F.; Tadjeddine, A.; Tenne, R.; Butler, J. E.; Kalish, R.; Levy-Clement, C. *J. Phys. Chem. B* **1998**, *102*, 134-140.

109. Tenne, R.; Levy-Clement, C. *Israel Journal of Chemistry* **1998**, *38*, 57-73.

110. Glesener, J. W.; Natishan, P. M.; O'Grady, W. E.; Morrish, A. A.; Stoner, B. R.; Hagans, P. L. In *U.S.*; (United States Dept. of the Navy, USA). Us, 2001, pp 5 pp.

111. Angus, J. C.; Will, H. A.; Stanko, W. S. *J. Appl. Phys.* **1968**, *39*, 2915-2922.

112. Poferl, D. J.; Gardner, N. C.; Angus, J. C. *J. Appl. Phys.* **1973**, *44*, 1428-1434.

113. Sunkara, M.; Angus, J. C.; Hayman, C. C.; Buck, F. A. *Carbon* **1990**, *28*, 745-746.

114. Anderson, A. B.; Mehandru, S. P.; Angus, J. C. *Abstr. Pap. Am. Chem. Soc.* **1991**, *202*, 36-FUEL.

115. Lambrecht, W. R. L.; Lee, C. H.; Segall, B.; Angus, J. C.; Li, Z. D.; Sunkara, M. *Nature* **1993**, *364*, 607-610.

116. Mearini, G. T.; Krainsky, I. L.; Dayton, J. A.; Wang, Y. X.; Zorman, C. A.; Angus, J. C.; Hoffman, R. W. *Appl. Phys. Lett.* **1994**, *65*, 2702-2704.

117. Prijaya, N. A.; Angus, J. C.; Bachmann, P. K. *Diam. Rel. Mat.* **1994**, *3*, 129-136.

118. Anderson, A. B.; Grantscharova, E. J.; Angus, J. C. *Phys. Rev. B* **1996**, *54*, 14341-14348.

119. Jungnickel, G.; Porezag, D.; Frauenheim, T.; Heggie, M. I.; Lambrecht, W. R. L.; Segall, B.; Angus, J. C. *Phys. Status Solidi A-Appl. Res.* **1996**, *154*, 109-125.

120. Morrison, P. W.; Taweechokesupsin, O.; Kovach, C. S.; Roozbehani, B.; Angus, J. C. *Diam. Rel. Mat.* **1996**, *5*, 242-246.

121. Li, L.-F.; Totir, D. A.; Vinokur, N.; Miller, B.; Chottiner, G.; Evans, E. A.; Angus, J. C.; Scherson, D. *Proc. - Electrochem. Soc.* **1997**, *97-17*, 394-409.

122. Martin, H. B.; D'Urso, J. J.; Morrison, P. W., Jr.; Landau, U.; Angus, J. C. *Proceedings - Electrochemical Society* **2000**, *99-32*, 491-501.

123. Albu, T. V.; Anderson, A. B.; Angus, J. C. *J. Electrochem. Soc.* **2002**, *149*, E143-E147.

124. Vinokur, N.; Miller, B.; Avyigal, Y.; Kalish, R. *J. Electrochem. Soc.* **1996**, *143*, L238-L240.

125. Miller, B.; Vinokur, N.; Avyigal, Y.; Kalish, R. *Book of Abstracts, 214th ACS National Meeting, Las Vegas, NV, September 7-11* **1997**, ANYL-191.

126. Vescan, A.; Daumiller, I.; Gluche, P.; Ebert, W.; Kohn, E. *IEEE Electron Device Lett.* **1997**, *18*, 556-558.

127. Vinokur, N.; Miller, B. *Proc. - Electrochem. Soc.* **1997**, *97-17*, 384-393.

128. Vinokur, N.; Miller, B.; Avyigal, Y.; Kalish, R. *Electrochemical and Solid-State Letters* **1998**, *1*, 265-267.

129. Vinokur, N.; Miller, B.; Avyigal, Y.; Kalish, R. *J. Electrochem. Soc.* **1999**, *146*, 125-130.

130. Yoo, K.; Miller, B.; Kalish, R.; Shi, X. *Proceedings - Electrochemical Society* **2000**, *99-32*, 440-447.

131. Sopchak, D.; Miller, B.; Kalish, R.; Avyigal, Y.; Shi, X. *Electroanalysis* **2002**, *14*, 473-478.

132. Prado, C.; Flechsig, G.-U.; Grundler, P.; Foord John, S.; Markenc, F.; Compton Richard, G. *Analyst* **2002**, *127*, 329-332.

133. Compton, R. G.; Marken, F.; Goeting, C. H.; McKeown, R. A. J.; Foord, J. S.; Scarsbrook, G.; Sussmann, R. S.; Whitehead, A. J. *Chemical Communications (Cambridge)* **1998**, 1961-1962.

134. Goeting, C. H.; Marken, F.; Gutierrez-Sosa, A.; Compton, R. G.; Foord, J. S. *New Diamond and Frontier Carbon Technology* **1999**, *9*, 207-228.

135. Saterlay, A. J.; Foord, J. S.; Compton, R. G. *Analyst* **1999**, *124*, 1791-1796.

136. Qiu, F.; Compton, R. G.; Marken, F.; Wilkins, S. J.; Goeting, C. H.; Foord, J. S. *Anal. Chem.* **2000**, *72*, 2362-2370.

137. Saterlay, A. J.; Tibbetts, D. F.; Compton, R. G. *Anal. Sci.* **2000**, *16*, 1055-1060.

138. Holt, K. B.; Del Campo, J.; Foord, J. S.; Compton, R. G.; Marken, F. *J. Electroanal. Chem.* **2001**, *513*, 94-99.

139. Saterlay, A. J.; Foord, J. S.; Compton, R. G. *Electroanalysis* **2001**, *13*, 1065-1070.

140. Saterlay, A. J.; Wilkins, S. J.; Holt, K. B.; Foord, J. S.; Compton, R. G.; Marken, F. *J. Electrochem. Soc.* **2001**, *148*, E66-E72.

141. Tsai, Y.-C.; Coles, B. A.; Holt, K.; Foord, J. S.; Marken, F.; Compton, R. G. *Electroanalysis* **2001**, *13*, 831-835.

142. Hyde, M.; Saterlay, A. J.; Wilkins, S. J.; Foord, J. S.; Compton, R. G.; Marken, F. *J. Solid State Electrochem.* **2002**, *6*, 183-187.

143. Prado, C.; Flechsig, G.-U.; Gruendler, P.; Foord, J. S.; Marken, F.; Compton, R. G. *Analyst* **2002**, *127*, 329-332.

144. Gruen, D. M.; Krauss, A. R.; Zuiker, C. D.; Csencsits, R.; Terminello, L. J.; Carlisle, J. A.; Jimenez, I.; Sutherland, D. G. J.; Shuh, D. K.; et al. *Appl. Phys. Lett.* **1996**, *68*, 1640-1642.

145. Qin, L. C.; Zhou, D.; Krauss, A. R.; Gruen, D. M. *Nanostructured Materials* **1998**, *10*, 649-660.

146. Zhou, D.; Gruen, D. M.; Qin, L. C.; McCauley, T. G.; Krauss, A. R. *J. Appl. Phys.* **1998**, *84*, 1981-1989.

147. Zhou, D.; McCauley, T. G.; Qin, L. C.; Krauss, A. R.; Gruen, D. M. *J. Appl. Phys.* **1998**, *83*, 540-543.

148. Gruen, D. M. *MRS Bull.* **1998**, *23*, 32-35.

149. Erdemir, A.; Fenske, G. R.; Krauss, A. R.; Gruen, D. M.; McCauley, T.; Csencsits, R. T. *Surface and Coatings Technology* **1999**, *120-121*, 565-572.

150. Fausett, B.; Granger, M. C.; Hupert, M. L.; Wang, J.; Swain, G. M.; Gruen, D. M. *Electroanalysis* **2000**, *12*, 7-15.

151. Bhattacharyya, S.; Auciello, O.; Birrell, J.; Carlisle, J. A.; Curtiss, L. A.; Goyette, A. N.; Gruen, D. M.; Krauss, A. R.; Schlueter, J.; Sumant, A.; Zapol, P. *Appl. Phys. Lett.* **2001**, *79*, 1441-1443.

152. Krauss, A. R.; Auciello, O.; Ding, M. Q.; Gruen, D. M.; Huang, Y.; Zhirnov, V. V.; Givargizov, E. I.; Breskin, A.; Chechen, R.; Shefer, E.; Konov, V.; Pimenov, S.; Karabutov, A.; Rakhimov, A.; Suetin, N. *J. Appl. Phys.* **2001**, *89*, 2958-2967.

153. Chen, Q.; Gruen, D. M.; Krauss, A. R.; Corrigan, T. D.; Witek, M.; Swain, G. M. *J. Electrochem. Soc.* **2001**, *148*, E44-E51.

154. Zapol, P.; Sternberg, M.; Curtiss, L. A.; Frauenheim, T.; Gruen, D. M. *Phys. Rev. B* **2002**, *6504*, art. no.-045403.

155. Krauss, A. R.; Gruen, D. M.; Auciello, O. H.; Carlisle, J. A.; Swain, G. M.; Ding, M. In *PCT Int. Appl.*; (The University of Chicago, USA). Wo, 2002, pp 44 pp.

156. Martin, H. B.; Morrison, P. W., Jr. *Electrochemical and Solid-State Letters* **2001**, *4*, E17-E20.

157. Witek, M.; Wang, J.; Stotter, J.; Hupert, M.; Haymond, S.; Sonthalia, P.; Swain, G. M.; Zak, J. K.; Chen, Q.; Gruen, D. M.; Butler, J. E.; Kobashi, K.; Tachibana, T. *Journal of Wide Bandgap Materials* **2002**, *8*, 171-188.

158. Argoitia, A.; Martin, H. B.; Rozak, E. J.; Landau, U.; Angus, J. C. *Mater. Res. Soc. Symp. Proc.* **1996**, *416*, 349-354.

159. Stotter, J. M.; Haymond, S.; Butler, J. E.; Swain, G. M.; Zak, J. K. *Abstracts of Papers, 222nd ACS National Meeting, Chicago, IL, United States, August 26-30, 2001* **2001**, ANYL-117.

160. Zak, J. K.; Butler, J. E.; Swain, G. M. *Anal. Chem.* **2001**, *73*, 908-914.

161. Xu, J. Z.; Swain, G. M. *Anal. Chem.* **1998**, *70*, 1502-1510.

162. Reuben, C.; Galun, E.; Tenne, R.; Kalish, R.; Muraki, Y.; Hashimoto, K.; Fujishima, A.; Butler, J. M.; Levy-Clement, C. *NATO ASI Ser., Ser. 3* **1995**, *1*, 137-142.

163. Granger, M. C.; Xu, J.; Strojek, J. W.; Swain, G. M. *Anal. Chim. Acta* **1999**, *397*, 145-161.

164. Gherardini, L.; Comninellis, C.; Vatistas, N. *Annali di Chim.* ***2001*** *Mar-Apr*, *91*, 161-168

165. Terashima, C.; Rao, T. N.; Sarada, B. V.; Fujishima, A. *Chemical Sensors* **2001**, *17*, 124-126.

166. Terashima, C.; Rao, T. N.; Sarada, B. V.; Tryk, D. A.; Fujishima, A. *Anal. Chem.* **2002**, *74*, 895-902.

167. Fujishima, A.; Terashima, C.; Honda, K.; Sarada, B. V.; Rao, T. N. *New Diamond and Frontier Carbon Technology* **2002**, *12*, 73-81.

168. Spataru, N.; Sarada, B. V.; Popa, E.; Tryk, D. A.; Fujishima, A. Anal. Chem. *2001 73*, 514-519

169. Show, Y. W., M. A.; Sonthalia, P.; Swain, G. M. *accepted Chem. Mater.*

170. Saterlay, A. J.; Foord, J. S.; Compton, R. G. *Analyst 1999*, *124*, 1791-1796

171. Manivannan, A.; Tryk, D. A.; Fujishima, A. *Electrochemical and Solid-State Letters* **1999**, *2*, 455-456.

172. Saterlay, A. J.; Agra-Gutierrez, C.; Taylor, M. P.; Marken, F.; Compton, R. G. *Electroanalysis* **1999**, *11*, 1083-1088.

173. Madore, C.; Duret, A.; Haenni, W.; Perret, A. *Proceedings - Electrochemical Society* **2000**, *2000-19*, 159-168.

174. Saterlay, A. J.; Marken, F.; Foord, J. S.; Compton, R. G. *Talanta* **2000**, *53*, 403-415.

175. Manivannan, A.; Seehra, M. S.; Tryk, D. A.; Fujishima, A. *Anal. Lett.* **2002**, *35*, 355-368.

176. Prado, C.; Wilkins, S. J.; Marken, F.; Compton, R. G. *Electroanalysis* **2002**, *14*, 262-272.

177. Angus, J. C. *MRS Bull.* **1996**, *21*, 4-4.

178. Angus, J. C.; Li, Z.; Sunkara, M.; Gat, R.; Anderson, A. B.; Mehandru, S. P.; Geis, M. W. *Proc. - Electrochem. Soc.* **1991**, *91-8*, 125-141.

179. Bachmann, P. K. *EMIS Datareviews Series* **1994**, *9*, 354-363.

180. Bachmann, P. K. *EMIS Datareviews Series* **1994**, *9*, 349-353.

181. Bachmann, P. K. *EMIS Datareviews Series* **1994**, *9*, 364-367.

182. Gruen, D. M. *Annual Review of Materials Science* **1999**, *29*, 211-259.

183. Spitsyn, B. V.; Aleksenko, A. E.; Sokolina, G. A.; Laptev, V. A. *New Diamond Sci. Technol., Proc. Int. Conf., 2nd* **1991**, 909-916.

184. Looi, H. J., Pang, L.Y.S. , Molloy, A.B., Jones, F., Foord, J.S., and Jackman, R.B. **1998**, *7*, 550.

185. Popa, E., Notsu, H., Miwa, T., Tryk, D. A., Fujishima, A. *Electrochem. Solid State Lett.* **1999**, 49.

186. Spear, K. E. a. D., J. P *Synthetic Diamond: Emerging CVD Science and Technology*; John Wiley & Sons, Inc.: New York, 1994.

187. Granger, M. C.; Swain, G. M. *J. Electrochem. Soc.* **1999**, *146*, 4551-4558.

188. Jolley, S.; Koppang, M.; Jackson, T.; Swain, G. M. *Anal. Chem.* **1997**, *69*, 4099-4107.

189. Perrin, D. D. *Dissociation Constant of Organic Bases in Aqueous Solution,*; London, Butterworth, 1965.

190. Swain, G. M. *J. Electrochem. Soc.* **1994**, *141*, 3382-3393.

191. Natishan, P. M. M., A. *Mater. Lett.* **1989**, *8*, 269.

192. Rosman, N. A., L.; Chabert, J.P.; Verven, G.; Lucazeau, G. *J. Appl. Phys.* **1995**, *78*, 519.

193. Martin, H. B.; Argoitia, A.; Angus, J. C.; Landau, U. *J. Electrochem. Soc.* **1999**, *146*, 2959-2964.

194. Beck, F.; Krohn, H.; Kaiser, W.; Fryda, M.; Klages, C. P.; Schafer, L. *Electrochim. Acta* **1998**, *44*, 525-532.

195. Fisher, V.; Gandini, D.; Laufer, S.; Blank, E.; Comninellis, C. *Electrochim. Acta* **1998**, *44*, 521-524.

196. Belton, D. N. S., S. J. *J. Appl. Phys.* **1989**, *66*, 4223.

197. Belton, D. N. S., S. J. *Thin Solid Films* **1992**, *212*, 68-80.

198. Tachibana, T. Y., Y.; Miyata, K.; Onishi, T.; Kobashi, K.; Tarutani, M.; Takai, Y.; Shimizu, R.; Shintani, Y. *Phys. Rev. B* **1997**, *56*, 15967.

199. Collins, A. T. *Diam. Rel. Mat.* **1992**, *1*, 457.

200. Mermoux, M.; Fayette, L.; Marcus, B.; Rosman, N.; Abello, L.; Lucazeau, G. *Physica Status Solidi A: Applied Research* **1996**, *154*, 55-68.

201. Michler, J.; Mermoux, M.; von Kaenel, Y.; Haouni, A.; Lucazeau, G.; Blank, E. *Thin Solid Films* **1999**, *357*, 189-201.

202. Chen, Q.; Granger, M. C.; Lister, T. E.; Swain, G. M. *J. Electrochem. Soc.* **1997**, *144*, 3806-3812.

203. Ushizawa, K.; Watanabe, K.; Ando, T.; Sakaguchi, I.; Nishitani-Gamo, M.; Sato, Y.; Kanda, H. *Diam. Rel. Mat.* **1998**, *7*, 1719.

204. Nicholson, R. *Analytical Chemistry* **1965**, *37*, 1351.

205. Natl. Bur. Stand. (U.S), C., II, 5, **1953**.

206. La Placa, S. P. I. o. B., Brooklyn, NY, ICDD Grant-In-Aid, **1959**.

207. Dennison, J. R.; Holtz, M.; Swain, G. *Spectroscopy* **1996**, *11*, 38-46.

208. Mermoux, M. F., L.; Marcus, B.; Rosman, N.; Abello, L.; Lucazeau, G. *Phys. Status Solidi* **1996**, *154*, 55.

209. CRC Handbook of Chemistry and Physics, t. E. **1985**.

210. Butler, J. E.; Windischmann, H. *MRS Bull.* **1998**, *23*, 22-27.

211. Frenklach, M. *J. Appl. Phys.* **1989**, *65*, 5142.

212. Hsu, W. L. *J. Vac. Sci. Technol., A* **1988**, *6*, 1803-1811.

213. McCauley, T. G.; Gruen, D. M.; Krauss, A. R. *Appl. Phys. Lett.* **1998**, *73*, 1646-1648.

214. Jiao, S.; Sumant, A.; Kirk, M. A.; Gruen, D. M.; Krauss, A. R.; Auciello, O. *J. Appl. Phys.* **2001**, *90*, 118-122.

215. Keblinski, P.; Wolf, D.; Cleri, F.; Phillpot, S. R.; Gleiter, H. *MRS Bull.* **1998**, *23*, 36-41.

216. Wang, J.; Swain, G. M.; Mermoux, M.; Lucazeau, G.; Zak, J.; Strojek, J. W. *New Diamond and Frontier Carbon Technology* **1999**, *9*, 317-343.

217. Yagi, I. N., H.; Kondo, T.; Tryk, D. A; Fujishima, A. *J. Electroanal. Chem.* **1999**, *173*, 473.

218. Alehashem, S.; Chambers, F.; Strojek, J. W.; Swain, G. M.; Ramesham, R. *Anal. Chem.* **1995**, *67*, 2812-2821.

219. Fujishima, A.; Rao, T. N.; Tryk, D. A. *Proceedings - Electrochemical Society* **2000**, *99-32*, 383-388.

220. Pleskov, Y. V.; Mazin, V. M.; Evstefeeva, Y. E.; Varnin, V. P.; Teremetskaya, I. G.; Laptev, V. A. *Electrochem. Solid State Lett.* **2000**, *3*, 141-143.

221. Vall, S. D.; Yang, H.-H.; McCreery, R. L. *Proceedings - Electrochemical Society* **1999**, *99-5*, 33-36.

222. Cvacka, J. a. S., G. M. unpublished results.

223. McDermott, C. A. K., K. R.; McCreery, R. L. *J. Electrochem. Soc.* **1993**, *140*, 2593.

224. Nemanich, R. J.; Glass, J. T.; Lucovsky, G.; Shroder, R. E. *J. Vac. Sci. Technol., A* **1988**, *6*, 1783-1787.

225. Knight, D. S.; White, W. B. *J. Mater. Res.* **1989**, *4*, 385-393.

226. Bergman, L.; Nemanich, R. J. *J. Appl. Phys.* **1995**, *78*, 6709-6719.

227. Prawer, S.; Nugent, K. W.; Jamieson, D. N.; Orwa, J. O.; Bursill, L. A.; Peng, J. L. *Chemical Physics Letters* **2000**, *332*, 93-97.

228. Ferrari, A. C.; Robertson, J. *Phys. Rev. B* **2001**, *63*, 121

229. Adams, R. N., 1969, Electrochemistry at Solid Electrodes, Marcel Dekker: New York.

230. He, L.; Anderson, J. R.; Franzen, H. F.; Johnson, D. C. *Chem. Mater.* **1997**, *9*, 715-722.

231. Luo, P., Zhang, F., Baldwin, R. P. *Anal. Chim. Acta* **1991**, *244*, 169.

232. Masui, M.; Sayo, H.; Tsuda, Y. *J. Chem. Soc., B* **1968**, 973-976.

233. Hampson, N. A.; Lee, J. B.; MacDonald, K. I.; Shaw, M. J. *J. Chem. Soc. B* **1970**, 1766-1769.

234. Hampson, N. A.; Lee, J. B.; Morley, J. R.; MacDonald, K. I.; Scanlon, B. F. *Tetrahedron* **1970**, *26*, 1109-1114.

235. Hampson, N. A.; Lee, J. B.; Morley, J. R.; Scanlon, B. F. *Can. J. Chem.* **1969**, *47*, 3729-3736.

236. Feng, J.; Johnson, D. C.; Lowery, S. N. *J. Electrochem. Soc.* **1995**, *142*, 2618-2620.

237. Popovic, N. D.; Johnson, D. C. *Anal. Chem.* **1998**, *70*, 468-472.

238. Yeo, I. H.; Johnson, D. C. *J. Electroanal. Chem.* **2001**, *495*, 110-119.

239. Yeo, I. H.; Lee, Y. S.; Mho, S. I.; Johnson, D. C. *J. Electrochem. Soc.* **1992**, *139*, L49-L50.

240. Yeo, I. H.; Kim, S.; Jacobson, R.; Johnson, D. C. *J. Electrochem. Soc.* **1989**, *136*, 1395-1401.

241. Yeo, I. H.; Johnson, D. C. *J. Electroanal. Chem.* **2000**, *484*, 157-163.

242. Popovic, N. D.; Johnson, D. C. *Anal. Chem.* **1998**, *70*, 468-472.

243. Austin-Harrison, D. S.; Johnson, D. C. *Electroanalysis* **1989**, *1*, 189-197.

244. Feng, J.; Houk, L. L.; Johnson, D. C.; Lowery, S. N.; Carey, J. J. *J. Electrochem. Soc.* **1995**, *142*, 3626-3632.

245. Feng, J.; Johnson, D. C.; Lowery, S. N.; Carey, J. J. *J. Electrochem. Soc.* **1994**, *141*, 2708-2711.

246. Hines, T. G.; Johnson, D. C. In *U.S.*; (Pine Instrument Co., USA). Us, 1975, pp 6 pp.

247. Houk, L. L.; Johnson, S. K.; Feng, J.; Houk, R. S.; Johnson, D. C. *J. Appl. Electrochem.* **1998**, *28*, 1167-1177.

248. Johll, M. E.; Wong, S. S.; Johnson, D. C. *Electroanalysis* **1999**, *11*, 1049-1054.

249. Johnson, D. C. *Clean and Efficient Processing: Electrochemical Technology for Synthesis, Separations, Recycle, and Environmental Improvement, International Forum, Electrolysis in the C hemical Industry, 12th, Clearwater Beach, Fla., Oct. 11-15,***1998**, 197-220 (Abstract)

250. Johnson, D. C.; Feng, J.; Houk, L. L. *Electrochim. Acta* **2000**, *46*, 323-330.

251. Johnson, D. C.; Houk, L. L.; Feng, J. In *U.S.*; (United States Dept. of Energy, USA), 2001, pp 15 pp.

252. Johnson, D. C.; Polta, J. A.; Polta, T. Z.; Neuburger, G. G.; Johnson, J.; Tang, A. P. C.; Yeo, I. H.; Baur, J. *J. Chem. Soc., Faraday Trans. 1* **1986**, *82*, 1081-1098.

253. Johnson, D. C.; Ryan, M. D.; Wilson, G. S. *Anal. Chem.* **1986**, *58*, 33R-49R.

254. Johnson, S. K.; Houk, L. L.; Feng, J.; Houk, R. S.; Johnson, D. C. *Env. Sci. Tech.* **1999**, *33*, 2638-2644.

255. Mho, S.; Johnson, D. C. *J. Electroanal. Chem.* **2001**, *495*, 152-159.

256. Xu, J. S.; Granger, M. C.; Chen, Q. Y.; Strojek, J. W.; Lister, T. E.; Swain, G. M. *Anal. Chem.* **1997**, *69*, A591-A597.

257. Xu, J., 2000, Logan, UT.

258. Swain, G. M. *Adv. Mater. (Weinheim, Ger.)* **1994**, *6*, 388-392.

259. Koppang, M. D.; Witek, M.; Blau, J.; Swain, G. M. *Anal. Chem.* **1999**, *71*, 1188-1195.

260. Ager, J. W.; Walukiewicz, W.; McCluskey, M.; Plano, M. A.; Landstrass, M. I. *Appl. Phys. Lett.* **1995**, *66*, 616-618.

261. Gonon, P.; Deneuville, A.; Fontaine, F.; Gheeraert, E.; Campargue, A.; Chenevier, M.; Rodolphe, S. *J. Appl. Phys.* **1995**, *78*, 7404-7406.

262. Gonon, P.; Gheeraert, E.; Deneuville, A.; Fontaine, F.; Abello, L.; Lucazeau, G. *J. Appl. Phys.* **1995**, *78*, 7059-7062.

263. Ushizawa, K.; Gamo, M. N.; Xiao, C.; Watanabe, K.; Sato, Y.; Ando, T. *Proceedings - Electrochemical Society* **2000**, *99-32*, 247-251.

264. Robins, L. H.; Farabaugh, E. N.; Feldman, A. *J. Mater. Res.* **1990**, *5*, 2456-2468.

265. Chow, Y. L.; Danen, W. C.; Nelsen, S. F.; Rosenblatt, D. H. *Chem. Rev.* **1978**, *78*, 243-274.

266. Patai, S. *The Chemistry of Amino Groups.*; John Wiley and Sons, 1982.

267. Baizer, M. M. *Organic electrochemistry; an introduction and a guide.*; M. Dekker: New York, 1973.

268. Parsons, R.; VanderNoot, T. *J. Electroanal. Chem. Interfacial Electrochem.* **1988**, *257*, 9-45.

269. Hull, L. A.; Davis, G. T.; Rosenblatt, D. H.; Mann, C. K. *J. Phys. Chem.* **1969**, *73*, 2142-2146.

270. Portis, L. C.; Bhat, V. V.; Mann, C. K. *J. Org. Chem.* **1970**, *35*, 2175-2178.

271. Buckley, D.; Dunstan, S.; Henbest, H. B. *J. Chem. Soc.* **1957**, 4901-4905.

272. Curragh, E. F.; Henbest, H. B.; Thomas, A. *J. Chem. Soc.* **1960**, 3559-3563.

273. Shechter, H.; Rawalay, S. S. *J. Am. Chem. Soc.* **1964**, *86*, 1706-1709.

274. Dunstan, S.; Henbest, H. B. *J. Chem. Soc.* **1957**, 4905-4908.

275. Nakagawa, K.; Onoue, H. *Chem. Commun.* **1965**, 396.

276. Nakagawa, K.; Onoue, H. *Tetrahedron Letters* **1965**, 1433-1436.

277. Clarke, T. G.; Hampson, N. A.; Lee, J. B.; Morley, J. R.; Scanlon, B. *Tetrahedron Lett.* **1968**, 5685-5688.

278. Clarke, T. G.; Hampson, N. A.; Lee, J. B.; Morley, J. R.; Scanlon, B. F. *J. Chem. Soc., C* **1970**, 815-817.

279. Rosenblatt, D. H.; Davis, G. T.; Hull, L. A.; Forberg, G. D. *J. Org. Chem.* **1968**, *33*, 1649-1650.

280. Mann, C. K. *Anal. Chem.* **1964**, *36*, 2424-2426.

281. Canizares, P.; Martinez, F.; Diaz, M.; Garcia-Gomez, J.; Rodrigo, M. A. *J. Electrochem. Soc.* **2002**, *149*, D118-D124.

282. Foti, G.; Gandini, D.; Comninellis, C.; Perret, A.; Haenni, W. *Electrochemical and Solid-State Letters* **1999**, *2*, 228-230.

283. Hull, L. A.; Giordano, W. P.; Rosenblatt, D. H.; Davis, G. T.; Mann, C. K.; Milliken, S. B. *J. Phys. Chem.* **1969**, *73*, 2147-2152.

284. Hull, L. A.; Davis, G. T.; Rosenblatt, D. H. *J. Amer. Chem. Soc.* **1969**, *91*, 6247-6250.

285. Ge, J.; Johnson, D. C. *Book of Abstracts, 210th ACS National Meeting, Chicago, IL, August 20-24* **1995**, ANYL-065.

286. Xu, J.; Swain, G. M. *Anal. Chem.* **1998**, *70*, 1502-1510.

287. Treimer, S. E.; Feng, J. R.; Scholten, M. D.; Johnson, D. C.; Davenport, A. J. *J. Electrochem. Soc.* **2001**, *148*, E459-E463.

288. Kawagoe, K. T.; Johnson, D. C. *J. Electrochem. Soc.* **1994**, *141*, 3404-3409.

289. Vitt, J. E.; Johnson, D. C. *J. Electrochem. Soc.* **1992**, *139*, 774-778.

290. Bard, A. J. F., L. R. *Electrochemical Methods*; John Wiley & Sons, 1980.

291. Witek, M. A.; Swain, G. M. *Anal. Chim. Acta* **2001**, *440*, 119-129.

292. Hughes, S.; Johnson, D. C. *Anal. Chim. Acta* **1983**, *149*, 1-10.

293. Casella, I. G.; Cataldi, T. R. I.; Salvi, A. M.; Desimoni, E. *Anal. Chem.* **1993**, *65*, 3143-3150.

294. Treimer, S.; Tang, A.; Johnson, D. C. *Electroanalysis* **2002**, *14*, 165-171.

295. Johll, M. E.; Asala, K. S.; Swarts, M.; Anderegg, J. W.; Johnson, D. C. *Electroanalysis* **2000**, *12*, 248-254.

296. Witek, M.; Swain, G. M. *submitted to Anal. Chem.*. **2002**.

297. Ruzicka, J.; Hansen, E. H. *Chemtech* **1979**, *9*, 756-764.

298. Ruzicka, J.; Hansen, E. H. *Anal. Chim. Acta* **1980**, *114*, 19-44.

299. Ruzicka, J. *Anal. Chem.* **1983**, *55*, 1040A-1042A, 1044A, 1046A-1048A, 1050A, 1052A-1053A.

300. Ruzicka, J.; Hansen, E. H. *TrAC, Trends in Analytical Chemistry* **1998**, *17*, 69-73.

301. Ruzicka, J.; Hansen, E. H. *Anal. Chem.* **2000**, *72*, 212A-217A.

302. Ruzicka, J. *Anal. Chem.* **2001**, *73*, 385A.

303. LaCourse, W. R. *Pulsed Electrochemical Detection in High-Performance Liquid Chromatography*, 1997.

304. Goss, C. A.; Brumfield, J. C.; Irene, E. A.; Murray, R. W. *Anal. Chem.* **1993**, *65*, 1378-1389.

305. Hathcock, K. W.; Brumfield, J. C.; Goss, C. A.; Irene, E. A.; Murray, R. W. *Anal. Chem.* **1995**, *67*, 2201-2206.

306. Notsu, H.; Yagi, I.; Tatsuma, T.; Tryk, D. A.; Fujishima, A. *Electrochemical and Solid-State Letters* **1999**, *2*, 522-524.

307. Martin, H. B.; Argoitia, A.; Landau, U.; Anderson, A. B.; Angus, J. C. *J. Electrochem. Soc.* **1996**, *143*, L133-L136.